Pore-Scale Modelling of Induced-Polarization Mechanisms in Geologic Materials

Dissertation
zur
Erlangung des Doktorgrades (Dr. rer. nat.)
der
Mathematisch-Naturwissenschaftlichen Fakultät
der
Rheinischen Friedrich-Wilhelms-Universität Bonn

vorgelegt von
Matthias Benedikt Bücker
aus
Augsburg

Bonn 2018

Angefertigt mit Genehmigung der Mathematisch-Naturwissenschaftlichen
Fakultät der Rheinischen Friedrich-Wilhelms-Universität Bonn

1. Gutachter: Prof. Dr. Andreas Kemna
2. Gutachter: Prof. Dr. Andreas Hördt

Tag der Promotion: 06.09.2018
Erscheinungsjahr: 2019

Abstract

This thesis is concerned with mechanistic pore-scale models, which relate the induced-polarization (IP) response of geologic materials to the underlying physical and chemical processes. Although a sound understanding of these processes is essential for the interpretation of measured IP responses, the development of suitable mechanistic models is lagging far behind the fast growing amount of experimental IP data. Therefore, the main objective of this thesis is to improve theoretical models and advance the general understanding of the polarization processes.

The first development is an analytic model to predict the influence of an immiscible liquid hydrocarbon phase on the membrane-polarization mechanism occurring in electrolyte-filled pore constrictions. The hydrocarbon is modelled as an electrically insulating phase with a negatively charged surface. Magnitude and phase of the predicted electrical conductivity of hydrocarbon-contaminated materials decrease with increasing hydrocarbon saturation irrespective of whether the hydrocarbon phase is wetting or non-wetting. Only non-wetting hydrocarbon droplets with highly charged surfaces yield an increase of the magnitude with the hydrocarbon saturation and a slight increase of the phase at intermediate hydrocarbon concentrations. This prediction offers the first theoretical explanation for a similar experimentally determined relation between complex conductivity and hydrocarbon saturation.

The next two parts of this thesis examine the electrode-polarization mechanism responsible for the IP response of metal-bearing materials. The polarization of uncharged metallic particles is studied based on an electrochemical model, which includes the effect of oxidation-reduction reactions at the particle surface. The full solution of the underlying Poisson-Nernst-Planck (PNP) system is presented, which allows to visualize the micro-scale manifestations of two simultaneously acting polarization mechanisms. The first mechanism is related to the dynamic charging of field-induced diffuse layers and the second is a volume-diffusion mechanism activated by reaction currents through the particle surface. For the relaxation times of both processes analytic expressions are derived and a critical particle radius is determined. While the response of particles smaller than this radius is mainly determined by the diffuse-layer polarization, the effect of the volume-diffusion mechanism becomes significant around larger particles.

The model is then extended to investigate the effect of surface charge on electrode polarization. Besides the dynamic charging of field-induced diffuse layers and the volume-diffusion processes related to the reaction currents, the numeric

solution of the modified PNP system reveals the action of an additional volume-diffusion process caused by the unequal transport rates of anions and cations within the static diffuse covering the charged surface. This mechanism is found to have a second-order effect on the macroscopic polarization response, which is still dominated by the first two mechanisms. While the volume-diffusion process due to the reaction currents remains practically unaffected by the surface charge, a moderate increase of the low-frequency conductivity and the relaxation time as well as a slight reduction of the polarization magnitude with the surface charge are observed if the diffuse-layer relaxation dominates, i.e. in the case of small particles.

In the last part of this thesis, the coupled polarization of Stern and diffuse layers covering dielectric surfaces is treated in a generalized numeric framework. First, this framework is used to model the response of spherical particles and guide the development of an improved analytic model for the coupled polarization of Stern and diffuse layer. Subsequently, it is applied to a cylindrical pore-constriction geometry. In the limiting case of a pure diffuse-layer polarization, the corresponding numeric results can be matched by an improved analytic membrane-polarization model. In both geometries, the response of the Stern layer dominates as long as the charged surfaces are not interconnected at the system scale. With increasing degree of interconnectivity, however, the response of the diffuse layer becomes more important and in the case of fully interconnected surfaces becomes as strong as the response of the Stern layer.

In summary, this thesis brings together significant improvements of analytic models for all relevant induced-polarization mechanisms: Membrane polarization, electrode polarization, and Stern- and diffuse-layer polarization. The carefully validated numeric modelling framework furthermore lays the foundation for the future investigation of more realistic geometrical configurations of the various solid and liquid phases of real geologic materials.

Zusammenfassung

Gegenstand dieser Dissertation sind mechanistische Porenskalenmodelle, die die Induzierte Polarisation (IP) geologischer Materialien mit den ihr zugrunde liegenden physikalischen und chemischen Prozessen verknüpfen. Obwohl ein umfassendes Verständnis dieser Prozesse für die Interpretation immer neuer experimenteller IP Daten wichtig wäre, hängt die Entwicklung mechanistischer Modelle weit hinterher. Ziel dieser Dissertation ist es daher, theoretische Modelle weiterzuentwickeln und damit das grundlegende Verständnis der Polarisationsprozesse zu verbessern.

Den ersten Beitrag dazu liefert ein analytisches Modell, das den Einfluss unvermischbarer flüssiger Kohlenwasserstoffe (KW) auf die Membranpolarisation in elektrolytgefüllten Porenengstellen vorhersagt. Der flüssige KW wird hier als nichtleitende Phase mit negativ geladener Oberfläche modelliert. Betrag und Phase der resultierenden elektrischen Leitfähigkeit nehmen mit zunehmendem KW-Anteil ab – unabhängig davon, ob der KW die benetzende oder die nichtbenetzende Phase ist. Nur im Falle stark negativ geladener nicht-benetzender KW-Tropfen nimmt der Betrag mit dem KW-Anteil zu. Auch die Phase durchläuft hier zunächst ein Maximum bevor sie bei hohen KW-Anteilen schließlich abfällt. Diese Vorhersage kann erstmals einen ähnlichen experimentell nachgewiesenen Zusammenhang zwischen komplexer elektrischer Leitfähigkeit und KW-Anteil theoretisch erklären.

Die folgenden zwei Teile behandeln die für die starke IP Antwort metallhaltiger Materialien verantwortliche Elektrodenpolarisation. Die Polarisierung ungeladener metallischer Partikel wird mithilfe eines elektrochemischen Modells untersucht, das auch Redoxreaktionen an der Partikeloberfläche einschließt. Die hier vorgestellte vollständige Lösung des zugrunde liegenden Poisson-Nernst-Planck (PNP) Gleichungssystems ermöglicht es die mikroskopischen Auswirkungen zweier gleichzeitig ablaufender Mechanismen grafisch darzustellen: Das dynamische Laden feldinduzierter diffuser Schichten und einen Volumendiffusionsmechanismus, der von Reaktionsströmen durch die Partikeloberfläche aktiviert wird. Für die Relaxationszeiten beider Prozesse werden analytische Ausdrücke abgeleitet und ein kritischer Partikelradius bestimmt. Während das Verhalten von Partikeln mit geringerem Radius hauptsächlich mit der Polarisation der diffusen Schicht zusammenhängt, wird im Fall größerer Partikel der Volumendiffusionsmechanismus bestimmend.

Im Folgenden wird dieses Modell erweitert, um die Auswirkung elektrischer Ladungen an der Metalloberfläche auf die Elektrodenpolarisation zu untersu-

chen. Neben der dynamischen Ladung der feldinduzierten diffusen Schichten und dem durch die Reaktionsströme bedingten Volumendiffusionsmechanismus beschreibt die numerische Lösung des erweiterten PNP Systems einen weiteren Volumendiffusionsprozess. Dieser wird durch die unterschiedlichen Anionen- und Kationenflüsse in der statischen diffusen Schicht an der geladenen Grenzfläche hervorgerufen, beeinflusst die makroskopische Antwort, allerdings nur geringfügig: Während der durch die Reaktionsströme hervorgerufene Volumendiffusionsprozess praktisch unverändert bleibt, macht sich die geladene Partikeloberfläche genau dann durch einen moderaten Anstieg von Gleichstromleitfähigkeit und Relaxationszeit sowie durch eine leichte Abnahme der Polarisationsstärke bemerkbar, wenn die Relaxation der diffusen Schicht wichtig wird, d.h. vor allem im Falle sehr kleiner Partikel.
Der letzte Teil widmet sich der gleichzeitigen Polarisierung von Stern-Schicht und diffuser Schicht an der geladenen Oberfläche dielektrischer Materialien. Ein entsprechender numerischer Modellierungsansatz wird zunächst benutzt, um die Polarisierung kugelförmiger Partikel zu simulieren und die analytische Modellierung der gleichzeitigen Polarisierung von Stern- und diffuser Schicht zu verbessern. Im Folgenden wird dieser Ansatz dann auf eine zylindrische Porenengstelle angewandt. Ein zu diesem Zweck verbessertes analytisches Modell der Membranpolarisation kann die Simulationsergebnisse allerdings nur im Grenzfall einer reinen Polarisierung der diffusen Schicht erklären. Solange die geladenen Oberflächen auf der Systemskala nicht durchgehend verbunden sind dominiert – wie im Falle kugelförmiger Partikel – die Polarisierung der Stern-Schicht. Mit zunehmender Kontinuität der Schichten nimmt der Beitrag der Polarisierung der diffusen Schicht aber zu. Bilden die Oberflächen durchgehende Verbindungen, sind beide Beiträge gleich groß.
Insgesamt vereint diese Dissertation wichtige Weiterentwicklungen analytischer Modelle aller relevanten Mechanismen der induzierten Polarisation: Membranpolarisation, Elektrodenpolarisation, sowie Polarisation von Stern- und diffuser Schicht. Der sorgfältig validierte numerische Modellierungsansatz bildet außerdem die Grundlage für zukünftige Untersuchungen komplexerer geometrischer Anordnungen der verschiedenen festen und flüssigen Phasen, die reale geologische Materialien besser abbilden können.

Acknowledgements

The idea of this thesis originated six years ago, when I met Adrián Flores Orozco during the IP workshop in Golden, Colorado. Fate had just sent me to Mexico and it is thanks to the confidence Andreas Kemna and Adrián had in me that I was able to start this project even though I was abroad. I was very lucky that both weren't afraid of the extra efforts and costs that a distance PhD involves, and I will always be thankful for that. Besides for his indispensable support, I wish to thank Andreas for our encouraging discussions and his guidance during the different phases of this project. I am especially happy that we share a common interest in all the apparently insignificant details, which fueled inspiring correspondences that more than once got us to recognize that exactly these details were of great importance. I thank Adrián for his constant help provided during countless calls and unexpectedly frequent personal meetings on both sides of the Atlantic Ocean. I am also very grateful to Adrián for encouraging me to do "real" geophysics in the field, for the many opportunities to collaborate in his projects, and for sharing his rich practical experience with me.

I wish to express my special thanks and appreciation to Sabine Undorf for our inspiring cooperation right in the beginning of this project, for laying the foundation for the numerical modelling, and for her continued support during the preparation of chapters 5 and 6 of this thesis. Andreas Hördt provided valuable feedback that helped to improve chapter 3 and kindly agreed to be the second referee of this thesis. Andreas also initially brought me in contact with the IP method and awoke my curiosity about the polarization mechanisms, for what I will always be grateful. I wish to acknowledge Edmundo Placencia Gómez and Lee Slater the valuable discussions that motivated the investigation of the electrode-polarization mechanism treated in chapters 4 and 5.

Besides Andreas Kemna and Andreas Hördt, I also gratefully acknowledge Prof. Dr. Clemens Simmer and Prof. Dr. Jochen Garcke for their indispensable contribution as members of my PhD committee.

Without the great help of Lisa Takacs, Maximilian Weigand, and Johannes Kenkel many administrative tasks would have been much more difficult to manage from a distance and the support of Andreas Dreist was indispensable for the remote access to the COMSOL software running on the server in Bonn. I also wish to thank them and all other members of the Department of Geophysics of the University of Bonn as well as the members of the Research Group Geophysics of the TU Wien for the warm welcome received during my sporadic visits. In Mexico I have received a lot of help and support from Carlos Pita, his

family, and the staff of Geotem Ingeniería S.A. de C.V., Edgar Sánchez Álvaro and the Departamento de Sismotectónica y Exploración Geofísica of the CFE, Sergio Rodríguez Elizarrarás, Wendy Morales Barrera, Gustavo Tolson, the Instituto de Geofísica and the Instituto de Geología of the Universidad Nacional Autónoma de México. Many thanks to them and all people and institutions I might not have mentioned here.

I gratefully acknowledge the Austrian Federal Ministry of Science, Research and Economy (project: Development of geophysical exploration methods for the characterization of mine-tailings towards exploitation) and the German Academic Exchange Service DAAD (Kennziffer D/12/44360) for the scholarships received during the work on important parts of this thesis. Additional financial support, particularly for the developments presented in chapter 3 of this thesis, was provided by the research project GEOCON, Advancing GEOlogical, geophysical and CONtaminant monitoring technologies for contaminated site investigation (contract 1305-00004B). The funding for GEOCON is provided by The Danish Council for Strategic Research under the Programme commission on sustainable energy and environment.

Finally, I wish to thank my parents for all their support, advice, and confidence, without which I would not have been able to reach this point. In the same manner, I want to thank my brother, my sisters, and my closest friends for their constant encouragement. Liseth and Lara and Jonas, I am indebted to you for your unconditional love and endless support. You have accompanied me through all the ups and downs of the work on this thesis and you have dedicated a lot of time and power to make this project succeed. Thank you so much!

Matthias Bücker

Contents

CHAPTER 1

Introduction

1.1 Background

Geologic materials are complex systems of solid, liquid, and gaseous phases. The electrical bulk properties of such multi-component systems are determined by the individual properties of the different phases and their microscopic geometric configuration. Due to the high electrical resistivity of gaseous and most solid phases, electrolytic conduction in the aqueous liquid phase is the principle mechanism of charge transport. While the bulk aqueous phase usually contributes a purely resistive component, polarizable interfacial regions at the geometrical boundaries of the aqueous phase introduce a capacitive component (energy storage) to the electrical bulk conductivity of geologic materials. In the low-frequency range, i.e. for excitations at frequencies < 1 MHz, the complex electrical conductivity readily describes both contributions, i.e. resistive and capacitive components.

Induced polarization (IP) is the geophysical method used to assess the complex electrical conductivity of geologic materials. In geophysical practice, where this method is also known as complex conductivity or complex resistivity, frequency-domain IP measurements are typically carried out in the range between 1 mHz and 1 kHz. Because of the strong IP response observed around highly-conductive particles, historically the method has been developed and employed for the exploration of metal ore deposits (e.g. Seigel et al., 2007). During the last two to three decades, the fast improvement of measurement devices and imaging algorithms laid the basis for a continued extension of the application range to non-metallic materials with less pronounced IP responses (e.g. Kemna et al., 2012).

In particular, there is a growing interest in using the IP method for environmental investigations in the shallow subsurface. New applications make use of the sensitivity of spectral IP data to textural properties (e.g. grain/pore size, specific surface area) to improve the lithological characterization of sediments

and sedimentary rocks and infer other texture-controlled properties such as hydraulic permeability (e.g. Slater and Glaser, 2003; Hördt et al., 2009). Also the (partial) displacement of pore water by liquid hydrocarbon contaminants has been shown to cause characteristic spectral IP responses (e.g. Flores Orozco et al., 2012; Johansson et al., 2015). Yet, geometrical properties of the different solid and liquid phases are not the only quantities controlling the IP response. Several studies have examined the sensitivity of the method to chemical properties of the pore-filling electrolyte such as composition, salinity, and pH (e.g. Weller and Slater, 2012; Lesmes and Frye, 2001), and to chemical changes in the fluid or on the surface of the solid phase caused by biogeochemical processes (e.g. Atekwana and Slater, 2009; Flores Orozco et al., 2011).

Also IP surveys for the characterization of metallic targets are experiencing a renaissance. While for the classic use in the mining industry the determination of size and volume content of metallic minerals played a key role, recent environmental studies pay special attention to a possible sensitivity of the method to the surface state of metallic particles (e.g. reactivity, surface potential). Among the latter are IP applications for the monitoring of permeable reactive barriers and metallic nano-particle injections (e.g. Slater and Binley, 2006; Flores Orozco et al., 2015; Abdel Aal et al., 2017), the detection of iron sulphide accumulations accompanying bioremediation experiments and naturally reduced zones related to biogeochemical hot spots (Flores Orozco et al., 2011; Wainwright et al., 2015).

Empirical polarization models are often used to reduce the extensive (spectral) IP data sets to a few meaningful parameters and facilitate the comparison of different measurements. Historically, Cole-Cole relaxation models (Cole and Cole, 1941; Pelton et al., 1978), which provide a practical means to adjust spectra with one clearly distinguishable relaxation peak, have been used extensively for this purpose. More recently, the decomposition of more complex spectra into a series of suitable Debye relaxation models (e.g. Nordsiek and Weller, 2008) has gained popularity. Although these empirical models are very useful to adjust measured data, they are not suited to explain the microscopic causes of specific signatures nor do they provide a link between the bulk electrical and petropysical properties of a geologic material.

1.2 Polarization mechanisms and theoretical models

To exploit the complete wealth of information contained in the measured spectral IP responses, a thorough understanding of the causative processes is essential.

On the basis of physical principles, mechanistic models relate the observed IP response to a limited set of physical and chemical parameters and give insight into the working principles of polarization mechanisms. In this manner, the IP response of different geologic materials has been attributed to five basic processes: (1) electrode polarization, (2) polarization of the Stern layer of the electric double layer (EDL), (3) polarization of the diffuse layer of the EDL, (4) membrane polarization, and (5) Maxwell-Wagner polarization.

All mechanistic models describing these mechanisms are based on solutions to the Poisson-Nernst-Planck (PNP) system of partial differential equations, which is used to describe ion transport (and polarization) in the pore-filling electrolyte and the boundary regions next to the solid-liquid interfaces. The model-specific characteristics of the obtained polarization responses originate from the particular geometrical configurations of the different phases and the physical and chemical properties of the phase boundaries accounted for by suitable boundary conditions.

Electrode polarization is a collective concept describing the interplay of different field-induced charge transport and storage mechanisms at metal-electrolyte interfaces. For geophysical applications, ideally polarizable surfaces characterized by an absence of charge-transfer reactions, and thus a zero faradaic current between the metal and the electrolyte, are of little relevance. Therefore, Angoran and Madden (1977) and Klein and Shuey (1978) investigated the effect of reaction currents through the solid-liquid interface, which render the polarization of the particle surfaces imperfect and largely affect the polarization response. Wong (1979) included these findings into a polarization model for suspensions of highly conductive particles, which was based on the solution of the PNP system for two inactive and one active ion species. Wong and Strangway (1981) extended this model to the case of elongated particles.

More recent theoretical treatments of the electrode-polarization mechanism in geophysical literature examined the role of the Stern layer at the metal surface (Merriam, 2007) or attempted to interpret the response of the Wong model in terms of a complex surface conductivity (e.g. Gurin et al., 2015; Placencia-Gómez and Slater, 2015). Because many relevant ore minerals are rather semiconductors than metallic conductors, Revil et al. (2015b) and Misra et al. (2016a) developed models for the polarization of semiconducting particles.

The Stern layer is the inner layer of the EDL, which develops on charged surfaces in contact with an electrolyte solution. Schwarz (1962) developed a first theoretical model of the diffusion-controlled polarization of this layer of firmly

bound ions to describe the large low-frequency dielectric dispersion of suspensions of dielectric (non-conductive) particles. His model was based on the PNP system to describe the field-induced displacement of the Stern-layer ions along the surface of spherical particles. Subsequently, Schurr (1964) included the conductivity increment caused by the excess of less firmly bound ions in the outer diffuse layer into Schwarz's model. However, this increment described a purely resistive contribution and did not account for an additional polarization of the diffuse layer as discussed in the next paragraph. Lyklema et al. (1983) examined the coupling of the field-induced charges in the Stern layer to the charges in the electrolyte (and the diffuse layer). Their treatment results in a correction to the relaxation time of the Schwarz model, which predicts a significant reduction of this spectral parameter. More recently, Leroy et al. (2008) adopted Schurr's model and included a detailed electro-chemical description of Stern and diffuse layer (e.g. Revil and Glover, 1997, 1998). This model has been successfully applied to predict the complex conductivity of granular media (Leroy et al., 2008) and later extended to account for an additional electrically insulating liquid phase to predict the response of sand-oil mixtures (Schmutz et al., 2010).

As mentioned above, the ions of the diffuse layer are much less firmly bound to the charged surface, and thus mainly increment the low-frequency conductivity of the composite material. However, the unequal anion and cation concentrations in this layer additionally give rise to a volume- or concentration-polarization mechanism. This phenomenon has been described theoretically by Dukhin and Shilov (1974), who developed a theory for the fluxes through thin diffuse layers. Also the models developed by Fixman (1980), Hinch et al. (1984), and Chew and Sen (1982a) address the volume-diffusion mechanism of the diffuse layer. To enable an analytic treatment, all these models are limited to thin diffuse layers compared to the particle size, sufficiently small surface potentials, and monovalent symmetric electrolytes. The numeric solution presented by DeLacey and White (1981) removed many of the limitations. More recently, Shilov et al. (2001) extend the classic Dukhin-Shilov theory by including the effect of the Maxwell-Wagner polarization at high frequencies.

Although the Stern-layer polarization model by Schurr (1964) (and later developments) contained a simple consideration of the surface conductivity of the diffuse layer and the model by Lyklema et al. (1983) included a coupling with the charges beyond the Stern layer, non of the above model describes the simultaneous polarization of both parts of the EDL. The first approach to assess the relative importance of the two processes was made by de Lima and Sharma

(1992) who compared the polarization magnitudes of the Schwarz-Schurr model and Fixman's model. While de Lima and Sharma (1992) treated both models separately, Lesmes and Morgan (2001) developed a first combined polarization model based on simple superposition of the individual responses. Shilov et al. (2001) describe a modification of the Dukhin-Shilov theory, which accounts for the contribution of Stern-layer ions to the diffuse-layer polarization as proposed by Kijlstra et al. (1992).

The occurrence of membrane polarization is generally being related to two scenarios, which cation transport is enhanced relative to anion transport: (1) In clay-rich zones along the pore channel, the high negative charge on clay-mineral surfaces significantly increases the concentration of cations and (2) in sufficiently narrow pore constrictions, diffuse layers coating (even moderately) charged pore surfaces have an important share of ion transport. Both clay-rich zones and pore constrictions are ion selective and cause a concentration-polarization mechanism similar to the one described as diffuse-layer polarization around spherical particles. A first one-dimensional model of this mechanism in geologic materials was developed by Marshall and Madden (1959) in order to estimate its possible magnitude. While Marshall and Madden just postulated different transport rates of anions and cations, subsequent treatments attributed the latter to the properties of the EDL at the pore wall (Fridrikhsberg and Sidorova, 1961; Buchheim and Irmer, 1979; Titov et al., 2002, 2004; Bücker and Hördt, 2013b). Still based on the simple assumption of unequal transport properties within pore constrictions, Blaschek and Hördt (2009) used numeric methods to study the response of more complex one- and two-dimensional pore networks. Volkmann and Klitzsch (2010) improved this numerical approach assuming unequal effective ion mobilities within a thin surface layer only. Finally, Bücker and Hördt (2013a) proposed an analytic model, which explicitly included pore radii and surface conductivity due to Stern and diffuse layer into the one-dimensional impedance model by Marshall and Madden. Subsequent extensions of this model allowed to predict the effect of temperature (Bairlein et al., 2016), fluid salinity, and pH (Hördt et al., 2016) on the polarization response.

If considered, the Maxwell-Wagner polarization (Maxwell, 1892; Wagner, 1914) usually dominates the high-frequency behaviour of the polarization models. It consists in the accumulation of surface charge along the geometrical boundaries between two (or more) phases with different electric conductivities and/or dielectric constants, which balances the unequal conduction and displacement current densities through the adjacent bulk media. O'Konski (1960) introduced the con-

cept of surface conductivity, which allowed to account for the effect of bound ions encountered at charged phase boundaries. Garcia et al. (1985) showed that the interfacial polarization changes significantly, if instead of a homogeneous conductivity local field-induced concentration variations are considered in the electrolyte solution.

1.3 Objectives and structure

The fundamental theoretical descriptions of these five main polarization mechanisms are well established. However, the interplay and relative importance of the different processes in real geologic materials as well as the control exerted by the numerous physical and chemical properties of the involved phases and phase boundaries is far from being fully understood (e.g. Kemna et al., 2012). The main shortcomings of the theoretical description of IP can be summarized in the following two issues: (1) Polarization models treat one or at most a few mechanisms in an isolated manner and no approach allows to study the relative importance of all mechanisms in a generalized theoretical framework. (2) Polarization models are too simple to account for slightly more complex situations, in which more than one solid (mineral) and one liquid (electrolyte) phase play an important role.
Therefore, the principal objective of this thesis is to advance the theoretical foundation of the IP method providing improved theoretical models for specific situations and initiate the development of a generalized modelling framework. These objectives are mainly addressed in chapters 3 through 6, which are based on eponymous self-contained manuscripts published or intended for publication in peer-reviewed journals.

- Chapter 3 describes a new analytic model to predict the characteristic response of hydrocarbon-contaminated sediments and rocks. This development is based on an earlier membrane-polarization model for clean materials (Bücker and Hördt, 2013a) and can be understood as a complement to the model proposed by Schmutz et al. (2010), which only examined the effect of a liquid hydrocarbon phase on the Stern-layer polarization mechanism.

- Chapter 4 reviews the electrode-polarization model by Wong (1979) in detail. Besides the derivation of explicit relaxation-time formulae and the full solution to the PNP system, which improve the mathematical

description of this polarization process, this chapter also aims at advancing the general understanding of this electrode-polarization model.

- Chapter 5 extends Wong's electrode-polarization model by including the effect of a non-zero charge at the surface of the metallic particles. As this problem cannot be solved analytically, a numeric solution of the PNP system is proposed, which allows to examine the role of surface charge in the electrode-polarization process and also lays the foundation for the development of a generalized numeric modelling framework.

- Chapter 6 describes a generalized theoretical treatment of Stern- and diffuse-layer polarization in dielectric porous media. The numeric solution of this problem around dielectric particles and in a pore-constriction setup allows to study the relative importance of both polarization processes depending on the geometric configuration of solid and liquid phases. The numeric solution is also used to guide the identification of improved analytic models for the combined Stern- and diffuse-layer polarization around spherical particles and the membrane-polarization mechanisms due to the diffuse layer.

These principal chapters are prefaced by an introductory chapter on the basic mathematics, physical concepts, and geometrical models used for the pore-scale modelling of IP signatures (chapter 2). A comprehensive conclusion including a brief discussion of the future perspectives of this research topic completes the thesis (chapter 7).

CHAPTER 2

Basic aspects and preliminary considerations

The induced-polarization method assesses electrical conduction (charge transport) and polarization (charge storage) properties of the subsurface. Although geologic materials have a complex micro-structure, the characteristic length scale of geophysical measurements is typically many orders of magnitude larger than would be required to resolve such microscopic heterogeneity. Even though, the bulk electrical properties are strongly correlated to relevant petrophysical parameters such as porosity, saturation, specific surface area, surface charge, metal content, etc., from which derives the power of geoelectric measurements. A sound physical understanding of these empirically established relations has the potential to significantly improve the interpretation of geophysical data. Therefore, the following chapters will use basic physical principles to examine some particular micro-structures in order to arrive at mathematical models that underpin and explain the experimentally observed relations.

The objective of the present chapter is to provide the physical, mathematical, and conceptual foundation of the principles used to develop these models. The first section (2.1) introduces the mathematical description of electric bulk properties and their relation to electric field and currents based on the macroscopic Maxwell equations. The next two sections focus on two widely-used approaches to model the micro-structure of heterogeneous media: The first (2.2) describes the geological material based on solid grains distributed at random in the pore-filling electrolyte solution, the second (2.3) breaks the medium down into a network of electrolyte-filled cylindrical pores embedded in a matrix representing the solid phase.

In order to get familiar with the concepts used to predict the particular responses of these elementary geometries, we will go through the derivation of the respective models for the simplest polarization mechanism encountered in heterogeneous media: the Maxwell-Wagner polarization. In the case of the grain-based model, this is essentially a summary of existing mathematical treatments; in the

case of the pore-based approach, the analytical approximation of the Maxwell-Wagner response due to the simple pore-constriction geometry presented here is an original contribution. Both sections conclude with some considerations about the approaches applied to estimate the macroscopic electrical properties based on the solutions for the elementary geometries.

2.1 Basic aspects

2.1.1 Mathematical description of macroscopic electrical properties

The macroscopic Maxwell equations describe electromagnetic phenomena in material media, and thus form the mathematical foundation of any geophysical method based on the interaction between electromagnetic fields and matter. In particular, Ampère's and Gauss's law relate electric and magnetic fields and their spatio-temporal variations to electrical charges and currents. According to Ampère's law

$$\nabla \times \mathbf{H} = \mathbf{J}_c + \frac{\partial \mathbf{D}}{\partial t}, \tag{2.1}$$

the total current density is composed of the conduction current density $\mathbf{J}_c$ and the displacement current density $\partial \mathbf{D}/\partial t$. $\mathbf{H}$ denotes the magnetic field and $\mathbf{D}$ the displacement field. Gauss's law relates the divergence of the displacement field to the electric charge density ρ:

$$\nabla \mathbf{D} = \rho \tag{2.2}$$

The macroscopic behaviour of matter upon excitation by an electric field $\mathbf{E}$ is described by the constitutive equation

$$\mathbf{D} = \varepsilon \mathbf{E} \tag{2.3}$$

and Ohm's law

$$\mathbf{J}_c = \sigma \mathbf{E}, \tag{2.4}$$

where ε denotes the macroscopic permittivity of the material and σ the electrical conductivity. Usually, permittivity is used to summarize the macroscopic polarization response of the material (e.g. due to dielectric polarization), while σ generally accounts for the transport of free charges (e.g. electrolytic conduction). Yet, the following considerations will make clear that this assignation is somewhat arbitrary and the boundaries between the two concepts are not as clear as it might seem.

The displacement field can be split into the displacement field in the vacuum $\varepsilon_0\mathbf{E}$ and the polarization density $\mathbf{P}$:

$$\mathbf{D} = \varepsilon_0\mathbf{E} + \mathbf{P}. \tag{2.5}$$

If the polarization response of the material is purely dielectric, we can write

$$\mathbf{D} = \varepsilon_0\varepsilon_r\mathbf{E}, \tag{2.6}$$

where the relative dielectric permittivity ε_r accounts for the microscopic displacement of bound charges, e.g. due to the alignment of polar molecules with the external field. The polarization density $\mathbf{P}_\varepsilon = \varepsilon_0(\varepsilon_r - 1)\mathbf{E}$ describes this response.
Combining Ohm's law (2.4) and the constitutive equation (2.6), the total current on the right hand side of Ampère's law (2.1) can be expressed as

$$\mathbf{J} = \sigma\mathbf{E} + \varepsilon_0\varepsilon_r\frac{\partial\mathbf{E}}{\partial t}. \tag{2.7}$$

Assuming a simple harmonic variation of all time-dependent quantities, for example due to the external excitation by an electric field with amplitude $E = E_0\exp(j\omega t)$, all derivatives $\partial/\partial t = j\omega$ and the total current writes

$$\mathbf{J} = \sigma^*(\omega)\mathbf{E}, \tag{2.8}$$

where we have defined the generalized complex conductivity

$$\sigma^*(\omega) = \sigma + j\omega\varepsilon_0\varepsilon_r, \tag{2.9}$$

which describes the contributions of both conduction and displacement current. Note that σ^* is frequency dependent due to the contribution of the displacement current describing the dispersive nature of the dielectric polarization. Equally, we could have expressed the total current as

$$\mathbf{J} = \varepsilon^*(\omega)\frac{\partial\mathbf{E}}{\partial t}, \quad \text{where} \tag{2.10}$$

$$\varepsilon^*(\omega) = \varepsilon_0\varepsilon_r - \frac{j\sigma}{\omega}, \tag{2.11}$$

denotes a generalized complex dielectric permittivity. Comparing the two expressions (2.9) and (2.11), we see that $\sigma^* = j\omega\varepsilon^*$. Consequently, both generalized electrical properties describe the contributions of conduction (charge transport) and displacement current (charge displacement or storage) equivalently.

As we will discuss in more detail, the combination of constituents with different bulk and surface properties in a composite material produces additional polarization mechanisms beside dielectric polarization. We can define the polarization density $\mathbf{P}_{\mathrm{IP}}$ as the property, which summarizes the induced-polarization response of geologic media typically observed at relatively low frequencies. The total polarization density then writes $\mathbf{P} = \mathbf{P}_{\varepsilon} + \mathbf{P}_{\mathrm{IP}}$ and results in the total displacement field

$$\mathbf{D} = \varepsilon_0 \mathbf{E} + \mathbf{P}_{\varepsilon} + \mathbf{P}_{\mathrm{IP}} = \varepsilon_0 \varepsilon_r \mathbf{E} + \mathbf{P}_{\mathrm{IP}} \tag{2.12}$$

and the total current density

$$\mathbf{J} = \sigma \mathbf{E} + \varepsilon_0 \varepsilon_r \frac{\partial \mathbf{E}}{\partial t} + \frac{\partial \mathbf{P}_{\mathrm{IP}}}{\partial t}. \tag{2.13}$$

If we encountered a suitable σ_{IP} to express the time derivative of the polarization density as $\partial \mathbf{P}_{\mathrm{IP}}/\partial t = \sigma_{\mathrm{IP}} \mathbf{E}$, we could summarize conduction current, dielectric and induced polarization in the effective conductivity $\sigma_{\mathrm{eff}} = \sigma + \sigma_{\mathrm{IP}} + j\omega\varepsilon_0\varepsilon_r$. Again, we could just as well define the effective dielectric permittiviy $\varepsilon_{\mathrm{eff}} = \varepsilon_0\varepsilon_r + \varepsilon_{\mathrm{IP}} - j\sigma/\omega$, where $j\omega\varepsilon_{\mathrm{IP}} = \sigma_{\mathrm{IP}}$ which satisfies $\mathbf{P}_{\mathrm{IP}} = \varepsilon_{\mathrm{IP}}\mathbf{E}$.
As the whole treatment shows, it is a matter of taste weather the IP response is expressed in terms of a conductivity increment or a permittivity increment. However, the polarization phenomena studied by means of the IP method are often expressed in terms of a contribution to σ. In general, both ε and σ are complex (due to polarization phenomena) and frequency-dependent (due to relaxation processes).

2.1.2 A word about complex quantities

Current density $\mathbf{J}(t)$ and electric field $\mathbf{E}(t)$, as well as the measurable quantities current and voltage, are always real-valued quantities. Microscopic charge storage processes taking place in polarizable materials manifest themselves macroscopically by the fact that the current density (or current) leads the electric field (or voltage) as shown in Figure 2.1. If the excitation is harmonic, the variation of the amplitudes of electric field and current density can readily be described by $E_0 \cos(\omega t)$ and $J_0 \cos(\omega t + \varphi)$, respectively, where the phase shift φ accounts for the time lag $\Delta t = \varphi/\omega$ between the two quantities.
In the understanding that only the real part describes the actual temporal variation, we could also represent the electric field as complex number $E(t) = E_0 \exp(j\omega t) = E_0[\cos(\omega t) + j \sin(\omega t)]$. The particular power of this complex

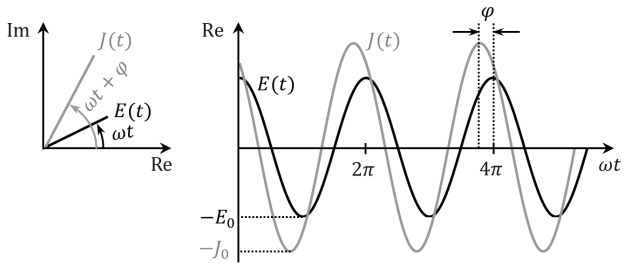

Figure 2.1: Harmonic variation of electric field E and current J with time t. *Left:* Representation on the complex plane. *Right:* Variation of real parts with time. In polarizable materials, the current runs ahead the electric field, the phase shift φ accounts for the time lag $\Delta t = \varphi/\omega$.

notation becomes clear, if we want to relate the temporal variations of electric field and current density via Ohm's law (2.4). A simple multiplication of $E(t)$ with the complex conductivity $\sigma^* = |\sigma^*| \exp(j\varphi)$ yields

$$\begin{aligned} J(t) &= \sigma^* E(t) \\ &= |\sigma^*| E_0 \exp[j(\omega t + \varphi)] \\ &= |\sigma^*| E_0 [\cos(\omega t + \varphi) + j \sin(\omega t + \varphi)]. \end{aligned} \tag{2.14}$$

Using the convention from above, i.e. only the real parts describe the actual temporal variation, and if $|\sigma^*| E_0 = J_0$ this is exactly the desired result. The same operation carried out using real number involves the addition of trigonometric functions with differing phases, which is algebraically much more laborious.

The complex conductivity (like any other complex quantity) can either be expressed in terms of its real part σ' and its imaginary part σ'', which gives $\sigma^* = \sigma' + j\sigma''$, or in the polar representation $\sigma^* = |\sigma^*| \exp(j\varphi)$, where $|\sigma^*| = \sqrt{(\sigma'^2) + (\sigma'')^2}$ is the magnitude and $\varphi = \arctan(\sigma''/\sigma')$ the phase. The relation $\sigma^* = |\sigma^*|(\cos\varphi + j\cos\varphi)$ closes the circuit.

In the context of the mathematical treatment of induced polarization phenomena, the complex notation is widely used to describe electrical conductivities (complex conductivity) or its inverse the electrical resistivity (complex resistivity). It is worth mentioning that this formalism, with the same advantages, works for the description of the time-harmonic variation of any physical quantity (e.g. ion concentration, electric potential, surface charge density, etc.) of

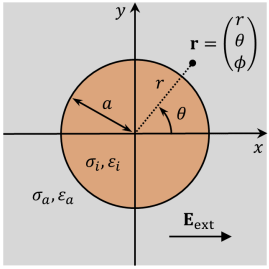

Figure 2.2: Standard geometry for the mathematical treatment of spherical particles: The spherical particle of radius a is centered at the origin of the spherical coordinate system $\mathbf{r} = (r, \theta, \phi)^T$. The bulk electrical properties of the sphere (solid phase) are characterized by σ_i and ε_i, those of the medium (electrolyte) by σ_a and ε_a. If the external electric field $\mathbf{E}_{\text{ext}}$ is applied parallel to the polar axis ($\theta = 0$), the problem becomes independent of the azimuth ϕ, i.e. all $\partial/\partial\phi = 0$.

interest. Particularly, chapters 4 and 5 will make extensive use of the complex notation to describe eventual phase shifts between an external electric field $E_0 \exp(j\omega t)$ and the time-harmonic variation of ion concentrations and electric potential. Here, non-vanishing imaginary parts of the respective quantities will always mean that this quantity is not completely "in-phase" with the external excitation.

2.2 Heterogeneous media: The grain-based approach

The solid phase of sediments and sedimentary rocks consists of fragments of minerals and pre-existing rocks. If the individual grains are loosely packed and the open fluid-filled pore spaces between them are relatively large, it appears appropriate to describe these geologic materials as a (concentrated) suspension of solid particles in an electrolyte solution. One approach to study the electrical properties of such a composite medium mathematically is to first derive the microscopic response around one single particle and then use the long-range response of this particle to obtain the macroscopic response of a medium, which consists of a larger number of such particles.

2.2.1 Effective conductivity of a single grain

As it has the most convenient geometrical shape to be treated mathematically, we start with a single spherical particle of radius a centered at the origin of a spherical coordinate system with position vector $\mathbf{r} = (r, \theta, \phi)^T$ (see Figure 2.2). The bulk electrical properties of the surrounding medium (the electrolyte) are described by the complex conductivity $\sigma_a^* = \sigma_a + j\omega\varepsilon_0\varepsilon_a$ and those of the inclusion (the particle) by the generalized complex conductivity $\sigma_i^* = \sigma_i + j\omega\varepsilon_0\varepsilon_i$. As this setup is completely symmetric so far, we are free to choose a suitable external excitation. The electric field described by the electric potential $U_{\text{ext}}(\mathbf{r}) = -E_0 r\cos\theta$ is parallel to the polar axis, i.e. the axis along $\theta = 0$, and has the advantage that the solution becomes independent of the azimuth ϕ.
Further more, we assume that both phases are homogeneous, such that electrical conductivity and relative permittivity are constant throughout the two regions $r < a$ and $r > a$, respectively, and the application of the external field will not produce any space charge within either region. Consequently, the spatial variation of the electric potentials $U_a(r, \theta)$ in the medium and $U_i(r, \theta)$ in the spherical inclusion must satisfy Laplace's equations

$$\nabla^2 U_a(r, \theta) = 0 \quad \text{for} \quad r > a \quad \text{and} \tag{2.15}$$

$$\nabla^2 U_i(r, \theta) = 0 \quad \text{for} \quad r < a. \tag{2.16}$$

For a complete description of the problem it remains to determine the boundary conditions on the electric potentials U_a and U_i. At a distance far from the inclusion and beyond the range of any perturbation of the electric potential due to induced polarization dipoles, the U_a electric potential must approach the potential U_{ext} describing the external excitation, i.e.

$$\lim_{r\to\infty} U_a(r, \theta) = -E_0 r\cos\theta. \tag{2.17}$$

At the same time, the potential within the sphere U_i must remain finite, particularly for $r \to 0$. At the geometrical boundary between the two phases, the electric potential must be continuous, i.e.

$$\lim_{r\to a} U_a(r > a, \theta) = \lim_{r\to a} U_i(r < a, \theta). \tag{2.18}$$

The continuity of the displacement current at this boundary relates the difference between the radial components inside and outside of the boundary to the surface charge density $\Sigma(\theta)$ distributed along this boundary:

$$-\varepsilon_0\varepsilon_a \frac{\partial U_a(r, \theta)}{\partial r}\bigg|_{r=a} + \varepsilon_0\varepsilon_i \frac{\partial U_i(r, \theta)}{\partial r}\bigg|_{r=a} = \Sigma(\theta). \tag{2.19}$$

At the same time, the continuity of the conduction current requires the difference between the two radial components to be equal to the temporal variation of $\Sigma(\theta)$:

$$-\sigma_a \frac{\partial U_a(r,\theta)}{\partial r}\bigg|_{r=a} + \sigma_i \frac{\partial U_i(r,\theta)}{\partial r}\bigg|_{r=a} = -j\omega\Sigma(\theta). \tag{2.20}$$

Depending on the frequency of the exciting field ω, the surface charge density $\Sigma(\theta)$ accumulates to balance the different conduction current densities in the two adjacent media. Boundary condition (2.19) can be obtained by application of Gauss's theorem to Gauss's law (2.2) and boundary condition (2.20) by application of Gauss's theorem on the continuity equation for the electric charge $\nabla \mathbf{J}_c = -\partial\rho/\partial t$.
Making use of the definition of the generalized complex conductivity (2.9), conditions (2.19) and (2.20) can be combined, which gives the following boundary condition on the total current:

$$-\sigma_a^* \frac{\partial U_a(r,\theta)}{\partial r}\bigg|_{r=a} + \sigma_i^* \frac{\partial U_i(r,\theta)}{\partial r}\bigg|_{r=a} = 0. \tag{2.21}$$

The solution of the boundary-value problem set up by equations (2.15) through (2.18) and (2.21) can be carried out applying standard methods: Due to the azimuthal symmetry of the setup, the solutions $U_a(r,\theta)$ and $U_i(r,\theta)$ can be expressed in terms of Legendre polynomials and the boundary conditions are used to find the unknown coefficients. The electric potential within the sphere, i.e. for $r \leq a$, is found to be

$$U_i(r,\theta) = \frac{-3\sigma_a^*}{2\sigma_a^* + \sigma_i^*} E_0 r \cos\theta \tag{2.22}$$

and the electric potential outside the sphere, i.e. for $r \geq a$, is given by

$$U_a(r,\theta) = -E_0 r\cos\theta + \frac{\sigma_i^* - \sigma_a^*}{2\sigma_a^* + \sigma_i^*} \frac{a^3 E_0}{r^2} \cos\theta. \tag{2.23}$$

From equation (2.22) we observe that the electric potential inside the sphere describes a uniform electric field oriented parallel to the exciting field. Equation (2.22) describes the electric potential outside the spherical particle as a superposition of the potential U_{ext} (first term on the right-hand side) and the potential $f a^3 E_0 \cos\theta / r^2$ describing the long-range dipole potential related to the field-induced surface charge $\Sigma(\theta,\omega)$. The reflection coefficient f defined as

$$f = \frac{\sigma_i^* - \sigma_a^*}{2\sigma_a^* + \sigma_i^*}, \tag{2.24}$$

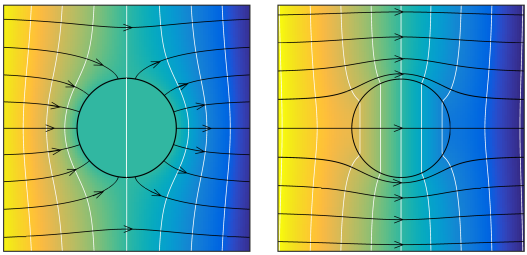

Figure 2.3: Electric potential (colour map and white equipotential lines) and electric field (black stream lines) around a highly conductive particle (left panel) and an isolating particle (right panel) embedded in a conductive medium for $\omega \to 0$.

fully describes this long-range perturbation and will subsequently turn out to be an effective means for the description of the macroscopic electric response of the composite system.
Figure 2.3 shows the low-frequency limits (i.e. $\omega \to 0$) of electric potential and electric field around a highly conductive particle, i.e. $\sigma_i \to \infty$ and $f \to 1$, and an isolating particle, i.e. $\sigma_i \to 0$ and $f \to -1/2$, embedded in a conductive medium. The electric field at the left and the right margins of the displayed section increases for $f \to 1$ resulting in an increase of the effective current flow trough the volume around the sphere. For $f \to -1/2$, the intensity of the electric field, and thus the effective current flow decrease. Consequently, the addition of conductive inclusion can be represented in terms of an increased effective conductivity of the composite medium, while the addition of isolating inclusions reduces the effective conductivity.

The concept of surface conductivity

So far, the surface of the spherical inclusion has only been taken into account as a simple geometric boundary between the two adjacent phases. As we saw above, this boundary can acquire a field-induced surface charge when an external field is applied. However, in geological materials, the solid-liquid interface can also be pre-charged, i.e. even without an external excitation the boundary carries a surface-charge density. At mineral surfaces in contact with the pore water, these charges are often due to cation-exchange reactions and arrange in electric double layers (EDL).

Different mathematical models exist to describe the behaviour of these additional charges. One of the simplest models considers an infinitely thin layer characterized by the surface conductivity K. Under the influence of an external electric field, the interface therefore transports additional charge along the boundary. O'Konski (1960) included this process into the above treatment by adjusting the boundary condition on the conduction current (2.20) as follows:

$$-\frac{K}{a^2\sin\theta}\frac{\partial}{\partial\theta}\left[\sin\theta\frac{\partial U_a(r,\theta)}{\partial\theta}\bigg|_a\right]-\sigma_a\frac{\partial U_a(r,\theta)}{\partial r}\bigg|_a+\sigma_i\frac{\partial U_i(r,\theta)}{\partial r}\bigg|_{r=a}=-j\omega\Sigma(\theta), \tag{2.25}$$

The additional first term describes the tangential transport along the surface caused the additional surface conductivity K and balances it with the charge transport from and into the adjacent bulk media as well as the temporal variation of the surface charge Σ. Note that this boundary condition includes an interchange of charges between the boundary layer and the adjacent media.

The solution to the resulting problem can be summarized in terms of the slightly modified reflection coefficient (O'Konski, 1960)

$$f_K=\frac{\sigma_i^*+2K/a-\sigma_a^*}{2\sigma_a^*+\sigma_i^*+2K/a}, \tag{2.26}$$

which describes both the field-induced polarization of the interface due to the different (generalized) bulk conductivities of the two media and the response of the conductive surface layer. As this result shows, the effect of the surface layer can be interpreted as increment of the conductivity of the sphere by $2K/a$, i.e. the coated spherical particle behaves like a particle of (homogeneous) conductivity σ_i^*+2K/a.

In general, the concept of surface conductivity can often be encountered in the description of conduction and polarization phenomena due to charges located in thin double layers around non-conducting particles. In this manner, eventual polarization effects in the interfacial layers themselves can easily be taken into account by defining complex frequency-dependent surface conductivities, i.e. $K\to K^*(\omega)$. Especially the treatment presented in chapter 6 will make extensive use of this concept, while chapters 4 and 5 will evidence its limited applicability for the mathematical description of polarization phenomena around highly conducting particles.

2.2.2 Up-scaling based on effective medium theory

As we have seen in the previous previous discussion, even in the case of a simple spherical inclusion, the electric field and thus electrical conduction is highly inhomogeneous at the microscopic scale. Quite apart from that, the exact mathematical treatment of a concentrated suspension of many spherical particles is impossible. Luckily, for the understanding of measured geophysical signatures, we are interested in the macroscopic response of composite media, i.e. we only need a prediction of the effective total conductivity, which relates the volume average of the electric field to the volume average of the electric current density:

$$\langle \mathbf{J} \rangle = \sigma_{\text{eff}} \langle \mathbf{E} \rangle \tag{2.27}$$

Of course, we want σ_{eff} to account not only for the contribution of conduction currents but also the effect of dielectric polarization and other possible polarization mechanisms. Therefore, σ_{eff} will generally be a complex frequency-dependent quantity.

Such a homogenization of the properties of microscopically heterogeneous composite media is the principle objective of any effective medium theory. For dilute suspensions of spherical particles with complex conductivity σ_i^* sparsely distributed in a host medium with complex conductivity σ_a^*, Wagner (1914) obtained the following expression for the effective complex electrical conductivity of the mixture:

$$\frac{\sigma_{\text{eff}} - \sigma_a^*}{\sigma_{\text{eff}} + 2\sigma_a^*} = \nu \frac{\sigma_i^* - \sigma_a^*}{\sigma_i^* + 2\sigma_a^*}, \tag{2.28}$$

where ν is the volume fraction of the spherical inclusions. Comparison of the right-hand side of this equation with the definition of f in equation (2.24) leads to the following alternative formulation of the effective conductivity of the mixture:

$$\sigma_{\text{eff}} = \sigma_a^* \frac{1 + \nu f}{1 - \nu f}. \tag{2.29}$$

To be able to calculate the effective electrical response of a composite material, besides the conductivity of the pore fluid we either need the reflection coefficient f of one inclusion or the effective conductivity of one particle (including possible contributions of a surface conductivity) to calculate f. As soon as we know the long-range potential around one polarized particle described by f, equation (2.29) allows to estimate the effective conductivity of an dispersion of a number of such particles.

If we now use $\sigma_i + j\omega\varepsilon_0\varepsilon_i$ to calculate f, equation (2.28) describes the response of the composite medium caused by the pure interfacial charge polarization known

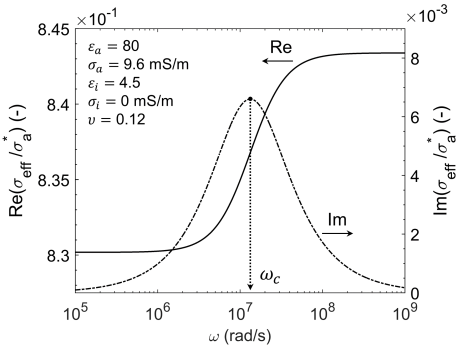

Figure 2.4: Maxwell-Wagner polarization response of a dilute suspension of insulating spherical particles in a conductive medium. Real and imaginary part of the effective conductivity σ_{eff} computed from equations (2.24) and (2.29) using the parameters specified in the figure. The characteristic angular frequency ω_c indicates the spectral position of the peak of the imaginary part. Note that σ_{eff} is normalized with the complex conductivity σ_a^* of the fluid, otherwise the imaginary part would diverge at high frequencies.

as Maxwell-Wagner polarization (see Figure 2.4). If we use f_K [equation (2.26)] instead, we obtain the effective conductivity of the mixture containing spheres with conductive coatings described by O'Konski (1960).

The main limitation of the up-scaling approach, which results in equations (2.28) and (2.29), is the lack of a suitable incorporation of interactions between neighbouring particles. At higher volume fractions of the inclusions, the omission of such inter-particle effects makes the predictions of this model increasingly inaccurate. For denser ensembles the less handy Hanai-Bruggeman effective medium theory (Bruggeman, 1935; Hanai, 1960) is more adequate.

2.3 Heterogeneous media: The pore-based approach

In the previous section the composite geologic material was described as a relatively loose arrangement of individual grains. With increasing degree of compaction and the development of new pore-filling minerals, however, this picture must become increasingly inaccurate. In tight and highly cemented materials characterized by reduced pore spaces and hardly recognizable boundaries between adjacent grains, the particular geometrical configuration of the remaining

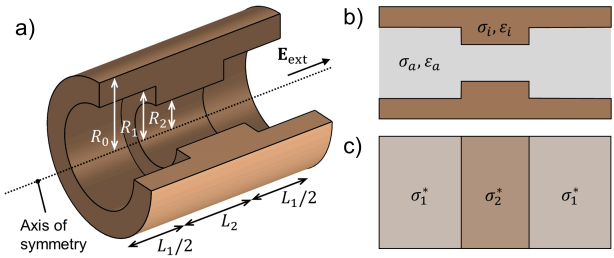

Figure 2.5: a) Standard pore-constriction geometry, b) longitudinal section through this model and, c) reduction to one spatial dimension based on the averaging approach described in the main text.

fluid-filled pore space can be expected to become more important. This section introduces a second approach, which honors this different situation and rather relates the macroscopic electric response of such materials to the morphology of the pore space.

2.3.1 Effective conductivity of a single pore constriction

One geometrical configuration, which is often examined in studies dealing with the membrane-polarization response is the pore-constriction geometry displayed in Figure 2.5. Although it is not the objective of this section to deal with the membrane polarization mechanism, the use of this particular pore-constriction geometry in pore-scale IP modelling illustrates the general relevance of the following treatment.

The configuration consists of two cylindrical half-pores of radius R_1 and length $L_1/2$, which are interconnected by a third cylindrical pore of radius R_2 and length L_2. Analogously to the treatment in the previous section, the bulk electrical properties of the volume enclosed by these pores (the electrolyte) are described by the complex conductivity $\sigma_a^* = \sigma_a + j\omega\varepsilon_0\varepsilon_a$. The entire pore sequence is embedded in a larger cylinder of radius R_0 and length $L = L_1 + L_2$. The volume between pores and outer cylinder represents the solid matrix with the complex conductivity $\sigma_i^* = \sigma_i + j\omega\varepsilon_0\varepsilon_i$. For convenience, we choose a cylindrical coordinate system with position vector $\mathbf{r} = (r, \phi, z)^T$, such that the symmetry axes of the three pores and outer cylinder coincide with the z-axis. Note that if we arranged various of these large cylinders in series along the z-axis, the

half-pores at the left and right boundaries would combine to one wide pore of length L_1.
The entire system is excited by the external electric field described by the electric potential $U_{\text{ext}}(\mathbf{r}) = -E_0 z$. As this field is oriented parallel to the common symmetry axis of the cylindrical pores, the problem becomes independent of the azimuth ϕ. As before, both phases are assumed to be homogeneous such that the electric field will not produce any space charge within either phase. Therefore, the spatial variation of the electric potentials $U_a(r,z)$ in the pore and $U_i(r,z)$ in the matrix must satisfy Laplace's equations

$$\nabla^2 U_a(r,z) = 0 \quad \text{in the pores and} \tag{2.30}$$

$$\nabla^2 U_i(r,z) = 0 \quad \text{in the matrix.} \tag{2.31}$$

The problem description is completed by the definition of the following set of boundary conditions: At the boundaries of the outer cylinder, i.e. at the left boundary at $z = -L/2$, the right boundary at $z = +L/2$, and the radial boundary at $r = R_0$, we require the electric potentials to be equal to U_{ext}:

$$U_a(r,z) = -E_0 r \quad \text{for } z = \pm(L/2) \quad \text{and} \tag{2.32}$$

$$U_i(r,z) = -E_0 r \quad \text{for } z = \pm(L/2) \quad \text{and} \quad r = R_0. \tag{2.33}$$

Along the geometrical boundaries between liquid and solid phase, the electric potential must be continuous. Therefore, we demand

$$\lim_{r \to R_k} U_a(r < R_k, z) = \lim_{r \to R_k} U_i(r > R_k, z). \tag{2.34}$$

on the radial boundaries of the k-th pore and

$$\lim_{z \to \pm L_2/2} U_a(r \geq R_2, |z| > L_2/2) = \lim_{z \to \pm L_2/2} U_i(r \geq R_2, |z| < L_2/2) \tag{2.35}$$

on the axial boundaries, where the wide pores and the narrow pore are joint together. On the same interphase boundaries, we also have to specify conditions on the total current. Adapting the corresponding boundary condition (2.21) formulated for the spherical geometry yields

$$-\sigma_i^* \nabla_{\mathbf{n}} U_i(r,z) + \sigma_a^* \nabla_{\mathbf{n}} U_a(r,z) = 0, \tag{2.36}$$

where $\nabla_{\mathbf{n}}$ denotes the normal derivative on the respective boundary.
While we saw that an analytical solution of the spherical counterpart of this boundary value problem exists, the exact analytical solution of the problem in

this – still rather simple – cylindrical geometry is impossible. Complications primarily arise from the description of the curved electric field in the transition regions between wide pores and pore-constriction (at $z = \pm L_2/2$). However, geometry and electrical properties within the regions of equal pore radius, i.e. $-L/2 \leq z \leq L_2/2$, $-L_2/2 \leq z \leq L_2/2$, and $L_2/2 \leq z \leq L/2$, only vary in radial direction and, consequently, the electric field will exhibit the same purely radial variation to a first approximation.
From this approximation derives the idea to compute the volume averages (actually radial averages) of the one-dimensional total current densities for each of the three regions separately. In a second step, these current densities are then combined in series and matched with a suitable set of boundary conditions to obtain the total current through the system. This approach is based on a variation of the approach used by Bücker and Hördt (2013a) to approximate the membrane-polarization response of a similar pore-constriction geometry.
The average total current density through the k-th pore and the matrix adjacent to it can be approximated by the scalar total current density

$$\langle J \rangle_k = \frac{1}{V} \int_V \sigma^*(r) E_k dV, \tag{2.37}$$

where $V = \pi R_0^2 L_k$ is the total volume considered by this average. Based on the solution of the Laplace equation in one spatial dimension and the continuity of the electrical potential at the boundary between the two phases, we can convince ourselves that the electric field E_k must be approximately constant along the z-axis and equal in both phases. Using the radial conductivity variation defined by $\sigma^*(r < R_k) = \sigma_a^*$ and $\sigma^*(r \geq R_k) = \sigma_i^*$, the integral can easily be evaluated yielding

$$\langle J \rangle_k = \left(\frac{R_k^2}{R_0^2} \sigma_a^* + \frac{R_0^2 - R_k^2}{R_0^2} \sigma_i^* \right) E_k. \tag{2.38}$$

The term between parentheses can be interpreted as the axial conductivity

$$\sigma_k^* = \frac{R_k^2}{R_0^2} \sigma_a^* + \frac{R_0^2 - R_k^2}{R_0^2} \sigma_i^* \tag{2.39}$$

describing the average conduction and dielectric polarization of the cylindrical pore and the surrounding annular matrix volume.
If evaluated in the appropriate limiting cases, the averaging approach used here and the one proposed by Bücker and Hördt (2013a) are equivalent: Under the conditions that (i) the generalized complex conductivity only accounts for the real-valued electrolytic conductivity of the pore water, i.e. $\sigma_a^* \to \sigma_a$, (ii) the

matrix is isolating and non-polarizable, i.e. $\sigma_i^* \to 0$, and (iii) the radius of the outer cylinder is equal to the radius of the wide pore, i.e. $R_0 \to R_1$, the equation (2.39) collapses to $\sigma_k^* \to \sigma_a R_k^2/R_1^2$. This is exactly the same expression, which results from the model by Bücker and Hördt (2013a), if it is evaluated in the limiting case of a vanishing surface potential, i.e. $\zeta \to 0$, and thus equal cation and anions concentrations in the electrolyte. In particular, both conductivities σ_1^* and σ_2^* are normalized by the cross-sectional area of the wide pore, the motivation for which might not be clear at first sight.
Either of these averaging approaches represents the pore sequence as an equivalent layered medium with the two complex conductivities σ_1 and σ_2 as depicted in Figure 2.5, which makes the solution of the problem straight forward: The Integration of the Laplace equation in one spatial dimension results in linearly varying potentials (i.e. constant electric fields) within each of the layers of homogeneous conductivity. The magnitudes of the electric fields E_k are connected by the continuity condition on the mean total currents at the inner boundaries at $z = \pm - L_2/2$:

$$\sigma_1^* E_1 = \sigma_2^* E_2, \tag{2.40}$$

Furthermore, the boundary condition on the potential at the left and right boundary at $z = \pm - L/2$ yields

$$E_1 L_1 + E_2 L_2 = E_0 L. \tag{2.41}$$

Equations (2.40) and (2.41) are solved by the electric fields

$$E_1 = \frac{L E_0}{L_1 + \sigma_1^*/\sigma_2^* L_2} \quad \text{and} \quad E_2 = \frac{L E_0}{\sigma_2^*/\sigma_1^* L_1 + L_2} \tag{2.42}$$

and the evaluation of the (constant) average total current in either of the pores yields the total current density

$$\langle J \rangle = \frac{\sigma_1^* \sigma_2^* L}{L_1 \sigma_2^* + L_2 \sigma_1^*} E_0 \tag{2.43}$$

for all $-L/2 \leq z \leq L/2$. Consequently, the effective conductivity of the complete volume embraced by the large cylinder of radius R_0 and length L can be approximated by

$$\sigma_{\text{eff}} = \frac{\sigma_1^* \sigma_2^* L}{L_1 \sigma_2^* + L_2 \sigma_1^*} \tag{2.44}$$

From the above derivation it is obvious that the conductivity of this representative volume is highly isotropic and σ_{eff} only describes the response for an excitation along the z-axis.

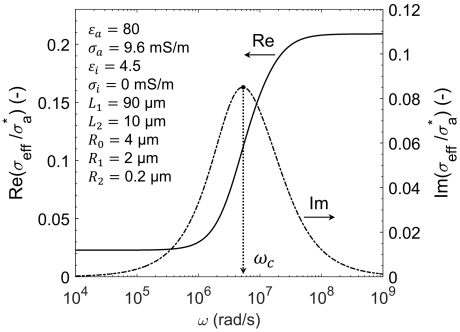

Figure 2.6: Maxwell-Wagner polarization response of the pore-constriction geometry. Real and imaginary part of the effective conductivity σ_{eff} computed from equations (2.39) and (2.44) using the parameters specified in the figure. The characteristic angular frequency ω_c indicates the spectral position of the peak of the imaginary part. As in Figure 2.4, the normalization of σ_{eff} with the complex conductivity σ_a^* of the fluid prevents the the imaginary part from diverging at high frequencies.

Figure 2.6 shows the Maxwell-Wagner polarization of the pore-constriction geometry described by the effective conductivity defined by equations (2.39) and (2.44). It is worth mentioning that the response is not sensible to variations of the two pore radii R_k. It does vary with L_1 and L_2 as long as the ratio L_1/L_2 varies.

It is noted that equation (2.44) is equivalent to the expression obtained by Maxwell for the complex conductivity of stratified heterogeneous systems (e.g. Hanai, 1962, his equation 7). If we define the volume fraction of zones with effective conductivity σ_2^* as $\nu = L_2/L$, we can rearrange equation (2.44) to obtain exactly the same expression as Maxwell:

$$\sigma_{\text{eff}} = \sigma_1^* \frac{\sigma_2^*}{\sigma_2^* + \nu(\sigma_1^* - \sigma_2^*)}. \tag{2.45}$$

This formulation is a generalization of equation (2.44) as it removes the limitation to sequences with the two fixed layer thicknesses L_1 and L_2. Rather, it describes the Maxwell-Wagner polarization response of any regularly or irregularly layered media with the volume fractions ν of layers of conductivity σ_2^*.

2.3.2 Up-scaling based on pore networks

The encountered concordance of the effective conductivity of the pore-constriction geometry with the one-dimensional Maxwell model (2.44) is a nice parallel to the effective conductivity of a suspension of spherical particles described by Wagner's equations (2.28) and (2.29). However, the effective conductivity of the Maxwell model also only describes the conductivity in one spatial direction (i.e along the cylinder axis) and is no appropriate model for the electrical properties of a representative porous medium. Particularly, the pores of real sedimentary materials and rocks are interconnected in three spatial dimensions, which is not included in the present model.
In order to match this complexity of real pore networks, Stebner and Hördt (2017) proposed to connect different realizations of the elementary pore-constriction cells to two- and three-dimensional networks. They simulate impedance networks consisting of impedances obtained from the membrane-polarization model developed by Bücker and Hördt (2013a) (and extended by Hördt et al., 2016) as elementary cells. As the resulting systems of equations are solved numerically, this approach allows the incorporation of elementary cells representing pores of different size to model pore-size distributions observed on real rock samples. In a similar manner, Maineult et al. (2017) combine elementary Cole-Cole model responses to random tube networks. Despite of their promising results, both studies show that the network-based upscaling approach is associated with a considerable additional effort compared to the relative simplicity of the upscaling of the elementary response of spherical particles.

2.4 Conclusion

In this chapter we got acquainted with the basic concepts and geometries generally used to model the electric response of heterogeneous media at the pore scale. In passing we discussed the physical foundation of the Maxwell-Wagner polarization and obtained mathematical models for this mechanism in two geometries: the grain-based model and the pore-constriction model. The latter has not been described before and is an important collateral product of this chapter. Although Maxwell-Wagner polarization is contained in most (grain-based) models, in IP literature it is rarely being addressed in such detail. This is primarily due to the fact that its influence is limited to the high-frequency limit of the typical IP frequency range from 1 mHz to 1 kHz. In summary, the treatment of this omnipresent polarization mechanism is an important com-

plement to the detailed discussion of the other polarization mechanisms in the remaining chapters.

CHAPTER 3

An analytical membrane-polarization model to predict the complex conductivity signature of immiscible liquid hydrocarbon contaminants

3.1 Introduction

Due to their low solubility in water, liquid hydrocarbon contaminants – also referred to as non-aqueous phase liquids (NAPLs) – released into the subsurface environment often persist as residual or free phase (e.g. Soga et al., 2004). Commonly, the detection of these separate hydrocarbon phases is an important objective of site characterization because they constitute a main source for continuing contamination of ground water (e.g. Atekwana and Atekwana, 2010). The characterization of these source zones usually relies on direct soil and/or groundwater sampling, which results in a limited spatial resolution of the site investigation due to the relatively high cost of drilling-based methods (e.g. Flores Orozco et al., 2012). Furthermore, screened wells generally used to monitor the progress of remediation measures are known to be unable to detect trapped (and thus immobile) residual hydrocarbon. Even though, mobile free-phase thicknesses measured in monitoring wells (i.e. the thickness of the immiscible liquid hydrocarbon layer floating on top of the ground water) typically exceed the real free-phase thicknesses in the formation, an effect that can be explained be the effect of capillary forces (Newell et al., 1995, and references therein).
If combined with conventional site characterization and monitoring techniques, geophysical exploration methods potentially help to overcome some of the above mentioned limitations (Atekwana and Atekwana, 2010) as they provide spatially quasi-continuous and highly resolved information on subsurface properties. In

This chapter is based on: Bücker, M., Flores Orozco, A., Hördt, A., and Kemna, A. (2017). *An analytical membrane-polarization model to predict the complex conductivity signature of immiscible liquid hydrocarbon contaminants.* Near Surface Geophysics, 15(6):547–562.

particular, direct current (DC) and induced polarization (IP) imaging techniques have received much attention because of the distinct electrical properties of liquid hydrocarbon contaminants. Due to the high electrical resistivity of most liquid hydrocarbons, fresh spills usually stand out as resistive anomalies (e.g. Börner et al., 1993; Chambers et al., 2004; Cassiani et al., 2009; Johansson et al., 2015). However, over time, the presence of hydrocarbon often enhances microbial activity and organic acids are released into the groundwater, which promote mineral weathering and dissolution of ions (e.g. Sauck, 2000; Cassidy et al., 2001). As a consequence, aged hydrocarbon spills are often associated with high electrical conductivities (e.g. Atekwana et al., 2000; Flores Orozco et al., 2012; Cassiani et al., 2014; Caterina et al., 2017). Although an indication of contaminated subsurface volumes based on DC-resistivity anomalies alone might be sufficient in some cases, several studies report circumstances under which no significant resistivity anomaly could be detected (e.g. Börner et al., 1993; Ustra et al., 2012; Kemna et al., 2004).

In order to explore the potential of the IP method – also known as complex resistivity or complex conductivity – for the detection of hydrocarbon contaminants, laboratory and field experiments have been undertaken with promising but seemingly contradictory results. While many studies report an increase of the measured IP phases or chargeabilities with hydrocarbon saturation (e.g. Olhoeft, 1985, 1992; Vanhala et al., 1992; Kemna et al., 1999, 2004; Abdel Aal et al., 2006; Sogade et al., 2006; Cassiani et al., 2009; Schmutz et al., 2010; Revil et al., 2011; Abdel Aal and Atekwana, 2013; Deceuster and Kaufmann, 2012; Flores Orozco et al., 2015), some results display the reverse effect (e.g. Vanhala et al., 1992; Weller and Börner, 1996; Weller et al., 1997; Vanhala, 1997; Chambers et al., 2004; Martinho et al., 2006; Cassiani et al., 2009; Revil et al., 2011), or even an increase of the polarization magnitude until a critical saturation is reached followed by a decrease towards higher hydrocarbon concentrations (e.g. Titov et al., 2004; Martinho et al., 2006; Flores Orozco et al., 2012; Johansson et al., 2015). As only a limited number of studies under certain conditions report weak or insignificant variations of the polarization response resulting from changes in hydrocarbon concentration (Olhoeft, 1985; Ustra et al., 2012), the potential of the IP method for the characterization of hydrocarbon-contaminated sites seems evident, but urges a more detailed knowledge of the underlying polarization effect mechanisms.

In order to connect experimental observations to the pore-scale configuration of immiscible liquid hydrocarbon, several conceptual models have been developed

by various authors (e.g. Titov et al., 2004; Martinho et al., 2006; Schmutz et al., 2010; Revil et al., 2011; Flores Orozco et al., 2012; Abdel Aal and Atekwana, 2013; Johansson et al., 2015). Most of these distinguish between two possible scenarios: (1) the solid phase is covered by a water film and the hydrocarbon forms discrete or interconnected droplets, a condition commonly referred to as "water-wet", while (2) under "hydrocarbon-wet" conditions the two liquids interchange their roles and a hydrocarbon film separates the aqueous phase from the solid phase. All authors then attribute the resulting polarization responses to mainly three mechanisms; (a) polarization of the electrical double layer (EDL) at the solid-water interface, (b) polarization of the EDL at the water-liquid hydrocarbon interface, and/or (c) membrane polarization due to geometrical constrictions in the electrolyte-filled pore space.

In order to verify the conceptual models and quantify individual contributions of the polarization mechanisms to the overall response, mechanistic models are needed. The polarization of the EDL at the solid-water interface has been studied intensively (O'Konski, 1960; Schwarz, 1962; Schurr, 1964) and a robust mechanistic model that links the IP effect in granular media to the polarization of the Stern-layer is available (Leroy et al., 2008; Leroy and Revil, 2009). Recently, this model has been extended to include the effect of non-wetting oil as an electrically insulating but non-polarizable phase (Schmutz et al., 2010). The extended model predicts a monotonous increase of the conductivity phase with oil saturation and has been tested successfully against experimental data. It also contains the only empirical model that had been developed earlier (Vinegar and Waxman, 1984) as a limiting case. However, the model by Schmutz et al. (2010) does not answer all open questions, because it cannot explain measured IP responses that decrease with hydrocarbon saturation or show a maximum behaviour at intermediate concentrations.

Although there are good reasons to assume that the EDL at the hydrocarbon-water interface also contributes to the overall polarization (e.g. Abdel Aal and Atekwana, 2013; Johansson et al., 2015), the model by Schmutz et al. (2010) does not consider the polarization response around liquid hydrocarbon droplets or hydrocarbon-covered mineral grains.

Membrane polarization – the third possible source mechanism – explains the measured IP response with the presence of ion-selective zones along the current pathway, which leads to the build-up of (salt) concentration gradients under the effect of an external electric field (Marshall and Madden, 1959). Generally, geometrical pore constrictions (pore throats, narrow passages) or clay minerals

are assumed to cause the ion-selective behaviour because of the unequal cation and anion concentrations in the EDL (e.g. Buchheim and Irmer, 1979; Vinegar and Waxman, 1984). Titov et al. (2004) undertake the only published attempt to adapt a mechanistic membrane-polarization model, i.e. the model by (Titov et al., 2002), to explain the IP response of hydrocarbon-contaminated sediments. In their laboratory experiments they observed a chargeability increase up to a critical hydrocarbon saturation followed by a decrease at higher saturations. Although their discussion suggests that this maximum behaviour of the chargeability is in agreement with the developed model, no rigorous quantitative treatment is provided.
Because of the evident lack of a more detailed understanding of membrane-polarization processes in hydrocarbon-contaminated sediments and rocks, the main objective of the present study is to place an analytical model to the disposal of the community. To this end, we first adapt the existing conceptual models and extract those parameters relevant to membrane polarization. Then we adapt a recently presented membrane polarization model, which allows to consider the effect of the EDL at the pore wall and varying pore radii (Bücker and Hördt, 2013a) to simulate the effect of both wetting and non-wetting liquid hydrocarbon in the pore space on the membrane-polarization mechanism. The discussion focusses on the possible implications for the interpretation of measured IP responses.

3.2 Theory

3.2.1 Conceptual model

Hydrocarbon contaminants in granular subsurface materials partition into four phases – vapor, aqueous (dissolved in water), separate (residual or free phase), and sorbed to solid particles (e.g. Newell et al., 1995). The physio-chemical properties of all involved materials (i.e. hydrocarbon, water, solid) and the contamination history determine the degree to which the contaminant partitions into each of the four phases. Separate liquid hydrocarbon trapped in the pore space often acts as a source for continuing contamination of ground water (e.g. Atekwana and Atekwana, 2010), which makes the delineation of the source zone one of the main objectives of site characterization and management. The present study therefore focusses on the effect of immiscible liquid hydrocarbon contaminants on the expected IP response. For the sake of simplicity, we will furthermore limit our treatment to the saturated zone, i.e. the pore space is

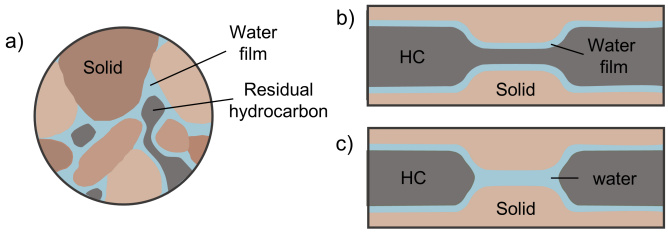

Figure 3.1: a) Conceptual model of the geometrical distribution of immiscible hydrocarbon (HC) droplets under water-wet conditions. Corresponding simplified capillary models for the cases of b) interconnected and c) separate hydrocarbon droplets.

completely occupied by pore water and liquid (free-phase) hydrocarbon at different ratios and no gaseous phase is considered. Following the approach of earlier studies, we will treat the cases of liquid hydrocarbon as non-wetting and wetting phase separately (Martinho et al., 2006; Schmutz et al., 2010; Revil et al., 2011; Abdel Aal and Atekwana, 2013; Johansson et al., 2015).

In most natural granular materials, water is the wetting fluid (e.g. Kanicky et al., 2001) and the liquid hydrocarbon is trapped in the open pore space forming discrete droplets or ganglia (Figure 3.1a). The geometrical configuration of the non-wetting liquid hydrocarbon depends on pore geometry and capillary pressure (e.g. Sahloul et al., 2002). In this study, we assume that the solid surface is covered by a continuous water film, which separates the hydrocarbon droplet from the solid phase. Low pore-throat diameter ratios (in the literature often referred to as aspect ratio) and/or high hydrocarbon saturations favour the formation of bridges between hydrocarbon droplets in adjacent pore spaces (Chatzis et al., 1983), as depicted in Figure 3.1b. Incoming water leads to the rupture of the bridge, if the hydrocarbon saturation decreases below a critical value, referred to as "snap-off" (e.g. Sahloul et al., 2002). Besides low hydrocarbon saturations, also high pore-throat diameter ratios promote the formation of discrete hydrocarbon droplets (see Figure 3.1c). The corresponding capillary models (Figures 3.1b and 3.1c) to be considered in this study represent these two limiting cases.

Surface-active components in the pore water can change the interfacial tensions and consequently the wettability of non-aqueous phase liquids (e.g. Zhao and Ioannidis, 2007). In particular, organic acids and bio-surfactants released as

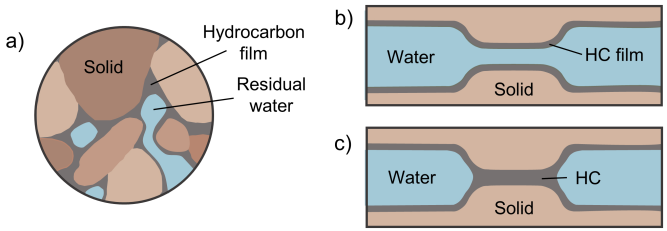

Figure 3.2: a) Conceptual model of the geometrical distribution of immiscible hydrocarbon (HC) droplets under hydrocarbon-wet conditions. Translation into the simplified capillary model for the cases of b) interconnected and c) separate water droplets.

metabolic by-products during biodegradation (e.g. Cassidy et al., 2001) presumably promote the change to the less usual hydrocarbon-wet situation. In such case liquid hydrocarbon and water reverse roles as compared to the water-wet situation (Figure 3.2a). Again, predominantly controlled by pore-throat diameter ratio and hydrocarbon saturation, water either forms interconnected droplets (Figure 3.2b) or is trapped as discrete droplets in the larger pore spaces (Figure 3.2c). In both limiting cases a continuous hydrocarbon film is assumed to coat the solid surface.

Besides the geometrical configuration of water and contaminant phases in the pore space, electrical and electrochemical properties of the two phases and the liquid-liquid interface need to be considered. The large resistivity contrast between the aqueous phase and most liquid hydrocarbons justifies the assumption of electrically insulating hydrocarbon droplets and films (e.g. Schmutz et al., 2010).

As proposed by Abdel Aal and Atekwana (2013) and Johansson et al. (2015), besides the EDL at the solid-water interface, we include a second EDL at the interface between liquid hydrocarbon and pore water into our model. We consider this second EDL essential because the magnitude of the ζ-potential at the hydrocarbon-water interface can be of the same order of magnitude or even higher (e.g. Buckley et al., 1989; Busscher et al., 1995) than that at the surface of common sediment minerals (e.g. Leroy et al., 2008). The corresponding surface charge can be explained based on the presence of interfacially active polar components in the liquid hydrocarbon; at normal pH the dissociation of acidic interfacial groups is responsible for the build-up of a negative surface charge and at very low pH the protonation of basic interfacial groups results in a positive

surface charge (e.g. Farooq et al., 2013). Specific adsorption of hydroxide ions (OH^-) can act as an additional source of interfacial charges – even in absence of polar components (Marinova et al., 1996). Usually, hydrocarbon mixtures with a higher fraction of short-chained hydrocarbons will show lower absolute ζ-potentials than mixtures of longer-chained hydrocarbons (e.g. Stachurski and MichaŁek, 1996). Beside this strong dependence on the composition of the liquid hydrocarbon, water pH and electrolyte concentration influence the ζ-potential (e.g. Farooq et al., 2013).

As the ζ-potential at the hydrocarbon-water interface strongly depends on the presence of interfacially active components, the wetting conditions in contaminated media become dependent on the signs and relative magnitudes of the ζ-potentials at both interfaces (i.e. hydrocarbon-water and solid-water). In general, an increasing number of polar components, and thus an increasing ζ-potential at the hydrocarbon-water interface, will favor the transition to hydrocarbon-wet conditions (e.g. Revil et al., 2011). Because a detailed modelling of the transition between the two regimes is beyond the scope of this study, we will not a priori limit the parameter ranges to be studied.

3.2.2 Analytical model

Recently, Bücker and Hördt (2013a) proposed a model that considers a sequence of wide and narrow cylindrical pores with pore radii R_1 and R_2 and pore lengths L_1 and L_2. The pores are saturated with an electrolyte solution with a bulk ion concentration of c_0 (in mol/m^3), and the pore wall or matrix is assumed to be non-conducting. A generally negative surface charge at the pore wall attracts an excess of cations, which accumulate in the Stern layer and the diffuse layer of the EDL, and causes a deficit of anions in the diffuse layer. The ζ-potential is used to approximate the electric potential at the interface between the Stern layer and the diffuse layer. The Gouy-Chapman theory permits to quantify the radial variation of electric potential $U(r)$ and ion concentrations $c_{p,n}(r)$ in the diffuse layer (subscript p denotes cation properties, subscript n anion properties). For a cylindrical pore of radius R_i, the electric potential can be approximated by solving the linearized Poisson-Boltzmann equation in cylindrical coordinates ($r = 0$ on the axis of the cylinder) with the boundary condition $U(R_i) = \zeta_m$ (e.g. Hunter, 1981):

$$U_i(r) = \zeta_m \frac{J_0(j\kappa r)}{J_0(j\kappa R_i)}. \tag{3.1}$$

Here, j is the imaginary unit with $j^2 = -1$, J_0 the Bessel function of the first kind and order zero, and $\kappa = \lambda_D^{-1}$ the inverse of the Debye length λ_D, which is a measure of the thickness of the diffuse layer. The subscripts $i = 1, 2$ denote properties of the wide and narrow pore, respectively. For symmetric monovalent electrolytes, the Debye length can be expressed as

$$\lambda_D = \sqrt{\frac{\varepsilon_0 \varepsilon_r kT}{2c_0 eF}}. \tag{3.2}$$

Here, ε_0 is the vacuum permittivity ($8.854 \cdot 10^{-12}$ C/(Vm)) and ε_r the relative permittivity of the pore fluid (≈ 80 for water), k Boltzmann's constant ($1.3806482 \cdot 10^{-23}$ J/K) (cf. Gaiser et al., 2017), T the absolute temperature, e the elementary charge ($1.6022 \cdot 10^{-19}$ C) and F Faraday's constant (96,485.3 C/mol). The radial variation of the ion concentrations is connected to the electric potential via (e.g. Butt et al., 2003)

$$c_{(p,n)i}(r) = c_0 \exp\left[\mp \frac{eU_i(r)}{kT}\right]. \tag{3.3}$$

Note that at large distances from the pore wall (i.e. $r \gg \lambda_D$), the potential approaches the reference potential of 0 mV and both ion concentrations become equal to the bulk ion concentration c_0.
Bücker and Hördt (2013a) argue that electric current through the system of wide and narrow pores, in a first approximation, will be determined by the mean ion concentrations. They average the ion concentrations over the pore cross sections as follows:

$$b_{(p,n)i} = \frac{2\pi}{c_0 A_1} \int_0^{R_i} c_{(p,n)i}(r) r dr. \tag{3.4}$$

Note that the integrated concentrations b are normalized by the bulk ion concentration c_0 and the area of the wide pore $A_1 = \pi R_1^2$. The latter accounts for the reduction of the total current through the narrow pore due to the smaller cross section (see Bücker and Hördt, 2013a). The dimensionless mean concentrations are then used to define average transference numbers for both pores,

$$t_{(p,n)i} = \frac{\mu_{p,n} b_{(p,n)i}}{\mu_p b_{pi} + \mu_n b_{ni}}, \tag{3.5}$$

where $\mu_{p,n}$ are the ion mobilities. By means of this approximation, the three-dimensional cylindrical pore system can be collapsed to a sequence of one-dimensional pores, the frequency-dependent impedance of which was studied in detail by Marshall and Madden (1959). As proposed by Bücker and Hördt (2013b),

we express the Marshall-Madden impedance × area $Z(\omega)$ in terms of its low-frequency limit $Z_{\mathrm{DC}} = \lim_{\omega\to 0} Z(\omega)$ a dimensionless polarizability η_0, and two time constants τ_i:

$$Z(\omega) = Z_{\mathrm{DC}}\left[1-\eta_0\left(1-\frac{\frac{L_1}{\tau_1}+\frac{L_2}{\tau_2}}{\frac{L_1}{\tau_1}\sqrt{j\omega\tau_1}\coth\sqrt{j\omega\tau_1}+\frac{L_2}{\tau_2}\sqrt{j\omega\tau_2}\coth\sqrt{j\omega\tau_2}}\right)\right], \quad (3.6)$$

$$Z_{\mathrm{DC}} = \frac{kT}{ec_0F}\left[\frac{L_1}{D_{p1}+D_{n1}}+\frac{L_2}{D_{p2}+D_{n2}}+\frac{8\left(t_{n2}t_{p1}-t_{n1}t_{p2}\right)^2}{\frac{L_1}{\tau_1}+\frac{L_2}{\tau_2}}\right], \quad (3.7)$$

$$\eta_0 = \frac{kT}{ec_0F}\frac{8\left(t_{n2}t_{p1}-t_{n1}t_{p2}\right)^2}{\frac{L_1}{\tau_1}+\frac{L_2}{\tau_2}}\frac{1}{Z_{\mathrm{DC}}}\ , \quad (3.8)$$

$$\tau_i = \frac{L_i^2}{8D_{pi}t_{ni}}, \quad \text{where} \quad (3.9)$$

$$D_{(p,n)i} = \frac{\mu_{p,n}b_{(p,n)i}kT}{e} \quad (3.10)$$

are corrected diffusion coefficients. Note that this correction for the diffusion coefficients and the modification of the transference numbers are the only changes of the Marshall-Madden impedance × area introduced by Bücker and Hördt (2013a).

To facilitate the direct comparison with measured data, Bairlein et al. (2016) propose a conversion of the impedance × area to an effective conductivity:

$$\sigma_{\mathrm{eff}}(\omega) = \frac{A_1}{Z(\omega)}\frac{L^2\Phi}{A_1L_1+A_2L_2} \quad (3.11)$$

Here, Φ is the porosity of the material, $L = L_1 + L_2$ the sum of the two pore lengths, and $A_i = \pi R_i^2$ are the cross-sectional areas of the two pores.

Adaptation of the analytical model

The analytical model can readily be adapted to account for the effect of non-wetting hydrocarbon droplets (water-wet model) as a second phase within the pore space. As in the model by Bücker and Hördt (2013a), we describe the pore space as an alternating sequence of wide and narrow cylindrical pores. The non-aqueous phase is modelled by placing a solid non-conducting cylinder at the centre of the cylindrical pore (see Figure 3.3). As discussed above, the resulting hydrocarbon-water interface can also be charged. Consequently, beside the fixed

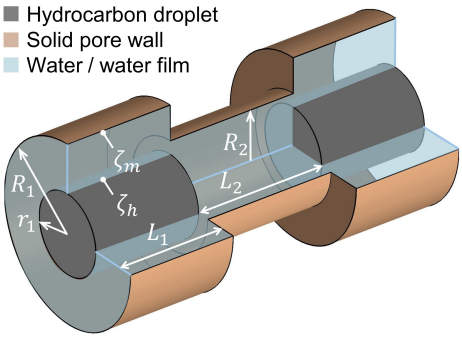

Figure 3.3: Three-dimensional sketch of the capillary model including hydrocarbon droplets in the wide pores. Note that both surfaces enclosing the water volume, the pore wall as well as the surface of the hydrocarbon droplet, can carry a surface charge indicated by the ζ-potentials ζ_m and ζ_h, respectively.

potential ζ_m at the pore wall ($r = R_i$), we assume a second fixed potential ζ_h at the hydrocarbon surface ($r = r_i$).
The radial variation of the electric potential in equation (3.1) was obtained from the linearized Poisson-Boltzmann equation in cylindrical coordinates:

$$\frac{1}{r}\frac{\partial}{\partial r}\left[r\frac{\partial U_i(r)}{\partial r}\right] = \kappa^2 U_i(r). \tag{3.12}$$

This is a zeroth-order modified Bessel equation with the general solution (e.g. Abramowitz and Stegun, 1965)

$$U_i(r) = A_i J_0(j\kappa r) + B_i Y_0(-j\kappa r), \tag{3.13}$$

where Y_0 is the Bessel function of the second kind. In order to estimate the radial electric potential profiles within a tubular water film between two cylinders (as needed for the water-wet model), we impose the boundary conditions $U_i(r_i) = \zeta_h$ and $U_i(R_i) = \zeta_m$, which yields the two coefficients

$$A_i = \frac{\zeta_h Y_0(-j\kappa R_i) - \zeta_m Y_0(-j\kappa r_i)}{Y_0(-j\kappa R_i)J_0(j\kappa r_i) - Y_0(-j\kappa r_i)J_0(j\kappa R_i)} \tag{3.14}$$

and

$$B_i = \frac{\zeta_m J_0(j\kappa r_i) - \zeta_h J_0(j\kappa R_i)}{Y_0(-j\kappa R_i)J_0(j\kappa r_i) - Y_0(-j\kappa r_i)J_0(j\kappa R_i)}. \tag{3.15}$$

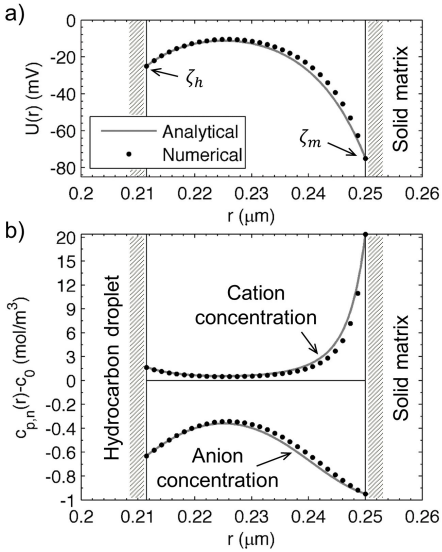

Figure 3.4: Radial variation of a) the electric potential and b) the excess ion concentrations in a tubular water film confined by two cylinders with $r \approx 0.21$ μm and $R = 0.25$ μm and with surface potentials $\zeta_h = -25$ mV and $\zeta_m = -75$ mV, respectively. The thickness of the water film is equal to four Debye lengths (here $\lambda_D \approx 0.01$ μm). Solid lines represent analytical solutions of the linearized Poisson-Boltzmann equation, black dots the full numerical solution. Note the different scaling of cation and anion concentrations (factor 15). Remaining parameter values: $c_0 = 1$ mol/m^3, $\varepsilon_r = 80$, $T = 293$ K, and $\mu_p = \mu_n = 5 \cdot 10^{-8}$ m^2/(Vs).

Figure 3.4a illustrates the variation of the electric potential within a thin water film of approximately four Debye lengths ($\lambda_D \approx 0.01$ μm for the chosen parameter values). The corresponding ion concentration profiles (Figure 3.4b) can be obtained by inserting the electric potential into the Boltzmann distribution, equation (3.3). Strictly speaking, the linearized Poisson-Boltzmann equation (3.12) is only valid for small surface potentials $e\zeta/kT \ll 1$ (or $|\zeta| \ll 25$ mV at room temperature) (e.g. Butt et al., 2003).
As typical ζ-potentials of silica minerals (e.g. Leroy et al., 2008) and liquid hydrocarbons (e.g. Buckley et al., 1989; Busscher et al., 1995) are in the range of -25 to -100 mV, we carry out numerical modelling to test how severe the violation of the condition of small potentials is. For this purpose, we solve the full Poisson-Boltzmann equation in cylindrical coordinates,

$$\frac{1}{r}\frac{\partial}{\partial r}\left[r\frac{\partial U_i(r)}{\partial r}\right] = \kappa^2 \frac{kT}{e}\sinh\left[\frac{e}{kT}U_i(r)\right]. \tag{3.16}$$

using the boundary conditions $U(r) = \zeta_h = -25$ mV and $U(R) = \zeta_m = -75$ mV.
Figure 3.4 shows that analytical and numerical results agree fairly well for typical ζ-potentials and a sufficiently thick water film between hydrocarbon droplet and solid matrix. As long as the thickness of the water film is larger than four Debye lengths (Figure 3.4), the small observable deviations can be considered negligible compared to other limitations of our model. However, within thinner water films, the two diffuse layers covering the hydrocarbon droplet and the solid surface overlap significantly and the predictions of the analytical model become increasingly inaccurate. In the present study, we will therefore clearly indicate modelling results related to water-film thicknesses below four Debye lengths.
In the next step, we calculate the mean ion concentrations normalized by the bulk concentration c_0 and the cross-sectional area of the wide pore A_1 as

$$b_{(p,n)i} = \frac{2\pi}{c_0 A_1}\int_{r_i}^{R_i} c_{(p,n)i}(r) r dr. \tag{3.17}$$

Figure 3.5 shows the variation of these dimensionless mean ion concentrations with the droplet radius for different potentials at the droplet surface. For $\zeta_h = 0$ mV the dimensionless mean cation concentration b_p decays monotonously with the droplet radius. This is an immediate consequence of the displacement of the electrolyte by the insulating droplet. For $\zeta_h < 0$ mV, b_p initially increases with increasing droplet radius. Here, the excess cation concentration of the EDL at the growing droplet surface overcompensates the displacement of the electrolyte

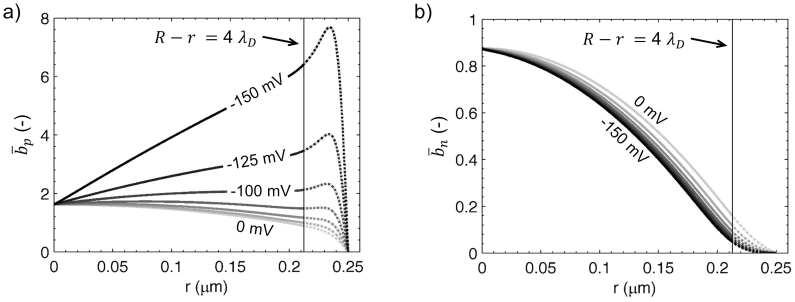

Figure 3.5: Variation of a) the dimensionless mean cation concentration and b) the dimensionless mean anion concentration with the droplet radius r given by equation (3.17). The radius of the pore $R = 0.25$ μm and the potential at the pore wall $\zeta_m = -75$ mV are kept constant. The dimensionless mean concentration vs. droplet radius curves are displayed for different potentials ζ_h between 0 and -125 mV (step width between curves 25 mV. The vertical lines indicate the critical droplet radius, at which the water-film thickness reaches the critical value of four Debye lengths. Remaining parameter values as in Figure 3.4.

by the insulating droplet. At water-film thicknesses of approximately four Debye lengths (here at $r > 0.21$ μm), this increase of b_p becomes even steeper, before b_p decays to zero for $r \to R$. As mentioned above, the results obtained for such small water-film thicknesses must be treated with caution due to the limited validity of the analytical solution in this case of significantly overlapping diffuse layers. The dimensionless mean anion concentrations b_n decay monotonously with the droplet radius. The deficit anion concentration in the EDL at the droplet surface makes the initial b_n decay stronger the larger the magnitude of ζ_h is.

Like in the original model by Bücker and Hördt (2013a), we use the dimensionless mean concentrations to calculate average transference numbers $t_{(p,n)i}$ via equation (3.5) and correct the ion diffusion coefficients $D_{(p,n)i}$ using equation (3.10). In this manner, we cast the effective transport properties of the capillary model into the 1D Marshall-Madden impedance given by equations (3.6) through (3.9). Note that unlike the original model, we do not consider a correction for the contribution of the Stern layer (i.e. the partition coefficient is assumed to be zero). The reason is the lack of information on the partitioning of cations into Stern and diffuse layer at the hydrocarbon-water interface.

Our approach allows us to study the variation of the frequency-dependent impedance of the pore sequence as a function of the radii of the hydrocarbon droplets. We will assume that the water films in both pores are of the same thickness, such that the radii of the two hydrocarbon droplets are coupled via $R_1 - r_1 = R_2 - r_2$. For the sake of simplicity, in our model, the hydrocarbon bridge across the narrow pore ruptures (snaps off) as soon as the film thickness is larger than the radius of the narrow pore (i.e. when $R_2 \leq R_1 - r_1$). This simplification ignores that as a result of surface tensions droplets are expected to snap off at much higher hydrocarbon saturations, which has to be taken into account in the interpretation of the results.
In order to facilitate the comparison with measured data, we convert the obtained droplet radii to equivalent residual water saturations. To this end, we express the total pore volume V_p and the total volume of the two droplets V_h as

$$V_p = \pi R_1^2 L_1 + \pi R_2^2 L_2 \quad \text{and} \quad V_h = \pi r_1^2 L_1 + \pi r_2^2 L_2. \tag{3.18}$$

Then the total hydrocarbon saturation and the residual water saturation are given by

$$S_h = \frac{V_h}{V_p} \quad \text{and} \quad S_w = 1 - S_h, \tag{3.19}$$

respectively.
To model the case of the liquid hydrocarbon as wetting phase, we can simply use the original model by Bücker and Hördt (2013a), i.e. equations (3.1) through (3.11). By substituting ζ_m by ζ_h in equation (3.1) and R_i by r_i in equations (3.1) and (3.4), we account for the fact that here the pore wall is completely covered by the hydrocarbon film and the water droplet (of radius r_i) is in contact with the hydrocarbon surface only. Accordingly, the total volume of the hydrocarbon film becomes

$$V_h = \pi(R_1^2 - r_1^2)L_1 + \pi(R_2^2 - r_2^2)L_2 \tag{3.20}$$

in the hydrocarbon-wet model. According to the precautions taken in the case of subcritical water-film thicknesses (smaller than four Debye lengths), we will clearly indicate all modelling results obtained for droplet radii smaller than two Debye lengths, where the diffuse layers covering the opposite boundaries of the water droplet. All other expressions remain unchanged.

3.3 Results

Unless otherwise stated, the following standard model parameter values are used to obtain the complex conductivity responses presented in this section. The bulk

ion concentration in the pore-filling electrolyte is set to $c_0 = 1$ mol/m^3. Cation and anion mobilities are $\mu_p = \mu_n = 5 \cdot 10^{-8}$ m^2/(Vs), which is approximately equal to the mobility of the sodium cation (e.g. Atkins and De Paula, 2013). In the water-wet case, the ζ-potential at the pore wall is assumed to be $\zeta_m = -75$ mV (with respect to reference potential of 0 mV at large distances from all interfaces), which is a typical value for silica mineral surfaces (e.g. Leroy et al., 2008). We use pore lengths of $L_1 = 50$ μm and $L_2 = 5$ μm and a porosity of $\Phi = 30\%$, which are representative values for fine sand or fine-grained sandstone (e.g. Morris and Johnson, 1967). In order to provide a significant polarization response of the capillary model (see e.g. Bairlein et al., 2016), we use pore radii $R_1 = 2.5$ μm and $R_2 = 0.25$ μm. The resulting (aspect) ratios between pore lengths and pore diameters, i.e. $L_i/(2R_i)$, are equal to 10 for both pores. This value is large compared to typical aspect ratios of $2 - 2.5$ in sedimentary rocks (Chatzis et al., 1983; Schmitt et al., 2016) but corresponds to the highest realistic aspect ratio proposed by Hördt et al. (2017).

3.3.1 Water-wet model

Figure 3.6 shows the spectral response of the water-wet model for varying residual water saturations and an absolute electric potential at the pore wall that is higher than the one at the hydrocarbon surface (i.e. $\zeta_h/\zeta_m < 1$). In the left panel (Figure 3.6a) we observe an increase of the conductivity magnitude with water saturation. The conductivity increase is most pronounced at low water saturations ($S_w < 0.19$), where the hydrocarbon droplet is continuous across both pores. Minor frequency variations of the conductivity magnitude only become visible at high water saturations.

Frequency variations of the conductivity phase are much more evident (Figure 3.6b). Maximum phase values (ca. 3.1 mrad) occur at high water saturations, monotonously decrease with the water saturation and practically vanish as saturation reaches the critical snap-off value. This phase decrease with decreasing water saturation can be understood by analysing equation (3.8), which directly relates variations of the polarization magnitude (here in terms of the polarizability) to the squared difference between the transference numbers of the two pores $(t_{n2}t_{p1} - t_{n1}t_{p2})^2$. Making use of the equality $t_{ni} = 1 - t_{pi}$, we can simplify this term to $(t_{p1} - t_{p2})^2$. At high water saturations, the EDL at the pore wall makes the narrow pore more ion-selective than the wide pore ($t_{p2} > t_{p1}$), which results in relatively high maximum phases. As water saturation decreases and the radius of the hydrocarbon droplet in the wide pore increases, the wide pore

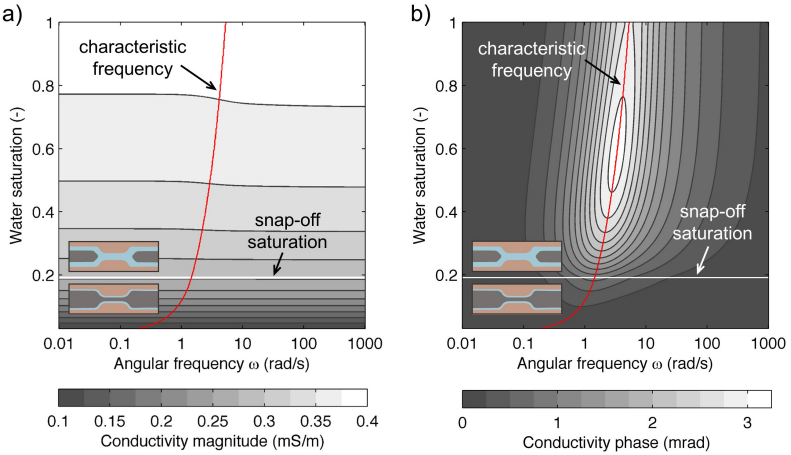

Figure 3.6: Frequency and saturation dependence of the effective conductivity of the water-wet model with surface potential $\zeta_h = -25$ mV. a) Magnitude and b) phase spectra as a function of residual water saturations. Contour lines are every 0.025 mS/m in a) and every 0.25 mrad in b). The white horizontal lines mark the snap-off saturation of $S_w \approx 0.19$, the red lines the variation of the characteristic angular frequency ω_c (as defined further below in the main text). Both plots are truncated at a saturation of $S_w \approx 0.03$, where the water-film thickness falls below four Debye lengths.

also becomes ion-selective (due to the EDL at the hydrocarbon surface) and the difference between the transference numbers decreases, leading to a reduction of the observed phases. At water saturations < 0.19, the hydrocarbon droplet penetrates the narrow pore and the water films in both pores are of the same thickness. As a result, the transference numbers in both pores are almost the same and no significant phases can be observed.

The decrease of the phase is accompanied by a decrease of the characteristic angular frequency ω_c, which we define as the angular frequency at which the phase peak is observed. For each water saturation, the phase spectrum comprises the phase values computed at 500 discrete angular frequencies (logarithmically equidistant between 0.01 and 1,000 rad/s); ω_c is then approximated by the discrete angular frequency, at which the calculated phase shift is maximum. At high water saturations ($S_w = 1$) the phase peak is centred on 5.3 rad/s, at the snap-off saturation ($S_w = 0.19$) it is encountered at 1.4 rad/s and reduces to 0.2 rad/s at the lowest saturation ($S_w = 0.03$).

This behaviour can be understood as follows: The characteristic angular frequency ω_c – or its inverse, the characteristic time constant $\tau_c = 1/\omega_c$ – is controlled by either of the two time constants τ_i as discussed in Bücker and Hördt (2013a). According to equations (3.9) and (3.10), both time constants τ_i depend on the dimensionless mean concentrations and the modified transference numbers as expressed by the proportionality $\tau_i \propto 1/(b_{pi}t_{ni})$ or equivalently $\tau_i \propto 1/(b_{ni}t_{pi})$. For negative surface potentials, the dimensionless mean concentration b_{ni} shows a steep decrease from ≤ 0.9 at small droplet radii to 0 at large droplet radii (see Figure 3.5), while the transference number b_{ni} only slightly increases from ~ 0.7 to 1 (as can also be inferred from Figure 3.5). Consequently, with increasing droplet radii r_i, i.e. with decreasing water saturation, both time constants τ_i are expected to increase, which explains the decrease of the characteristic angular frequency.

Although in practice high absolute values of ζ_h will most probably result in a transition to hydrocarbon-wet conditions, in Figure 3.7 we show that the variation of the effective conductivity changes significantly, when the absolute electric potential at the hydrocarbon surface becomes larger than the one at the pore wall (i.e. $\zeta_h/\zeta_m > 1$). Instead of the increase observed for $\zeta_h/\zeta_m < 1$, here, the conductivity magnitude varies only little with increasing water saturation. This observation might seem counterintuitive, but can be explained by the high cation excess concentration in the EDL at the hydrocarbon surface, which overcompensates the displacement of the aqueous electrolyte by the insulating hydrocarbon

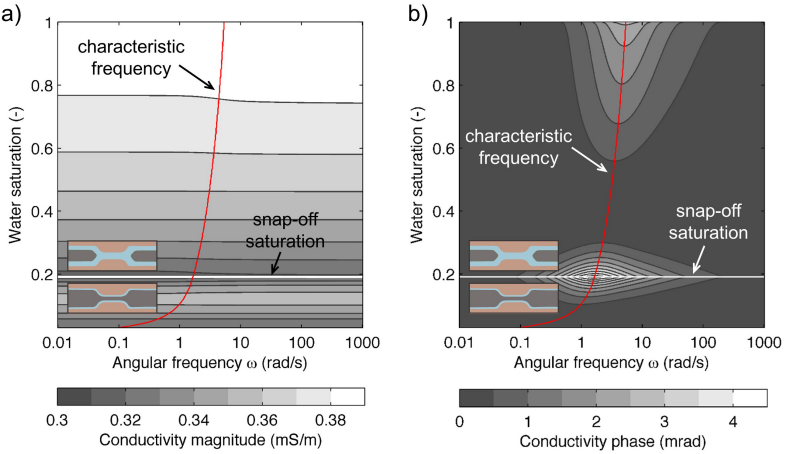

Figure 3.7: Frequency and saturation dependence of the effective conductivity of the water-wet model with surface potential $\zeta_h = -125$ mV. a) Magnitude and b) phase spectra as a function of residual water saturations. Contour lines are every 0.01 mS/m in a) and every 0.5 mrad in b). The white horizontal lines mark the snap-off saturation ($S_w \approx 0.19$), the red lines the variation of the characteristic angular frequency ω_c with the water saturation. Both plots are truncated at a saturation of $S_w \approx 0.03$ where the water-film thickness falls below four Debye lengths.

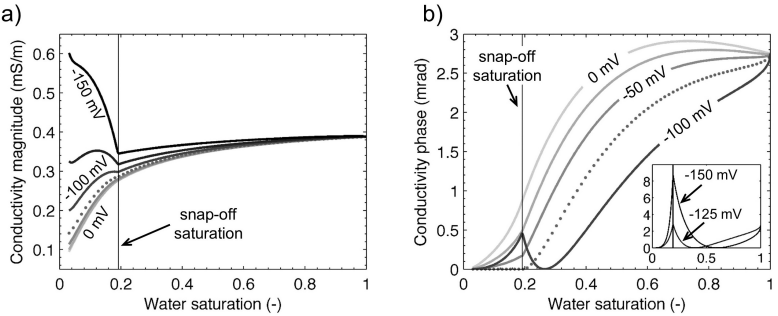

Figure 3.8: Variation of conductivity a) magnitude and b) phase of the water-wet model with the water saturation at $\omega = 1$ rad/s. While the surface potential at the pore wall is fixed at $\zeta_m = -75$ mV, the one at the hydrocarbon-water interface ζ_h is varied from 0 to -150 mV in steps of 25 mV. The dotted lines indicate the curve for the critical surface potential of $\zeta_h = -75$ mV. The solid vertical lines mark the snap-off saturation ($S_w \approx 0.19$). All curves are truncated at the saturation of $S_w \approx 0.03$, where the water-film thickness falls below four Debye lengths.

droplet.

In comparison to the case $\zeta_h/\zeta_m < 1$, maximum phases decrease much faster with decreasing water saturation. This is a direct consequence of the large excess cation concentration in the EDL at the hydrocarbon-water interface, which renders the wide pore ion selective at much higher water saturations (compared to the case $\zeta_h/\zeta_m < 1$). Interestingly, around the snap-off saturation (i.e. before the hydrocarbon droplet penetrates the narrow pore) the wide pore becomes more ion selective than the narrow pore. The reason is that the ion concentrations in the small pore are not yet affected by the large absolute ζ-potential at the hydrocarbon surface. As a result, a second phase maximum is obtained. However, once the snap-off (hydrocarbon-) saturation is exceeded, phase values decrease rapidly with decreasing water saturation as the difference of the transference numbers of both zones decreases too. At the same time, the variation of the characteristic angular frequency becomes more pronounced; from 5.3 rad/s ($S_w = 1$) it reduces to 0.1 rad/s ($S_w = 0.03$).

Obviously, the ratio ζ_h/ζ_m has a strong influence on the effective conductivity response of the capillary model. In order to study this dependence in more detail, we extract the magnitude and phase vs. saturation curves for different ratios

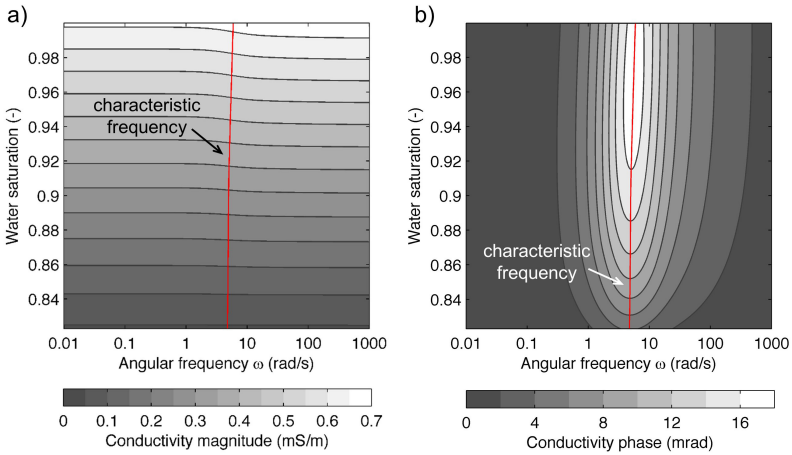

Figure 3.9: Frequency and saturation dependence of the effective conductivity of the hydrocarbon-wet model with surface potential $\zeta_h = -125$ mV. a) Magnitude and b) phase spectra as a function of residual water saturation. Contour lines are every 0.05 mS/S in a) and every 2 mrad in b). The red lines mark the variation of the characteristic angular frequency ω_c with the water saturation. Both plots are truncated at the critical saturation of $S_w \approx 0.82$, where the radius of the water droplet in the narrow pore falls below two Debye lengths; at a slightly lower water saturation ($S_w \approx 0.81$), the residual water becomes discontinuous in the narrow pore.

ζ_h/ζ_m at an angular frequency of $\omega = 1$ rad/s, a typical value used for single-frequency IP measurements. Figure 3.8 shows that (i) the transition between the two limiting situations observed above is continuous while increasing the ratio ζ_h/ζ_m; (ii) the critical value of this ratio seems to be $\zeta_h/\zeta_m = 1$; and (iii) for larger ratios, the second phase maximum begins to occur around the snap-off saturation. This behaviour of the phase response can also be reproduced for other electric surface potentials at the pore wall (not shown here for brevity).

3.3.2 Hydrocarbon-wet model

In the hydrocarbon-wet model, the liquid hydrocarbon and the water interchange roles. In particular, there is no EDL at the water-pore wall interface (characterized by ζ_m) because the pore wall is completely covered by a hydro-

carbon film. Consequently, the conductivity of the pore sequence will be completely determined by the radii of the residual water droplets and the potential ζ_h at the hydrocarbon surface.

Figure 3.9 shows the spectral response of this hydrocarbon-wet model. The conductivity magnitude increases almost linearly with the water saturation, which simply reflects the fact that the effective (water-filled) cross section increases with the water saturation. Note that as soon as the water saturation falls below the snap-off saturation ($S_w \approx 0.81$), the entire cross-section of the narrow pore throat is occupied by the insulating liquid hydrocarbon, which completely blocks electric current.

In contrast to the behavior of the water-wet model, the maximum phases observed in the hydrocarbon-wet model first increase slightly with increasing hydrocarbon saturation (decreasing water saturation) and then decrease rapidly towards the critical saturation. Based on the simple analysis of the term $(t_{p1}-t_{p2})^2$ made above, one would expect a monotonous increase of the phase response with hydrocarbon saturation as a result of the increasingly ion-selective behaviour of the narrow pore. However, as discussed before by Bücker and Hördt (2013a) and recently substantiated by Hördt et al. (2017), the ratio of pore radii that provides maximum phases also depends on the length ratio of the pores (more specifically, phases are maximum if $R_1^2/R_2^2 = L_1/L_2$). Decreasing the radius of the narrow pore beyond this optimum ratio does not further increase the phase response. In the present example this optimum ratio is reached approximately midway between full water saturation and the critical saturation at $S_w \approx 0.81$ (Figure 3.9b).

The characteristic angular frequency varies little over the narrow range of relevant saturations (from 5.9 rad/s at $S_w = 1$ to 4.7 rad/s at $S_w = 0.82$). At the same time the corrected ion diffusivity in the narrow pore must vary strongly as a result of the reduction of the effective cross section, see equations (3.10) and (3.4) (including the substitution $R_i \rightarrow r_i$). From the negligible effect of the corrected ion diffusivity in the narrow pore on the characteristic angular frequency, we can conclude that the relaxation process is largely controlled by the time constant of the wide pore. This behavior corresponds to the long narrow pore or wide pore regime discussed in detail in Bücker and Hördt (2013b) and Hördt et al. (2017), in which the concentration gradients that cause the membrane-polarization effect are largely generated and relaxed via the wide pore.

To study possible effects due to the variation of ζ_h, we display magnitude and

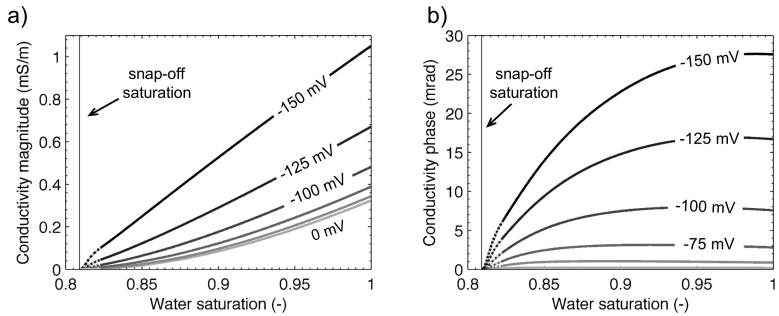

Figure 3.10: Variation of conductivity a) magnitude and b) phase of the hydrocarbon-wet model with the water saturation at $\omega = 1$ rad/s. The surface potential at the hydrocarbon-water interface ζ_h is varied from 0 to -150 mV in steps of 25 mV. The vertical lines mark the snap-off saturation. Note that as soon as the water droplet is expelled from the narrow pore, no electric current can pass and the pore system becomes insulating. Dotted lines indicate parts of the curve, which correspond to water-droplet radii below two Debye lengths.

phase vs. water saturation curves at $\omega = 1$ rad/s for seven different values of ζ_h. Because of the increasingly large excess cation concentration in the EDL, the conductivity magnitude increases monotonically with the absolute value of the surface potential. The almost linear increase of the conductivity magnitude with water saturation can be observed for all values of ζ_h.

As a result of the increasing difference between the transference numbers of the two pores as the absolute surface potential increases, the phase response increases too. At the same time, the water saturation, at which the phase maximum is observed increases from approximately $S_w \approx 0.87$ at $\zeta_h = -25$ mV to $S_w \approx= 0.99$ at $\zeta_h = -150$ mV. We attribute the two last observations to the above mentioned optimum ratio of pore radii. Furthermore, Hördt et al. (2017) show that the optimum ratio also depends on the ζ-potential, an effect which is expected to become important at large absolute ζ-potentials.

3.4 Discussion

3.4.1 Comparison with experimental data - conductivity magnitude

The general trend of a decreasing conductivity magnitude with increasing hydrocarbon saturation predicted by both the water-wet and and the hydrocarbon-wet model is in agreement with most laboratory experiments on hydrocarbon-contaminated sediments that have not undergone biodegradation (Olhoeft, 1985, 1992; Vanhala et al., 1992; Börner et al., 1993; Daily et al., 1995; Chambers et al., 2004; Titov et al., 2004; Ustra et al., 2012; Martinho et al., 2006; Cassiani et al., 2009; Schmutz et al., 2010; Abdel Aal and Atekwana, 2013). Only for high absolute ζ-potentials at the hydrocarbon surface (i.e. for mixtures containing a larger fraction of long-chain components) in the case of a non-wetting hydrocarbon, we observe a reversal of this pattern. We explained the resulting increase of conductivity with hydrocarbon saturation with the high cation concentration in the EDL that outbalances the displacement of conducting electrolyte by the insulating hydrocarbon droplet.
Revil et al. (2011) anticipated a similar relationship in their discussion of the conductivity increase observed on sand samples that were contaminated with a wetting oil characterized by a larger fraction of polar components (i.e. resins and asphaltenes), and consequently with a higher absolute ζ-potential. Additional experimental evidence for the conductivity magnitude increase with the saturation of wetting oil can be found in Li et al. (2001). The predictions of our model, which only indicate this increase if hydrocarbon is the non-wetting phase, do not seem to fit the experimental findings. A possible explanation is the cylindrical geometry of our model, which in the case of a wetting hydrocarbon results in a decrease of the surface area of the hydrocarbon-water interface with increasing hydrocarbon saturation. As the contribution of the EDL to the total electric current scales with the surface area, our hydrocarbon-wet model predicts a conductivity decrease with hydrocarbon saturation. However, in three-dimensional media consisting of mineral grains, the surface area of the grain-coating hydrocarbon will definitely increase with increasing hydrocarbon saturation – at least for low to intermediate hydrocarbon saturations.

3.4.2 Comparison with experimental data - conductivity phase

To our best knowledge, the proposed models (i.e. the water-wet and the hydrocarbon-wet model) represent the first mechanistic approach offering a possible explanation for the decrease of IP phase shifts with increasing hydrocarbon

saturation and, under certain conditions, for the occurrence of a phase maximum at intermediate saturations. While the model by Schmutz et al. (2010) predicts a monotonous increase of IP phase shifts with hydrocarbon contamination, various authors (e.g. Martinho et al., 2006; Flores Orozco et al., 2012; Johansson et al., 2015) mention the possibility of a different behaviour – often linked to the yet unconsidered effect of membrane polarization but always in terms of conceptual models. In our models, we can explain the variations of the phase response based on the modification of the relation between the respective transport properties of the large pore spaces (wide pore) and the pore throats (narrow pore).

In absence of hydrocarbon contamination, membrane polarization is a result of the interplay of ion-selective pore throats and non-selective open pore spaces. In the case of a non-wetting hydrocarbon, discontinuous droplets (and their EDL) also render the wide pores ion-selective, which decreases the membrane polarization effect with increasing hydrocarbon saturation. A high absolute value of ζ_h enhances this effect to such an extent that the wide pore (together with the trapped droplet) becomes more ion selective than the pore throat. As a result, we observe a local phase maximum at intermediate hydrocarbon saturations, before the droplet penetrates the pore throat and becomes continuous over various neighbouring pores. Part of this mechanism has been anticipated by Johansson et al. (2015) in their model A.

In the case of the liquid hydrocarbon as wetting phase, we observe a slight increase of the phase with hydrocarbon saturation, before it rapidly decreases to zero as the saturation approaches the critical snap-off value. As the discussion of Johansson et al. (2015) (their model D) illustrates, the initial increase of the membrane-polarization phase seems intuitive as the pore throats are expected to become increasingly ion-selective with increasing hydrocarbon saturation. Yet, after the initial increase our quantitative modelling predicts an overall decrease of the phase, consistent with the experimental results reported by Revil et al. (2011) for measurements on sand samples contaminated with wetting oil.

Furthermore, we observe a good agreement of the predictions of our hydrocarbon-wet model with the experimentally determined phase vs. benzene concentration curve reported by Flores Orozco et al. (2012). In their results, the sudden decrease of IP phases appears at benzene concentrations just above the solubility of benzene in water. Although these concentrations are just enough to indicate the presence of free-phase benzene, actual concentrations of the separate hydrocarbon in the formation are often considerably higher than those determined from groundwater samples (e.g. Abdul et al., 1989). The comparison with our

model predictions suggests (i) that the conditions at the site studied by Flores Orozco et al. (2012) are predominantly hydrocarbon-wet and (ii) that the separate benzene phase occupies those narrow pore throats with a significant membrane polarization response.

The only spectral IP parameter considered in our modelling study is the characteristic frequency. Its decrease with increasing hydrocarbon saturation, which is predicted by the water-wet and the hydrocarbon-wet model, is in agreement with most experimental studies that allow to assess this parameter (e.g. Olhoeft, 1992; Kemna et al., 1999; Cassiani et al., 2009; Schmutz et al., 2010; Revil et al., 2011; Flores Orozco et al., 2012). Most authors attribute the corresponding increase of the relaxation time to an increase of the characteristic length scale of the system, such as mean grain diameters, pore lengths, or pore throat diameters. This is straight forward, as the diffusion time $\tau \propto L^2/D$ (e.g. Bücker and Hördt, 2013b) is proportional to the square of the characteristic length scale L. In our model, both pore lengths are kept constant. Instead, the variation of the effective pore cross-sections and the mean concentrations determine transport rates within the electrolyte, which affects the relaxation time via the diffusivity D. As discussed in more detail above, with increasing hydrocarbon saturation, the increasing constriction of the volume of the aqueous electrolyte reduces the corrected (or effective) diffusivity and thereby delays the relaxation process.

3.4.3 Implications for the detectability of free-phase hydrocarbon

The detectability of free-phase hydrocarbon contamination is primarily determined by the contrast between the IP signatures (i.e. conductivity magnitude and phase) of the contaminated and the clean host medium. Although in practice macroscopic IP signatures will comprise responses of various polarization mechanisms at different amounts (e.g. membrane polarization, Stern-layer polarization), we can deduce some qualitative relationships between the physical and electro-chemical properties of the hydrocarbon and the host medium on the one hand and the magnitude of the membrane-polarization response due to the contaminant phase on the other hand. In our model, the magnitude of the ζ-potential at the hydrocarbon surface, the wettability conditions, and the geometrical parameters of the two cylindrical pores significantly influence the hydrocarbon-induced variation of the response.

Under water-wet conditions (cf. Figure 3.8), the relation between conductivity magnitude and hydrocarbon saturation is ambiguous: Depending on the particular value of the ζ-potential at the hydrocarbon surface, the modelled

conductivity magnitude can increase, keep almost constant, or decrease with the hydrocarbon concentration. The phase response of the water-wet model, in contrast, shows an unambiguous variation between the clean host medium (full water saturation), where the phase response is large, and a highly contaminated medium (water saturation close to zero), where the phase response reduces to zero. The only exception from this tendency has been discussed before and consists in the phase maximum observed around the snap-off-saturation in the case of high magnitudes of the ζ-potential at the hydrocarbon surface. In summary, these model predictions imply a strong detectability of source zones (i.e. zones with high hydrocarbon and low water saturations close to zero) by variations of the conductivity phase.

At the same time, our results suggest that the ζ-potential at the (non-wetting) hydrocarbon surface does not affect the efficiency of the IP method for the characterization of hydrocarbon-impacted sites. Instead, variations of this surface property only influence the particular shape of the phase response vs. water saturation curves of the water-wet model. The maximum contrast between clean and highly contaminated media – and thus the source-zone detectability – is completely independent of the ζ-potential at the hydrocarbon surface. Instead, this contrast is controlled by the magnitude of the membrane-polarization response of the clean medium: In general, narrow pores with relatively small cross-sections favour the generation of high maximum phase shifts. Consequently, the membrane-polarization response of the clean medium (and thus the maximum contrast between clean and highly contaminated media) can be expected to increase with decreasing pore size. For a more detailed discussion of the geometrical constraints of the polarization response of the clean membrane-polarization model, we refer to Hördt et al. (2017).

In our hydrocarbon-wet model, both parts of the complex conductivity show similar variations with the hydrocarbon saturation and the ζ-potential at the hydrocarbon surface: While an increasing hydrocarbon saturation results in a clear decrease of conductivity magnitude and conductivity phase, the contrast between slightly and highly contaminated sediments increases with the magnitude of the ζ-potential at the hydrocarbon surface. Consequently, our model predicts a higher sensibility of both parts of the IP response, i.e. conductivity magnitude and phase, to variations of hydrocarbon saturation. However, also in the hydrocarbon-wet model, the complex conductivity contrasts between a completely clean medium and a highly contaminated medium – and thus the detectability of source zones – are limited by the maximum response of the clean

medium.

3.4.4 Scope of the proposed model

The scope of the proposed model can be extended to partially saturated sediments and rocks. As observed experimentally, quite similar effects on the IP response are obtained when the pore-filling electrolyte is displaced either by a (non-wetting) liquid hydrocarbon or air (e.g. Titov et al., 2004; Cassiani et al., 2009). As far as modelling aspects are concerned, this observation is completely plausible because (1) non-wetting liquid hydrocarbon droplets and air bubbles/ganglia are expected to take similar geometrical configurations within the pore space (e.g. Titov et al., 2004; Johansson et al., 2015), (2) both liquid hydrocarbon (high resistivities) and air (insulator) have much higher resistivities than the pore water, and (3) the air-water interface is usually negatively charged (e.g. Yang et al., 2001; Jia et al., 2013) as it is the case with the hydrocarbon-water interface.

However, the predictive power of the proposed model is limited by a series of severe simplifications. First of all, in order to treat the underlying physical problem analytically, the complex three-dimensional pore system of real subsurface materials is cast into a simple (two-dimensional) capillary model and the complex conductivities presented in this study reflect the response of a bundle of such parallel 1D capillaries. While this restriction might already be significant in the hydrocarbon-free case, it becomes considerably more important in presence of the liquid hydrocarbon. Depending on the dynamic contamination history, the latter can take highly complex three-dimensional geometrical configurations on both the pore scale (e.g Gvirtzman and Roberts, 1991) and the pore-network scale (e.g. Chatzis et al., 1983; Zhao and Ioannidis, 2003, 2007). In this sense, the responses of the proposed model need to be understood either as the basic responses of elementary cells, which are part of a larger cell network, or as the responses of bundles of pores of similar size and with similar geometrical configurations of the liquid hydrocarbon.

Important aspects that have not been incorporated in our model are biodegradation and stimulated microbial activity. Notwithstanding, the metabolic degradation and/or transformation of hydrocarbon compounds by indigenous soil microorganisms and products released by redox reactions potentially affect all relevant model parameters. The release of CO_2 and organic acids changes the pH in the pore water in contact with liquid (or dissolved) hydrocarbon (e.g. Sauck, 2000). Such acids, ions directly released by reduction processes, as well

as dissolved minerals of the aquifer sediments that become instable under the changed pH conditions usually lead to an increase of water conductivity (e.g. Sauck, 2000). Both, pH and ion concentration in the pore water are the most important parameters controlling the ζ-potential at the mineral-water interface (e.g. Leroy et al., 2008) and the hydrocarbon-water interface (e.g. Buckley et al., 1989; Busscher et al., 1995). The effect of variable ion concentration and pH on our membrane polarization model was studied in some detail by Hördt et al. (2016). In summary, the polarization magnitude increases monotonically with pH, whereas it increases with ion concentrations only at low to moderate salinities and decreases at high salinities. These model predictions are in good qualitative agreement with the experimental findings of Weller et al. (2013) and Weller et al. (2015). Biodegradation also changes the composition of the residual hydrocarbon as it generally increases the fraction of polar and long-chained components, which leads to an increase of the absolute surface potential and might possibly alter wettability. Geometrical parameters can be affected too. On the one hand, changes of the ζ-potential as well as the release of surface-active compounds as by-products of the degradation reactions (e.g. Kanicky et al., 2001) can alter interfacial tensions and wettability conditions, which can result in the geometrical reconfiguration of the two liquid phases in the pore space. On the other hand, mineral dissolution and the formation of new stable minerals (e.g. Schumacher, 1996) can alter the solid phase and affect porosity, pore radii and lengths, as well as the interconnectivity of the pore system. In some cases, the precipitated solids might be electronically conducting (e.g. Cozzarelli et al., 1999), which would give rise to electrode polarization (e.g. Wong, 1979) as an additional source mechanism.

Dissolution of hydrocarbon into the pore water and sorption of dissolved compounds to the solid surface are also not considered. There are good reasons to believe that dissolved hydrocarbon compounds do neither change the conductivity magnitude of the pore water (e.g. Lee et al., 2003) nor the polarization response of the composite system (e.g. Cassiani et al., 2009). Furthermore, these experimental observations might indicate that the effect of sorption on the polarization response is negligible, too: Because of their low solubility in water, dissolved hydrocarbon compounds can be expected to readily sorb onto the surface of the solid phase. Although they might there occupy charged surface sites and alter the ζ-potential (e.g. Forté and Bentley, 2013), in the experiments conducted by Cassiani et al. (2009), no significant differences could be observed between samples saturated with clean water and samples saturated with water

containing dissolved hydrocarbons.

3.5 Conclusions

We developed a first mechanistic model which allows to predict how a liquid hydrocarbon in the pore space affects membrane polarization in contaminated sediments or sedimentary rocks. In our model the pore space is described as a sequence of two types of cylindrical pores with different pore radii and lengths. The separate hydrocarbon-contaminant phase is either considered as additional cylinder in the pore space or as film covering the pore walls.
Our modelling results indicate that the EDL at the hydrocarbon-water interface significantly influences the membrane-polarization response of the model system. For low absolute ζ-potentials and a non-wetting hydrocarbon, the modelled conductivity magnitudes and phases decrease with hydrocarbon saturation. If high ζ-potentials are assumed increasing phases are observed for increasing hydrocarbon saturation, until the non-wetting hydrocarbon becomes continuous across the narrow pore throats.
Regardless of the ζ-potential at the hydrocarbon-water interface, our model for wetting hydrocarbon predicts a monotonous decrease of the conductivity magnitude with increasing hydrocarbon saturation. At the same time, the conductivity phase shows an initial increase with contaminant saturation, which is followed by a steep decrease towards the critical water saturation at with the aqueous phase becomes discontinuous within the narrow pore throat.
As can be seen from the above results, our model provides a framework for the interpretation of phase responses that depart from the increasing phase vs. hydrocarbon saturation behaviour predicted by an earlier pore-scale model that attributes the IP response to the polarization of the Stern layer of the EDL at the solid-water interface (Schmutz et al., 2010).
Although some of the derived IP responses show a good agreement with laboratory and field data, due to the strongly simplified geometry the proposed model is definitely not meant as a sole basis for the interpretation of specific experimental data. Further developments of the proposed approach should consider more realistic pore geometries and geometric liquid hydrocarbon configurations. Besides the use of numerical methods to approach more realistic pore geometries, an interesting possibility is to connect several impedances in a network, as suggested by Stebner and Hördt (2017).

CHAPTER 4

Electrochemical polarization around metallic particles – Part 1: The role of diffuse-layer and volume-diffusion relaxation

4.1 Introduction

Due to the strong polarization response of metallic minerals, the Induced Polarization (IP) method has been used for decades in the exploration of ore deposits (e.g. Seigel et al., 2007). From the beginning, the observed frequency dispersion of the measured electrical conductivities was attributed to the polarization of the solid-liquid interface between highly conductive mineral grains and the surrounding electrolyte (e.g. Wait, 1958), often referred to as *electrode polarization*. Pelton et al. (1978) later adapted the empirical Cole-Cole relaxation model (Cole and Cole, 1941) to describe the frequency-dependence of IP measurements, which to date is a common practice. In order to improve the understanding of the microscopic causes of the polarization effect taking place around metallic particles, Angoran and Madden (1977) and Klein and Shuey (1978) studied the effect of reaction currents, which arise from charge-transfer reactions of electroactive cation species at the solid-liquid interface. Because reaction currents short-circuit the charge accumulations at both sides of the interface, the polarization of the particle surfaces becomes imperfect, which in turn largely affects the polarization response. The two aforementioned studies laid the foundation for the models by Wong (1979) and Wong and Strangway (1981), which directly relate the observed IP response to geometrical and electrochemical properties of highly conductive particles suspended in electrolyte solution.

During the last two decades, technical advances regarding measuring devices and imaging algorithms led to a renewed interest in the IP method (e.g. Kemna et al., 2012). Ongoing research provides detailed knowledge on complex-conductivity

This chapter is based on: Bücker, M., Flores Orozco, A., and Kemna, A. (2018). *Electrochemical polarization around metallic particles – Part 1: The role of diffuse-layer and volume-diffusion relaxation.* Geophysics, 83(4):E203–E217.

responses of composite geomaterials leading to a continued widening of the range of near-surface applications of the method (Kemna et al., 2012). As a result, today the polarization response of metallic particles is also taken advantage of for environmental investigations, such as the detection and characterization of metal-bearing contaminant plumes (e.g. Placencia-Gómez et al., 2015; Günther and Martin, 2016), the accumulation of iron sulphides accompanying bioremediation (Flores Orozco et al., 2011, 2013), or naturally reduced zones related to biogeochemical hot spots (e.g. Wainwright et al., 2015), the monitoring of permeable reactive barriers (e.g. Slater and Binley, 2006) or metallic nano-particle injections (e.g. Flores Orozco et al., 2015; Abdel Aal et al., 2017), amongst others.

As the classical models cannot explain the broad variety of measured IP responses (e.g. Flores Orozco et al., 2011, 2013), the rapid experimental advances also stimulate a search for improved models and a deeper understanding of the polarization of conducting particles. Merriam (2007) emphasized the importance of charge storage in the Stern layer - the inner fixed layer of the electrical double layer coating the solid-liquid interface, which had so far not been taken into account explicitly. However, the limitation of his treatment to one spatial dimension might overlook the more complex responses of two- or three-dimensional media. Flekkøy (2013) developed a semi-empirical diffusion-polarization model (also in one spatial dimension), which relates the well-known Cole-Cole relaxation model to microscopic parameters. Placencia-Gómez and Slater (2014) used the model by Wong (1979) to reproduce most characteristics of IP responses measured on artificial sulfide-sand mixtures, but also point out important limitations of this highly parameterized model regarding the fitting of real IP spectra. In an attempt to reduce the complexity of Wong's model, Gurin et al. (2015) and Placencia-Gómez and Slater (2015) reinterpreted the polarization of metallic particles in terms of the polarization of nonconducting dielectric particles (e.g. O'Konski, 1960; Schwarz, 1962; Schurr, 1964). Possible shortcomings of these recent studies will be addressed in the discussion section. Because many important ore minerals are semiconductors (e.g. Pearce et al., 2006), Revil et al. (2015b) and Misra et al. (2016a) disputed Wong's assumption of perfectly conducting particles as inappropriate for most ore minerals and developed models for the polarization of semiconducting particles. These models additionally include the contribution of the non-metallic background material (e.g. of clay minerals) to the overall polarization response.

Considering the lack of a unified theory of the electrode polarization mecha-

nisms as described above, this study further analyzes Wong's electrochemical model. Particular emphasis is placed on the control that particle size and chemical composition of the electrolyte (i.e., electrolyte concentration and fraction of electro-active ions) exert over the polarization response. In contrast to the compact treatment provided by Wong (1979), we include the derivation of the full solution of the underlying Poisson-Nernst-Planck system of differential equations. We also derive explicit expressions for the time constants of the two main relaxation processes inherent to the model - the diffuse-layer and the volume-diffusion relaxation. Our improvements of the mathematical description permits us to illustrate the spatial variation of ion concentrations and electric potential around the particle and set the basis for a better understanding of the electrode polarization mechanism. Following our systematic analysis, it is then possible to reveal and discuss some notable misinterpretations of Wong's model that arose in the more recent literature.

4.2 Theory

Wong (1979) bases his model of the polarization response of metal-bearing geomaterials on the treatment of perfectly conducting particles suspended in an electrolyte. The electrolyte is characterized by the concentrations of three ionic species; anions c_1, inactive cations c_2, and active cations c_3. Inactive cations are those cations, which are not able to penetrate the solid-liquid interface, while active cations engage in reduction-oxidation reactions at the metal surface, which allow electric charges to be transferred between the two phases. Typical examples for inactive cations are Na^+ or K^+ and active cations will generally be dissolved metal ions.

Under the influence of an external electric field $\mathbf{E}_{\text{ext}}$, the concentrations of the three ionic species and the electric potential U are perturbed from their equilibrium values. For a periodic excitation with $E_{\text{ext}} = E_0 e^{i\omega t}$, where ω denotes the angular frequency and t the time, the ion concentrations can be expressed in terms of uniform equilibrium concentrations in the bulk electrolyte c_j^∞ and frequency-dependent perturbation concentrations δc_j as follows.

$$c_j(\mathbf{r}, t) = c_j^\infty + \delta c_j(\mathbf{r}, \omega) e^{i\omega t} \tag{4.1}$$

Unlike Wong, who defines the ion concentrations in ions/m^3, here we use molar concentrations in mol/m^3. If no excitation is imposed, the electric potential U is zero everywhere. Consequently, under the influence of a harmonic external field

the total electric potential is equal to the corresponding perturbation potential

$$U(\mathbf{r},t) = \delta U(\mathbf{r},\omega)e^{i\omega t}. \tag{4.2}$$

In the perturbed system, concentration gradients drive diffusion currents and electric fields cause electro-migration currents. For sufficiently small amplitudes E_0 of the external field, the corresponding linearized ion flux densities read

$$\mathbf{J}_j(\mathbf{r},t) = -D_j\nabla\delta c_j(\mathbf{r},\omega)e^{i\omega t} - \mu_j z_j c_j^\infty \nabla\delta U(\mathbf{r},\omega)e^{i\omega t}, \tag{4.3}$$

where D_j, μ_j, and z_j denote the diffusion coefficient, the mobility, and the valence of the j-th ionic species, respectively. With the conservation laws $\partial_t\delta c_j = -\nabla\mathbf{J}_j$ and the Einstein relation $D_j = \mu_j kT/e$ (e.g. Atkins and De Paula, 2013), equation (4.3) becomes

$$\frac{i\omega}{D_j}\delta c_j(\mathbf{r},\omega) = \nabla^2\delta c_j(\mathbf{r},\omega) + \frac{e}{kT}z_j c_j^\infty \nabla^2\delta U(\mathbf{r},\omega), \tag{4.4}$$

where $k = 8.617\cdot10^{-5}$ eV/K denotes Boltzmann's constant, T the absolute temperature and $e = 1.602\cdot10^{-19}$ C the elementary charge. While the bulk electrolyte is electrically neutral, i.e. $c_1^\infty = c_2^\infty + c_3^\infty$, non-zero charge densities arising from unbalanced total cation and anion perturbation concentrations generate electric fields as quantified by Poisson's equation

$$\nabla^2\delta U(\mathbf{r},\omega) = -\frac{F}{\varepsilon_0\varepsilon_r}\sum_{j=1}^{3} z_j\delta c_j(\mathbf{r},\omega). \tag{4.5}$$

Here, $F = 96485$ As/mol is Faraday's constant, $\varepsilon_0 = 8.85\cdot10^{-12}$ F/m the vacuum permittivity, and ε_r the relative permittivity of the solution. Equations (4.4) and (4.5) constitute the Poisson-Nernst-Planck (PNP) system of partial differential equations, which is used to describe ion transport through the electrolyte solution around the conducting particle.

4.2.1 Full analytic solution

To model the complex frequency-dependent response of a suspension of metallic particles, the PNP system is first solved for a single spherical particle of radius a centered at the origin of a polar coordinate system r, θ, ϕ. Choosing $\theta = 0$ in the direction of the external field, the latter can be described by the electric potential $\delta U_{\text{ext}} = -E_0 r\cos\theta$ and the solution becomes independent of the azimuthal angle ϕ. In order to simplify the algebraic expressions, ion mobilities and diffusion

coefficients are assumed to be the same for all three ionic species, i.e. $\mu_j = \mu$ and $D_j = D$ for all j, and the treatment is limited to a symmetric monovalent electrolyte, i.e. $z_1 = -1$ and $z_2 = z_3 = 1$. A general solution of the PNP system can then be given in terms of the three perturbation concentrations (Wong, 1979)

$$\delta c_1(\mathbf{r},\omega) = -A(\omega)k_1(\lambda_1 r)\cos\theta + B(\omega)k_1(\lambda_2 r)\cos\theta, \tag{4.6}$$

$$\delta c_2(\mathbf{r},\omega) = \frac{c_2^\infty}{c_1^\infty}A(\omega)k_1(\lambda_1 r)\cos\theta + \left[B(\omega) - M(\omega)\right]k_1(\lambda_2 r)\cos\theta, \tag{4.7}$$

$$\delta c_3(\mathbf{r},\omega) = \frac{c_3^\infty}{c_1^\infty}A(\omega)k_1(\lambda_1 r)\cos\theta + M(\omega)k_1(\lambda_2 r)\cos\theta, \tag{4.8}$$

and the perturbation potential

$$\delta U(\mathbf{r},\omega) = \left[-\frac{2F}{\lambda_1^2\varepsilon_0\varepsilon_r}A(\omega)k_1(\lambda_1 r) - E_0 r + E(\omega)\frac{a^3}{r^2}\right]\cos\theta. \tag{4.9}$$

The radial variation of the perturbation concentrations is controlled by the modified spherical Bessel function of the second kind

$$k_1(\lambda r) = \frac{\pi}{2}e^{-\lambda r}\left(\frac{1}{\lambda r} + \frac{1}{\lambda^2 r^2}\right). \tag{4.10}$$

and the two reciprocal length scales

$$\lambda_1^2 = \frac{i\omega}{D} + \kappa^2 \text{ and } \lambda_2^2 = \frac{i\omega}{D}, \tag{4.11}$$

where $\kappa = [2c_1^\infty eF/(\varepsilon_0\varepsilon_r kT)]^{1/2}$ is equal to the inverse of the Debye length λ_D. The four unknown coefficients $A(\omega)$, $B(\omega)$, $E(\omega)$, and $M(\omega)$ are determined from boundary conditions on the three ion flux densities and the perturbation potential at the metal surface. For brevity, here we only present the final expressions for the coefficients. Intermediate steps of this derivation are given in appendix A. The coefficient $E(\omega)$ is the only provided and discussed in the treatment by Wong (1979).

$$E(\omega) = E_0\left\{1+ \frac{3\left(1+\frac{\beta a}{D}f_3\right) + \frac{3c_3^\infty}{c_3^\infty - 2c_1^\infty}\left(\frac{\alpha}{\mu}-1\right)}{\frac{c_3^\infty}{c_3^\infty-2c_1^\infty}\left[f_1 + \frac{\alpha}{\mu}(f_2-2) + \frac{\beta a\lambda_1^2}{D\kappa^2}+2\right] - (2+f_1)\left(1+\frac{\beta a}{D}f_3\right)}\right\}, \tag{4.12}$$

where

$$f_1 := f_2 \frac{i\omega}{D\kappa^2}, \quad f_2 := \frac{\lambda_1^2 a^2 + 2\lambda_1 a + 2}{\lambda_1 a + 1}, \text{ and } \quad f_3 := \frac{\lambda_2 a + 1}{\lambda_2^2 a^2 + 2\lambda_2 a + 2}. \tag{4.13}$$

With the coefficient $E(\omega)$ at hand, the remaining unknown coefficients, which control the short-range perturbations around the polarized particle, can be expressed as

$$A(\omega) = \frac{E_0 a - E(\omega) a}{-2F/(\lambda_1^2 \varepsilon_0 \varepsilon_r) k_1(\lambda_1 a)}, \tag{4.14}$$

$$B(\omega) = \frac{E_0 - E(\omega)}{k_1'(\lambda_2 a)} \left\{ \frac{\lambda_1^2 \varepsilon_0 \varepsilon_r}{2F} f_2 - \frac{\mu}{D} c_1^\infty \left[f_2 + \frac{E_0 + 2E(\omega)}{E_0 - E(\omega)} \right] \right\}, \text{ and} \tag{4.15}$$

$$M(\omega) = -\frac{c_3^\infty}{c_1^\infty} \frac{E_0 - E(\omega)}{k_1'(\lambda_2 a)\left(1 + \frac{\beta a}{D} f_3\right)} \left\{ \frac{\lambda_1^2 \varepsilon_0 \varepsilon_r}{2F} \left(f_2 + \frac{\beta a}{D} \right) - \frac{c_1^\infty}{D} (\mu - \alpha) \left[f_2 + \frac{E_0 + 2E(\omega)}{E_0 - E(\omega)} \right] \right\}, \tag{4.16}$$

where $k_1'(\lambda a)$ denotes the partial derivative of the modified spherical Bessel function of the second kind evaluated at the metal surface. Differentiation of equation (4.10) yields

$$k_1'(\lambda a) = \partial_r k_1(\lambda r)\Big|_{r=a} = -\lambda k_1(\lambda a) - \frac{\pi}{2} \frac{e^{-\lambda a}}{a} \left(\frac{1}{\lambda a} + \frac{2}{\lambda^2 a^2} \right). \tag{4.17}$$

The four coefficients, equations (4.12) through (4.16), substituted into the general solution, equations (4.6) through (4.9), constitute the full solution of the problem, which shall now be further analyzed.

The first terms on the right-hand sides of equations (4.6) through (4.8) describe the space charge $F[\delta c_2(\mathbf{r}, \omega) + \delta c_3(\mathbf{r}, \omega) - \delta c_1(\mathbf{r}, \omega)]$, which accumulates in a field-induced Gouy-Chapman diffuse layer. For sufficiently small frequencies, $\lambda_1 \approx \kappa$ and the term $k_1(\lambda_1 r)$ controlling the spatial extension of the space charge decays roughly with $e^{-\kappa r}$. The characteristic length of this decay is the Debye length $\lambda_D = 1/\kappa$, which may thus be used to approximate the thickness of the diffuse layer. The second terms of equations (4.6) through (4.8), in contrast, describe electro-neutral concentration perturbations, the spatial extension of which is controlled by the ratio $k_1(\lambda_2 r)/k_1'(\lambda_2 a)$. At low frequencies, i.e. for $\omega \to 0$, this ratio approaches $-a^3/(2r^2)$ and thus describes a $1/r^2$ decay, which allows the concentration perturbation to extend much deeper into the electrolyte. As

an estimator for the thickness of the layer affected by the concentration perturbation, we will use the distance of $a\sqrt{e} - a$ from the surface, at which the concentration perturbations reduce to $1/e$ of their (virtual) values at the particle surface.

The total perturbation potential consists of three contributions. The first term on the right-hand side of equation (4.9) corresponds to the field-induced space charge that accumulates in the diffuse layer. Just like the space charge, the related potential perturbation decays exponentially with the distance from the surface. The second term describes the contribution of the uniform external electric field. The last term corresponds to the effective or long-range induced dipole moment of the polarized particle including the surrounding perturbation layer. The dipole potential decays quadratically with the distance from the centre of the particle.

For the quantification of the macroscopic polarization response of the suspended particle it is sufficient to know the reflection coefficient $f(\omega) = E(\omega)/E_0$, which describes the long-range potential perturbation [third term in equation (4.9)] produced by the polarized particle together with the space charges that accumulate in its immediate vicinity. The effective conductivity σ_{eff} describes the effect of the suspended spherical particles on the macroscopic electrical properties of the inhomogeneous medium in terms of the conductivity of an equivalent homogeneous medium. To approximate the effective conductivity σ_{eff} of a two-phase system consisting of a number of metallic particles randomly dispersed in the electrolytic host medium, the dipole coefficient enters into the mixing rule (Wong, 1979)

$$\frac{\sigma_{\text{eff}}(\omega)}{\sigma_0} = \frac{1 + 2\nu f(\omega)}{1 - \nu f(\omega)}, \tag{4.18}$$

where $\sigma_0 = 2\mu c_1^\infty F$ denotes the electrical conductivity of the bulk electrolyte and ν the volumetric fraction of metallic particles.

4.3 Polarization mechanism

The treatment provided by Wong (1979) does not provide a comprehensive discussion of the contributions of the different micro-scale processes described by his theory, neither does he detail the relation between these physical processes and the model parameters, such as particle size and electrolyte composition. This lack has resulted in fundamental misconceptions of the model. Based on the full solution of the PNP system, we can provide visual insight into the polarization phenomena and more thorough explanations of the underlying physical

processes. This section therefore aims at realigning the understanding of the Wong model in general and the parameters controlling amplitude and shape of the frequency-dependence electric conductivity in particular.
Under the influence of an external electric field, mobile charges on the perfectly conducting particle – the electrons in the case of a metallic conductor – instantaneously redistribute along its surface. Within the particle, the electric field of the resulting charge distribution exactly cancels out the external field. This property of the perfect conductor is taken into account by a zero-potential boundary condition on the particle surface, see equation (4.25). As we show in appendix B, the surface charge density required to cancel out the mere external field is given by

$$\Sigma_\infty(\theta) = 3\varepsilon_0\varepsilon_r E_0 \cos\theta. \tag{4.19}$$

On the electrolyte side, the induced surface charge Σ_∞ attracts ions of the same sign (counter-ions) and repels those of opposite sign (co-ions). This situation corresponds to an excitation with high frequencies or to early times after switching on a constant external field.
In addition to this very fast polarization process, migration currents through the bulk solution further charge the electrolyte around the poles of the particle (see Figure 4.1). The charging continues until the effect of the electro-migration currents is balanced by opposed diffusion currents around the particle. In this manner, at sufficiently low excitation frequencies a new quasi-equilibrium situation is established, in which Gouy-Chapman diffuse layers build up at the particle surface. Because the continued accumulation of charges in the diffuse layers induces opposite image charges on the conducting sphere, this process also blows up the surface charge on the particle. In appendix B, we show that the total charge in the fully developed diffuse layer can be approximated by

$$\Sigma_0(\theta) = \Sigma_\infty(\theta)\frac{\kappa a}{2}. \tag{4.20}$$

As for typical particle sizes and electrolyte concentrations the double layer is much thinner than the particle radius and thus $\kappa a \gg 1$, the charge stored in the diffuse layer and mirrored on the particle surface exceeds by far the one necessary to cancel out the electric field within the sphere.
Figure 4.2 illustrates the field-induced perturbations around the conducting particle in terms of their real (upper half of each panel) and imaginary parts (lower half). Where indicated, small magnitudes of the imaginary components are magnified by the factors defined in the lower halves of the panels. The first line of Figure 4.2 shows the four perturbation quantities at the low-frequency limit,

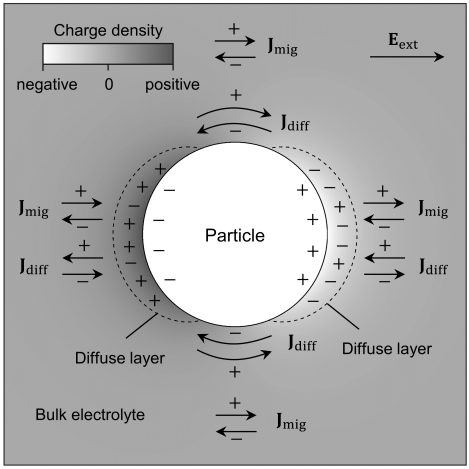

Figure 4.1: Schematic representation of the double-layer charging mechanism. Over the right side of the sphere, the migration current $\mathbf{J}_{\mathrm{mig}}$ in the bulk electrolyte depletes cations (+) from the diffuse layer and fills it with anions (−). The resulting space charge in the diffuse layer induces positive image charges on the particle, which hold the space charge next to the surface. Over the left side, the process is the same but with opposite polarity, such that concentrations gradients arise between the two hemispheres. As soon as the charging migration currents are balanced by (tangential and normal) diffusion currents $\mathbf{J}_{\mathrm{diff}}$ driven by the concentration gradients, a quasi-equilibrium state is reached with a fully charged diffuse layer.

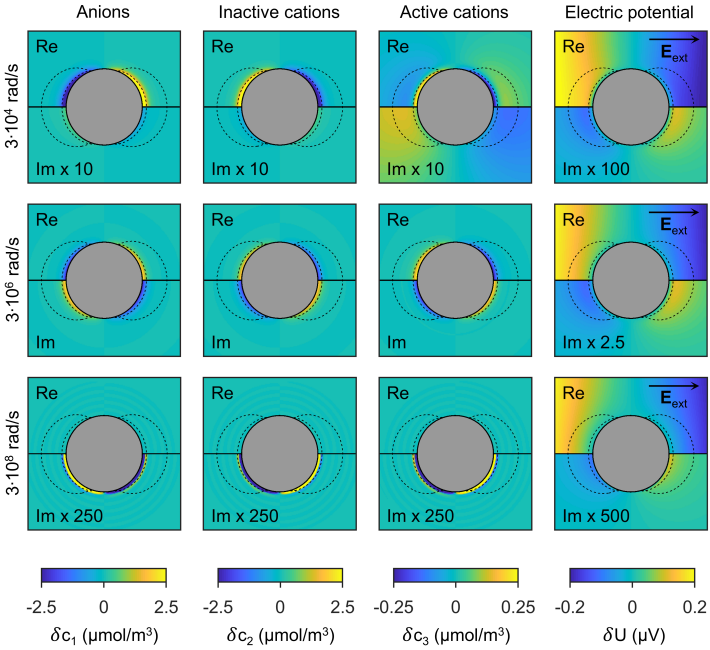

Figure 4.2: Perturbation concentrations and potentials around a perfectly conducting sphere of radius $a = 0.1$ μm for three different angular frequencies. The upper part of each panel shows the real part, the lower the imaginary part. Note that some imaginary parts were scaled to make small variations visible. The inner dashed line indicates the diffuse double layer, the outer the volume-diffusion layer. Parameter values are $\varepsilon_r = 80$, $\mu = 5 \cdot 10^{-8}$ m^2/(Vs), $c_1^\infty = 1$ mol/m^3, $c_3^\infty = 0.12 c_1^\infty$, $\alpha = 1 \cdot 10^{-10}$ m^2/(Vs), $\beta = 1 \cdot 10^{-2}$ m/s, $T = 293$ K, and $E_0 = 1$ V/m.

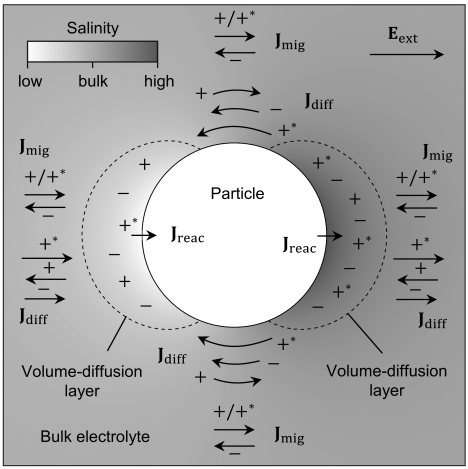

Figure 4.3: Schematic representation of the volume-diffusion mechanism. For the sake of clarity, the diffuse layer is omitted although in reality it would be superimposed. The reaction current $\mathbf{J}_{\mathrm{reac}}$ depletes active cations ($+^*$) from the left and fills the right volume-diffusion layer with active cations. The migration currents $\mathbf{J}_{\mathrm{mig}}$ through the bulk electrolyte transport active ($+^*$) and inactive cations ($+$) with the fixed proportion c_3^∞/c_2^∞ and can therefore not balance the resulting concentration surpluses and deficits. Instead, these perturbation concentrations increase until the resulting concentration gradients between the two opposite sides of the particle are sufficiently large to drive diffusion currents $\mathbf{J}_{\mathrm{diff}}$, which compensate the excess of active ion current caused by $\mathbf{J}_{\mathrm{reac}}$.

the second line at an intermediate frequency, and the third line at the high-frequency limit. For a justification of the selected frequencies, please refer to the spectral responses included at the end of this section. At the low-frequency limit, we recognize fully developed diffuse layers covering the two sides of a sub-micron particle ($a = 0.1$ μm). We select a very small particle for the visualization because it permits to distinguish the diffuse layer of thickness λ_D as indicated by the inner dashed line. According to the orientation of the external electric field (pointing right), the induced surface charge is negative on the left side and positive on the right. Correspondingly, the polarities of the induced diffuse layers are opposite left and right of the particle.

Still in the first line of Figure 4.2 and outside the diffuse layer, we identify a second zone of non-zero perturbation concentrations indicated by the outer

dashed line. This anomaly, which is most pronounced for the active cations but balanced by corresponding perturbations of the concentrations of the two inactive ionic species, corresponds to the electro-neutral parts of the perturbation concentrations described by the second terms of equations (4.6) through (4.8). The build-up of the concentration cloud is linked to reaction currents across the solid-liquid interface and thus disappears in absence of active cations (not shown here for brevity). The formation of the concentration cloud can be understood in terms of the volume- or bulk-diffusion process explained in Figure 4.3. In summary, perturbations of the active cation concentrations produced by the reaction currents cannot be balanced by electro-migration currents through the bulk electrolyte. Instead, a concentration gradient arises, which by means of diffusion transports active cations from the anodic (cations are released into the solution) to the cathodic side of the particle (cations adsorb to the particle). Effectively, in Figure 4.2 we can convince ourselves that the accumulation of a c_3 surplus to the right and a deficit to the left of the particle corresponds to a concentration gradient, which drives a left-pointing diffusion current, while the electro-migration current points right (in the direction of the external field).

The volume-diffusion process introduced in Figure 4.3 and the previous paragraph is similar to the the semi-finite diffusion problem over a planar electrode, which leads to the more familiar Warburg impedance (e.g. Bazant et al., 2004). Warburg-type impedances are generally encountered in electro-chemical systems, in which the transport of ions to the electrode (if ions are consumed) or from the electrode away (if ions are produced) is primarily by diffusion and not by electro-migration.

So far, we have only considered the polarization mechanism around a very small particle ($a = 0.1$ μm), the relaxation responses of which occur far beyond the maximum frequencies of typical field- and even laboratory-scale IP measurements. Yet, the radial concentration profiles (i.e. for $\theta = 0$) presented in Figure 4.4 show that both diffuse layer and volume-diffusion layer also build up and have similar characteristics around much larger particles (here $a = 10$ mm) associated with relaxations at typical IP frequencies. For comparison, Figure 4.5 shows the radial concentration profiles around the small particle in the same fashion. Besides obvious scaling effects, the most significant difference between the radial profiles of differently sized particles concerns the perturbation concentrations of the active cations δc_3 within the diffuse layer. While to the right of the small particle (Figure 4.2 and Figure 4.5) the perturbation concentrations are negative, i.e. active cations are depleted compared to the bulk electrolyte,

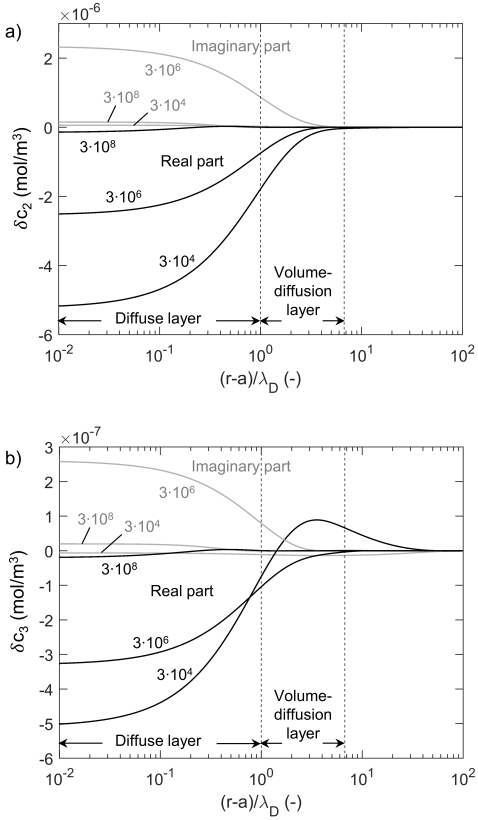

Figure 4.4: Radial variation (r is the distance from the centre of the spherical particle) of the cation perturbation concentrations δc_2 (inactive) and δc_3 (active) along the symmetry axis ($\theta = 0$) in the vicinity if a metallic sphere of radius $a = 10$ mm at three different angular frequencies ($\omega = 10^{-4},\ 0.1,\ 10$ rad/s). The left dashed line indicates the extensions of the diffuse layer (DL, distance to surface λ_D), the right those of the volume-diffusion layer (distance $a\sqrt{e} - a$). Besides the much larger particle radius, all other parameters as in Figure 4.2.

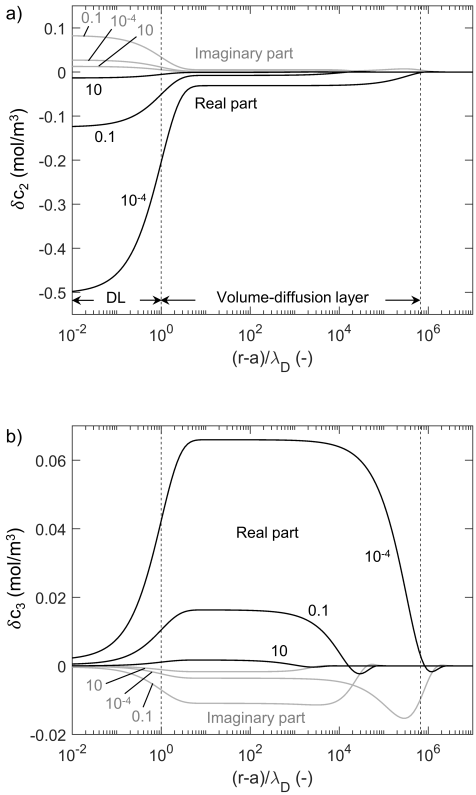

Figure 4.5: Radial variation (r is the distance from the centre of the spherical particle) of the cation perturbation concentrations δc_2 (inactive) and δc_3 (active) along the symmetry axis ($\theta = 0$) in the vicinity if a metallic sphere of radius $a = 0.1$ μm at three different angular frequencies ($\omega = 3 \cdot 10^4,\ 3 \cdot 10^6,\ 3 \cdot 10^8$ rad/s). The left dashed line indicates the extensions of the diffuse layer (DL, distance to surface λ_D), the right those of the volume-diffusion layer (distance $a\sqrt{e} - a$). All parameters as in Figure 4.2.

they become positive in the case of a much larger particle (Figure 4.4, bottom) representing an increase over the active cation bulk concentration.

We explain this observation by the different overlaps of diffuse (thickness λ_D) and volume-diffusion layer (thickness $\approx 0.65a$). Around the sub-micron particle, the diffuse layer occupies a large fraction of $\lambda_D/(0.65a) \approx 0.15$ of the volume-diffusion layer, which seems to be large enough to inhibit a full development of the volume-diffusion layer. Around the large particle, this fraction is much smaller (10^{-6}) and the volume-diffusion layer fully develops. Further below, the strong control the ratio λ_D/a or its inverse κa exerts on the volume-diffusion polarization will be reconfirmed.

When the frequency of the external excitation is increased until it approaches the respective characteristic frequency (i.e. $3 \cdot 10^6$ rad/s and 0.1 rad/s around the small and the large particle, respectively), large imaginary parts of the perturbation concentrations appear within the electrical double layer indicating that a relaxation is taking place. At the same time, the perturbation concentrations in the volume-diffusion layer practically disappear around the small (second line in Figure 4.2 and Figure 4.5) and reduce significantly around the large particle (see $\omega = 0.1$ rad/s in Figure 4.4). A reduced diffuse layer persists in both cases. If the frequency is further increased, the temporal variation of the excitation is too fast to permit the ions to rearrange and form the diffuse layer. As a consequence, in the respective high-frequency limits, both real and imaginary part of the perturbation concentrations approach zero.

As we can see from the perturbation potential (Figure 4.6), the development of a quasi-equilibrium diffuse layer at low frequencies largely screens (counterbalances) the field-induced surface charge Σ on the conducting particle. As a result, outside the diffuse layer the potential distribution approaches the one of an insulating particle, the reflection coefficient of which can be obtained as $f = -1/2$ from potential theory[1]. The remaining difference to the potential of an insulating sphere is due to the large non-zero exchange currents (a consequence of the large active cation concentration $c_3^\infty = 0.12$ mol/m^3) but disappears, if $c_3^\infty \to 0$ (not shown here for brevity). As mentioned above, with increasing frequency, the diffuse layer cannot fully develop and the screening of the surface charge becomes increasingly imperfect. At the high-frequency limit, the potential distribution therefore approaches the one of a perfect conductor[1] with $f = 1$ (see again Figure 4.6).

[1] The reflection coefficient f of a sphere with conductivity σ_s embedded in a medium with homogeneous conductivity σ_m is $(\sigma_s - \sigma_m)/(\sigma_s + 2\sigma_m)$ (e.g. Maxwell, 1891).

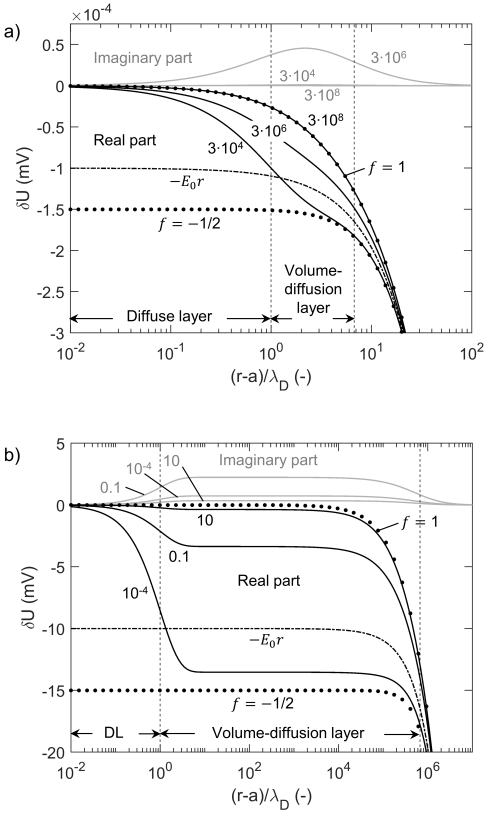

Figure 4.6: Radial variation (r is the distance from the centre of the spherical particle) of the electric perturbation potential δU along the symmetry axis ($\theta = 0$) in the vicinity of metallic spheres of (a) radius $a = 0.1$ μm at the angular frequencies $\omega = 3{\cdot}10^4$, $3{\cdot}10^6$, and $3 \cdot 10^8$ rad/s and (b) radius $a = 10$ mm at $\omega = 10^{-4}$, 0.1, and 10 rad/s. The left dashed lines indicate the extensions of the diffuse layer (DL, distance to surface λ_D), the right those of the volume-diffusion layer (distance $a\sqrt{e}-a$). Besides the much larger particle radius in (b), all other parameters as in Figure 4.2.

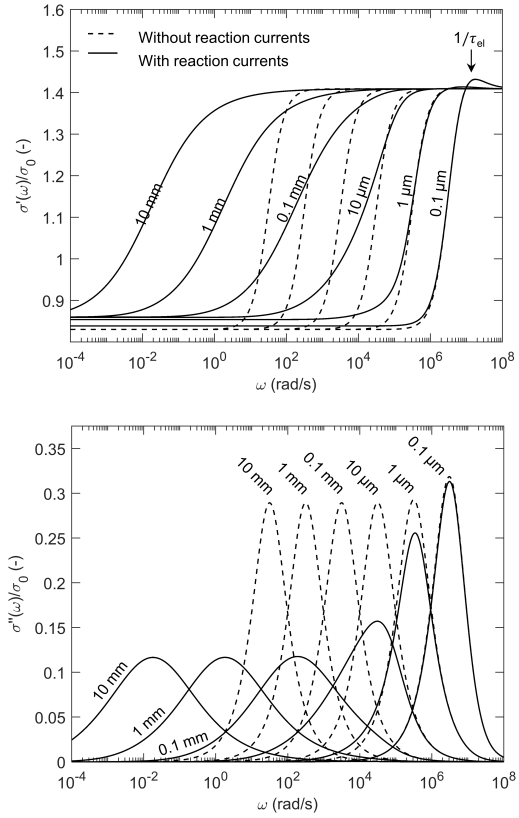

Figure 4.7: Effective normalized conductivity spectra for particles with different radii a between 0.1 μm and 10 mm. Responses in absence (dashed lines) and presence (solid lines) of active cations responsible for the occurence reactions currents are included. The complex-valued conductivities are expressed in terms of real σ' (top) and imaginary effective conductivity σ'' (bottom). The arrow in the top panel marks the characteristic frequency $\omega_{el} = 1/\tau_{el}$ discussed further below. Volumetric fraction of conducting spheres $\nu = 0.12$; all other model parameters as in Figure 4.2.

The microscopic frequency dependencies around a single spherical particle directly relate to the macroscopic response of a suspension of a larger number of equal particles. Figure 4.7 shows the spectral response of a suspension with a volumetric particle content of $\nu = 0.12$ in terms of real σ' and imaginary part σ'' of the effective electric conductivity defined in equation (4.18). The spectra of the two particle sizes discussed in detail in this section (i.e. $a = 0.1$ μm and 10 mm) appear as limiting cases and are accompanied by additional spectra that correspond to intermediate particle sizes. In order to start differentiating between the macroscopic effects of diffuse-layer polarization and volume-diffusion relaxation, Figure 4.7 includes spectra for $c_3^\infty = 0$ (without reaction current, dashed curves) and $c_3^\infty = 0.12 c_1^\infty$ (with large reaction currents, solid curves).

Regardless of particle size and the concentration of active cations, the low- and high-frequency limits of all σ' spectra are (almost) the same. At low frequencies, they all approach a direct-current conductivity σ_{DC} well below σ_0. In this limit, the diffuse layer builds up, which fully screens the electric field of the induced surface charges and gives the particle (not the suspension) a vanishing effective conductivity. As a result, the particles – although perfect conductors – decrease the effective conductivity of the suspension below the conductivity of the electrolyte. Only the contribution of the reaction current through the particle slightly increases σ_{DC} and, thus, explains the small deviations between the values of σ_{DC} of the models with and without reaction currents.

At the high-frequency limit, the diffuse layer does not develop, induced charges are not screened and the particle behaves like a perfect conductor. Consequently, the suspended particles significantly increase the conductivity of the mixture. Obviously, even the contribution of reaction currents cannot further increase the (already infinite) effective conductivity of the sphere and no differences are observed between the high-frequency limits with and without reaction currents.

Particle size and active cation concentrations, however, largely affect the transition between these limits. If no active cations are present, i.e. in the absence of the volume-diffusion process, the relaxation of the diffuse layer controls the increase of σ' and causes a narrow peak of σ''. The flanks of the σ'' peak increase and decrease with steep slopes $\propto \omega$ and $\propto 1/\omega$, respectively. This frequency dependence corresponds to the behaviour of a resistor-capacitor (RC) circuit, which is a plausible parallelism for a charge-relaxation process as it is the case with the diffuse-layer polarization. An increase of the particle size shifts the characteristic angular frequency ω_{c}, i.e. the frequency at which σ' transition and σ'' peak are observed, to lower angular frequencies, while it does practically

not affect the maximum of σ'' (except for very small particles).

The presence of active cations changes the spectral response significantly. As we observe in Figure 4.7, the contribution of the associated volume-diffusion process driven by the non-zero reaction currents broadens the σ' transition region and the σ'' peak, reduces the maximum of σ'', and notably shifts ω_c towards lower frequencies. These changes are almost imperceptible for small particles, while they become most pronounced for large particles. As in this context metallic minerals in the sub-millimeter range are considered large particles, it cannot be stressed enough that besides geometry, also fluid chemistry exerts a large control over the characteristic frequency. The slopes of the broadened peaks (e.g. for $a = 10$ mm) increase and decrease with $\propto \sqrt{\omega}$ and $\propto 1/\sqrt{\omega}$, respectively. As previously mentioned by Wong (1979) and in accordance with our present understanding of the volume-diffusion process, the occurrence of the quantity $1/\sqrt{i\omega}$ is typical for purely diffusion-controlled relaxations and can therefore also be encountered in the Warburg impedance (e.g. Merriam, 2007). In comparison to the case without reaction currents, the decrease of ω_c with the particle size is much more pronounced.

The comparison of the two cases also has an important practical implication. Although the presence of active cations largely affects the spectral response of the suspension, it is clearly no necessary condition for a polarization process to occur. This conclusion is in agreement with the findings of other recent studies into the polarization response of conducting particles with inert surfaces (J. Quian and P.N. Sen, personal communication, 2016). However, the absence of active cations can – especially in the case of relatively large particles – shift the overall polarization response to much higher frequencies, where it can typically not be observed with IP field or laboratory instruments.

4.4 Relaxation time scales

Due to the above observed dependence on the particle size, the characteristic frequency – or its inverse, the relaxation time – can often be used to infer this important geometrical parameter from spectral IP data. However, as we also recognized in Figure 4.7, relaxations times for one particle size vary considerably depending on the concentration of active cations. The analysis of this subject provided by Wong (1979) is brief, only states that for smaller particles the relaxation time varies with $\propto a\lambda_D/D$ and for larger particles with $\propto a^2/D$ and does not explicitly refer to the chemical composition of pore the water.

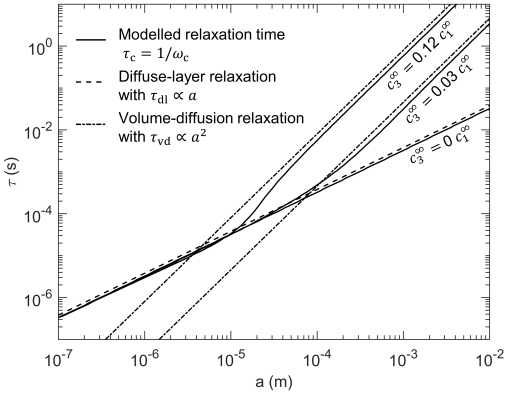

Figure 4.8: Variation of relaxation times τ with the particle radius a for three different concentrations of active anions $c_3^\infty/c_1^\infty = 0,\ 0.03$, and 0.12. Modelled relaxation times τ_c correspond to the inverse of the characteristic angular frequency ω_c, at which the peak of the imaginary is observed. Dashed lines correspond to the relaxation time of the diffuse layer τ_{dl}, equation (4.22), and dash-dotted lines to to the relaxation time of the volume diffusion τ_{vd}, equation (4.23). All other parameter values as in Figure 4.2.

Because of its importance as proxy for the particle size and because it potentially determines if a relaxation can be detected at all using band-limited measuring devices (see discussion at the end of the previous section), in this section we will investigate the relaxation times of the polarization model in more detail.

Figure 4.8 shows the variation of the relaxation times, determined from modelled spectra as $\tau_c = 1/\omega_c$, with the particle radius for three different concentrations of active cations (solid lines). For non-zero active cation concentrations, the curves reconfirm the transition from a linear increase of τ_c with a for small particles to a quadratic increase for large particles as reported by Wong (1979). In the case of vanishing active cation concentrations, the linear increase of τ_c continues even for large particles. As without active cations no reaction currents are active, only the diffuse-layer polarization develops and the linear increase must be related to the charge-relaxation process of the diffuse layer. Consequently, the presence of volume-diffusion processes in the opposite case must be responsible for the quadratic increase. Although reaction currents are also active at the surface of small particles, the overall polarization response seems to be dominated by the relaxation of the diffuse layer. As Figure 4.8 further indicates, the critical

particle radius, at which the transition between the two regimes is observed, strongly varies with the fraction of active cations in the electrolyte solution.

Relaxation of the electrolyte solution

The fastest polarization process inherent to this model is related to the relaxation of the electrolyte solution. The corresponding relaxation time (e.g. Shilov et al., 2001)

$$\tau_{\mathrm{el}} = \frac{\varepsilon_0 \varepsilon_r}{\sigma_0} = \frac{\lambda_D^2}{D} \tag{4.21}$$

is a measure of the time that it takes the ions of the solution to screen the initial surface charge Σ_∞ before the charging of the diffuse layer takes effect. τ_{el} is also referred to as Debye time or the time scale of charge relaxation (e.g. Bazant et al., 2004). Its inverse ω_{el} marks the angular frequency, at which the characteristic magnitudes of conduction and displacement current density become equal. Therefore, in the treatment of the dielectric dispersion of suspensions, ω_{el} is used to define the limit between low- and high-frequency range (e.g. Shilov et al., 2001). In the equations of the Wong model, ω_{el} marks the angular frequency, at which real and imaginary part of λ_1, equation (4.11), are equal.
In the spectra in Figure 4.7, the relaxation of the electrolyte solution can be related to the small overshoot of over the high-frequency asymptote of the σ' spectra for small particle sizes. This overshoot and its relaxation at ω_{el} are present in the spectra of larger particles, too, but can only be distinguished at high zoom levels (not shown here for brevity). Also note that in the context of induced-polarization studies with frequency ranges that hardly reach 1 kHz, the relaxation of the electrolyte is of little relevance, as for typical aqueous solutions in geomaterials it corresponds to characteristic frequencies ≥ 1 MHz.

Diffuse-layer relaxation

The first relevant time scale can be related to the relaxation of the space charge stored in the field-induced diffuse layer covering the poles of the particle. Because this polarization persists even if reaction currents are absent, an approximate expression for the corresponding time scale can be obtained by evaluating equation (4.12) in the limit $c_3^\infty \to 0$. As we show in more detail in appendix C, this yields the expression

$$\tau_{\mathrm{dl}} = \frac{a\lambda_D}{2D} \tag{4.22}$$

for the relaxation time of the diffuse-layer polarization. Generally, time scales $\propto \lambda_D L/D$, where L denotes the characteristic system length, are often found in the description of problems involving dynamic charging of electric double layers. Because these processes involve simultaneously acting diffusion and electro-migration currents, both the bulk conductivity σ_0 (via λ_D) and the geometric scale a of the problem control this "mixed" time scale (Bazant et al., 2004). The same time scale as expressed in equation (4.22) was also found by Qian and Sen (J. Quian and P.N. Sen, personal communication, 2016) for the diffuse-layer relaxation of inert conducting particles.

In the context of the Wong model, excess and defect ion concentrations within the diffuse layers covering the two poles of the particle are controlled by a complex balance of tangential and normal electro-migration and diffusion currents around the particle. Consequently, the time it takes the ions to move to their new quasi-equilibrium positions τ_{dl} depends on both processes. The contribution of the electro-migration process causes the dependence on λ_D, while the diffuse transport introduces the dependence on the particle radius a. The induced double layers (diffuse layers and their image charges on the particle surface) on the two poles of the particle can be interpreted as capacitors connected in parallel through the bulk electrolyte, which acts like an ohmic resistance. The relaxation time of such a RC circuit increases linearly with the resistance and the capacitance (e.g. Pelton et al., 1978). In the context of the Wong mode, the dependence on the resistance corresponds to the variation of τ_{dl} with the resistivity of the bulk electrolyte $\rho_0 = 1/\sigma_0$. The capacitance is the charge stored in the capacitor per applied voltage, which according to equation (4.20) in our model scales with $a\kappa$ and multiplied by $1/\sigma_0$ results in a relaxation time $\propto a/\sqrt{\sigma_0}$ as predicted τ_{dl}.

Figure 4.8 shows that τ_{dl} describes the variation of the modelled relaxation time τ_{c} with a quite well, as long as no active cations exist in the electrolyte, i.e. $c_3^{\infty} = 0$, and the diffuse-layer polarization dominates. Therefore, even for $c_3^{\infty} > 0$ the modelled curves coincide with τ_{dl} as long as the particle radius is sufficiently small.

Volume-diffusion relaxation and critical particle size

The second relevant time scale is related to the relaxation of electro-neutral perturbations of the electrolyte concentration caused by the volume-diffusion process driven by non-zero reaction currents through the particle surface. In

appendix C, we derive the characteristic time scale

$$\tau_{\mathrm{vd}} = \frac{a^2}{4D\left(1 - 2c_1^\infty/c_3^\infty\right)^2} \tag{4.23}$$

for this process, which only becomes evident if the particles are large enough. Time scales $\propto L^2/D$, where L is the characteristic system length, are typical for concentration-polarization processes also referred to as volume-diffusion or bulk-diffusion processes (Bazant et al., 2004; Shilov et al., 2001). In contrast to the relaxation of the diffuse layer, these relaxation processes are controlled by diffusion only, which is reflected by the fact that τ_{vd} does not vary with $1/\sqrt{\sigma_0}$ as it was the case with τ_{dl}. This is plausible, as diffusion currents only depend on concentration gradients and not on bulk ion concentrations [see e.g. equation (4.3)].

While the bulk conductivity does not affect τ_{vd}, equation (4.23) predicts a clear dependence on the fraction of active cations via c_1^∞/c_3^∞. From Figure 4.8 it is obvious that for a fixed bulk conductivity $\sigma_0 \propto c_1^\infty$ an increase of the fraction of active cations shifts the critical radius a_c, i.e. the radius at which the transition between the two relaxation time regimes happens, towards smaller particle sizes. By equating τ_{dl} and τ_{vd} we can approximate

$$a_c \approx 2\lambda_D(1 - 2c_1^\infty/c_3^\infty)^2 \approx 8\lambda_D \left(\frac{c_1^\infty}{c_3^\infty}\right)^2. \tag{4.24}$$

Besides the ratio c_1^∞/c_3^∞, the critical particle radius also depends on the Debye length λ_D. Around small particles with $a\kappa < 8(c_1^\infty/c_3^\infty)^2$, the relaxation of the field-induced diffuse layer dominates the response, whereas around larger particles with $a\kappa > 8(c_1^\infty/c_3^\infty)^2$ the volume-diffusion mechanism related to the field-induced concentration gradients controls the effective conductivity.

Equation (4.24) also reconfirms the strong control the ratio $a\kappa$, i.e. the overlap of diffuse and volume-diffusion layer, exerts over the development of the volume-diffusion layer and thus its relaxation. For small particles, the relatively thick diffuse layer inhibits the full development of a volume-diffusion layer. As a consequence, the relaxation of the diffuse layer with $\tau_{\mathrm{dl}} \propto a\lambda_D$ dominates the response. Around much larger particles, the volume-diffusion layer can fully develop and its relaxation becomes dominant as can be seen from the variation of the relaxation time with the particle radius $\tau_{\mathrm{vd}} \propto a^2$. It should be noted, that in complete absence of the diffuse double layer, i.e. where $\omega_{\mathrm{vd}} \gg \omega_{\mathrm{dl}}$, the exchange current approaches zero (not shown here for brevity), which inhibits the build-up of a concentration gradient even if $\omega < \omega_{\mathrm{vd}}$. In other words, for the

volume-diffusion process to be activated the presence of a diffuse layer seems to be a necessary condition.
Both the relaxation time of the volume-diffusion process as well as the critical particle radius defined in equations (4.23) and (4.24), respectively, underscore the important role of active cations in the electrolyte solution in the determination of the polarization response of the model. Although implicit in the treatment by Wong, their effect on the overall relaxation time has not been discussed in detail nor quantified as done here.

4.5 Discussion

An important achievement of the present study is the improved general understanding of the processes inherent to Wong's polarization model. The detailed mathematical analysis and the – to our best knowledge – first visualization of the physical processes provide an appropriate basis to correct some misleading reinterpretations of the model, which can be found in the more recent literature. Based on the theory developed by Wong (1979) and Wong and Strangway (1981), Gurin et al. (2015) and Placencia-Gómez and Slater (2015) propose conceptual models aiming at a description of the polarization response of metallic particles by means of a complex frequency-dependent surface conductivity. Their approach is motivated by the difficulties to fit real IP spectra based on Wong's model (Placencia-Gómez and Slater, 2014). In order to derive a simpler model, which meets the requirements of interpreting real IP data, they resort to theories describing the polarization response of suspensions of non-conducting particles (e.g. O'Konski, 1960; Schwarz, 1962; Schurr, 1964; Leroy et al., 2008). These theories consider dielectric particles with non-zero surface charge densities (e.g. due to cation exchange reactions) surrounded by an electrical double layer. Complex surface conductivities are then defined to describe the polarization of the fixed Stern layer and the diffuse layer caused by an external electric field. Critical analysis reveals two important discrepancies between the rigorous treatment by Wong and these new conceptual models:
(1) In absence of active cations, Gurin et al. (2015) and Placencia-Gómez and Slater (2015) attribute the polarization response of metallic particles to a complex surface conductivity related to the excess of ions in an electrical double layer at the particle surface. Surface conductivity generally considers the contribution of the equilibrium diffuse and Stern layer covering (e.g. Schurr, 1964; Leroy et al., 2008) and does not consider the charging of the field-induced diffuse

layer responsible for the large electrode-polarization response. Furthermore, the Wong model, does not even consider fixed surface charges or equilibrium double layers at the surface of the metallic particle. Rather, from Poisson's equation (4.5) it is clear that without external excitation the electrolyte solution is electroneutral – even at the very particle surface. The only double layers described by the Wong model are field-induced. In conclusion, the conceptual models developed by Gurin et al. (2015) and Placencia-Gómez and Slater (2015) are not suited to reproduce the electrode polarization process described by the Wong model. Rather, they suppose a different polarization mechanism around metallic particles, which has not yet been studied in a mathematically rigorous way. Although the existence of such a mechanism cannot be discarded beforehand, the proposed conceptual models should be used with caution.

(2) A further difficulty arises from the conceptual model by Gurin et al. (2015), which contains the argumentation that in absence of active cations, i.e. if no reaction current through the interface is considered, "the metallic particle behaves as an insulator". This conclusion is a fundamental misconception because the determination whether a particle behaves like a perfect conductor or an insulator does not depend on the amount of charges that can be transferred across its surface. Rather, the criterion must be the distribution of the electric field within the particle. While the electric field is always zero within a perfect conductor (this is warranted by an instantaneous redistribution of charges along the surface), the electric field readily penetrates the non-conducting particle. Mathematically, the first case requires a zero or constant potential boundary condition at the particle surface as realized in the Wong model [see equation (4.25)]. The second case, in contrast, implies a significant variation of the electric potential along the particle surface. This difference between the two cases is not a mathematical subtlety but gives rise to fundamentally different polarization processes (and magnitudes). Therefore, the polarization response of a highly conducting particle can by no means be interpreted as a special case of the polarization of the corresponding non-conducting sphere.

Of course, the assumption of an infinite conductivity of the particle represents an important limitation of the Wong model. In their contributions, Revil et al. (2015b) and Misra et al. (2016a) indicate a physically sensitive way to include a finite particle conductivity into a mechanistic polarization model for semiconducting particles. Although pioneering, the models of these authors do not yet include the effect of reaction currents through the solid-liquid interface. As stressed repeatedly in the present paper, the effect of reaction currents through

the particle in conjunction with the resulting volume-diffusion mechanism has a huge impact on the relaxation response. Therefore, future improvements of the polarization models for semi-conducting particles should definitely include the effect of electro-active ions.

While they explicitly address the important role of active cations, the interpretation provided by Flores Orozco et al. (2011) for the polarization response of metallic precipitates deviates in an important point from the predictions made by the Wong model. During a field-scale biostimulation experiment these researchers observed a decrease of the polarization response (in terms of the imaginary conductivity) during phases with low concentrations of active cations (here Fe(II)) in the pore water. Furthermore, below a critical concentration of Fe(II), no significant polarization response was observed at all. Flores Orozco et al. (2011) attribute this behaviour to the strong control active ions exert over the polarization magnitude and conclude that in absence of active ions electrode polarization becomes negligible (at least in the investigated frequency band). As far as the predictions of the Wong model are concerned, this perception is erroneous because the presence of active cations is no necessary condition for the occurrence of diffuse-layer polarization, which produces high polarization magnitudes (in terms of the maximum imaginary conductivity). From Figure 4.7 it is evident that the maximum imaginary conductivity rather increases with decreasing concentration of active cations, which in the present study could be linked to the decreasing influence of the volume-diffusion mechanism. At the same time, the characteristic frequency moves towards higher frequencies. Interestingly, Flores Orozco et al. (2011) observed that the decrease of Fe(II) concentrations was accompanied by a decrease of the phase response at low frequencies (0.25 Hz), while the phase increased at higher frequencies (4 Hz). Rather than an overall reduction of the polarization magnitude, this experimental finding indicates a shift of the polarization maximum to higher frequencies, when the dissolved Fe(II) is depleted from the solution, which is in good agreement with the predictions of the Wong model.

While the preceding discussion may suggest that the Wong model can still be considered one of the most complete polarization models for metal-bearing geomaterials, it also shows that there is room for further improvements:

(1) The eventual effect of surface charges at the metal surface and the associated electrical double layer on the polarization response of conducting particles is not included. For instances, on bare metal surfaces of synthetic iron and gold nanoparticles ζ-potentials can be up to -40 mV at neutral pH (Comba and Sethi,

2009; Sonavane et al., 2008). Particularly in the context of applications of the IP method for the monitoring of fate and transport of metallic nano-particles injections (e.g. Flores Orozco et al., 2015), an improved discrimination between the effects due to electrolyte composition (in particular the role of electro-active ions), particle geometry, and the electro-chemical state of the surface (e.g. ζ-potential and reactivity) seems necessary.

(2) Following the argumentation of Misra et al. (2016a), many metallic targets – whether natural ore minerals or metal-oxide nano-particles – are rather semiconductors than metallic conductors. The polarization of such a semiconducting particle including the effect of reaction currents through the solid-liquid interface could be studied incorporating the corresponding boundary condition of the Wong model into the approach of Misra et al. (2016a).

(3) For the one-dimensional system investigated in his treatment, Merriam (2007) stresses the relative importance of the frequency-dependent impedance of the Stern or Helmholtz layer in the electrode polarization process. The Wong model does not consider effects related to the charging of the Stern layer at the metal surface.

(4) The effective medium approach used by Wong (1979) to determine the response of an ensemble of more than one particle [see equation (4.18)] does not consider any interaction between neighbouring particles. In particular, the relatively long-range perturbations related to the volume-diffusion process described by his polarization model are likely to overlap if the average distance between particles becomes equal to or smaller than the particle diameter. Furthermore, may the volume-diffusion mechanism eventually couple to long-range polarization layers around the non-conducting grains of the background material, such as the concentration polarization due to a static double layer (e.g. Shilov et al., 2001). Both interactions between densely packed metallic particles and with the non-metallic background material should be investigated in more detail.

(5) Although suited to develop a gross idea of the expected polarization response, the simple geometrical models used in the analytic approaches (spheres and ellipsoids in Wong, 1979; Wong and Strangway, 1981) are necessarily a poor representation of the generally irregular shapes of natural mineral grains. From studies on non-conducting particles, we already know that surface roughness can produce an additional relaxation at higher frequencies (e.g. Leroy et al., 2008). Indeed, IP measurements on slug grains carried out by Nordsiek and Weller (2008) provide indications that surface roughness may contribute in a similar manner to the polarization of metallic particles.

(6) It has been shown that the application of Wong's model to real data can be tedious (Placencia-Gómez and Slater, 2014) or result in a poor fitting of experimental IP spectra (Placencia-Gómez and Slater, 2015; Gurin et al., 2015). One of the main drawbacks is the relatively large number of parameters, of which particularly the electro-chemical parameters are poorly constrained. While further improvements of the model addressing the first five issues of this list likely result in an even larger number of model parameters, future research should not sight of the need for simpler conceptualizations and mathematical descriptions of the polarization of metallic particles - especially for the interpretation of real laboratory or field data.

This list is certainly not complete, but shows that to date many possibly important effects can still not be accounted for on the basis of existing mathematical theories. At the same time, the constant delivery of new interesting experimental IP data therefore urges the development of improved theoretical models for their interpretation.

4.6 Conclusion

We complete the solution of the Poisson-Nernst-Planck system of partial differential equations around a perfectly conducting particle under consideration of charge-exchange reactions at the particle surface. This model was initially developed by Wong (1979) to describe the induced-polarization response of disseminated sulphide ores. We extend his treatment and derive the full analytic solution consisting of three unknown coefficients, which control short-range perturbations of ion concentrations and electric potential close to the particle surface. Although not needed for the determination of the effective polarization response of the suspended particle, the knowledge of such short-range perturbations allows a much more comprehensive analysis of the underlying polarization mechanisms.

We discuss the two relaxation processes inherent to the model and, as a further extension of the classical theory, provide analytic approximations for the characteristic time scales of both. Based on the full solution provided in the present study, we are able to visualize the microscopic manifestations of the two relaxation processes in terms of perturbations of the ion concentrations in the electrolyte solution. Promoted by the deepened understanding of the underlying mechanisms, we associate the two relaxation times with the relaxation of (i) field-induced diffuse layers and (ii) field-induced concentration gradients.

The first process corresponds to the build-up of diffuse double layers that screen field-induced surface charges at the particle surface. Its relaxation time is proportional to the Debye length of the electrolyte solution and the particle radius. The second process only occurs if charge-exchange reactions are considered, which are directly related to the build-up of concentration gradients in electroneutral electrolyte beyond the diffuse layer. Its relaxation time is proportional to the particle radius squared, which is typical for volume or bulk-diffusion phenomena.
Provided that active cations are present, both polarization mechanisms occur simultaneously. However, around sufficiently small particles the diffuse-layer relaxation dominates the overall polarization response, while volume-diffusion relaxation becomes dominant around larger particles. The transition between the two regimes is observed at a critical particle radius, which is approximately proportional to the thickness of the diffuse layer (λ_D) and the inverse of the normalized concentration of active anions squared $[(c_1^\infty/c_3^\infty)^2]$. Because under typical conditions this critical radius is related to characteristic frequencies > 1 kHz, to our best knowledge, no experimental for the transition has been published. Our findings can open the possibility to design laboratory measurements – by increasing the Debye length and adjusting the active ion concentration – that may be suited to detect the predicted transition and further test the theoretical model.

Appendices

4.A Derivation of the three remaining unknown coefficients

The potential on the surface of the perfectly conducting particle must have a constant value and from the symmetry of the external excitation follows that this constant value must be zero. Because this condition must hold for any θ, we write [from equation (4.9)]

$$-2F/(\lambda_1^2\varepsilon_0\varepsilon_r)A(\omega)\kappa_1(\lambda_1 a) - E_0 a + E(\omega)a = 0. \tag{4.25}$$

The two inactive ionic species do not react at the particle surface, such that the corresponding fluxes through the surface must also be zero. From equation (4.3), we get

$$\begin{aligned} &-D\partial_r\left[-A(\omega)\kappa_1(\lambda_1 r) + B(\omega)\kappa_1(\lambda_2 r)\right] \\ &\quad + \mu c_1^\infty \partial_r\left[-2F/(\lambda_1^2\varepsilon_0\varepsilon_r)A(\omega)\kappa_1(\lambda_1 r) - E_0 r + E(\omega)\frac{a^3}{r^2}\right] = 0 \end{aligned} \tag{4.26}$$

evaluated at $r = a$ for the anion flux density and

$$\begin{aligned} &-D\partial_r\left\{c_2^\infty/c_1^\infty A(\omega)\kappa_1(\lambda_1 r) + \left[B(\omega) - M(\omega)\right]\kappa_1(\lambda_2 r)\right\} \\ &\quad - \mu c_2^\infty \partial_r\left[-2F/(\lambda_1^2\varepsilon_0\varepsilon_r)A(\omega)\kappa_1(\lambda_1 r) - E_0 r + E(\omega)\frac{a^3}{r^2}\right] = 0 \end{aligned} \tag{4.27}$$

evaluated at $r = a$ for the flux density of the passive cations. Only the normal flux of the active cations through the metal surface does not vanish. It depends on the perturbation concentration of the active cations δc_3 and the radial electric field $-\partial_r \delta U$ at the particle surface. This boundary condition writes

$$\begin{aligned} &-D\partial_r\left[c_3^\infty/c_1^\infty A(\omega)\kappa_1(\lambda_1 r) + M(\omega)\kappa_1(\lambda_2 r)\right] \\ &\quad - \mu c_3^\infty \partial_r\left[-2F/(\lambda_1^2\varepsilon_0\varepsilon_r)A(\omega)\kappa_1(\lambda_1 r) - E_0 r + E(\omega)\frac{a^3}{r^2}\right] = \\ &\qquad -\beta\left[c_3^\infty/c_1^\infty A(\omega)\kappa_1(\lambda_1 r) + M(\omega)\kappa_1(\lambda_2 r)\right] \\ &\qquad - \alpha c_3^\infty \partial_r\left[-2F/(\lambda_1^2\varepsilon_0\varepsilon_r)A(\omega)\kappa_1(\lambda_1 r) - E_0 r + E(\omega)\frac{a^3}{r^2}\right] \end{aligned} \tag{4.28}$$

evaluated at $r = a$. The right-hand side of equation (4.28) is the exchange current across the metal electrolyte interface as defined by Wong (1979) in terms

of the electrochemical reaction-current parameters α (in Cs/kg) and β (in m/s). In our treatment, the reaction current is given in mol/(m^{2}s), which has to be multiplied by Faraday's constant $F = eN_A$ to obtain the corresponding electric current density in A/m^2 actually defined by Wong (his equation 28).
Note that boundary conditions far away from the particle surface, here zero perturbation concentrations and a perturbation potential equal to the external electric field, are implicit in the selection of the modified spherical Bessel function of the second kind $k_1(\lambda r)$.
Because the coefficient $E(\omega)$ given in equation (4.12) can be looked up in Wong (1979), we do not include its lengthy derivation. To solve equations (4.25) through (4.28) for the three remaining unknown coefficients, we first carry out the partial derivatives ∂_r, introduce the abbreviation $k_1'(\lambda a) := \partial_r k_1(\lambda r)|_{r=a}$ and do some minor manipulations, which yields

$$A(\omega) = \frac{E_0 a - E(\omega) a}{-2F/(\lambda_1^2 \varepsilon_0 \varepsilon_r) k_1(\lambda_1 a)}, \tag{4.29}$$

$$\begin{aligned} &DA(\omega)k_1'(\lambda_1 a) - DB(\omega)k_1'(\lambda_2 a) \\ &\qquad + \mu c_1^\infty \left[-2F/(\lambda_1^2 \varepsilon_0 \varepsilon_r) A(\omega) k_1'(\lambda_1 a) - E_0 - 2E(\omega)\right] = 0, \end{aligned} \tag{4.30}$$

$$\begin{aligned} &Dc_2^\infty/c_1^\infty A(\omega)k_1'(\lambda_1 a) + D\left(B(\omega) - M(\omega)\right)k_1'(\lambda_2 a) \\ &\qquad + \mu c_2^\infty \left[-2F/(\lambda_1^2 \varepsilon_0 \varepsilon_r) A(\omega) k_1'(\lambda_1 a) - E_0 - 2E(\omega)\right] = 0, \text{ and} \end{aligned} \tag{4.31}$$

$$\begin{aligned} &- Dc_3^\infty/c_1^\infty A(\omega)k_1'(\lambda_1 a) - DM(\omega)k_1'(\lambda_2 a) \\ &\qquad - \mu c_3^\infty \left[-2F/(\lambda_1^2 \varepsilon_0 \varepsilon_r) A(\omega) k_1'(\lambda_1 a) - E_0 - 2E(\omega)\right] = \\ &\qquad\quad - \beta \left[c_3^\infty/c_1^\infty A(\omega)k_1(\lambda_1 a) + M(\omega)k_1(\lambda_2 a)\right] \\ &\qquad\quad - \alpha c_3^\infty \left[-2F/(\lambda_1^2 \varepsilon_0 \varepsilon_r) A(\omega) k_1'(\lambda_1 a) - E_0 - 2E(\omega)\right]. \end{aligned} \tag{4.32}$$

Equation (4.29) already expresses the coefficient $A(\omega)$ in terms of the known coefficient $E(\omega)$ and no further manipulation is needed. Using the solution for $A(\omega)$ from equation (4.29) and the definition of f_2 in equation (4.13), the coefficient $B(\omega)$ is readily obtained from equation (4.30) as

$$B(\omega) = \frac{E_0 - E(\omega)}{k_1'(\lambda_2 a)} \left\{ \frac{\lambda_1^2 \varepsilon_0 \varepsilon_r}{2F} f_2 - \frac{\mu}{D} c_1^\infty \left[f_2 + \frac{E_0 + 2E(\omega)}{E_0 - E(\omega)} \right] \right\}. \tag{4.33}$$

For last unknown coefficient $M(\omega)$, we rearrange equation (4.32) using the definitions of f_2 and f_3 in equation (4.13) and substituting $A(\omega)$ from equation (4.29), which yields

$$M(\omega) = \frac{-c_3^\infty/c_1^\infty\,(E_0 - E(\omega))}{k_1'(\lambda_2 a)\left(1 + \frac{\beta a}{D} f_3\right)} \left\{ \frac{\lambda_1^2 \varepsilon_0 \varepsilon_r}{2F} \left(f_2 + \frac{\beta a}{D} \right) - \frac{c_1^\infty}{D}(\mu - \alpha) \left[f_2 + \frac{E_0 + 2E(\omega)}{E_0 - E(\omega)} \right] \right\}. \quad (4.34)$$

4.B Derivation of induced surface charge density

The charge density Σ on the surface of the perfectly conducting sphere can be related to the normal component of the electric field at its surface as

$$\Sigma(\theta, \omega) = -\varepsilon_0 \varepsilon_r \partial_r \delta U(\mathbf{r}, \omega)\Big|_{r=a}. \quad (4.35)$$

Inserting equations (4.9) and (4.14) and carrying out the partial derivative with respect to r yields

$$\Sigma(\theta, \omega) = \varepsilon_0 \varepsilon_r E_0 \left[(1 - f(\omega)) \frac{\lambda_1^2 a^2 + 2\lambda_1 a + 2}{\lambda_1 a + 1} + 1 + 2 f(\omega) \right] \cos\theta. \quad (4.36)$$

At the high-frequency limit, i.e. for $\omega \to \infty$ the reflection coefficient $f(\omega)$ approaches 1 and the surface charge density reduces to $\Sigma_\infty(\theta) = 3\varepsilon_0 \varepsilon_r E_0 \cos\theta$. In this limit, the excitation is too fast to permit the diffuse layer to build up and Σ_∞ is the minimal charge required to cancel out the electrical field within the sphere. The same result can be obtained from standard electrostatic potential theory for a perfectly conducting sphere surrounded by a medium of finite conductivity.

At the low-frequency limit, i.e. for $\omega \to 0$, the reflection coefficient approaches $-1/2$ and λ_1 becomes κ. For sufficiently large particles $\kappa a \gg 1$ and the surface can be approximated by $\Sigma_0(\theta) = 3/2 \varepsilon_0 \varepsilon_r E_0 \kappa a \cos\theta$. In this limit, the external excitation is sufficiently slow as to permit the diffuse layer to fully develop. The charge stored on the electrolyte side induces image charges on the particle surface, which increases Σ by the large factor of $\kappa a/2$.

4.C Derivation of relaxation times

Diffuse-layer relaxation

In order to derive an expression for the relaxation time of the diffuse-layer polarization, we consider the limiting case of vanishing concentrations of active cations in the electrolyte solution. Evaluating equation (4.12) for $c_3^\infty \to 0$ yields the frequency-dependent reflection coefficient

$$f(\omega) = E(\omega)/E_0 \approx 1 - \frac{3/2}{1 + f_1/2}, \tag{4.37}$$

where $f_1 = f_2 i\omega\lambda_D^2/D$. If we further limit our analysis to frequencies $\omega \ll \omega_{\mathrm{el}} \approx 1$ MHz, which is appropriate for the particle sizes we are mainly interested in, we can approximate λ_1 by $\kappa = 1/\lambda_D$. For sufficiently thin diffuse double layers compared to the particle radius, i.e. $a/\lambda_D \gg 1$, the coefficient f_2 defined in equation (4.13) approaches a/λ_D. In this limit, the frequency-dependent reflection coefficient becomes

$$f(\omega) \approx 1 - \frac{3/2}{1 + i\omega\frac{a\lambda_D}{2D}}. \tag{4.38}$$

From equation (4.38) we can extract the approximate relaxation time of the double-layer polarization $\tau_{\mathrm{dl}} = a\lambda_D/(2D)$.

Volume-diffusion relaxation

In order to identify the relaxation time of the volume-diffusion polarization, we evaluate the appropriate limit of the reflection coefficient f. As argued before for the relaxation of the diffuse-layer, the characteristic frequency of the volume-diffusion relaxation will also be $\omega \ll \omega_{\mathrm{el}}$, from which follows that $\lambda_1 \approx \lambda_D^{-1}$. For sufficiently thin diffuse double layers compared to the particle radius, we still have $a/\lambda_D \gg 1$. Furthermore, we will assume that for angular frequencies ω around the characteristic frequency of the volume-diffusion relaxation ω_{vd} the inequality $\lambda_2 a \gg 1$ holds. We leave it to the reader to verify this assumption by evaluating $\lambda_2 a$ at the angular frequency $\omega_{\mathrm{vd}} = \tau_{\mathrm{vd}}$, were τ_{vd} refers to the final result of this derivation. Under the above assumptions, the three coefficients f_i can be approximated by

$$f_1 \approx i\omega\frac{a\lambda_D}{D},\ f_2 \approx \frac{a}{\lambda_D} \gg 1,\quad \text{and}\quad f_3 \approx \frac{1}{a\lambda_2}. \tag{4.39}$$

From Figure 4.8 it is obvious that $\tau_{\mathrm{vd}} > \tau_{\mathrm{dl}}$ for all particle sizes with dominant volume-diffusion relaxation. Consequently, for sufficiently large particles the characteristic frequency of this relaxation must be searched for at frequencies $\omega \ll \omega_{\mathrm{dl}}$. Substituting this inequality into the above expression for f_1 yields $f_1 \ll 2i$. Using the same inequality, we obtain $\beta a/(D\lambda_2) \gg 1$ for typical parameters values (i.e. $\beta \approx 10^{-2}$ m/s). In summary, under the above approximations and assumptions the frequency-dependent reflection coefficient from equation (4.12) becomes

$$f(\omega) = E(\omega)/E_0 \approx 1 + \frac{3\frac{\beta}{D\lambda_2} + \frac{3c_3^\infty}{c_3^\infty - 2c_1^\infty}\left(\frac{\alpha}{\mu} - 1\right)}{\frac{c_3^\infty}{c_3^\infty - 2c_1^\infty}\left[\frac{\alpha a}{\mu\lambda_D} + \frac{\beta a}{D} + 2\right] - 2\frac{\beta}{D\lambda_2}}. \tag{4.40}$$

This expression can be further simplified, if we take into account that $\alpha/\mu \ll 1$ and $\alpha D/(\mu\lambda_D\beta)$ for typical parameter values [i.e. $\alpha = 10^{-10}$ m^2/(Vs)] as well as $\beta a/D \gg 1$ for all relevant particle size. Together with our last assumption of sufficiently small concentrations of active cations $c_3^\infty \ll c_1^\infty$ and after some manipulations, we obtain

$$f(\omega) \approx 1 - \frac{3/2}{1 - \sqrt{\frac{i\omega}{4D}}\frac{a}{1 - 2c_1^\infty/c_3^\infty}}. \tag{4.41}$$

From equation (4.41) we can extract the approximate relaxation time of the volume-diffusion polarization $\tau_{\mathrm{vd}} = a^2/\left[4D\left(1 - 2c_1^\infty/c_3^\infty\right)^2\right]$.

CHAPTER 5

Electrochemical polarization around metallic particles — Part 2: The role of diffuse surface charge

5.1 Introduction

In a previous study (Bücker et al., 2018a), we have presented the full analytical solution for the classical electrode-polarization model of the induced-polarization (IP) response of uncharged metallic particles proposed by Wong (1979). In the present paper, we extend this polarization model and develop a numerical scheme to study the response of charged metallic particles. The pre-charged surfaces of such particles immersed in an electrolyte solution are covered by static diffuse clouds of counter charges known as the diffuse part of the electric double layer (EDL), which must not be confused with the field-induced diffuse layers caused by an external excitation. Neither the classical model by Wong (1979) nor the more recent numerical modelling study carried out by Abdulsamad et al. (2017) or the semiconductor-polarization models developed by Revil et al. (2015b) and Misra et al. (2016a) consider the effect of such a static diffuse charge. Although it was claimed to be the actual cause of the polarization response of highly conductive particles in the conceptual models proposed by Gurin et al. (2015) and Placencia-Gómez and Slater (2015), to date no mechanistic polarization model has been developed to describe the effect of a fixed surface charge – independently of whether it is located in the inner Stern layer or the outer diffuse layer.

Depending on the chemical composition and the concentration of the electrolyte, diffuse charges on the surfaces of pure metals and metal-bearing minerals vary over a wide range of positive and negative values. The potential drop across the diffuse layer, which can be approximated by the experimentally determinable ζ-potential at the plane of shear, is often used to parameterize the charge stored in

This chapter is based on: Bücker, M., Undorf, S., Flores Orozco, A., and Kemna, A. (2019). *Electrochemical polarization around metallic particles – Part 2: The role of diffuse surface charge. Geophysics, 84(2):E57–E73.*

the diffuse layer. The ζ-potential of metallic and metal-bearing surfaces ranges from values as low as -50 mV on stainless steel at 10 mM NaCl and pH 7 (Boulangé-Petermann et al., 1995) to $+20$ mV on pyrite at 1 mM KNO_3 and pH 6 (Reyes-Bozo et al., 2015). As these values differ significantly from zero, a possible effect of the corresponding static EDL over the polarization response of metallic particles should not simply be discarded a priori. Reversely, recent laboratory and field studies with metallic nano-particles (e.g. Joyce et al., 2012; Flores Orozco et al., 2015; Abdel Aal et al., 2017) indicate that it might be possible to use IP measurements to retrieve information on the in-situ chemical condition and reactivity of the surfaces of metallic particles (Shi et al., 2015), which is strongly correlated with the ζ-potential.

It is the objective of the present study to develop a model, which describes the polarization response due to a static diffuse layer covering the surface of the metallic particles, and study the effect of varying charge densities in this layer. Our theoretical treatment is based on a modification of the system of partial differential equations proposed by Wong (1979) and therefore also permits to include the effect of reaction currents through the metal-electrolyte interface. As to our best knowledge the modified problem, which includes the polarization response of a static diffuse layer, cannot be solved analytically, we adopt a finite-element approach to obtain a numerical solution. Our results comprise the micro-scale perturbations of ion concentrations and electrical potential around the particle as well as the effect of the static diffuse layer on the effective electrical conductivity spectra of the composite system. Here, we focus on the impact of the diffuse charge on relevant descriptive parameters such as direct-current (DC) conductivity, relaxation time, and maximum polarization response. In the discussion section, we further analyze the practical relevance of our findings and implications for the interpretation of IP measurements.

5.2 Theory

The electro-chemical polarization model introduced by Wong (1979) and Wong and Strangway (1981) describes the IP response of metal-bearing ores based on the frequency-dependent complex conductivity of perfectly conducting particles (e.g., metallic conductors) immersed in an electrolyte solution. As discussed in detail in Bücker et al. (2018a), the primary polarization phenomenon inherent to this model is related to the dynamic charging of field-induced diffuse layers at the particle surface (see Bazant et al., 2004, for a comprehensive discussion

of diffuse-charge dynamics). This mechanism does not require the presence of electro-active ions to establish. Rather, electro-active ions additionally allow reaction currents to cross the solid-liquid interface and trigger a volume-diffusion mechanism, which largely changes the polarization response, particularly around larger particles.

Fundamental equations and extended model

Like Wong (1979), we consider a perfectly conducting sphere immersed in an electrolyte solution that consists of three ionic species. The supporting electrolyte consists of anions (subscript 1) and inactive cations (subscript 2), which do not engage in electrochemical reactions at the particle surface (e.g. Cl^- and Na^+). A smaller fraction of active cations (subscript 3), in contrast, does participate in reduction and oxidation reactions at the metallic surface, which allows a net electric current to cross the solid-liquid interface. Upon excitation by the uniform electric field $\mathbf{E}_{\text{ext}} = \mathbf{E}_0 e^{i\omega t}$, where ω and t denote angular frequency and time, respectively, the electric potential U and the ion concentrations c_j (in mol/m^3) around the particle will be perturbed from their equilibrium values. In three-dimensional coordinates, the total ion flux densities caused by the external excitation are described by the Nernst-Planck equations (Nernst, 1888, 1889; Planck, 1890)

$$\mathbf{J}_j(\mathbf{r},t) = -D_j \nabla c_j(\mathbf{r},t) - \mu_j z_j c_j(\mathbf{r},t) \nabla U(\mathbf{r},t), \tag{5.1}$$

where D_j, μ_j, and z_j denote diffusion coefficient, mobility, and signed valence of the j-th ionic species. The first term on the right-hand side of equation (5.1) describes a diffusion current, while the second term corresponds to a conduction or electro-migration current. For the sake of simplicity, we limit our treatment to monovalent ions of symmetric electrolytes, i.e., $z_1 = -1$ and $z_2 = z_3 = 1$. Assuming, furthermore, the conservation of each ionic species expressed by the continuity equation $\nabla J_j(\mathbf{r},t) = -\partial_t c_j(\mathbf{r},t)$, equation (5.1) becomes

$$\partial_t c_j(\mathbf{r},t) = \nabla \left[D_j \nabla c_j(\mathbf{r},t) + \mu_j z_j c_j(\mathbf{r},t) \nabla U(\mathbf{r},t) \right]. \tag{5.2}$$

We use the compact notation $\partial_x f := \partial f / \partial x$ for partial derivatives with respect to x. The three ion concentrations are coupled amongst each other and to the total electric potential via Poisson's equation

$$\nabla^2 U(\mathbf{r},t) = -\frac{F}{\varepsilon_0 \varepsilon_r} \sum_{j=1}^{3} z_j c_j(\mathbf{r},t), \tag{5.3}$$

where $F = 96,485$ C/mol is Faraday's constant, $\varepsilon_0 = 8.85 \cdot 10^{-12}$ C/(Vm) the vacuum permittivity, and ε_r the constant relative permittivity of the aqueous electrolyte. The system of partial differential equations described by equations (5.2) and (5.3) is also known as the Poisson-Nernst-Planck (PNP) system for ion transport.

Following the treatment by Wong (1979), we decompose the concentration of the j-th ionic species into a static background concentration $c_j^{(0)}(\mathbf{r})$ and a perturbation $\delta c_j(\mathbf{r})$ imposed by the oscillating external field.

$$c_j(\mathbf{r}, t) = c_j^{(0)}(\mathbf{r}) + \delta c_j(\mathbf{r}) \cdot e^{i\omega t} \tag{5.4}$$

In a similar fashion, the total electric potential can be decomposed into the background potential $U^{(0)}(\mathbf{r})$ and a perturbation potential $\delta U(\mathbf{r})$ as follows:

$$U(\mathbf{r}, t) = U^{(0)}(\mathbf{r}) + \delta U(\mathbf{r}) \cdot e^{i\omega t} \tag{5.5}$$

Unlike in Wong's model, the background concentration $c_j^{(0)}(\mathbf{r})$ is not equal to the bulk concentration c_j^{∞} but includes the excess and defect concentrations caused by a fixed diffuse charge density at the particle surface. For the same reason, the background potential $U^{(0)}(\mathbf{r})$ can no longer be assumed to be zero as done in Wong's model.

Besides the differentiation between active and passive cations made here, equations (5.2) through (5.5) are essentially the same as used e.g. by Chew and Sen (1982b,a) to describe ion transport through the electrolyte around a charged particle. Although these authors model the polarization response of non-conducting particles, the physics controlling the response of the electrolyte solution is identical. The fundamentally different electrical characteristics of the suspended particles (non-conducting vs. perfectly conducting) are later taken into account by imposing appropriate boundary conditions at the particle surface.

According to these authors, the problem can be decomposed into the solution of a static part of the problem, which essentially yields the equilibrium ion concentrations $c_j^{(0)}(\mathbf{r})$ and electric potentials $U^{(0)}(\mathbf{r})$ in the static diffuse layer and the bulk electrolyte (Chew and Sen, 1982b), and the solution of a frequency-dependent part (Chew and Sen, 1982a), which yields the perturbation quantities $\delta c_j(\mathbf{r})$ and $\delta U(\mathbf{r})$ caused by the external excitation. While the static part does not depend on the perturbation quantities, the frequency-dependent solution couples to the static solution. Both parts of the solution are introduced in the following two subsections.

Static solution

In a variation of the approach by Chew and Sen (1982b,a), in absence of an external field, i.e for $\delta c_j(\mathbf{r}) = 0$ for all j and $\delta U(\mathbf{r}) = 0$, we write [from equation (5.2)]

$$0 = \nabla \left[D_j \nabla c_j^{(0)}(\mathbf{r}) + \mu_j z_j c_j^{(0)}(\mathbf{r}) \nabla U^{(0)}(\mathbf{r}) \right]. \tag{5.6}$$

We assume that in equilibrium, i.e., without an external excitation, all three ion current densities through the particle surface vanish. This is obvious for the inactive ionic species, which do not penetrate the particle surface by definition, and also sensible for the active cations (see appendix A for more details). Under this condition, equation (5.6) is solved by the Boltzmann-distributed concentrations (e.g. Chew and Sen, 1982b)

$$c_j^{(0)}(\mathbf{r}) = c_j^{\infty} \exp\left(-\frac{z_j e}{kT} U^{(0)}(\mathbf{r}) \right), \tag{5.7}$$

where e denotes the elementary charge ($1.602 \cdot 10^{-19}$ C), k Boltzmann's constant ($8.617 \cdot 10^{-5}$ eV/K), and T the absolute temperature. The spatial variation of the static background potential $U^{(0)}(\mathbf{r})$ is coupled to the space charge resulting from equation (5.7) via Poisson's equation [from equation (5.3)]

$$\nabla^2 U^{(0)}(\mathbf{r}) = -\frac{F}{\varepsilon_0 \varepsilon_r} \sum_{j=1}^{3} z_j c_j^{(0)}(\mathbf{r}). \tag{5.8}$$

Inserting equation (5.7) into (5.8) gives the well-known Poisson-Boltzmann equation, which together with the boundary conditions at the particle surface,

$$U^{(0)}(\mathbf{r})\Big|_{\text{surface}} = \zeta, \tag{5.9}$$

and at a far distance from the particle

$$U^{(0)}(\mathbf{r}) \xrightarrow[r\to\infty]{} 0, \tag{5.10}$$

determines the static background potential. Note that we placed the origin of our coordinate system ($r = 0$) in the centre of the particle.

Because the static boundary conditions, i.e., equations (5.9) and (5.10), are the same as those used to describe the diffuse layer around a non-conducting particle, an approximate solution of the static potential $U^{(0)}(\mathbf{r})$ can be looked up in Chew and Sen (1982b) and inserted into equation (5.7) to obtain the static concentrations $c_j^{(0)}(\mathbf{r})$. Nevertheless, because the frequency-dependent solution requires the use of numerical methods, in the present study we will solve the static problem numerically, too.

Frequency-dependent solution

The static solution can then be used to obtain the perturbation potential $\delta U(\mathbf{r})$ and the perturbation ion concentrations $\delta c_j(\mathbf{r})$. Assuming that the amplitude $E_0 = |\mathbf{E}_0|$ of the external field is small (i.e., $E_0^2 \ll E_0$), all perturbation quantities are approximately proportional to the external excitation E_0. Extending the approach by Chew and Sen (1982a) to the case of three ionic species, the linearized frequency-dependent part of equation (5.2) writes

$$\begin{aligned} i\omega\delta c_j(\mathbf{r},\omega) = \nabla\Big\{ & D_j\nabla\delta c_j(\mathbf{r},\omega) \\ & + \mu_j z_j \left[c_j^{(0)}(\mathbf{r})\nabla\delta U(\mathbf{r},\omega) + \delta c_j(\mathbf{r},\omega)\nabla U^{(0)}(\mathbf{r})\right]\Big\} + \mathcal{O}(E_0^2), \end{aligned} \tag{5.11}$$

where the term $\mathcal{O}(E_0^2)$ represents the neglected products of two perturbation quantities, and the perturbation potential satisfies Poisson's equation:

$$\nabla^2\delta U(\mathbf{r},\omega) = -\frac{F}{\varepsilon_0\varepsilon_r}\sum_{j=1}^{3} z_j\delta c_j(\mathbf{r},\omega). \tag{5.12}$$

Equations (5.11) and (5.12) constitute four coupled differential equation that describe the variation of the perturbation quantities within the electrolyte and it only remains to specify suitable boundary conditions. At a distance far from the particle, the perturbation potential should approach values corresponding to the external electric field, i.e.,

$$\delta U(\mathbf{r},\omega) \xrightarrow[r\to\infty]{} -\mathbf{E}_{\text{ext}}\cdot\mathbf{r}, \tag{5.13}$$

while the ion concentrations should approach the static solution, i.e., the perturbation concentrations should vanish as described by

$$\delta c_j(\mathbf{r},\omega) \xrightarrow[r\to\infty]{} 0. \tag{5.14}$$

We will assume that the particle can be considered a perfect conductor, such that the perturbation potential must be constant along the particle surface (see discussion section for a more detailed analysis of this assumption). If the external excitation is symmetric around the sphere, this constant potential must be zero, i.e.,

$$\delta U(\mathbf{r},\omega)\Big|_{\text{surface}} = 0. \tag{5.15}$$

As inactive ions are neither produced nor consumed at the particle surface, the normal fluxes of both inactive ionic species through the surface, i.e., equation (5.1) for $j = 1, 2$, must also be zero:

$$\Big[- D_j \nabla \delta c_j(\mathbf{r},\omega) - \mu_j z_j \Big(c_j^{(0)}(\mathbf{r},\omega) \nabla \delta U(\mathbf{r},\omega) + \delta c_j(\mathbf{r},\omega) \nabla U^{(0)}(\mathbf{r},\omega) \Big) \Big] \cdot \mathbf{n} \Big|_{\text{surface}} = 0, \quad (5.16)$$

with $\mathbf{n}$ denoting the unit normal vector to the surface (pointing into the electrolyte). Only the normal flux of the active cations through the metal surface is non-zero due to the oxidation-reduction reactions. The rate of ion production or consumption at the surface depends on the perturbation concentration of the active ions and the electric field at the surface as expressed by

$$\Big[- D_3 \nabla \delta c_3(\mathbf{r},\omega) - \mu_3 \Big(c_3^{(0)}(\mathbf{r},\omega) \nabla \delta U(\mathbf{r},\omega) + \delta c_3(\mathbf{r},\omega) \nabla U^{(0)}(\mathbf{r},\omega) \Big) \Big] \cdot \mathbf{n} \Big|_{\text{surface}} = - \alpha(\zeta) c_3^{(0)}(\mathbf{r},\omega) \nabla \delta U(\mathbf{r},\omega) \cdot \mathbf{n} - \beta(\zeta) \delta c_3(\mathbf{r},\omega), \quad (5.17)$$

where we already made use of the equality $z_3 = 1$. As we show in more detail in appendix A, the right-hand side of equation (5.17) corresponds to the exchange current across the metal electrolyte interface defined by Wong (1979) adapted to our extended model. The two parameters α (in Cs/kg) and β (in m/s) control the dependence of the reaction current on the overpotential at the particle surface and the perturbation of the active ion concentration, respectively. Details on the exchange current can be found in Appendix A. In the same appendix, we show that — assuming a constant reaction-current density i_0 — the two reaction-current parameters vary with the ζ-potential as follows:

$$\alpha(\zeta) = \alpha(0) \exp\left(\frac{e\zeta}{kT}\right) \ , \ \beta(\zeta) = \beta(0) \exp\left(\frac{e\zeta}{kT}\right), \quad (5.18)$$

where $\alpha(0)$ and $\beta(0)$ describe the reaction current in absence of a static surface potential as used in the study by Wong (1979). Note that in our case, the reaction current is given in terms of an ion flux density in mol/(m^{2}s), which has to be multiplied by Faraday's constant F to obtain the corresponding electric current density in A/m^2 as defined by Wong (1979) [his equation (28)].

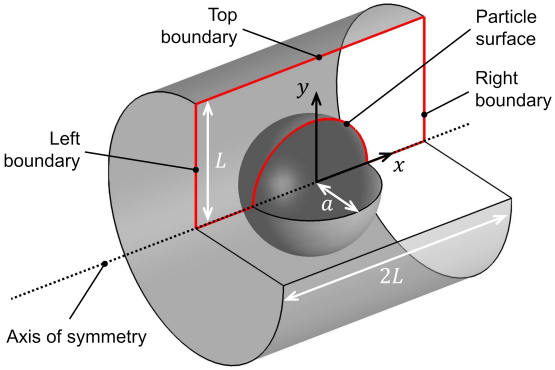

Figure 5.1: Three-dimensional sketch of the modelled volume. The spherical particle of radius a is enclosed by a cylinder of radius L and height $2L$ representing the surrounding electrolyte solution. Red lines mark the actual two-dimensional model domain discretized for the numerical simulation. Due to the particular set of boundary conditions on the surface of the particle, it is not necessary to model any of the perturbation quantities in its interior.

5.3 Numerical implementation

To our best knowledge, no closed analytical solution of the problem set up by the partial differential equations (5.11) and (5.12) and the boundary conditions expressed in equations (5.13) through (5.17) exists in the literature. This is also true for similar systems of partial differential equations with boundary conditions adjusted to the problem of charged non-conducting particles, for which only approximate analytical (e.g. Chew and Sen, 1982a; Shilov et al., 2001) or numerical solutions (e.g. DeLacey and White, 1981) have been reported.
Here, we use the finite-element software package COMSOL Multiphysics to successively obtain the static and the frequency-dependent solution. Although the numerical solution would also permit to study irregularly shaped particles, here we limit our treatment to spherical particles. This enables us to compare our results for the charged particle with the predictions of the analytical Wong model for an uncharged particle of equal size. Figure 5.1 illustrates the modelled volume with the particle of radius a centered at the origin of coordinates. The uniform external field is imposed, such that $\mathbf{E}_0 = E_0\mathbf{e}_x$.
Due to the cylindrical symmetry of the problem, the numerical simulation only needs to be carried out on the two-dimensional model domain of length $2L$ (in

x-direction) and height L (in y-direction) marked in red in Figure 5.1. This approach, which helps to solve the numerical problem efficiently, is based on taking the x-coordinate of the Cartesian space as the z-coordinate of the cylindrical coordinate system and the y-coordinate as the radial coordinate r. As the problem is completely symmetric around the x- or z-axis, there is no variation in azimuthal direction. Additionally, this approach requires a suitable coordinate transformation, which accounts for the different form of the differential operators in cylindrical coordinates (see Appendix B for details).

As we saw earlier, in the case of vanishing equilibrium reaction current densities, the static problem reduces to the solution of the Poisson-Boltzmann equation, which contains $U^{(0)}(\mathbf{r})$ as only unknown variable. The boundary conditions, equations (5.9) and (5.10), are translated into the following boundary conditions for the numerical simulation: $U^{(0)} = \zeta$ on the particle surface; $U^{(0)} = 0$ on the left, right, and top boundary (see Figure 5.1); and $\partial_y U(0) = 0$ on the axis of symmetry. For technical details on the implementation in COMSOL Multiphysics, see appendix B.

Because bulk values are imposed as boundary conditions on the left, right, and top boundary, these should be placed sufficiently far away from the static diffuse layer and the frequency-dependent induced perturbations around the particle. As a trade-off between computational cost and accuracy, we use a standard domain size L of four times the particle radius, i.e. $L = 4a$. We checked the suitability of this length scale by comparing the modelled perturbation potential at the boundary (for $\zeta = 0$) with the corresponding values of the analytical solution (Wong, 1979; Bücker et al., 2018a). As our modelling results do not yield a longer-scale perturbation caused by the effect of the static diffuse layer (see next section), this criterion will turn out to be sufficient.

Furthermore, the discretization of the two-dimensional modelling domain should account for the expected small-scale variation of the solution within the diffuse layer at the particle surface. While particle sizes of at least 1 mm may be of interest, the thickness of the diffuse layer is only of the order of one Debye length

$$\lambda_D = \left(\frac{\varepsilon_0 \varepsilon_r kT}{2 c_1^\infty e F} \right)^{1/2}, \tag{5.19}$$

which for typical ionic strengths of the electrolyte is as small as 10^{-8} m. In order to be able to resolve the diffuse layer, we therefore discretizise the electrolyte next to the surface with a special boundary-layer mesh consisting of rectangular elements with a size of $\pi a/400$ along the boundary (tangential direction). In radial direction this boundary-layer mesh is much finer and consists of a fixed

number of 8 elements with sizes increasing from $\lambda_D/2$ at the surface to $\approx 1.8\lambda_D$ at the outer limit of the boundary layer. The remaining volume is filled with triangular elements, the maximum sizes of which increase from $\lambda_D/2$ at the outer limit of the boundary-layer mesh to $L/20$ at the remote boundaries. Resulting meshes consist of $\approx 9,250$ elements for particle sizes between 0.1 μm and 10 mm, of which the constant number of $3,200$ elements corresponds to the boundary-layer mesh.

After having solved the static problem, the frequency-dependent solution is obtained using the same mesh. The static background ion concentrations needed for the frequency-dependent solution, are computed by inserting $U^{(0)}(\mathbf{r})$ into equation (5.7). For the detailed implementation of the partial differential equations (5.11) through (5.12) in COMSOL Multiphysics, see appendix B. The analytical boundary conditions for the frequency-dependent problem, equations (5.13) through (5.17), merge into the following numerical formulation: Unchanged on the particle surface; $\delta c_j = 0$ for all j and $\delta U = \pm E_0 L$ on the left and right boundary, respectively; $\mathbf{J}_j = 0$ for all j and $\partial_y \delta U$ on the top boundary and the axis of symmetry. While the static solution only needs to be computed once for each set of model parameters (i.e., a, ζ, c_j^∞, etc.), the frequency-dependent problem has to be solved for each value of the angular frequency ω separately.

Further below, we will display the modelling results either directly, i.e., the actual solutions for the four perturbation quantities, or in terms of the effective conductivity of the modelled volume. The latter can be obtained from a numerical integration of the total ionic fluxes through the left (or right) boundary, i.e.,

$$\sigma_{\mathrm{mod}} = \frac{2}{E_0 L^2} \int_0^L \sum_{j=1}^{3} \mathbf{J}_j(x = L, y)\mathbf{e}_x y dy, \tag{5.20}$$

where the term ydy accounts for the area element of the circular surface of the boundary and the factor $2/L^2$ stems from the normalization to its total area.

As mentioned above, the standard domain size is $L = 4a$ to ensure that the boundaries are located far enough from the polarized particle. However, this corresponds to a rather small particle volume fraction of $\nu_{\mathrm{mod}} \approx 0.01$. In order to facilitate the comparison with the spectral responses discussed in Part 1 of this series (Bücker et al., 2018a), the modelled effective conductivities σ_{mod} are scaled to the volumetric content of $\nu = 0.12$ using the Maxwell-Garnett mixing rule (e.g. Wong, 1979)

$$\frac{\sigma_{\mathrm{eff}}}{\sigma_0} = \frac{1 + 2\nu f}{1 - \nu f}, \tag{5.21}$$

where $\sigma_0 = 2\mu c_1^\infty F$ is the bulk conductivity of the electrolyte and

$$f = \frac{1}{\nu_{\mathrm{mod}}} \frac{\sigma_{\mathrm{mod}} - \sigma_0}{\sigma_{\mathrm{mod}} + 2\sigma_0} \tag{5.22}$$

the modelled frequency-dependent reflection coefficient of the spherical particle. Due to the lack of an appropriate analytical model, the numerical solution around the charged particle itself cannot be validated rigorously. However, for the limiting case of a particle without diffuse charge, i.e., $\zeta = 0$, the numerical solution can be compared to the analytical solutions provided by Wong (1979) and Bücker et al. (2018a) in order to detect possible problems due to an inappropriate discretization or other issues arising from the numerical implementation. In the results section, all numerical results are therefore presented along with the corresponding analytical solutions for an uncharged particle.

5.4 Results

Unless otherwise stated, the standard model parameters listed in Table 5.1 are used to obtain the results presented in this section. As mentioned above, all numerical results are scaled to a standard volumetric content of 12%, which ensures a significant spectral variation of the effective conductivity. The ζ-potential on the surface of the charged particle is set to $\zeta = -50$ mV, which is a typical value for stainless steel surfaces at neutral pH (Boulangé-Petermann et al., 1995) and high enough to render the small changes of the spectral response induced by the static diffuse layer visible. In a similar fashion, we use a relatively high bulk concentration of the active cations of $c_3^\infty = 0.12$ mol/m^3 to also highlight the effect of the reaction current. The values of the reaction current parameters $\alpha(0)$ and $\beta(0)$ for the uncharged particle are taken over from Wong (1979). A uniform ion mobility of $\mu_1 = \mu_2 = \mu_3 = \mu = 5 \cdot 10^{-8}$ m^2/(Vs), which is approximately the mobility of the sodium cation at room temperature (e.g. Atkins and De Paula, 2013), is assumed for all three ionic species.

Polarization mechanism

In part 1 (Bücker et al., 2018a), we analyzed the two main relaxation processes inherent to Wong's electro-chemical polarization model: The first is related to the accumulation and relaxation of electrical charges in thin diffuse layers induced next to the two hemispheres of the particle. This dynamic charging relaxes on a characteristic time scale that increases linearly with the particle

Table 5.1: Standard parameter values for numerical modelling studies.

Parameter (unit)	Symbol	Value
Absolute temperature (K)	T	293
Volumetric metal content (-)	ν	0.12
Particle radius (μm)	a	0.1
ζ-Potential (mV)	ζ	-50
Relative permittivity of the fluid (-)	ε_r	80
Ion mobility [$m^2/(Vs)$]	μ	$5 \cdot 10^{-8}$
Signed ion valences (-)	z_1, z_2, z_3	-1, 1, 1
Bulk anion concentration (mol/m^3)	c_1^∞	1
Bulk concentration of active cations (mol/m^3)	c_3^∞	0.12
Reaction-current parameter [$m^2/(Vs)$]	$\alpha(0)$	10^{-10}
Reaction-current parameter (m/s)	$\beta(0)$	10^{-2}
Magnitude of external field (V/m)	E_0	1

radius as $\tau_{\mathrm{dl}} = a\lambda_D/(2D)$. The second is a volume-diffusion process related to the build-up of an electrically neutral concentration gradient around the particle. This gradient is required to balance reaction currents through the particle and is therefore only observed in the presence of active cations (i.e., $c_3^\infty > 0$) and a non-zero exchange current (i.e., $\alpha(0), \beta(0) > 0$) at the particle surface. The relaxation of the concentration gradient occurs on a time scale $\tau_{\mathrm{vd}} \propto a^2/D$ and becomes dominant around particles with radius $8\lambda_D(c_1^\infty/c_3^\infty)^2$ or larger (see Bücker et al., 2018a).

Figures 5.2 to 5.5 give an insight into the micro-scale manifestations of both mechanisms and the changes produced by adding a static diffuse layer. The first row of Figure 5.2 shows the (purely radial) variation of the background ion concentrations $c_j^{(0)}(\mathbf{r})$ and the background potential $U^{(0)}(\mathbf{r})$ within such a static diffuse layer around a charged sub-micron particle with a radius of 0.1 μm and a ζ-potential of -50 mV. The dashed line indicates the approximate thickness $\lambda_D \approx 10$ nm of the diffuse layer. While the negative charges at the particle surface deplete anions (co-ions) almost completely from the diffuse layer, they increase both cation concentrations (counter-ions) at the surface by a factor of ≈ 7.2. Because the excess of counter-ions outnumbers the deficit of co-ions, the effective conductivity of the interfacial layer is larger than the one of the bulk electrolyte. Outside the diffuse layer, all three ion concentrations approach their respective bulk concentrations and the static potential decays to 0 mV.

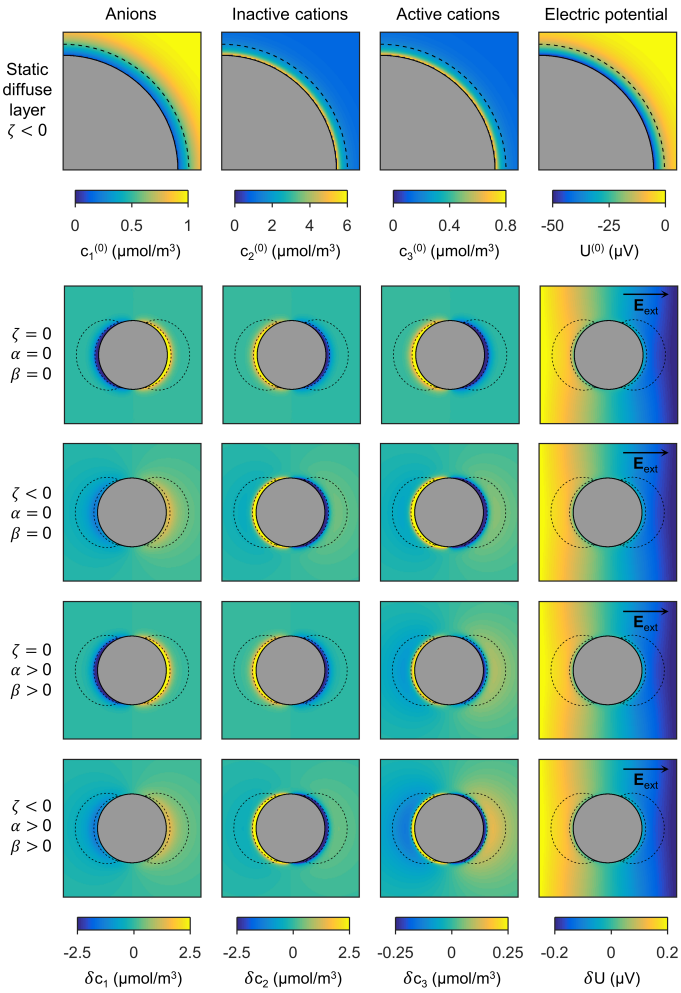

Figure 5.2: Static diffuse layer (first row) and field-induced perturbations around a sub-micron particle with $a = 0.1$ μm at the low-frequency limit $\omega = 3 \cdot 10^4$ rad/s (other four rows). Only the real parts of the complex-valued perturbation quantities are illustrated; the respective imaginary parts are much smaller at the low-frequency limit displayed here. The inner dashed line indicates the diffuse layer, the outer the volume-diffusion layer. All remaining parameters as listed in Table 5.1.

The other four rows of Figure 5.2 show particles of the same size (0.1 μm) but with different surface characteristics under the influence of an external field. The selected angular frequency of $\omega = 3 \cdot 10^4$ rad/s of the external excitation is well below the characteristic frequencies of all relaxations of interest, such that the corresponding perturbations can fully develop. Figure 5.2 displays the real parts of the complex-valued perturbation quantities. The corresponding imaginary parts are not displayed because they are much (at least by a factor of 10) smaller at the selected low angular frequency.

Complex-valued concentrations and potentials might be less familiar to some readers. But in the mathematical formalism used here, which describes harmonic oscillations by complex numbers, the occurrence of non-zero imaginary parts simply indicates that these quantities are out-of-phase compared to the external electrical field, the phase of which is given by the product ωt.

Upon excitation by the external field, the perfectly conducting sphere always responds with an quasi-instantaneous redistribution of charges along its surface. The resulting induced surface charges $\Sigma_\infty \propto \varepsilon_0 \varepsilon_r 3 E_0$ (see e.g. Bücker et al., 2018a) ensure that the external field is cancelled out within the particle, which is being accounted for by the boundary condition (5.15). This early-time or high-frequency behaviour of the particle itself is the same, regardless of reaction currents through the particle surface or the assumption of a fixed diffuse surface charge. However, due to slower processes, the variation of the late-time or low-frequency perturbations of ion concentrations and electric potentials within the electrolyte next to the particle depends largely on the particular set of surface properties. In the following we will discuss the different effects of ζ-potential and reaction currents in detail.

The second row of Figure 5.2 and the solid grey curves in Figures 5.3 and 5.4 illustrate the low-frequency polarization of the uncharged conducting particle, i.e., $\zeta = 0$, with no reaction currents through the solid-liquid interface, here realized by setting $\alpha(0), \beta(0) = 0$. Under these conditions, only the effect of the diffuse-layer polarization can be observed, the fundamental polarization of the perfect conductor. As discussed in more detail in Bücker et al. (2018a), normal electro-migration currents around the poles of the particle charge the electrolyte next to the particle surface until they are balanced by opposed diffusion currents driven by the resulting concentration gradients. At sufficiently small frequencies or after sufficiently long times, the total charge stored in the diffuse layer and mirrored on the particle is by a factor $a\kappa$ (where $\kappa = 1/\lambda_D$) larger than the quasi-instantaneously induced surface charge Σ_∞ (Bücker et al., 2018a). The

perturbation concentrations in the diffuse layer decay approximately exponentially with the distance from the surface, i.e., $\propto \exp[-\kappa(r-a)]$ (Wong, 1979; Bücker et al., 2018a). The inner dashed lines in Figures 5.2 to 5.4 mark the distance at which the perturbations decay to $1/e$ of their respective values at the particle surface indicating the spatial extension of the field-induced diffuse layers.

From the third row of Figure 5.2 and the dashed grey curves in Figures 5.3 and 5.4 it is evident that the situation changes if a fixed surface potential of $\zeta = -50$ mV is considered: Here, we observe a significant reduction of the anion perturbation concentrations within the diffuse layer (first panel), while the resulting lack of charge is compensated by an amplification of the cation perturbation concentrations in the diffuse layer (second and third panel, better recognizable from the radial sections in Figures 5.3 and 5.4). Beyond the diffuse layer covering the sub-micron particle (Figures 5.2 and 5.3), all ion concentrations increase (or respectively decrease) uniformly on the two opposite sides of the particle resulting in an electrically neutral salinity gradient around the particle. The development of this relatively long-range concentration gradient can be understood as a direct consequence of the unequal contributions of anions and cations to the conductivity of the static diffuse layer. Tangentially to the surface, electromigration currents transport much more cations than anions, which in Figure 5.2 depletes cations to the left of the particle and accumulates them to the right. At the same time, more anions arrive at (are pulled away from) the right (left) side of the particle than can be transported through the diffuse layer, which explains the net electro-neutrality of the perturbation. The concentrations increase until the resulting opposite diffusion currents can balance the effect of the electro-migration currents, leading to the quasi-equilibrium situation seen in Figure 5.2. The process described in this paragraph is a volume-diffusion mechanism, which is similar to but should not be confused with the one arising from the reaction currents discussed in the next paragraph. Obviously, this mechanism is much weaker around the larger particle (Figure 5.4), where the presence of a static diffuse layer does not result in recognizable changes of the ion concentration in the zone marked as volume-diffusion layer.

The fourth row of Figure 5.2 and the black solid curves in Figures 5.3 and 5.4 show the influence of non-zero reaction currents, i.e., $\alpha, \beta > 0$, on the perturbations around an uncharged particle, i.e., $\zeta = 0$ mV. Here, not the unequal population of the static diffuse layer with anions and cations but the exclusive release and absorption of active cations at the surface causes an imbalance of

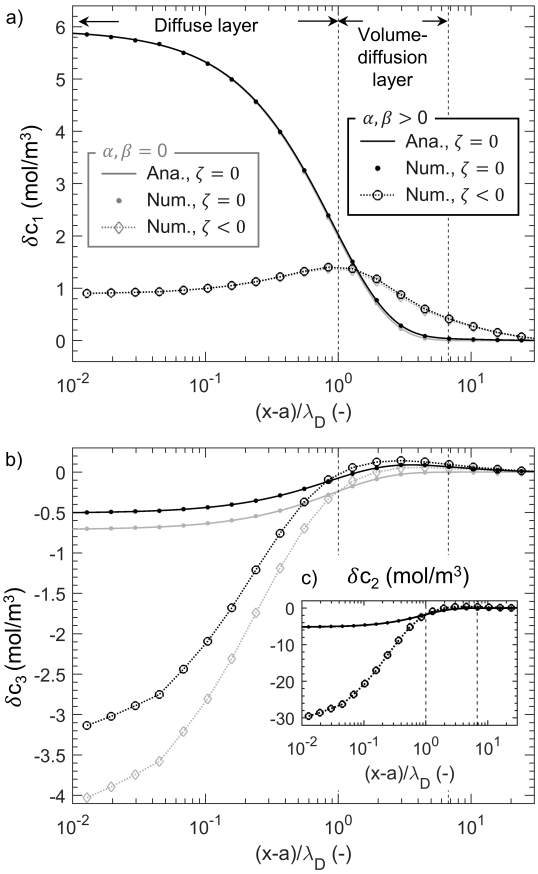

Figure 5.3: Radial profiles ($y = 0$, $x > 0$) of the real parts of the perturbation concentrations of (a) anions, (b) active, and (c) passive cations at $\omega = 3 \cdot 10^4$ rad/s. For $\zeta = 0$, numerical results (filled circles) are plotted along with the respective analytical solutions (solid lines) from Bücker et al. (2018a). For $\zeta < 0$, only numerical results (open symbols, dashed lines) exist. For both cases, results without (grey) and with (black) reaction current are displayed. The vertical dashed lines indicate the extensions of the diffuse layer (DL, left line) and of the volume-diffusion layer (right line). All other parameter values as in Table 5.1.

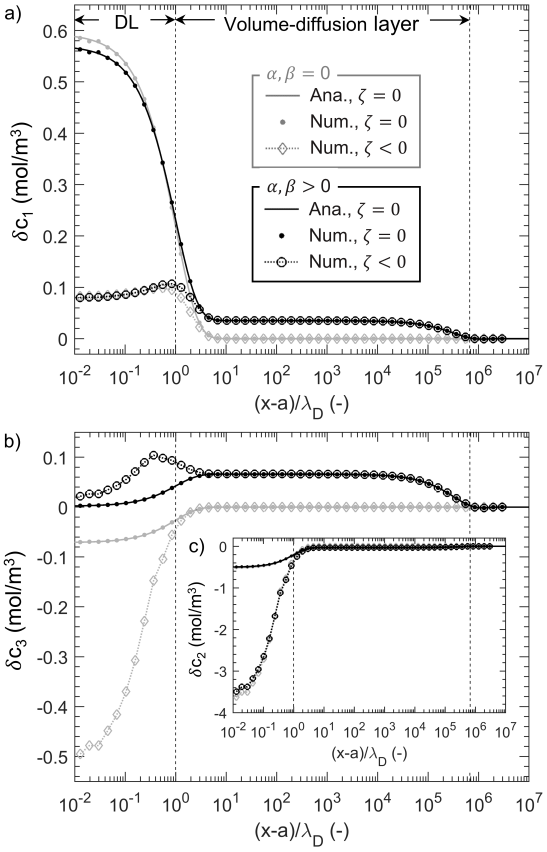

Figure 5.4: Radial profiles ($y = 0$, $x > 0$) of the real parts of the perturbation concentrations of (a) anions, (b) active, and (c) passive cations in the vicinity of a conducting sphere of radius $a = 10$ mm at $\omega = 10^{-4}$ rad/s. For $\zeta = 0$, numerical results (filled circles) are plotted along with the respective analytical solutions (solid lines) from Bücker et al. (2018a). For $\zeta < 0$, only numerical results (open symbols, dashed lines) exist. For both cases, results without (grey) and with (black) reaction current are displayed. The vertical dashed lines indicate the extensions of the diffuse layer (DL, left line) and of the volume-diffusion layer (right line). All other parameter values as in Table 5.1.

electro-migration fluxes between the electrolyte far away and in the vicinity of the particle. As discussed in more detail previously (Bücker et al., 2018a), the result is a coupling of the diffuse-layer polarization and the volume-diffusion process. While the perturbations caused by the volume-diffusion process around charged particles (previous paragraph) appear clearly and have the same sign in all three ion concentrations; the reaction currents mainly affect the concentration of the active ions (see δc_3) and electro-neutrality in the volume-diffusion region is ensured by a small reduction of δc_2 and a small increase of δc_1. The radial profiles in Figures 5.3 and 5.4 illustrate these distinct effects clearly.

The radial profiles in Figure 5.4 also show a second important difference between the concentration gradients due to the two different volume-diffusion mechanisms, which cannot be distinguished around the small particle: Only the reaction currents produce the plateaus observed in the region marked as volume-diffusion layer (black lines and symbols), which together with the decay at larger distances represent the $1/r^2$-dependence of the corresponding perturbation concentrations. The absence of these plateaus in the perturbation concentrations related to the asymmetric transport in the static diffuse layer (grey lines and symbols in Figure 5.4) indicates a much faster – probably exponential – decay with the distance from the particle surface and thus a much smaller thickness of the volume affected by the concentration gradient.

The last row of Figure 5.2 and the dashed black curves in Figures 5.3 and 5.4 show the coupling of all three polarization processes. From a direct comparison among the different maps and profiles, it can be seen that in this case, (1) the perturbation concentrations within the diffuse layer around small and large particles are largely controlled by the static diffuse layer, (2) those in the volume-diffusion region around the large particle only by the reaction current through the particle surface, and (3) those in the volume-diffusion region around the small particle by the reaction current through the particle surface and the static diffuse layer.

While effects of and interactions between the different polarization mechanisms are clearly reflected in the perturbation concentrations around the sub-micron particle, the resulting electric perturbation potentials (last column in Figure 5.2) hardly show any noticeable variation. The radial profiles of the perturbation potentials presented in Figure 5.5 show also only subtle differences. In both cases, the perturbation potential primarily shows the steep exponential decrease due to the space charge stored in the diffuse layer followed by a plateau due to the $1/r^2$ decay of the effective dipole moment of the particle. If no reaction

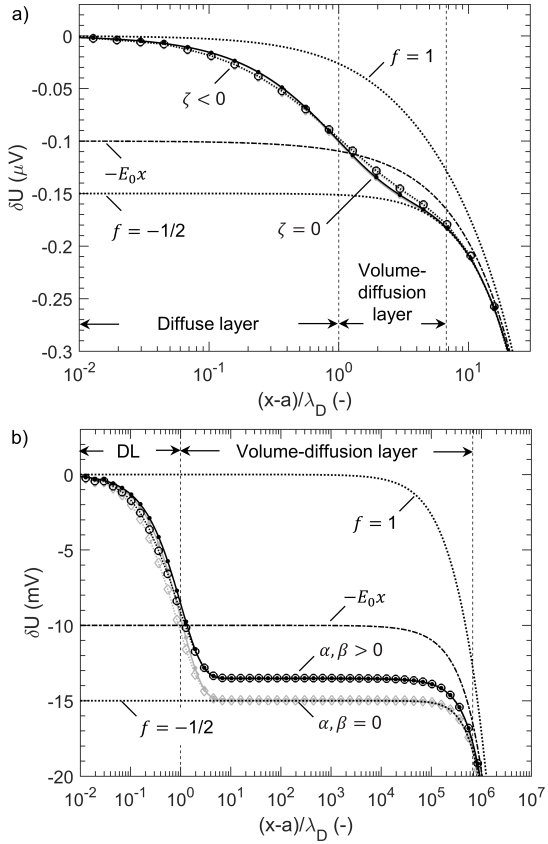

Figure 5.5: Radial profiles ($y = 0$, $x > 0$) of the real part of the perturbation potential in the vicinity of conducting spheres (a) of radius $a = 0.1$ μm at $\omega = 3{\cdot}10^4$ rad/s and (b) of radius $a = 10$ mm at $\omega = 10^{-4}$ rad/s. For $\zeta = 0$, numerical results (filled circles) are plotted along with the respective analytical solutions (solid lines) from Bücker et al. (2018a). For $\zeta < 0$, only numerical results (open symbols, dashed lines) exist. For both cases, results without (grey) and with (black) reaction current are displayed. The potential $-E_0 x$ associated with the uniform external field $\mathbf{E}_{\mathrm{ext}}$ as well as the potentials around a non-conducting ($f = -1/2$) and a perfectly conducting ($f = 1$) sphere are also included. The vertical dashed lines indicate the extensions of the diffuse layer (DL, left line) and the volume-diffusion layer (right line). All other parameter values as in Table 5.1.

currents are considered, i.e., for $\alpha, \beta = 0$, the charges of the diffuse layer fully screen the electric field. In this case, the potential profile outside the diffuse layer is equal to the one around a perfectly insulating sphere, the reflection coefficient of which can be obtained as $f = -1/2$ from potential theory. The reflection coefficient f of a sphere with conductivity σ_s embedded in a medium with homogeneous conductivity σ_m is $(\sigma_s - \sigma_m)/(\sigma_s + 2\sigma_m)$ (e.g. Maxwell, 1891). Reaction currents through the interface (i.e., $\alpha, \beta > 0$) leak charges from the diffuse layer into the particle (and vice versa), which reduces the effective dipole moment of the particle and thus the perturbation potential along the plateau in Figure 5.5. The almost identical variations of the potential around charged (open symbols) and uncharged (filled symbols) particles suggest that the static diffuse layer has hardly any effect on the macroscopic response of the particle. As mentioned in the previous section, Figures 5.3 to 5.5 show a good agreement of numerical (solid lines) and analytical (filled circles) results for the case of the uncharged particle, i.e., $\zeta = 0$ mV. The full analytical solution for all four perturbation quantities can be looked up in Bücker et al. (2018a). Slight deviations between numerical and analytical solutions only become visible very close to the particle surface. As an explanation, we recall that the smallest radial element size of our finite-element mesh is $\lambda_D/2$, which is a factor of 50 larger than the smallest radial distance displayed in the radial profiles in Figures 5.3 to 5.5. Thus the observed misfit does not indicate a systematic error but could be reduced by increasing the resolution of the mesh.

Spectral response

Figure 5.6 displays the effective conductivity spectra obtained for the sub-micron particle, i.e., $a = 0.1$ μm, in terms of the respective real ($\sigma'(\omega)$) and imaginary ($\sigma''(\omega)$) parts. The diffuse-layer relaxation, which dominates around such small particles, leads to a steep transition between the low and high-frequency limits of σ' and a narrow peak in the σ'' spectra. The small overshots of σ' at the angular frequency $1/\tau_{\mathrm{el}} = \sigma_0/(\varepsilon_0\varepsilon_r) \approx 10^{-7}$ rad/s can be attributed to the relaxation of the electrolyte solution (Bücker et al., 2018a) and obey the Kramers-Kronig relations with the corresponding imaginary spectra (not shown here for brevity). The effect of a non-zero ζ-potential on the spectra in Figure 5.6 can be summarized under the following three main changes: The presence of a static diffuse layer (1) increases the direct-current limit of σ' (subsequently denominated by σ_{DC}), (2) reduces the maximum of σ'' (subsequently σ''_{max}), and (3) shifts the characteristic angular frequency, at which σ''_{max} is encountered, towards lower

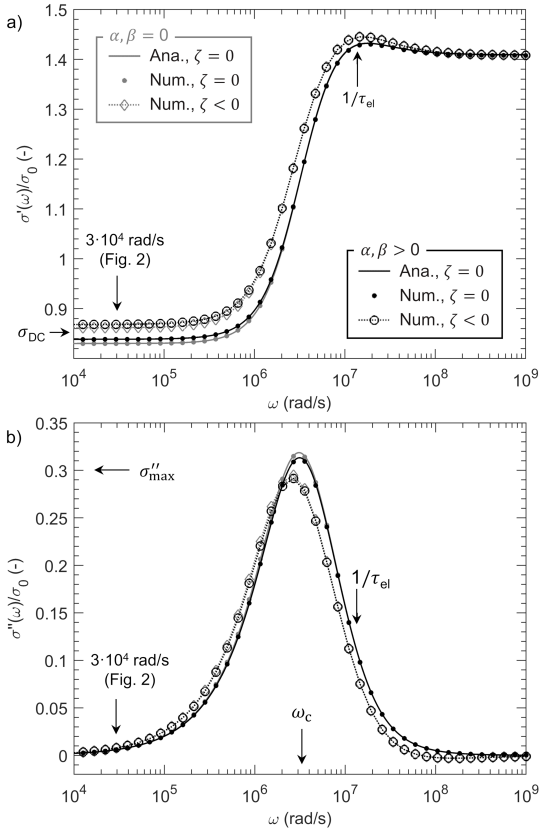

Figure 5.6: Variation of real (σ', top) and imaginary (σ'', bottom) part of the effective normalized conductivity with angular frequency. For the uncharged particle ($\zeta = 0$), numerical spectra (filled circles) can be compared to the analytical solution (solid lines) from Wong (1979). For the charged particle ($\zeta < 0$), only numerical spectra (open symbols, dashed lines) exist. For both uncharged and charged particles, spectra without (grey) and with (black) reaction currents are displayed. All other parameter values as in Table 5.1.

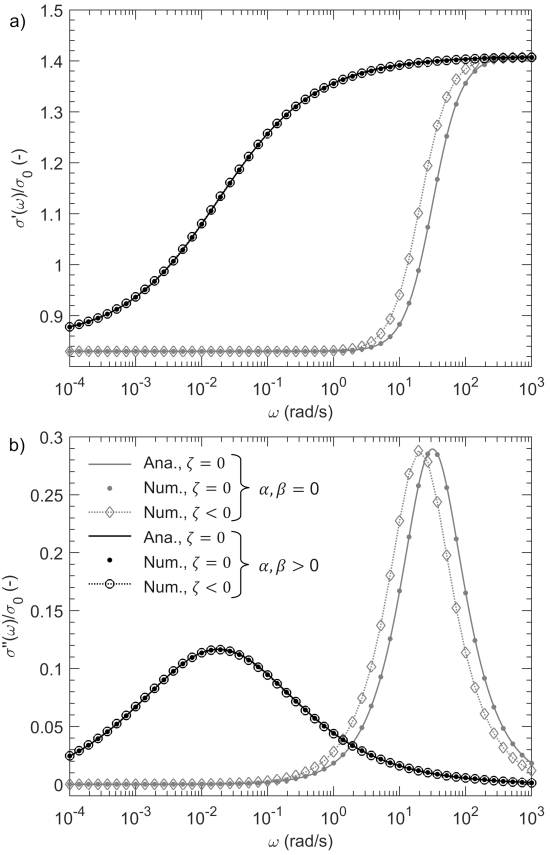

Figure 5.7: As Figure 5.6 but for larger particle with $a = 10$ mm.

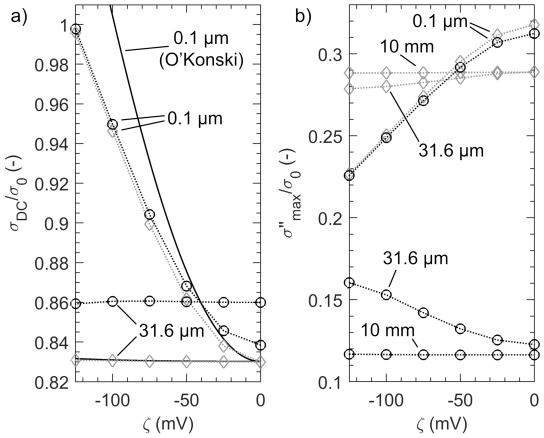

Figure 5.8: Variation of the low-frequency limit of the effective conductivity σ_{DC} (left panel) and the maximum imaginary conductivity σ''_{max} (right panel) with the ζ-potential for radii $a = 0.1$ µm, 31.6 µm (left and right panel), and 10 mm (right panel only). Conductivity variations are displayed for simulations with (black circles) and without (grey diamonds) reaction currents. The black solid lines illustrate the analytical approximation of σ_{DC} based on the surface conductivity according to O'Konski (1960). Besides a and ζ, all parameter values as in Table 5.1.

frequencies (subsequently ω_c).

Figure 5.7 shows that the effect of a non-zero ζ-potential on the spectral response of the large particle with $a = 10$ mm is different. For vanishing reaction currents, i.e., $\alpha(0), \beta(0) = 0$, we still observe the steep transition of σ' and the narrow peak of σ'' related to the diffuse-layer polarization. However, here σ_{DC} and σ''_{max} remain unaffected by the static diffuse layer and only the shift of ω_c to lower frequencies can be observed. If non-zero reaction currents through the surface of the large particle are taken into account, i.e., for $\alpha(0), \beta(0) > 0$, the volume-diffusion process becomes dominant resulting in a broadening of the transition region, a broadening and reduction of the σ''-peak, and a substential reduction of the characteristic angular frequency ω_c. In this regime no effect of the static diffuse layer on the spectral response can be detected.

In the following, we will study the dependency of the three spectral parameters σ_{DC}, σ''_{max}, and ω_c on the ζ-potential in more detail and provide some possible explanations for the observed changes.

The left panel of Figure 5.8 shows the variation of σ_{DC} with the ζ-potential for two different particle radii ($a = 0.1$ and 31.6 μm). As we know, an increasing magnitude of the (negative) ζ-potential results in an increase of cation and a decrease of anion concentrations in the static diffuse layer. Because the increase of the cation concentrations with ζ is much larger than the decrease of the anion concentration, the surface conductivity increases with the magnitude of the ζ-potential, which results in the increase of σ_{DC} observed in Figure 5.8. As the total volume fraction occupied by the static diffuse layer of fixed thickness λ_D decreases with increasing particle size, the increase of σ_{DC} with ζ is most pronounced around the smaller particle (0.1 μm) and becomes almost negligible around the larger (31.6 μm) particle.

Above we saw that – provided that no reaction currents are allowed to cross the surface – a fully developed induced diffuse layer lets the perfectly conducting particle effectively (i.e., outside the diffuse layer) behave like a non-conducting particle (see Figure 5.5). At the same time, the static diffuse layer partly compensates the effect of the induced diffuse layer and slightly increases the effective conductivity. In order to understand the contribution of the static diffuse layer, we can try to describe the variation of σ_{DC} with ζ by the corresponding expressions known from the classical theory for non-conducting particles.

According to O'Konski (1960), the effect of the surface conductivity K can be taken into account by adding the conductivity $2K/a$ to the conductivity of the particle. If the particle is non-conducting, which in our case is true in the low-frequency limit and outside the induced diffuse layer, the effective conductivity of the particle is given by

$$\sigma_p = \frac{2K}{a}. \tag{5.23}$$

As our model does not include a Stern layer, K only considers the conductivity increment due to the static diffuse layer. For a thin static diffuse layer, i.e., $a\kappa \gg 1$, the surface conductivity K can be approximated using Bikerman's formula (e.g. Shilov et al., 2001). Because we do not consider electro-osmotic coupling, we evaluate this formula in the high-viscosity limit, where

$$K \approx 2\sigma_0\lambda_D \left[\cosh\left(\frac{e\zeta}{2kT}\right) - 1\right]. \tag{5.24}$$

The effective DC conductivity of a particle with conductivity σ_p immersed in a medium of conductivity σ_0 can be obtained from inserting the effective reflection or dipole coefficient (e.g. from Shilov et al., 2001)

$$f_{\mathrm{DC}} = \frac{\sigma_p - \sigma_0}{\sigma_p + 2\sigma_0}, \tag{5.25}$$

into the Maxwell-Garnett mixing rule, equation (5.21). The predicted variation of σ_{DC} with ζ is illustrated in the left panel of Figure 5.8 (solid lines) along with the corresponding numerical results (black open symbols).

Particularly for the smaller particle, this analytical approximation overestimates the conductivity increment produced by the static diffuse layer. There are various reasons for the observed deviation: Equations (5.23) through (5.25) are only valid in the thin double layer limit, i.e., $a \gg \lambda_D$. Furthermore, the Bikerman model of surface conductivity does not consider the volume-diffusion polarization of the static diffuse layer observed in our simulation results, which is expected to reduce the effective conductivity increment, nor the coupling with the induced diffuse layer. Despite these shortcomings, the qualitative agreement with the modelled response is relatively good and provides an additional plausibility check of our numerical implementation.

Note that the comparison with the response of a non-conducting particle is only sensible in the low-frequency limit, where the perfectly conducting particle behaves like an insulator. At higher frequencies, the different natures of the particles lead to fundamentally different frequency dependencies of the effective conductivity (see the Discussion section for more detail).

The right panel of Figure 5.8 shows the variation of σ''_{max} (i.e., the value of σ'' at the characteristic frequency of each individual spectral response), which is often taken as a measure of the magnitude of the polarization. If no reaction currents are considered (grey diamonds), σ''_{max} decreases with the magnitude of ζ. This decrease is most pronounced for the smallest particle, i.e., $a = 0.1$ μm, and hardly noticeable for the largest, i.e., $a = 10$ mm. For the smallest particle, the variation of σ''_{max} with ζ does almost not change when reaction currents are added to the model (black circles). All responses discussed so far are dominated by the relaxation of the diffuse layer, such that we can conclude that the magnitude of this polarization process generally decreases with increasing diffuse charge density at the particle surface. The opposite is the case when the volume-diffusion process becomes dominant, σ''_{max} increases with the magnitude of ζ. We observe this around the intermediate particle, i.e., $a = 31.6$ μm, if reaction currents are considered. Also in the case of non-zero reaction currents, the effect of ζ becomes almost imperceptible around the largest particle, i.e., $a = 10$ mm.

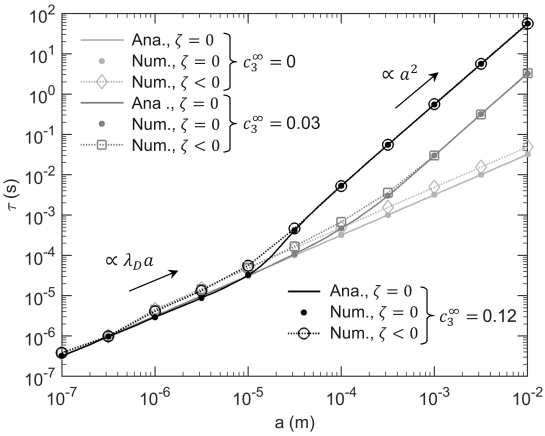

Figure 5.9: Variation of relaxation times τ with particle radius a for three different concentrations of active anions $c_3^\infty = 0, 0.03$, and 0.12 mol/m^3 (light grey, dark grey, and black, respectively). For the uncharged particle ($\zeta = 0$), numerical results (filled circles) can be compared to the analytical solution (solid lines) from Wong (1979). For the charged particle ($\zeta < 0$), only numerical results (open symbols, dashed lines) can be displayed. Beside a, ζ, and c_3^∞, all other parameters as in Table 5.1.

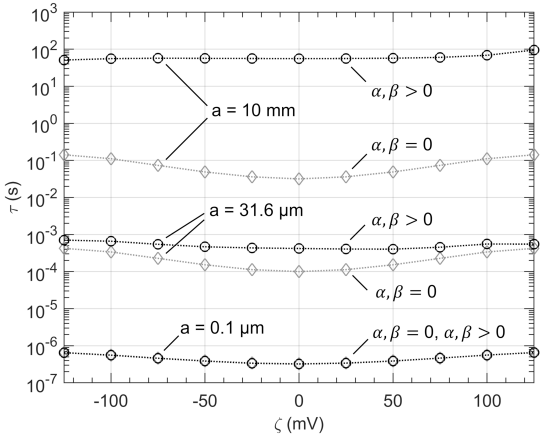

Figure 5.10: Variation of relaxation times τ with the ζ-potential for three different particle radii $a = 10^{-7}, 3.16{\cdot}10^{-5}$, and 10^{-2} m with (black) and without (grey) reaction currents. All other parameter values are equal to those given in Table 5.1.

5.4.1 Relaxation time

Due to its strong dependence on geometrical parameters, the relaxation time τ, here defined as the inverse of the characteristic angular frequency ω_c, is often used as a proxy for the size of the conducting particles. Hence, a good understanding of the effect of the ζ-potential on this important spectral parameter would be desirable. Figure 5.9 illustrates the variation of τ with the particle radius a for different surface characteristics. The response of uncharged particles shows the typical division into two regimes (e.g. Bücker et al., 2018a): The $\tau \propto \lambda_D a$ increase can be attributed to the diffuse-layer relaxation, while the much steeper $\tau \propto a^2$ variation is related to the volume-diffusion mechanism, which dominates around larger particles if reaction currents through the particle surface are taken into account. This division into two regimes is also valid for charged particles, i.e., $\zeta = -50$ mV. The only effect of the static diffuse layer around the particles is a slight increase of of the relaxation times of the diffuse layer ($\propto \lambda_D a$) for radii $a \gtrsim 1$ μm. The relaxation times of the volume-diffusion polarization ($\propto a^2$), in contrast, remain practically unaffected.

Figure 5.10, which illustrates the variation of the relaxation times with the ζ-potential for three differently sized particles, confirms this general observation.

We also see that the variation of the relaxation time of the diffuse layer, i.e., $\alpha(0), \beta(0) = 0$, with ζ is relatively flat around 0 mV, becomes steepest around ± 25 to ± 75 mV and then again flattens out towards higher magnitudes of ζ. This behavior is symmetric with respect to $\zeta = 0$ mV and thus not affected by the sign of the diffuse surface charge. In contrast, the practically constant relaxation time of the volume-diffusion mechanism (black lines and symbols in Figure 5.10) presents a slightly asymmetric behaviour, which becomes most noticeable at large magnitudes of the ζ-potential.
At first glance, the increase of the relaxation time of the diffuse layer with ζ seems counter-intuitive: The static diffuse layer increases the conductivity in the vicinity of the particle as described by the surface conductivity K. At the same time, the relaxation time is proportional to the Debye length and thus to the square root of the inverse of the conductivity of the electrolyte around the particle, i.e., $\tau \propto 1/\sqrt{\sigma_0}$ (e.g. from Bücker et al., 2018a), which would rather imply a decrease of τ with ζ. However, the concentration polarization produced by the unequal anion and cation fluxes through the static diffuse layer rather seems to delay charging and relaxation of the induced diffuse layers related to the observed increase of τ with ζ.
The relative insensitivity of the relaxation time of the volume-diffusion process (the one produced by the reaction currents) to changes in ζ is in accordance to the fact that the corresponding volume-diffusion layer is practically unaffected by the presence of the static diffuse layer (see e.g. Figure 5.4). Obviously, this process does not respond to changes in the (surface) conductivity, which is plausible for a purely diffusion-controlled mechanism.

5.5 Discussion

Perfectly conducting vs. non-conducting particles

Treatments of the low-frequency polarization response of charged (non-conducting) dielectric particles can be roughly classified into two groups; models of the first group stress the polarization response of the Stern or Helmholtz layer of counter-ions tightly bound to the particle surface (e.g. Schwarz, 1962; Schurr, 1964; Leroy et al., 2008). Under the influence of an external electric field, these charges rearrange along the surface but cannot leave (or enter) the Stern layer. The maximum polarization is assumed to be controlled by an equilibrium between tangential electro-migration and diffusion currents resulting in the typical relaxation time scale of the Stern layer $\tau = a^2/(2D)$. The influence of the outer

diffuse layer is only considered in terms of the real-valued conductivity increment $2K/a$ proposed by O'Konski (1960), which does not actively contribute to the polarization. Models of the second group, in contrast, only study the polarization response of the diffuse layer. While most treatments neglect the polarization response of the Stern layer (e.g. Chew and Sen, 1982a; DeLacey and White, 1981), there are also approaches attempting to incorporate its effect (e.g. Shilov et al., 2001). The polarization of the static diffuse layer arises due to the unequal cation and anion transport by electro-migration currents along the surface and usually also relaxes on a time scale $\tau \propto a^2/D$. In absence of a fixed diffuse surface charge and thus for a vanishing ζ-potential, the models of both groups do not predict any polarization response, except for the Maxwell-Wagner polarization at high frequencies (i.e., $\approx 1/\tau_{\mathrm{el}}$).

In comparison to these polarization mechanisms around non-conducting particles, the case of perfectly conducting particles is fundamentally different. Here, the main mechanism responsible for the large low-frequency dispersion of the effective conductivity of the suspension is the dynamic charging of the field-induced (and not the static) diffuse layer, which is a direct consequence of the high conductivity contrast between particle and electrolyte. In contrast to both mechanisms observed for non-conducting particles, the pure polarization of the field-induced diffuse layer relaxes on a time scale $\tau = \lambda_D a/(2D)$. Only if reaction currents, which have not been addressed in the theories for non-conducting particles, are taken into account the coupling with the resulting volume-diffusion mechanism yields a relaxation time $\tau \propto a^2$.

The present numerical study indicates that the effect of ζ-potential and static diffuse layer should be considered of secondary importance for the effective conductivity of suspensions of perfectly conducting particles – at least for typical parameter values. Interestingly, the corresponding surface conductivity rather decreases the polarization magnitude, i.e., σ''_{max}, and thus its effect is exactly opposite to the one it has in the case of non-conducting particles.

In the case of non-conducting particles, the Stern layer usually plays an even more important role for the observed polarization phenomena (e.g. Schwarz, 1962; Schurr, 1964; Leroy et al., 2008) than the diffuse layer. However, our model does not include any polarization effect due to the Stern layer. We justify this simplification based on the assumed infinite conductivity of the particle, which results in a vanishing tangential electric field along the particle surface (and at small distances from the surface). This is due to an immediate redistribution of charges, which cancels out any electric field within the particle volume and

along its surface. Thus, tangential electromigration currents within a thin Stern layer, which cause a large polarization around non-conducting particles, should either be zero or very small.
In summary, the role of surface conductivity around perfectly conducting particles is completely different to the one it plays for the polarization of non-conducting particles. Therefore, the polarization of the static diffuse layer around perfectly conducting particles should by no means be confused with the main polarization mechanisms due to the dynamic charging of the diffuse layer and the volume-diffusion process driven by reaction currents.

Potential for nano-particle characterization

To date only few studies have investigated the particular IP response of metallic nano-particles (Joyce et al., 2012; Shi et al., 2015; Abdel Aal et al., 2017), but the obtained results encourage further research to advance this exciting new application. The strong response of metallic particles and the well-known fact that the polarization magnitude scales with the volumetric metal content (e.g. Wong, 1979; Misra et al., 2017) make it a suitable method to monitor nano-particle injection experiments (Flores Orozco et al., 2015). Besides the mere localization and quantification, some researchers have even suggested that IP measurements could aid in the characterization of the in-situ chemical condition and reactivity of the particle surfaces (e.g. Shi et al., 2015). The strong correlation between the ζ-potential (i.e., the fixed diffuse surface charge) on both surface reactivity (e.g. Sund et al., 2011) and IP response of non-conducting particles (e.g. Leroy et al., 2008) justified this hope.
Generally speaking, our modelling results also indicate that the sheer size of nano-particles favours such applications of the IP method: From Figure 5.8 we see that the smaller the particle is, the more sensitive both σ_{DC} and σ''_{max} become with respect to variations of the ζ-potential. For the 0.1 μm particle, the maximum relative changes of both spectral parameters are approximately 15% over the studied range of ζ-potentials from 0 to -125 mV. These variations are small but detectable. With increasing particle size, the sensitivity of both parameters to changes in ζ decreases rapidly. Already for micro-scale particles, here 31.6 μm, they are expected to be almost insensitive – except for σ''_{max} in the case of non-zero reaction currents.
The situation is very different with regard to the sensitivity of the relaxation time to variations of the ζ-potential. Figures 5.9 and 5.10 show that here, in contrast to σ_{DC} and σ''_{max}, a significant increase of the relaxation time can

only be observed for micro-particles or larger, i.e., $a \gtrsim 1$ μm, and in absence of reaction currents. Under these conditions, the relaxation time of the pure diffuse-layer polarization increases by a factor 5 from 0 mV to $\pm$125 mV, with the highest sensitivity in the range between $\pm$25 through $\pm$75 mV. As the same two Figures show, the relaxation time of the volume-diffusion process, which dominates for larger particles sizes and non-zero reaction currents, is expected to be practically insensitive to changes of the ζ-potential. However, in this regime the relaxation time is highly sensitive to the reaction current through the particle surface, which in turn is a direct measure for the reactivity of the particle surface. This effect can be of interest to monitor particle-injection experiments, where particle-surface properties change over time (e.g., engineered particle coatings, Flores Orozco et al., 2015), or conditions with varying availability of active ionic species, e.g. due to biogeochemical processes (e.g., Flores Orozco et al., 2011). Despite of the theoretical potential of the IP method to characterize surface properties such as ζ-potential and reactivity, the high characteristic frequencies of the relaxation processes around nano-particles impose a practical limit: Typical laboratory set-ups only permit to determine the complex conductivity response of material samples up to frequencies of 1 to 40 kHz, and can therefore only resolve the increasing flank of the relaxation peak (e.g. Abdel Aal et al., 2017). In this case, the determination of the characteristic frequency might become too imprecise to detect the small variations of τ with ζ. Other researchers, in contrast, were able to observe the relaxation peak of sub-micron silver and zero-valent iron particles at sufficiently low frequencies (Joyce et al., 2012). In field experiments with array lengths in the meter to dekameter range, electromagnetic induction usually masks the IP response at frequencies $> 10 - 100$ Hz (e.g. Flores Orozco et al., 2011, 2012), which further reduces the detectability of nano-particles in larger-scale applications.

Limitations of the model

In part 1 of this series (Bücker et al., 2018a), we discussed the limitations inherent to the model by Wong (1979) – including our own extensions. Obviously, the numerical model presented in this second part suffers from the same set of shortcomings inherited from the base model. To mention some of the remaining issues, (1) it ignores the fact that most metal-bearing minerals are rather semiconductors than metallic conductors, (2) it does not consider dynamic charging of the Stern layer (e.g. Merriam, 2007), (3) it neglects particle-–particle interactions between adjacent grains, which is inherent to the mixing rule used for

the up-scaling, (4) it does not treat effects of non-spherical geometries or surface roughness, and (5) having even more model parameters, its application to real data is expected to be even more tedious (e.g. Placencia-Gómez and Slater, 2014).

In the light of recently developed semiconductor-polarization models (e.g., Revil et al., 2015b; Misra et al., 2016a,b; Abdulsamad et al., 2017), it is worth reconsidering the assumption of an infinite conductivity of the metallic particle. In his analysis, Wong (1979) argued that if "the conductivity [...] of the mineral is a hundred or a thousand times the conductivity [...] of the surrounding medium" (i.e. the electrolyte), the particle could be considered a perfect conductor. However, this argumentation only assesses the (direct-current) conductivity of the involved materials, which is not sufficient in the context of a frequency-dependent model.

The situation described by the zero-potential boundary condition (5.15) requires the charges on the particle to relax much faster than the variation of the external excitation. In metallic conductors, the charge relaxation time can be roughly approximated by twice the collision time of the free electrons (e.g., Ashby, 1975). At room temperature, typical collision times in elemental metals are in the order of 10^{-15} s to 10^{-14} s, such that the characteristic frequency of charge relaxation is well beyond the relevant frequency range and the assumption of a perfect conductor remains justified. The analysis by Revil et al. (2015b) and Revil et al. (2015a) suggests that the situation changes fundamentally if semiconducting minerals, such as pyrite or magnetite, are considered. Here, the diffusion-controlled relaxation of the charge carriers inside the semiconducting particle not only leads to a much slower response of the solid particle but seems to be the main polarization mechanism in the typical IP frequency range. With this in mind, the application of the present polarization model (as well as any model that rests on the assumption of a perfectly conductive solid phase) should clearly be limited to the case of metallic conductors.

In addition to the known limitations (1) through (5), the assumption of a constant ζ-potential used in this study might also be unrealistic. In particular, the large field-induced variations of the ion concentrations close to the particle surface raise doubts whether the constant-ζ-potential boundary condition, i.e., equation (5.15), can be adequate. This limitation is also inherited from the Wong model, which – from our new perspective – simply describes the special case of $\zeta = 0$, i.e., at the point of zero charge of the metal surface. Determining the ζ-potential self-consistently from a speciation model for the particle-electrolyte

interface might result in a more realistic boundary condition, which can account for the complex mutual dependency between the diffuse layer and the surface (including the Stern layer).

Appendices

5.A Adaptation of the exchange current

Our description of the exchange current strictly adheres to the one proposed by Wong (1979). However, while Wong can assume the bulk concentration of the active cations c_3^∞ at the particle surface, according to equation (5.7), the equilibrium concentration at a charged surface is given by $c_3^{(0)}(\zeta) = c_3^\infty \exp\left[-e\zeta/(kT)\right]$, which requires some adaptions of the known expressions.
The fundamental metal deposition-dissolution reaction

$$\mathrm{M}^+ + \mathrm{e}^- \leftrightarrows \mathrm{M}_{(\mathrm{ads})} \tag{5.26}$$

remains unchanged. Here, M^+ denotes the metal cation in solution, e^- an electron and $\mathrm{M}_{(\mathrm{ads})}$ a metal atom adsorbed to the particle surface. The net exchange current density due to the above reaction writes [equation (23) in Wong (1979)]

$$i = k_-[\mathrm{M}_{(\mathrm{ads})}]e \exp\left[e\eta/(2kT)\right] - k_+[\mathrm{M}^+]e \exp\left[-e\eta/(2kT)\right], \tag{5.27}$$

where we have already assumed a symmetry factor of 1/2. The parameters k_+ and k_- are rate constants, $[\mathrm{M}_{(\mathrm{ads})}]$ and $[\mathrm{M}^+]$ are concentrations of active cations and adsorbed atoms (in ions/m^3), and η is the current-producing overpotential. Under undisturbed conditions, i.e., without any external excitation, the overpotential η is zero by definition and the modified concentration of active cations at the particle surface is given by $c_3^{(0)}(\zeta)$, which includes the cation excess in the static diffuse layer caused by the non-vanishing surface potential ζ. Wong's expression for the equilibrium exchange current, his equation (24), therefore becomes

$$i_0 = k_-[\mathrm{M}_{(\mathrm{ads})}]e = k_+ c_3^{(0)}(\zeta) N_A e, \tag{5.28}$$

where N_A is Avogadro's constant ($6.0221 \cdot 10^{23}$ mol^{-1}).
As Wong (1979) discusses in more detail, for small overpotentials $\eta \ll e/(2kT)$) the non-equilibrium exchange current due to a non-zero overpotential can be linearized resulting in

$$i \approx i_0 e\eta/(kT) \quad \text{or} \quad i \approx i_0 e/(kT)\mathbf{E}\cdot\mathbf{n}\, l, \tag{5.29}$$

where $\mathbf{E}\cdot\mathbf{n}$ is the component of the electrical field normal to the particle surface ($\mathbf{n}$ is the unit normal vector pointing into the electrolyte) and l is the characteristic distance of closest approach by the active cations to the surface.

Even in absence of a current-producing overpotential, a perturbation $\delta c_3(\zeta)$ of the active cation concentration from the equilibrium value $c_3^{(0)}(\zeta)$ can generate the net exchange current

$$\begin{aligned} i &= k_-[\mathrm{M}_{(\mathrm{ads})}]e - k_+[c_3^{(0)}(\zeta) + \delta c_3(\zeta)]N_A e \\ &= i_0 - i_0 - k_+ \delta c_3(\zeta) N_A e \\ &= -k_+ \delta c_3(\zeta) N_A e. \end{aligned} \tag{5.30}$$

Note that the net current density due to a positive $\delta c_3(\zeta)$ is negative (toward the center of the particle).
The total exchange current density is then obtained as the sum of the one caused by a non-zero overpotential and a perturbation of the active cation concentration from the equilibrium and writes

$$i \approx \alpha(\zeta) c_3^{(0)}(\zeta) N_A e \mathbf{E} \cdot \mathbf{n} - \beta(\zeta) \delta c_3(\zeta) N_A e, \tag{5.31}$$

where $\alpha(\zeta) = i_0 l/[c_3^{(0)}(\zeta) N_A kT]$ and $\beta = k_+ = i_0/[c_3^{(0)}(\zeta) N_A e]$ are functions of the ζ-potential. Wong (1979) estimates his values of $\alpha(0) = i_0 l/(c_3^\infty N_A kT)$ and $\beta(0) = i_0/(e c_3^\infty N_A)$ from experimentally determined values of the equilibrium reaction current density i_0. If we use the same experimental values as starting point and assume that the particles used also had a non-vanishing static surface potential, we find $\alpha(\zeta) = \alpha(0) \exp[e\zeta/(kT)]$ and $\beta(\zeta) = \beta(0) \exp[e\zeta/(kT)]$ (by comparison with the expressions by Wong). Note that Equation (5.31) defines an electrical current density in $\mathrm{A/m^2}$, i.e. the corresponding current densities in $\mathrm{mol/(m^2 s)}$ as needed for the corresponding boundary condition, equation (5.17), can be obtained by dividing i by $F = N_A e$.

5.B Implementation into the COMSOL coefficient form PDE

The COMSOL partial differential equation (PDE) interface in coefficient form allows the specification of PDEs and systems of PDEs of the general type

$$e_a \frac{\partial^2 u}{\partial t^2} + d_a \frac{\partial u}{\partial t} + \nabla \cdot (-c \nabla u - \alpha u + \gamma) + \beta \cdot \nabla u + a u = f \tag{5.32}$$

with general boundary conditions

$$-\mathbf{n} \cdot (-c \nabla u - \alpha u + \gamma) = g - q u \quad \text{and} \tag{5.33}$$

$$u = s, \tag{5.34}$$

where u denotes the dependent variable and $\mathbf{n}$ is the inward-pointing unit normal vector (i.e., into the electrolyte) on the respective boundary. Note that actually COMSOL defines the normal vector reversely (outward-pointing) and consequently it appears with reversed sign in equation (5.33). The coefficients e_a, d_a, c, α, γ, β, a, f, q, g, and s are used to describe the specific problem to be modelled. Equation (5.33) is a generalized Neumann boundary condition and equation (5.34) a Dirichlet boundary condition.

Static solution

With these definitions, the numerical implementation of the static problem from equations (5.7) and (5.8) with boundary conditions (5.9) and (5.10) is straightforward. If we define the dependent variable $u_1 = U^{(0)}(\mathbf{r})$, the PDE coefficients must be

$$c = 1 \quad \text{and} \tag{5.35}$$

$$f = \frac{F}{\varepsilon_0 \varepsilon_r} \sum_{j=1}^{3} z_j c_j^{\infty} \exp\left(-\frac{z_j e}{kT} u\right). \tag{5.36}$$

Note that throughout this step-by-step instruction we will use the convention that all coefficients that are not mentioned specifically are assumed to be zero. Assuming mono-valent ions $|z_j| = 1$ and making use of the electro-neutrality condition in the bulk electrolyte $c_1^{\infty} = c_2^{\infty} + c_3^{\infty}$, the coefficient f can be simplified to

$$f = -\frac{2c_1^{\infty} F}{\varepsilon_0 \varepsilon_r} \sinh\left(\frac{e}{kT} u\right). \tag{5.37}$$

On the top boundary (at $y = L$), on the left ($x = -L$), and on the right ($x = L$) boundary, we define

$$s = 0, \tag{5.38}$$

while on for the metal surface (at $x^2 + y^2 = a^2$ for the spherical particle) we set

$$s = \zeta \tag{5.39}$$

to implement the Dirichlet boundary conditions (5.10) and (5.9), respectively. Defining the axis $y = 0$ as symmetry axis (selecting rotational symmetry in the model setup), no specific boundary conditions must be defined on this boundary.

Frequency-dependent solution

For the solution of the frequency-dependent case, we need to implement the system of four coupled PDEs described in equations (5.11) and (5.12). In the system case, the dependent variable u in equation (5.32) becomes a column vector of length 4. We define

$$\mathbf{u}_2 = \begin{bmatrix} u_{21} \\ u_{22} \\ u_{23} \\ u_{24} \end{bmatrix} = \begin{bmatrix} \delta c_1(\mathbf{r},\omega) \\ \delta c_2(\mathbf{r},\omega) \\ \delta c_3(\mathbf{r},\omega) \\ \delta U(\mathbf{r},\omega) \end{bmatrix}. \tag{5.40}$$

Assuming isotropy of all of its elements, the coefficient c becomes a 4-by4 coefficient matrix. In our case, $\underline{c}$ writes

$$\underline{c} = \begin{bmatrix} D & 0 & 0 & -\mu_1 c_1^\infty \exp(\frac{e}{kT} u_1) \\ 0 & D & 0 & \mu_2 c_2^\infty \exp(-\frac{e}{kT} u_1) \\ 0 & 0 & D & \mu_3 c_3^\infty \exp(-\frac{e}{kT} u_1) \\ 0 & 0 & 0 & 1 \end{bmatrix}, \tag{5.41}$$

where u_1 denotes the scalar static solution (for the electrical potential only). The coefficient matrices

$$\underline{\alpha} = \begin{bmatrix} -\mu_1 \nabla u_1 & 0 & 0 & 0 \\ 0 & \mu_2 \nabla u_1 & 0 & 0 \\ 0 & 0 & \mu_3 \nabla u_1 & 0 \\ 0 & 0 & 0 & 0 \end{bmatrix}, \tag{5.42}$$

and

$$\underline{a} = \begin{bmatrix} i\omega & 0 & 0 & 0 \\ 0 & i\omega & 0 & 0 \\ 0 & 0 & i\omega & 0 \\ \frac{F}{\varepsilon_0 \varepsilon_r} & -\frac{F}{\varepsilon_0 \varepsilon_r} & -\frac{F}{\varepsilon_0 \varepsilon_r} & 0 \end{bmatrix} \tag{5.43}$$

complete the description of our system of PDEs in coefficient form. Note that each element $\alpha_{i,j} = [\alpha_{i,j,1}, \alpha_{i,j,2}]^T$ is a two-element column vector where the third indices correspond to the spatial coordinates x and y.

As mentioned in the main text, because of the cylindrical symmetry, the solution of the system of PDEs can be carried out on a two-dimensional modelling domain with coordinates x and y (see Figure 5.1). Thus, the position vector and the gradient operator become

$$\mathbf{r} = \begin{bmatrix} x \\ y \end{bmatrix} \text{ and } \nabla = \begin{bmatrix} \partial_x \\ \partial_y \end{bmatrix}, \tag{5.44}$$

respectively. Although we are actually interested in solving the system of PDEs in cylindrical coordinates, we will first proceed with the formulation of the system in the two Cartesian coordinates x and y and further below provide a simple conversion to cylindrical coordinates.

The problem description for the numerical modelling is completed by the following boundary conditions. Far from the particle surface (i.e., for $r \to \infty$), we requested the perturbation potential to approximate the exciting potential $-\mathbf{E}\cdot\mathbf{r}$ and the perturbation ion concentrations to vanish. Therefore, on the **left and right boundary**, we define Dirichlet boundary conditions by setting

$$\mathbf{s} = \begin{bmatrix} 0 \\ 0 \\ 0 \\ E_0 L \end{bmatrix} \quad \text{and} \quad \mathbf{s} = \begin{bmatrix} 0 \\ 0 \\ 0 \\ -E_0 L \end{bmatrix}, \tag{5.45}$$

respectively.

On the **top boundary**, we implement a zero-flux boundary condition for all four dependent variables. This results in vanishing normal fluxes for all three ionic species and a vanishing normal electrical field. Again, due to the rotational symmetry, no boundary conditions must be defined on the symmetry axis (i.e., along $y = 0$).

On the **particle surface**, we implement mixed boundary conditions consisting of one Dirichlet condition for the electric potential, equation (5.15), and generalized Neumann conditions for the three ion fluxes, equations (5.16) through (5.17). To define the boundary conditions on the ion fluxes, we set

$$\underline{g} = \begin{bmatrix} 0 & 0 & 0 & 0 \\ 0 & 0 & 0 & 0 \\ 0 & 0 & \beta(\zeta) & 0 \\ 0 & 0 & 0 & 0 \end{bmatrix} \tag{5.46}$$

and

$$\mathbf{g} = \begin{bmatrix} 0 \\ 0 \\ \alpha(\zeta) c_3^{\infty} \exp\left(-\frac{e}{kT} u_1\right) \mathbf{n} \cdot \nabla u_{24} \\ 0 \end{bmatrix}, \tag{5.47}$$

where $\mathbf{n}\cdot\nabla u_{24} = n_x \partial_x u_{24} + n_y \partial_y u_{24}$. A Dirichlet boundary condition component is specified for the fourth component by setting

$$s = 0, \tag{5.48}$$

which overwrites the above no-flux boundary condition (only for the perturbation potential). The Dirichlet boundary condition for the first three components are deactivated and the generalized Neumann boundary conditions described by $\underline{q}$ and $\mathbf{g}$ remain valid for the first three components.

Conversion to cylindrical coordinates

As mentioned above, the software expects the equations to be defined in a Cartesian system with two space dimensions. That means, that if we assume isotropic media (i.e., $\underline{c}$ is a 4-by-4 matrix) the i-th equation of our system is given by

$$\sum_j \left[-\left(\partial_x c_{i,j}\partial_x + \partial_y c_{i,j}\partial_y\right) u_j - \left(\partial_x \alpha_{i,j,1} + \partial_y \alpha_{i,j,2}\right) u_j + a_{i,j} u_j \right] = 0, \quad (5.49)$$

where we have already dropped all vanishing coefficients (i.e., e_a, d_a, γ, etc.). However, we actually seek to solve a system in cylindrical coordinates, the i-th component of which should write

$$\sum_j \left[-\left(\frac{1}{r}\partial_r r c_{i,j}\partial_r + \partial_z c_{i,j}\partial_z\right) u_j - \left(\frac{1}{r}\partial_r r \alpha_{i,j,1} + \partial_z \alpha_{i,j,2}\right) u_j + a_{i,j} u_j \right] = 0 \quad (5.50)$$

instead. If we simply multiply the entire system by r, we get

$$\sum_j \left[-\left(\partial_r r c_{i,j,1,1}\partial_r + \partial_z r c_{i,j,2,2}\partial_z\right) u_j - \left(\partial_r r \alpha_{i,j,1} + \partial_z r \alpha_{i,j,2}\right) u_j + r a_{i,j} u_j \right] = 0, \quad (5.51)$$

which can be converted to the form supported by software. Defining r as y and z as x yields the modified system

$$\nabla \cdot \left(-y\underline{c}\nabla \mathbf{u} - y\underline{\alpha}\mathbf{u}\right) + y\underline{a}\mathbf{u} = 0 \quad (5.52)$$

Thus, it is sufficient to multiply the three coefficient matrices $\underline{c}$, $\underline{\alpha}$, and $\underline{a}$ by y to transform the problem to cylindrical coordinates. Note that the boundary coefficients $\underline{q}$ and $\mathbf{g}$ have to be multiplied by y, too, while $\mathbf{r}$ remains unchanged.

CHAPTER 6

On the Role of Stern- and Diffuse-Layer Polarization Mechanisms in Porous Media

6.1 Introduction

In absence of metallic minerals, mainly four mechanisms contribute to the low-frequency (typically < 1 MHz) dispersion of the complex conductivity of geomaterials, all of which are sensitive to the polarization of different parts of the electric double layer at the solid-liquid interface (e.g. Lesmes and Morgan, 2001; Kemna et al., 2012): (1) Maxwell-Wagner polarization, (2) polarization of the Stern layer, (3) polarization of the diffuse layer, and (4) membrane polarization. The Maxwell-Wagner theory (Maxwell, 1892; Wagner, 1914) describes the interfacial polarization observed in heterogeneous media consisting of two or more phases with different electric conductivities and/or dielectric constants. Upon excitation by an external electric field, the unequal conduction and displacement current densities in the different phases are balanced by an accumulation of charges along the geometrical boundaries. O'Konski (1960) extended the Maxwell-Wagner theory to include the polarization of bound charges located at the surface of charged particles. Later, Garcia et al. (1985) treated the case of an uncharged dielectric particle surrounded by an electrolyte solution. In contrast to earlier theories, which assume homogeneous conductivities in the involved phases resulting in pure surface charge distributions, their treatment explicitly accounts for local field-induced concentration variations and thus volume charge distributions of finite extension. The characteristic time scales of the different types of Maxwell-Wagner polarization are relatively short, such that this relaxation is usually found at the high-frequency limit of the complex-conductivity response of typical geomaterials (e.g. Leroy et al., 2008; Lesmes and Morgan, 2001).

This chapter is based on: Bücker, M., Flores Orozco, A., Undorf, S., and Kemna, A. (2019). *On the role of Stern- and diffuse-layer polarization mechanisms in porous media.* Manuscript submitted for publication in Journal of Geophysical Research.

The first theoretical model describing the polarization of the Stern layer was presented by Schwarz (1962) and improved by Schurr (1964). Schurr's theory accounts for the diffusion-controlled polarization of the Stern layer of bound counter-ions as studied by Schwarz and a frequency-independent contribution of the surface conductivity due to the excess of charge carriers in the diffuse layer as introduced by O'Konski. Consequently, the frequency dispersion of the effective conductivity is explained with the relaxation of the Stern-layer polarization and the effect of the diffuse layer only results in a uniform increase of the real part of the conductivity over the entire range of frequencies. Later, this model provided the basis for the Stern-layer polarization model proposed by Leroy et al. (2008), who included a detailed electro-chemical model to quantify the surface conductivity contributions of Stern and diffuse layer (see e.g. Revil and Glover, 1997, 1998) and explicitly accounted for a distribution of different grain sizes. This model has been successfully applied to predict the complex-conductivity response of densely packed glass beads (Leroy et al., 2008) and later extended to sand-oil mixtures (Schmutz et al., 2010).

The polarization of the diffuse layer has been studied extensively by Dukhin and Shilov (1974), who developed a theory for the fluxes through thin diffuse layers, which lead to the development of field-induced concentration variations in the diffuse layer and the adjacent electrolyte. This concentration-polarization mechanism has also been treated analytically by Fixman (1980), Hinch et al. (1984), and Chew and Sen (1982a) among others. A numerical solution removing many of the limitations of the analytical models – e.g. the assumption of a thin diffuse layer compared to the particle radius, sufficiently small surface potential, and the limitation to monovalent symmetric electrolyte – was presented by DeLacey and White (1981). Shilov et al. (2001) extend the classic Dukhin-Shilov theory by including the effect of the Maxwell-Wagner polarization at high frequencies, which yields a very good agreement with the numerical model by DeLacey and White (1981).

Different attempts have been made to determine the relative importance of Stern- and diffuse-layer polarization and to develop combined models. To this end, Lyklema et al. (1983) generalized the Schwarz-Schurr model by including a largely simplified coupling with the diffuse layer, which mainly results in an increase of the characteristic frequency of the Stern-layer relaxation. de Lima and Sharma (1992) analyzed the models by Schwarz-Schurr and Fixman in detail but separately in order to assess their relative importance for the overall polarization response. By means of a simple superposition of the individual responses,

Lesmes and Morgan (2001) developed a combined model considering all three polarization mechanisms, i.e. Stern-, diffuse-layer and Maxwell-Wagner polarization. They also included a volume-averaging approach, which enabled them to study the response of a water-particle mixtures characterized by a grain-size distribution. Based on the work of Kijlstra et al. (1992), Shilov et al. (2001) provide a modification of the Dukhin-Shilov theory, which accounts for the contribution of counter-ions in the Stern layer to the surface conductivity of charged particles. Due to the complexity of the equations needed to model a fully coupled system including all three polarization mechanisms, to date all analytical solutions suffer from strong simplifications and/or only treat particular limiting cases.

Most theories describing the first three polarization mechanism rest on the analytical solution of the underlying system of partial differential equations around one isolated spherical particle. The effective induced dipole moment of the polarized particle obtained from this treatment can then be used to derive the effective conductivity and/or the effective dielectric constant of ensembles of more than one particle. The effective medium theory provides mixing laws for dilute suspensions (e.g. Maxwell, 1892; Wagner, 1914) or mixtures with higher particle concentrations (e.g. Bruggeman, 1935; Hanai, 1960).

In contrast, the membrane polarization mechanism is generally studied on pore network models with different levels of complexity. Marshall and Madden (1959) developed the first simplistic model for an alternating sequence of two types of one-dimensional pores or zones, where the membrane effect is introduced by assuming different effective ion mobilities for cations and anions in one of the zones. While Marshall and Madden (1959) do not further specify the origin of the different transport rates through this "active" zone, subsequent developments explained the ion selectivity based on the unequal contributions of cations and anions to the surface conductivity at the pore wall (Fridrikhsberg and Sidorova, 1961; Buchheim and Irmer, 1979; Titov et al., 2002, 2004). Blaschek and Hördt (2009) carried out numerical simulations on more complex one- and two-dimensional pore network models, where the ion-selective behaviour of narrow pores is still parameterized in terms of unequal ion mobilities, which are constant over the pore's cross section. Volkmann and Klitzsch (2010) improved this numerical approach and limited the ion selective characteristics – expressed in terms of unequal effective ion mobilities – to a thin layer covering the pore walls.

Bücker and Hördt (2013a,b) summarized the previous developments and derived

an analytical model, which allowed to explicitly include pore radii and surface conductivity due to Stern and diffuse layer into the one-dimensional impedance model by Marshall and Madden (Bücker and Hördt, 2013a). This model has later been extended to model the effect of variations of temperature (Bairlein et al., 2016) as well as fluid salinity and pH (Hördt et al., 2016) on the polarization response. In order to study the characteristic signature of different concentrations of immiscible hydrocarbon contaminants, Bücker et al. (2017) extended the model to the case of two liquid phases in the pore space. Based on the same model, Stebner and Hördt (2017) explored the possibility to use impedance networks to model the membrane polarization of porous media. Because the model by Bücker and Hördt typically requires large aspect ratios, i.e. the length of a pore divided by its diameter, to produce measurable polarization magnitudes in the typical frequency range of geophysical applications, Hördt et al. (2017) further investigated into the geometrical constraints of this membrane-polarization model.

Besides the geometrical constraints, the to date over-simplified consideration of Stern layer in all above mentioned membrane-polarization models is a major limitation of the theoretical treatment of such pore-constriction geometries. While combined treatments of Stern-, diffuse-layer, and Maxwell-Wagner polarization mechanisms exist for grain-based models, the incorporation of the coupling between the individual mechanisms is often largely simplified in membrane-polarization models.

With the present paper, we address the repeatedly stated need for "a mechanistic approach and [...] general framework in which all these mechanisms are explained and quantified in their relative importance" (Kemna et al., 2012). In the theory section, we compile the mathematical descriptions of all relevant physical processes and provide a generalized mathematical framework, which allows modelling the fully coupled interplay of Stern- and diffuse-layer polarization on arbitrary geometries. In the next section, we derive an improved analytical approximation for the polarization response around a single grain, which matches the results obtained from numerically solving the equations of the generalized mathematical framework. We then apply the previously validated modelling framework to pore-constriction geometries to check (and improve) the analytical membrane-polarization model of Bücker and Hördt (2013a) for the limiting case of a pure diffuse-layer polarization and afterwards study the effect of a coupled Stern- and diffuse-layer polarization.

6.2 Theory

In order to overcome the limitations of previous studies developed for specific geometric shapes of solid and liquid phase (spheres, cylinders, etc.), in this section we will set up a generalized theoretical framework, which – in principle – can be used to model the low-frequency polarization response for arbitrary geometric configurations of these two phases.

6.2.1 Electric double layer model

Most solid surfaces in contact with aqueous solutions are charged. Depending on the chemical compositions of solid and liquid phase, different processes can produce this surface charge. In the present study, we will consider silica surfaces in contact with a monovalent electrolyte solution, such as NaCl. In this system, the deprotonation of silanol surface sites in known to produce a negative surface charge density Σ over a wide range of pH values (e.g. Somasundaran, 2006; Leroy et al., 2008).

In the electrolyte solution next to the silica surface, the electric field of Σ attracts counter-ions (ions of opposite sign, cations if $\Sigma < 0$) and repels co-ions (ions of the same sign, here anions) giving rise to the development of an *electric double layer* (EDL) consisting of two layers: The inner part – also known as Stern or Helmholtz layer – consists of counter-ions directly adsorbed to the surface. The outer part – the diffuse or Gouy-Chapman layer – is mainly populated by counter-ions and a minor fraction of co-ions both obeying Poisson-Boltzmann statistics.

For the purpose of the present study, it is sufficient to adopt the simplified model displayed in Figure 6.1. Here, the Stern layer is treated as an infinitely thin layer of tightly bound counter-ions (e.g. Schwarz, 1962; Schurr, 1964; Leroy et al., 2008). Due to its vanishing thickness, i.e. $\Delta d = 0$, the Stern layer becomes part of the surface and is only characterized by the uniform surface charge density $|\Sigma_S^{(0)}| < |\Sigma|$ [the superscript (0) indicates quantities in the equlibrium state, i.e. without external excitation], which partly shields the electric field of Σ. A further simplification regards the strong binding of the counter-ions to the surface, which leads to the assumption that the charges in the Stern layer can only move along the surface (if a suitable tangential field is applied).

The ions in the diffuse layer, in contrast, can move in normal direction to the surface. As a result of an equilibrium between simultaneously acting electrostatic forces and thermal fluctuations, counter-ion excess and co-ion deficit concentra-

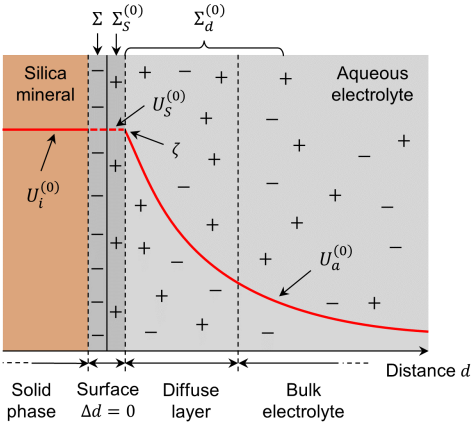

Figure 6.1: Simplified model of the equilibrium electric double layer at the charged silica surface in contact with the electrolyte solution. Due to deprotonation of silanol surface sites, the mineral surface acquires the surface charge Σ. On the electrolyte site, this usually negative charge is screened by an equal number of the positive charges distributed over the Stern layer ($\Sigma_S^{(0)}$) and the diffuse layer ($\Sigma_d^{(0)}$). $U_i^{(0)}$, $U_S^{(0)}$, and $U_a^{(0)}$ are the electric potentials in the solid phase, the Stern layer, and the electrolyte, respectively.

tions smoothly decay with the distance d from the surface. At a distance of several Debye lengths, which is in the order of a few nm to a few tens of nm for typical solutions, both ion concentrations approach their values in the bulk electrolyte. Together with $\Sigma_S^{(0)}$, the positive charge density $\rho(d)$ in the diffuse layer completely screens the negative charge Σ at the surface. By integrating $\rho(d)$ from the bulk electrolyte to the silica surface, we can express the total charge stored in the diffuse layer in terms of the equivalent surface charge density $\Sigma_d^{(0)}$. In equilibrium, the whole electrical double (or triple) layer consisting of charged surface sites, Stern layer, and diffuse layer is electro-neutral and we have $\Sigma_S^{(0)} + \Sigma_d^{(0)} = -\Sigma$.
The electric potential at the inner limit of the diffuse layer is usually identified with the ζ-potential at the plane of shear (e.g. Leroy et al., 2008; Bücker and Hördt, 2013a). Due to the space charge ρ, the electric potential $U_a^{(0)}$ in the electrolyte solution decays from ζ at the solid-liquid interface to zero in the bulk electrolyte. Note that in our greatly simplified model, the vanishing thickness of the Stern layer implies that the solid surface and the inner limit of the diffuse layer collapse into one point, such that the (equilibrium) potentials in the solid phase $U_i^{(0)}$, in the Stern layer $U_S^{(0)}$, and in the electrolyte $U_a^{(0)}$ are equal to ζ at the surface.

6.2.2 Basic equations

Bulk electrolyte and diffuse layer

The electrolyte solution is characterized by its relative permittivity ε_a as well as the valences $z_\pm$, electrical mobilities $\mu_\pm$, and bulk concentrations $C_\pm^\infty$ of the dissolved ions. For the sake of simplicity, we assume that the mobilities of cations (subindex +) and anions (subindex −) are equal, i.e. $\mu_+ = \mu_- = \mu$. As mentioned above, we furthermore limit our treatment to the case of a monovalent electrolyte, i.e. $z_\pm = \pm 1$.
Spatial and temporal variations of ion concentrations $C_\pm(\mathbf{r}, t)$ and electric potential $U_a(\mathbf{r}, t)$ in the solution, i.e. in the diffuse layer and the bulk electrolyte, are controlled by the steady-state Nernst-Planck, continuity, and Poisson equations (e.g. Garcia et al., 1985):

$$\mathbf{J}_\pm(\mathbf{r}, t) = -D\nabla C_\pm(\mathbf{r}, t) - z_\pm \mu C_\pm(\mathbf{r}, t)\nabla U_a(\mathbf{r}, t) \tag{6.1}$$

$$\nabla \mathbf{J}_\pm(\mathbf{r}, t) = -\partial_t C_\pm(\mathbf{r}, t) \tag{6.2}$$

$$\nabla^2 U_a(\mathbf{r}, t) = -\frac{e}{\varepsilon_0 \varepsilon_a}\left[C_+(\mathbf{r}, t) - C_-(\mathbf{r}, t)\right] \tag{6.3}$$

Here, D denotes the diffusion coefficient, $e = 1.602 \cdot 10^{-19}$ C the elementary charge, and $\varepsilon_0 = 8.85 \cdot 10^{-12}$ As/(Vm) the vacuum permittivity. Diffusion coefficient and mobility of the ions are connected via the Einstein relation $D = \mu kT/e$, where $k = 8.617 \cdot 10^{-5}$ eV/K is Boltzmann's constant and T the absolute temperature of the system. The current densities $\mathbf{J}_\pm$ defined by the steady-state Nernst-Planck equation (6.1) consider diffusion $-D\nabla C_\pm$ and electro-migration fluxes $-z_\pm \mu C_\pm \nabla U_a$.

If the system is excited by a sufficiently weak time-harmonic electric field $E_0 e^{i\omega t}$, where ω and t denote angular frequency and time, respectively, the ion concentrations $C_\pm(\mathbf{r}, t)$ can be approximated by the sums of the static equilibrium concentrations $C_\pm^{(0)}$ and small perturbations $|\delta C_\pm| \ll C_\pm^{(0)}$, which vary linearly with the external excitation (e.g. Garcia et al., 1985):

$$C_\pm(\mathbf{r}, t) = C_\pm^{(0)}(\mathbf{r}) + \delta C_\pm(\mathbf{r}, \omega) \cdot e^{i\omega t} \tag{6.4}$$

In the same way, the electric potential $U_a(\mathbf{r}, t)$ can be decomposed into the static equilibrium potential $U_a^{(0)}$ and the much smaller perturbation $|\delta U_a| \ll U_a^{(0)}$ as follows.

$$U_a(\mathbf{r}, t) = U_a^{(0)}(\mathbf{r}) + \delta U_a(\mathbf{r}, \omega) \cdot e^{i\omega t} \tag{6.5}$$

By inserting equations (6.4) and (6.5) into equations (6.1) through (6.3) and Fourier-transforming the resulting system, the problem can be decomposed into a static part and a frequency-dependent part (e.g. Chew and Sen, 1982b,a; Bücker et al., 2018b). While the frequency-dependent part couples to the static solution, the static part can be solved independently.

To obtain the static part of the system, we only have to set set $\delta C_\pm, \delta U_a, \partial_t = 0$, which after a few additional manipulations yields the Boltzmann-distributed equilibrium ion concentrations (Chew and Sen, 1982b)

$$C_\pm^{(0)}(\mathbf{r}) = C_\pm^\infty \exp\left[-\frac{z_\pm e}{kT} U_a^{(0)}(\mathbf{r})\right] \tag{6.6}$$

and the Poisson-Boltzmann equation (e.g Chew and Sen, 1982b)

$$\nabla^2 U_a^{(0)}(\mathbf{r}) = -\kappa^2 \frac{kT}{e} \sinh\left[\frac{e}{kT} U_a^{(0)}(\mathbf{r})\right], \tag{6.7}$$

where $\kappa = \left[2e^2 C_\pm^\infty / (\varepsilon_0 \varepsilon_f kT)\right]^{1/2}$ is equal to the inverse Debye screening length. Together with the appropriate boundary conditions discussed below, equations (6.6) and (6.7) describe the spatial variations of the equilibrium ion concentrations $C_\pm^\infty$ and the static electric potential $U_a^{(0)}$ in the diffuse layer and the bulk electrolyte.

In order to obtain the solution of the frequency-dependent system under the influence of a weak external field $E_0 \exp(i\omega t)$, the steady-state Nernst-Planck equation (6.1) is inserted into the continuity equation (6.2), Fourier-transformed and linearized, which gives (e.g. Chew and Sen, 1982a)

$$i\omega\delta C_\pm(\mathbf{r},\omega) = \nabla\Big\{ D\nabla\delta C_\pm(\mathbf{r},\omega) + \mu z_\pm \left[C_\pm^{(0)}(\mathbf{r})\nabla\delta U_a(\mathbf{r},\omega) + \delta C_\pm(\mathbf{r},\omega)\nabla U_a^{(0)}(\mathbf{r}) \right] \Big\} + \mathcal{O}(E_0^2). \quad (6.8)$$

The frequency-dependent perturbation concentrations of the two ion species and the potentials are coupled among each other by the also Fourier-transformed Poisson equation (e.g. Chew and Sen, 1982a)

$$\nabla^2\delta U_a(\mathbf{r},\omega) = -\frac{e}{\varepsilon_0\varepsilon_r}\left[\delta C_+(\mathbf{r},\omega) - \delta C_+(\mathbf{r},\omega)\right]. \quad (6.9)$$

Equations (6.8) and (6.9) constitute three coupled differential equations that describe the spatial variations of the perturbation quantities within the diffuse layer and the bulk electrolyte. As the boundary conditions at the solid surface couple the solution in the electrolyte to the corresponding solutions in the Stern layer and the interior of the solid phase, we will discuss the appropriate boundary conditions further below.

Stern layer

As discussed above, the Stern layer is modelled as an infinitely thin layer situated at the solid-liquid interface. In absence of an external excitation, the counter-ions in the Stern layer are uniformly distributed along the interface, such that the corresponding surface charge density $\Sigma_S^{(0)}$ is a constant. Under the influence of the electric field $E_0 \exp(i\omega t)$, the counter-ions are assumed to move along the surface in tangential direction, but no charge exchange with the surrounding electrolyte nor the solid phase are considered. Following the same linearizing scheme used for diffuse layer and bulk electrolyte, the surface charge density can also be described in terms of the constant equilibrium value $\Sigma_S^{(0)}$ and a much smaller perturbation surface charge density $|\delta\Sigma_S| \ll \Sigma_S^{(0)}$ as

$$\Sigma_S(\mathbf{r}_S,t) = \Sigma_S^{(0)} + \delta\Sigma_S(\mathbf{r}_S,\omega)\exp(i\omega t), \quad (6.10)$$

where $\mathbf{r}_S$ denotes the position vector expressed in suitable local coordinates, i.e. coordinates on the solid-liquid interface. By means of generalizing the

classic treatment of the bound surface charge densities on spherical particles proposed by Schwarz (1962) and Schurr (1964), the perturbations of the counter-ion surface charge density in the Stern layer is controlled by

$$i\omega\delta\Sigma_S(\mathbf{r}_S,\omega) = \nabla_S\left[D_S\nabla_S\delta\Sigma_S(\mathbf{r}_S,\omega) + \mu_S\Sigma_S^{(0)}\nabla_S\delta U_S(\mathbf{r}_S,\omega)\right] + \mathcal{O}(E_0^2), \tag{6.11}$$

where ∇_S is the surface Laplacian operating on functions defined on the solid-liquid interface (Laplace-Beltrami operator), μ_S the mobility, D_S the diffusion coefficient, and δU_S the perturbation potential in the Stern layer. Note that equation (6.11) is the surface equivalent of equation (6.8) describing diffusion and electro-migration surface flux densities within the Stern layer. Only the third term on the right hand side of equation (6.8) has no equivalent because the constant potential results in a vanishing tangential electric field $-\nabla_S U_S^{(0)}$. For spherical particles of radius a centered at the origin of the spherical coordinates system (r,θ,ϕ) and an external excitation parallel to the polar axis $\theta = 0$, equation (6.11) takes the well-known form (e.g. Schurr, 1964; Schwarz, 1962)

$$i\omega\delta\Sigma_S(\theta,\omega) = \frac{1}{a^2\sin\theta}\frac{\partial}{\partial\theta}\left[D_S\sin\theta\frac{\partial}{\partial\theta}\delta\Sigma_S(\theta,\omega) + \mu_S\Sigma_S^{(0)}\sin\theta\frac{\partial}{\partial\theta}\delta U_S(\theta,\omega)\right]. \tag{6.12}$$

There is no particular surface equivalent of Poisson's equation (6.9). Instead the continuity of the electric potential at the solid surface (in conjunction with the vanishing thickness of the Stern layer) directly couples δU_S and the surface density $\delta\Sigma_S$ to the adjacent perturbation potentials in solid phase and electrolyte.

Solid dielectric

The solid phase of the porous medium is represented by a dielectric material with relative permittivity ε_i and vanishing electrical conductivity. The spatial and temporal variation of the potential within the solid phase are therefore governed by the Laplace equation $\nabla^2 U_i(\mathbf{r},t) = 0$.
In the equilibrium state, the static electric potential $U_i^{(0)}$ must be equal to the constant ζ-potential at any point of the surface. Under this condition, $U_i^{(0)}$ becomes constant throughout the entire volume of the solid phase.
Upon excitation by the weak external field, the Fourier-transformed frequency-dependent Laplace equation writes

$$\nabla^2\delta U_i(\mathbf{r},\omega) = 0, \tag{6.13}$$

which in conjunction with the spatially varying surface potential $\delta U_S(\mathbf{r}_S,\omega)$ determines the perturbation potential $\delta U_i(\mathbf{r},\omega)$ within the solid phase.

6.2.3 Boundary conditions

At far distances d from the solid-liquid interface, the static background potential in the electrolyte solution should approach zero, i.e.

$$U_a^{(0)} \xrightarrow[d\to\infty]{} 0. \tag{6.14}$$

At the solid surface, we can either use a given ζ-potential to set the Dirichlet boundary condition

$$U_a^{(0)}\Big|_{\text{surface}} = \zeta. \tag{6.15}$$

Or we take advantage of our knowledge of the constant potential $U_i^{(0)}$ inside of the solid (see above) and use the continuity of the displacement current to define the Neumann boundary condition

$$-\varepsilon_0\varepsilon_a \nabla U_a^{(0)}\Big|_{\text{surface}} \cdot \mathbf{n} = \Sigma + \Sigma_S^{(0)}, \tag{6.16}$$

where $\mathbf{n}$ denotes the unit normal vector to the solid surface (pointing out of the solid into the electrolyte) and $\Sigma + \Sigma_S^{(0)} = -\Sigma_d^{(0)}$ the net surface charge at the solid-liquid interface. The boundary conditions on the equilibrium ion concentrations $C_\pm^{(0)}$ are implicit to equation (6.6).
For the frequency-dependent solution, we demand that the perturbation potential at far distances d from the surface be equal to values corresponding to the external electrical field, i.e.

$$\delta U_a(\mathbf{r},\omega) \xrightarrow[d\to\infty]{} -\mathbf{E}_{\text{ext}}(\mathbf{r}) \cdot \mathbf{r}, \tag{6.17}$$

while the ion concentrations should approach their values in the bulk electrolyte, i.e. the perturbation concentrations should vanish

$$\delta C_\pm(\mathbf{r},\omega) \xrightarrow[d\to\infty]{} 0. \tag{6.18}$$

Finally, at the surface of the solid, the solutions for the three domains of the model – electrolyte solution, Stern layer, and dielectric solid – are pieced together. The continuity of the electric potential demands the three perturbation potentials to be equal at any point $\mathbf{r}_S$ along the solid-liquid interface, i.e.

$$\delta U_i(\mathbf{r}_S,\omega) = \delta U_S(\mathbf{r}_S,\omega) = \delta U_a(\mathbf{r}_S,\omega). \tag{6.19}$$

We will assume that on the time-scales of interest, ions of the solution do not engage in reactions at the solid surface, thus they are neither produced nor

consumed and the normal fluxes of both ion species through the surface must be zero, i.e.

$$\left\{ -D\nabla\delta C_{\pm}(\mathbf{r},\omega) \right.$$
$$\left. -\mu z_{\pm}\left[C_{\pm}^{(0)}(\mathbf{r},\omega)\nabla\delta U_a(\mathbf{r},\omega)+\delta C_{\pm}(\mathbf{r},\omega)\nabla U_a^{(0)}(\mathbf{r},\omega)\right]\right\}\Big|_{\mathbf{r}=\mathbf{r}_S}\cdot\mathbf{n}=0. \quad (6.20)$$

The continuity of the displacement current implies that (e.g. Schwarz, 1962)

$$\left[-\varepsilon_0\varepsilon_a\nabla\delta U_a(\mathbf{r},\omega)+\varepsilon_0\varepsilon_i\nabla\delta U_i(\mathbf{r},\omega)\right]\Big|_{\mathbf{r}=\mathbf{r}_S}\cdot\mathbf{n}=\delta\Sigma_S(\mathbf{r}_S), \quad (6.21)$$

which completes the set of boundary conditions for the frequency-dependent system.

6.3 Polarization of spherical grains

The frequency-dependent system set up in the previous section describes both the charge polarization of the Stern layer and the concentration polarization produced by the unequal contributions of anions and cations to the electric conductivity within the diffuse layer. In this section, we will study the relative contributions of the two polarization mechanisms to the macroscopic response of dilute suspensions of dielectric spheres for varying charge densities in both layers. Because even for spherical particle geometries no analytical solution of the fully-coupled problem is known, we first obtain a suitable analytical approximation of the coupled polarization process, which combines (i) the Stern-layer polarization model by Schwarz (1962) including the correction of the corresponding relaxation time proposed by Lyklema et al. (1983) and (ii) the diffuse-layer polarization model developed by Dukhin and Shilov (1974). In order to assess the quality of our analytical model and open the possibility to model the polarization response of more complex geometrical configurations, we also present a numerical finite-element solution of the problem.

6.3.1 Analytical model

At distances sufficiently far from a single spherical particle of radius a centered at the origin of a spherical coordinate system $\mathbf{r}=(r,\theta,\phi)$, all approximate analytical solutions of the present polarization problem take the form (e.g. Maxwell,

1892; Wagner, 1914; Schurr, 1964; Dukhin and Shilov, 1974)

$$\delta U_a(\mathbf{r},\omega) = E_0\left[-r + \frac{f(\omega)a^3}{r^2}\right]\cos\theta. \tag{6.22}$$

Here, we assumed that the external excitation is parallel to the polar axis, i.e. $\theta = 0$. The first term of this expression accounts for the potential due to the external field and the second term describes the effective long-range dipole moment due to the polarization of the spherical particle. The frequency-dependent reflection coefficient f contains the full information on the macroscopic polarization response of the particle. If only Maxwell-Wagner polarization is to be taken into account, it writes

$$f(\omega) = \frac{\sigma_i^*(\omega) - \sigma_a^*(\omega)}{2\sigma_a^*(\omega) + \sigma_a^*(\omega)}, \tag{6.23}$$

where $\sigma_a^*(\omega) = \sigma_a + i\omega\varepsilon_0\varepsilon_a$ and $\sigma_i^*(\omega) = i\omega\varepsilon_0\varepsilon_i$ are the complex conductivities of the bulk electrolyte and the particle, respectively. The term $\sigma_a = 2e\mu C_\pm^\infty$ denotes the direct-current (DC) conductivity of the electrolyte and the solid phase is assumed to be non-conducting.

With $f(\omega)$ for one spherical particle at hand, the effective complex conductivity $\sigma^*(\omega)$ of a (dilute) suspension of a number of equal particles can be obtained using a generalized form of the theory by Wagner (1914)

$$\frac{\sigma^*(\omega)}{\sigma_a^*} = \frac{1 + 2\nu f(\omega)}{1 - \nu f(\omega)}, \tag{6.24}$$

where ν denotes the volume fraction of suspended particles. For higher particle concentrations, the mixing formulae developed by Bruggeman (1935) and Hanai (1960) are more appropriate.

Together with the definitions of the complex conductivities σ_a^* and σ_i^*, equations (6.23) and (6.24) describe the pure Maxwell-Wagner polarization of suspensions of dielectric particles in a medium with homogeneous complex conductivity $\sigma_a^*(\omega)$. In particular, they do not account for heterogeneities in the conductivity of the medium due to local field-induced variations of the ion concentrations (e.g. Garcia et al., 1985) around the particles; nor do they include the effect of a surface charge located at the geometrical boundary between the two phases.

In his treatment, O'Konski (1960) improved this model by including the effect of an uniform surface charge density Σ_x corresponding to charge carriers, which can move freely along the particle surface. He found that the effect of this

surface conductivity can be taken into account by simply adding the effective conductivity increment $\sigma_x = 2\mu_x\Sigma_x/a$ to the complex conductivity σ_i^* of the particle.
The thicknesses of both parts of the electric double layer are typically much smaller than the particle radius, i.e. $\kappa a \ll 1$. Therefore it is useful for the treatment of the interfacial polarization effects related to the different parts of the electric double layer to define effective conductivity increments for the counter-ions in the Stern layer, the counter-, and the co-ions in the diffuse layer separately. In this manner, the effective conductivity of the diffuse layer can be expressed as

$$\sigma_d = |\sigma_{d+} + \sigma_{d-}| = \frac{2\mu|\Sigma_{d+}^{(0)} - \Sigma_{d-}^{(0)}|}{a}, \tag{6.25}$$

where the contributions of the two types of ions to the effective conductivity of the diffuse layer are defined as

$$\sigma_{d\pm} = \frac{\pm 2\mu\Sigma_{d\pm}^{(0)}}{a}. \tag{6.26}$$

For sufficiently thin diffuse layers, i.e. $\kappa a \ll 1$, the equivalent surface charge densities in the diffuse layer can be related to the surface charge using a variation of Bikerman's equation for the surface conductivity near a (highly) charged plane surface (e.g. Shilov et al., 2001)

$$\Sigma_{d\pm}^{(0)} = \pm\frac{2eC_{\pm}^{\infty}}{\kappa}\left[\exp\left(\mp\frac{e\zeta}{2kT}\right) - 1\right]. \tag{6.27}$$

Note that while the total charge stored in the diffuse layer is represented by the sum of both contributions, i.e. $\Sigma_d^{(0)} = \Sigma_{d+}^{(0)} + \Sigma_{d-}^{(0)}$, the total surface conductivity of the diffuse layer σ_d is proportional to their difference. For a given surface charge density $\Sigma_d^{(0)}$, the ζ-potential can be obtained from

$$\zeta(\Sigma_d^{(0)}) = -\frac{2kT}{e}\sinh^{-1}\left(\Sigma_d^{(0)}\frac{\kappa}{4eC_{\pm}^{\infty}}\right). \tag{6.28}$$

This relation can readily be obtained from equation (6.27). Resolved for $\Sigma_d^{(0)}(\zeta)$, it is also known as Grahame equation (Grahame, 1947).
The surface charge density related to the counter-ions located in the Stern layer can also be expressed in terms of the effective conductivity

$$\sigma_S = \frac{2\mu_S|\Sigma_S^{(0)}|}{a}. \tag{6.29}$$

In the present study, the partition of counter-ions into diffuse layer and Stern layer will be expressed in terms of the ratio $p = -\Sigma_S^{(0)}/\Sigma$. Note that this definition is slightly different from the partition coefficient f_Q introduced by Leroy and Revil (2004) as the ratio $\Sigma_S^{(0)}/(\Sigma_{d+}^{(0)} + \Sigma_S^{(0)})$.

Stern-layer polarization

In the thin double layer limit, i.e. $\kappa a \ll 1$, and if the entire surface charge Σ is screened by an equal amount of counter-charges in the Stern layer, i.e. $p = 1$ and $\Sigma_d^{(0)}, \zeta = 0$, the solution of the polarization problem can be approximated as done by Schwarz (1962). In terms of the frequency-dependent reflection coefficient f, the final result obtained by Schwarz (1962) can be expressed as [from his equation (13)]

$$f_S(\omega) = \frac{\sigma_S^*(\omega) - \sigma_a^*(\omega)}{2\sigma_a^*(\omega) + \sigma_S^*(\omega)}, \tag{6.30}$$

where σ_S^* is the effective complex conductivity of the spherical particle, which writes (from Schwarz, 1962, eq. 14 and 16)

$$\sigma_S^*(\omega) = \sigma_S \frac{i\omega\tau_S}{1 + i\omega\tau_S} + i\omega\varepsilon_0\varepsilon_i. \tag{6.31}$$

Note that we assumed a non-conducting particle, i.e. $\sigma_i = 0$. The relaxation of the Stern-layer polarization τ_S can be expressed as (Lyklema et al., 1983, eq. 36)

$$\tau_S = \frac{a^2}{2D_S M}, \tag{6.32}$$

where the coefficient M defined as (Lyklema et al., 1983, eq. 34)

$$M = 1 + \frac{\kappa\Sigma_S^{(0)}}{2eC_\pm^\infty \cosh[e\zeta/(2kT)]} \tag{6.33}$$

accounts for the coupling of the electrolyte to the charges in the Stern layer, which had not been considered in the original model by Schwarz (1962). Because $\zeta = 0$, in this hypothetical case no diffuse layer builds up in the electrolyte and the polarization response is only due to the polarization of the Stern layer, first term in equation (6.31), and the simple Maxwell-Wagner polarization accounted for by the second term.

Diffuse-layer polarization

In the opposite case, i.e. if $p = 0$, the entire counter-charge is located in the diffuse layer. This case of a pure diffuse-layer polarization has been treated by Dukhin and Shilov (1974) and resulted in a theory for the low-frequency polarization response of dielectric spheres covered by a thin diffuse layer. If electro-osmotic effects are neglected, i.e. in the limit of an infinitely large fluid viscosity, the result of the classic Dukhin-Shilov theory can be expressed in terms of the frequency-dependent refection coefficient (e.g. Grosse and Shilov, 1996; Shilov et al., 2001)

$$f_d(\omega) = \frac{2Du(\zeta) - 1}{2Du(\zeta) + 2} - \frac{3S}{2} \frac{(\sigma_{d+} - \sigma_{d-})^2}{\sigma_a^2 [2Du(\zeta) + 2]^2} \left[1 - \frac{i\omega\tau_\alpha}{1 + \sqrt{i\omega 2\tau_\alpha / S} + i\omega\tau_\alpha} \right], \tag{6.34}$$

where $Du(\zeta) = \sigma_d/(2\sigma_a)$ is the Dukhin number, which sets the surface conductivity of the diffuse layer into a relation with the bulk conductivity of the electrolyte solution. The coefficient S, which appears in the expression for f_d, writes

$$S = \frac{[Du(\zeta) + 1]\,\sigma_a^2}{(\sigma_{d+} + \sigma_a)(\sigma_{d-} + \sigma_a)} \tag{6.35}$$

and the time constant is defined as $\tau_\alpha = a^2 S/(2D)$. The effective conductivity of the suspension can then be obtained from equation (6.24) by substituting f by f_d. Note that this formulation only accounts for the polarization of the diffuse layer. An extension, which also includes the contribution of the Maxwell-Wagner polarization can be found in Shilov et al. (2001).

Coupled polarization

For any value of $0 < p < 1$, the counter charges are distributed over Stern and diffuse layer, which leads to a simultaneous polarization of both parts of the electric double layer. As argued by Lesmes and Morgan (2001), this coupled polarization can be approximated by a simple superposition of the individual responses realized by a simple addition of the effective complex dielectric constants (or the corresponding effective complex conductivity increments) of the particle. In order to obtain an adequate description of the diffuse-layer polarization, we can rearrange equation (6.23) and solve for the effective conductivity of the particle, which gives

$$\sigma_d^*(\omega) = \sigma_a^*(\omega) \frac{1 + 2f_d(\omega)}{1 - f_d(\omega)}. \tag{6.36}$$

The effective conductivity σ_S^*, which accounts for Stern-layer and Maxwell-Wagner polarization, is given by equations (6.31) through (6.33) and the total effective conductivity of the particle including all three mechanisms writes

$$\sigma_c^*(\omega) = \sigma_d^*(\omega) + \sigma_S^*(\omega) = \sigma_d^*(\omega) + \sigma_S \frac{i\omega\tau_S}{1 + i\omega\tau_S} + i\omega\varepsilon_0\varepsilon_i. \tag{6.37}$$

Note that this expression is almost the same result as the one obtained by Schurr (1964) except for the decrease of τ_S by the factor M and the substitution of σ_d by $\sigma_d^*(\omega)$, i.e. the frequency-independent contribution of the diffuse layer is replaced by the adequate frequency-dependent one defined by equations (6.34) through (6.36).
Our model is also similar to the model proposed by Lesmes and Morgan (2001), from which it differs with regard to (1) the relaxation time of the Stern layer τ_S, where we use the correction by Lyklema et al. (1983), (2) the constant contribution σ_S of the Stern layer (their equations 5 and 6), which we do not consider; and (2) the selection of the model describing the diffuse-layer polarization, where we use the Dukhin-Shilov theory instead of the model by Fixman (1980). Based on our analysis of Fixman's solution and the direct comparison to the Dukhin-Shilov solution, Fixman's assumption that the co-ion contribution to the surface conductivity can be ignored for sufficiently high ζ-potentials does not hold for the range of ζ-potentials studied here. This oversimplification was found to largely affect the real part of the complex conductivity, while the imaginary part of Fixmann's solution is almost identical to the Dukhin-Shilov solution (not shown here for brevity).

6.3.2 Numerical model

Figure 6.2 shows the geometrical set-up with the dielectric particle of radius a centered at the origin of coordinates. The external electric field is imposed in x-direction, i.e. $\mathbf{E}_{\text{ext}} = E_0\mathbf{e}_x$, where $\mathbf{e}_x$ denotes the unit vector in x-direction. Due to the cylindrical symmetry of the problem, the numerical simulation only needs to be carried out on the two-dimensional model domain in Carthesian coordinates $\mathbf{r} = (x, y)$ marked in red in Figure 6.2.
We use the finite-element software package COMSOL Multiphysics to successively obtain the static and the frequency-dependent solution. We first solve the Poisson-Boltzmann equation (6.7), which contains $U^{(0)}(\mathbf{r})$ as only unknown variable. The analytical boundary conditions, equations (6.14) and (6.16), are translated into the following boundary conditions for the numerical solution:

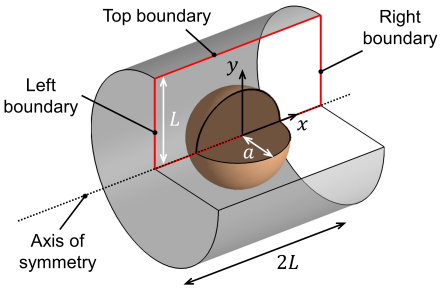

Figure 6.2: Three-dimensional sketch of the geometrical set-up used for the numerical simulation of the polarization phenomena around spherical particles. The particle of radius a is enclosed by a cylinder of radius L and height $2L$, which represents the electrolyte solution. The red rectangle marks the actual two-dimensional model domain.

$U^{(0)} = 0$ on the left, right, and top boundary; $[\varepsilon_0\varepsilon_i\nabla U_i^{(0)} - \varepsilon_0\varepsilon_a\nabla U_a^{(0)}]\mathbf{n} = -\Sigma_d^{(0)}$ on the particle surface; and $\partial U(0)/\partial_y = 0$ on the axis of symmetry. The static background ion concentrations in the electrolyte solution, are computed by inserting $U_a^{(0)}$ into equation (6.6).

Subsequently, we solve the frequency-dependent part of the problem described by the partial differential equations (6.8), (6.9), (6.11), and (6.13) and the boundary conditions (6.17) through (6.21). For the numerical solution, the latter are adjusted as follows: $\delta n_\pm = 0$ and $\delta U_a = \pm E_0 L$ on the left and right boundary, respectively; $\mathbf{J}_\pm = 0$ and $\partial\delta U/\partial_y = 0$ on top boundary and on the axis of symmetry; unchanged on the particle surface. While the static solution only needs to be computed once for each set of model parameters (i.e. a, Σ, p, etc.), the frequency-dependent problem has to be solved for each value of the angular frequency ω separately. For technical details on the implementation of both static and frequency-dependent model, see appendix 6.A.

Special care has to be taken with the discretization of the modelling domain. While particle sizes are in the micro- to millimeter range, the thickness of the diffuse layer is orders of magnitude smaller. In order to resolve this thin layer, we discretizise electrolyte and solid phase next to the solid-liquid interface with a special boundary-layer mesh consisting of rectangular elements with a size of $\pi a/400$ along the boundary (tangential direction). In radial direction the boundary-layer mesh is much finer and consists of a fixed number of 8 elements with sizes increasing from $\lambda_D/2$ at the surface to $\approx 1.8\lambda_D$ at the outer limit

of the boundary layer. The remaining volumes of solid and electrolyte solution are filled with triangular elements, the maximum sizes of which increase from $\lambda_D/2$ at the outer limit of the boundary-layer meshes to $L/20$ at the remote boundaries. For a particle size of $a = 5$ μm, the resulting mesh consist of $\approx$ 20900 elements, of which 6400 elements corresponds to the boundary-layer mesh.

Because bulk values are implicitly assumed on the left, right, and top boundary, the domain boundaries must be placed sufficiently far away from the particle surface, where the polarization phenomena are expected to take place. As a trade-off between precision and computational cost, we define a standard domain size of $L = 4a$.

The effective conductivity of the modelled volume can be obtained from the numerical integration of the total ion flux densities through the left (or likewise the right) boundary, i.e.

$$\sigma^*_{\mathrm{mod}} = \frac{2}{E_0 L^2} \int_0^L \left[\mathbf{J}_+(y) + \mathbf{J}_-(y)\right] \mathbf{e}_x y dy, \tag{6.38}$$

where the term ydy accounts for the area element of the boundary and the factor $2/L^2$ stems from the normalization with the total area.

As mentioned above, the standard domain size is $L = 4a$, which corresponds to a rather small volume fraction of the dielectric particles ($\nu_{\mathrm{mod}} \approx 0.01$). Therefore, we scale the modelled effective conductivities $\sigma^*_{\mathrm{mod}}(\omega)$ to the more realistic volumetric content of $\nu = 0.4$ using the mixing rule defined in equation 6.24 with

$$f(\omega) = \frac{1}{\nu_{\mathrm{mod}}} \frac{\sigma^*_{\mathrm{mod}}(\omega) - \sigma^*_a(\omega)}{\sigma^*_{\mathrm{mod}}(\omega) + 2\sigma^*_a(\omega)}. \tag{6.39}$$

6.3.3 Comparison of analytical and numerical solution

Unless otherwise stated, the parameter values listed in Table 6.1 are used to obtain both numerical and analytical results. The relative permittivity of $\varepsilon_i = 4.5$ is a typical value for quartz sand (e.g. Robinson and Friedman, 2003). The uniform ion mobility of $\mu = 5 \cdot 10^{-8}$ m^2/(Vs) is approximately equal to the mobility of the sodium cation (e.g. Atkins and De Paula, 2013) and will be used for both ion species in the electrolyte solution. The mobility of the counter-ions in the Stern layer is assumed to be reduced to 10% of the ion mobility in the bulk electrolyte, i.e. $\mu_S = \mu/10$. This value corresponds to the reduction of the cation mobility in the Stern layer inferred for K^+ on latex surfaces by Zukoski and Saville (1986) and for Na^+ on clay surfaces by Revil and Glover (1998). For

Table 6.1: Model parameter values used to model the complex-conductivity spectra unless specified otherwise.

Parameter (unit)	Symbol	Value
Absolute temperature (K)	T	293
Relative permittivity of the fluid (-)	ε_a	80
Relative permittivity of the solid (-)	ε_i	4.5
Bulk ion concentrations ($1/m^3$)	$C_{\pm}^{\infty}$	1 mol
Ion mobility in electrolyte [$m^2/(Vs)$]	μ	$5 \cdot 10^{-8}$
Ion mobility in Stern layer [$m^2/(Vs)$]	μ_S	$5 \cdot 10^{-9}$
Surface charge density (C/m^2)	Σ	-0.01
Volumetric content of solid particles (-)	ν	0.4

near-neutral pH of the solution and ion concentrations in the bulk electrolyte of $C_{\pm}^{\infty} = 1$ mol/m^3, it is adequate to assume a surface charge density of $\Sigma = -0.01$ C/m^3 (e.g. Kosmulski, 2006).

Figure 6.3 displays the conductivity spectra of a suspension of spherical particles of radius $a = 10$ μm for six different values of p between 0 and 1. The complex-valued effective conductivities of the mixture σ^* are expressed in terms of the corresponding real (σ') and imaginary (σ'') parts. In the upper panel, we observe a continuous decrease of σ' with increasing p. The contribution of the counter-ions to the surface conductivity is much more efficient for those located in the diffuse layer than for those in the Stern layer. On the one hand this is due to the significantly reduced mobility of the counter-ions in the Stern layer, which affects all frequencies equally. On the other hand, at low frequencies, the Stern-layer is completely polarized and does not at all contribute to the DC conductivity because we assume that it cannot exchange ions with the bulk electrolyte. At frequencies beyond the characteristic frequency of the Stern-layer polarization, however, the Stern layer does contribute to the high-frequency limit of σ'. The higher p and thus $\Sigma_S^{(0)}$ and the surface conductivity σ_S of this layer, the larger becomes the difference between high- and low-frequency limits of σ', which is largest in the case of a pure Stern-layer polarization ($p = 1$). In contrast, in the case of a sole diffuse-layer polarization ($p = 0$), we hardly recognize any variation of σ' with the angular frequency.

The variation of the frequency dispersion of σ' with p (top panel in Figure 6.3) is also reflected by the peak imaginary conductivity σ'' (bottom panel in Figure 6.3), which increases almost linearly with p and thus the charge density in

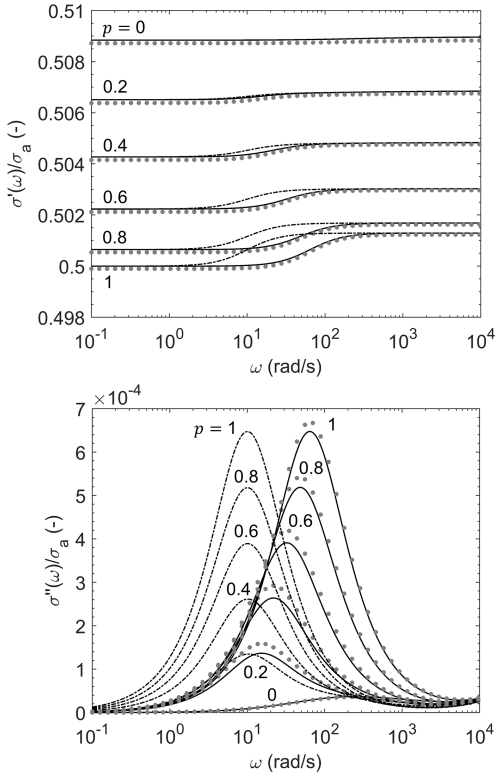

Figure 6.3: Complex-conductivity spectra of a suspension of dielectric particles of radius $a = 5$ μm with surface charge density $\Sigma = -0.01$ C/m^2 at different ratios $p = -\Sigma_S^{(0)}/\Sigma$. Complex-valued conductivties in terms of real (top) and imaginary parts (bottom) normalized to the bulk conductivity σ_a. Numeric results (grey circles) are displayed along with the corresponding analytical models according to equation (6.37) using the simple relaxation time after Schwarz (1962) ($M = 1$, dash-dotted line) and using the corrected relaxation time after Lyklema et al. (1983) ($M \neq 1$, dash-dottend line). All other parameter values as listed in Table 6.1.

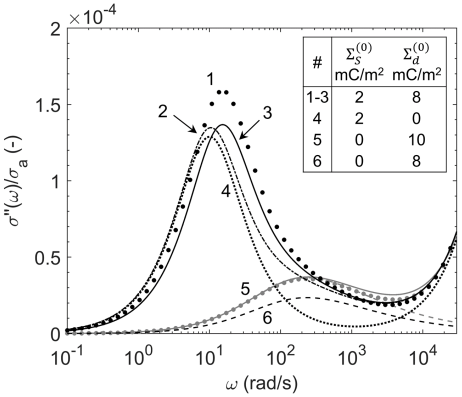

Figure 6.4: Numeric (grey circles) and analytical (lines) imaginary conductivity spectra for small surface charge densities $\Sigma_S^{(0)}$ in the Stern layer. Curve 1 coupled polarization numerical; curves 2 and 3 coupled polarization using $M = 1$ and $M \neq 1$, respectively; curve 4 Stern-layer polarization only using $M = 1$; curves 5 and 6 diffuse-layer polarization only. Analytic curves calculated from the new analytical model defined in equation (6.37), using the values of $\Sigma_S^{(0)}$ and $\Sigma_d^{(0)}$ given in this Figure. All other parameter values as listed in Table 6.1.

the Stern layer. For the same surface charge densities, the Stern-layer polarization ($p = 1$) σ'' results in a maximum of σ'', which is approximately an order of magnitude larger than the one produced by the corresponding diffuse-layer polarization ($p = 0$). From Figure 6.4, which shows a close-up of the small imaginary conductivities generated in the case of (almost) pure diffuse-layer polarization, it is evident that even a relatively small fraction of 20% of the positive charge located in the Stern-layer still produces a much stronger response than the other 80% (and even 100%) located in the diffuse layer. It is worth mentioning that the polarization magnitude (here in terms of the maximum of σ'') largely varies with the mobility of the counter-ions in the Stern layer. In a separate analysis, we observed a difference between the magnitudes of the two polarization processes of two orders of magnitude when a larger mobility of $\mu_S = \mu/2$ was assumed (not shown here for brevity). This observation is in good agreement with the results obtained earlier by Lesmes and Morgan (2001) and confirms their conclusion that the Stern-layer polarization produces a much stronger frequency dispersion than the diffuse-layer polarization.

For sufficiently small values of p, Figure 6.4 also shows that the contribution of the diffuse-layer polarization produces slight increases of polarization magnitude and characteristic angular frequency (curves 1 and 3) as compared to the pure Stern-layer polarization (curve 4). The latter is related to the higher characteristic frequency of the diffuse-layer relaxation as a consequence of the shorter relaxation time, here $\tau_\alpha \approx \tau_S/2$ because $S \approx 1$.

The comparison of analytical and numerical curves in Figures 6.3 and 6.4 also serves as cross-validation of our finite-difference implementation and our new analytical approximation for the coupled polarization response. For angular frequencies between 0.1 and 10^4 mrad/s, the relative deviation between the analytical and numerical results is $< 0.3\%$ in the real part but reaches almost 20% in the imaginary part of the effective conductivity. Here the analytical approximation clearly underestimates the polarization magnitude. A good agreement, however, is observed between the characteristic frequencies, i.e. the angular frequency at which the σ'' peaks are observed. Apart from the underestimated polarization magnitude, the good agreement between numerical and analytical curves confirms the approach to model the coupled polarization process by a simple superposition of the individual responses of Stern and diffuse layer.

6.4 Membrane polarization

In this section, we will study the polarization response of ion-selective pore constrictions better known as membrane polarization. For this purpose, we represent the pore space of a porous medium by an alternating series of wide and narrow cylinders. The solid-liquid interfaces – in this geometric setup the cylinder walls – are negatively charged and covered by an EDL consisting of a Stern and a diffuse layer. As in the case of the polarization of spherical grains discussed in the previous section, both parts of the EDL contribute to the macroscopic polarization response of the system. In order to assess their relative contributions, effective-conductivity spectra are computed for varying charge densities in the two layers. After a minor adjustment, the analytical membrane polarization model proposed by Bücker and Hördt (2013a) satisfactorily predicts the response due to the polarization of the diffuse layer on the highly charged cylinder walls. No analytical models exist for the contribution of the Stern-layer polarization in this geometric set up. Therefore, to study the combined polarization response of Stern and diffuse layer, we make use of the numerical finite-element solution developed and validated in the previous section.

6.4.1 Analytical model for diffuse-layer polarization

The membrane-polarization model by Bücker and Hördt (2013a) considers an alternating sequence of wide and narrow pores, which are characterized by their respective pore radii R_i and lengths L_i (see Figure 6.5). The subindex 1 denotes properties of the wide pore and the subindex 2 those of the narrow pore. A non-zero ζ-potential at the cylinder walls causes diffuse layers to build up along the circumferences of the pores. Upon excitation by the external electrical field (along the symmetry axis), the electric current will be controlled by the mean ion concentrations. Therefore, Bücker and Hördt (2013a) average the ion concentrations over the pore cross sections as follows:

$$b_{\pm,i} = \frac{2\pi}{C^{\infty}_{\pm} A_1} \int_0^{R_i} r C^{(0)}_{\pm,i}(r) dr \tag{6.40}$$

Note that these mean ion concentrations are normalized by the bulk ion concentration $C^{\infty}_{\pm}$ and the area of the wide pore $A_1 = \pi R_1^2$. The latter accounts for the reduction of the total current through the narrow pore due to the smaller cross section (see Bücker and Hördt, 2013a).
For sufficiently small ζ-potentials, i.e. $\zeta \ll kT/e$, the radial variation of the electric potential in the pore can be approximated by solving the linearized

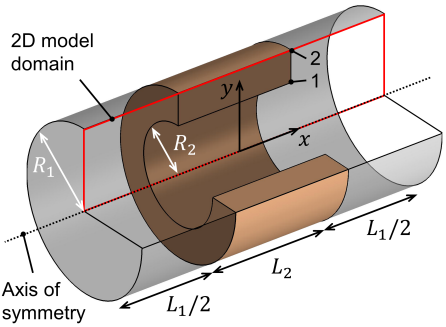

Figure 6.5: Three-dimensional sketch of the geometrical set-up used for the numerical simulation of membrane polarization phenomena related to pore constrictions. The basic model consists of two wide cylinders of length $L_1/2$ and radius R_1 and one narrow cylinder of length L_2 and radius R_2. All three cylinders are saturated with electrolyte solution. The annular volume, which encloses the narrow pore, is assumed to be a solid dielectric with dielectric constant ε_i. The red rectangle marks the actual two-dimensional model domain.

Poisson-Boltzmann equation in cylindrical coordinates, which gives (Hunter, 1981; Bücker and Hördt, 2013a)

$$U_a^{(0)}(r) = \zeta \frac{J_0(i\kappa r)}{J_0(i\kappa R)}, \tag{6.41}$$

where J_0 is the Bessel function of the first kind and order zero. The radial variation of the ion concentrations $C_{\pm,i}^{(0)}(r)$ needed to compute the mean ion concentrations $b_{\pm,i}$ can be obtained by inserting $U_a^{(0)}(r)$ into equation (6.6).
For the often much higher ζ-potential values of up to -100 mV related to typical surface charges on silica surfaces (here $\Sigma = -0.01$ C/m^2), the solution of the linearized Poisson-Boltzmann equation becomes imprecise. If we instead limit our treatment to sufficiently wide pore radii, i.e. $\kappa R_i \gg 1$, we can make use of Bikerman's equation (6.27), which is more adequate for highly charged surfaces. In this case, the dimensionless mean ion concentrations can be approximated by

$$b_{\pm,i} \approx \frac{A_i}{A_1} \left(\frac{\pm 2\Sigma_{d\pm}^{(0)}}{eC_{\pm}^{\infty} R_i} + 1 \right). \tag{6.42}$$

Either of these definitions of $b_{\pm,i}$, i.e. equation (6.40) or (6.42), can then be

used to express the effective transference numbers

$$t_{\pm,1} = \frac{b_{\pm,i}}{b_{+,i} + b_{-,i}} \tag{6.43}$$

of the two types of pores. By means of this approximation, the three-dimensional cylindrical pore system from Figure 6.5 can be collapsed to a simple sequence of one-dimensional pores, the frequency-dependent impedance of which can be looked up in the study by Marshall and Madden (1959). According to Bücker and Hördt (2013b) and Bücker et al. (2017), the Marshall-Madden impedance can be written as

$$Z(\omega) = \frac{2}{\sigma_a}\left[\frac{L_1}{b_{+,1} + b_{-,1}} + \frac{L_2}{b_{+,2} + b_{-,2}} + \frac{8D\left(t_{+,1} - t_{+,2}\right)^2}{\frac{L_1}{\tau_1}\sqrt{i\omega\tau_1}\coth\sqrt{i\omega\tau_1} + \frac{L_2}{\tau_2}\sqrt{i\omega\tau_2}\coth\sqrt{i\omega\tau_2}}\right], \tag{6.44}$$

where the frequency dependence is controlled by the two time constants

$$\tau_i = \frac{L_i^2}{2D} S_i \quad \text{with} \quad S_i = \frac{1}{4 b_{+,i} t_{-,i}}. \tag{6.45}$$

In order to stress the structural similarities between these two relaxation times and the relaxation time of the diffuse layer around spherical grains, we can rewrite the dimensionless mean ion concentrations $b_{\pm,i}$ defined in equation (6.42) in terms of a Dukhin number for cylindrical geometries, which we define as

$$Du(\zeta, R_i) = \frac{\sigma_d(R_i)}{2\sigma_a} = \frac{|\sigma_{d+}(R_i) + \sigma_{d-}(R_i)|}{2\sigma_a}. \tag{6.46}$$

Here, in analogy to equation (6.26), the surface conductivities write $\sigma_{d\pm}(R_i) = \pm 2\mu\Sigma^{(0)}_{d\pm}/R_i$. The coefficients S_i take the form

$$S_i = \frac{A_1}{2A_i}\frac{[2Du(\zeta, R_i) + 1]\sigma_a^2}{[2\sigma_{d+}(R_i) + 1][2\sigma_{d-}(R_i) + 1]}. \tag{6.47}$$

Besides the factor $A_1/(2A_i)$ and the factor 2, with which the Dukhin numbers and the individual conductivities $\sigma_{d\pm}$ are multiplied, this definition of S_i is equivalent to the definition of S in equation (6.35), which controls the relaxation time of the diffuse layer around a spherical particle.

6.4.2 Numerical model

The numerical modelling of the membrane polarization is carried out using the same finite-element software package as before. Again, the cylindrical symmetry of the problem permits limiting the numerical simulation to a two-dimensional model domain (shown as red rectangle in Figure 6.5). The formulation of the systems of partial differential equations describing the static and the frequency-dependent parts of the polarization problem remain unchanged and only boundary conditions and finite-element mesh need to be adapted to the new geometrical set-up.

The boundary conditions for the static solution, i.e. equations (6.14) and (6.16), merge into the following boundary conditions: $U^{(0)} = 0$ on the left and right boundary; $[\varepsilon_0\varepsilon_i\nabla U_i^{(0)} - \varepsilon_0\varepsilon_a\nabla U_a^{(0)}]\mathbf{n} = -\Sigma_d^{(0)}$ on the solid-liquid interface; and $\partial U(0)/\partial_y = 0$ on the axis of symmetry and the entire top boundary. This set-up represents an EDL, which only covers the surfaces of the brownish volume in Figure 6.5, and is thus discontinuous in the wide pore. Additionally, we compute the response of a model, where the EDL is continuous in the wide pore. In this case, the boundary condition on the corresponding parts of the top boundary writes $[-\varepsilon_0\varepsilon_a\nabla U_a^{(0)}]\mathbf{n} = -\Sigma_d^{(0)}$.

For the frequency-dependent part of the problem, the boundary conditions (6.17) through (6.21) are adjusted as follows: $\delta n_\pm = 0$ and $\delta U_a = \pm E_0 L$ on the left and right boundary, respectively; $\mathbf{J}_\pm = 0$ and $\partial\delta U/\partial_y = 0$ on the axis of symmetry and the top boundary; equations (6.19) through (6.21) remain unchanged on the solid-liquid interface. In the additional model with a continuous EDL, the boundary conditions on those parts of the top boundary, which delimit the wide pore, are given by the unchanged zero-flux condition (6.20) and the continuity of the displacement current, which here writes $-\varepsilon_0\varepsilon_a\nabla\delta U_a(\mathbf{r}_S)\cdot\mathbf{n} = \delta\Sigma_S(\mathbf{r}_S)$. For further technical details on the implementation, see appendix 6.A.

In order to accurately resolve the diffuse layers, we discretizise the electrolyte (and if present also the solid phase) next to the solid-liquid interface with a boundary-layer mesh consisting of rectangular elements with a size of $R_2/5$ along the boundary (tangential direction). Normal to the boundary, the boundary-layer mesh is much finer and consists of a fixed number of 8 elements with sizes increasing from $\lambda_D/2$ at the surface to $\approx 1.8\lambda_D$ at the outer limit of the boundary layer. The remaining volumes of electrolyte and solid are filled with triangular elements, the maximum sizes of which increase from $R_2/5$ at the outer limit of the boundary-layer meshes to $R_1/5$ at the remaining boundaries. For pore the lengths $L_1 = 90$ μm and $L_2 = 10$ μn and the pore radii $R_1 = 2$ μm

and $R_2 = 0.2$ μm, the resulting meshes consist of $\approx$ 14700 elements ($\approx$ 11000 for the continuous EDL), of which $\approx$ 5200 ($\approx$ 7600) elements corresponds to the boundary-layer mesh.
In order to avoid artifacts related to parts of the Stern layer covering sharp corners, the vertices 1 in Figure 6.5 are rounded off for the model with discontinuous EDL and the vertices 1 and 2 are rounded off for the model with continuous EDL. In both cases, the radius of the rounded vertices is $(R_1 - R_2)/2$.
Like in the case of the spherical particle, the effective conductivity of the modelled volume can be obtained from the numerical integration of the total ion flux densities through the left (or right) boundary. Adapting equation (6.38) to the geometry of the membrane-polarization model, we get

$$\sigma^*_{\mathrm{mod}} = \frac{2}{E_0 R_1^2} \int_0^{R_1} \left[\mathbf{J}_+(y) + \mathbf{J}_-(y)\right] \mathbf{e}_x y dy. \tag{6.48}$$

In the model with the continuous EDL in the wide pore, the contribution of the surface current in the Stern layer has to be considered, too. In this case, the corresponding conductivity increment $-2/(E_0 R_1)[D_S \partial\delta\Sigma_S/\partial y + \mu_S \Sigma_S \partial\delta U_S/\partial y]$ has to be added to σ^*_{mod}. The analytical expression for the effective conductivity writes $\sigma_{\mathrm{eff}}(\omega) = (L_1 + L_2)/Z(\omega)$, where $Z(\omega)$ is the one-dimensional Marshall-Madden impedance defined in equation (6.44).

6.4.3 Comparison of analytical and numerical solution

The effective conductivity spectra obtained from the model with the discontinuous EDL are shown in Figure 6.6. In the analytical models for the case $p = 0$, the absence of the EDL in the wide pore has to be taken into account by setting $b_{\pm,1} = 1$ instead of using equations (6.40) or (6.42) for the calculation of the corresponding mean ion concentrations. The length of the narrow pore $L_2 = 10$ μn was selected to match the diameter of the spherical particle modelled earlier in this study. The length of the wide pore $L_1 = 90$ μm as well as the two pore radii $R_1 = 2$ μm and $R_2 = 0.2$ μm were adjusted to achieve a significant polarization response. As discussed in more detail in Hördt et al. (2017), the magnitude of the contribution of the diffuse layer to the membrane polarization largely depends on the selection of the relation between the two ratios R_1/R_2 and L_1/L_2.
In the top panel of Figure 6.6, we observe a similar variation of the magnitude of σ' with the ratio p as obtained above for the polarization around a spherical particle. In both cases the contribution of the surface conductivity to σ' is

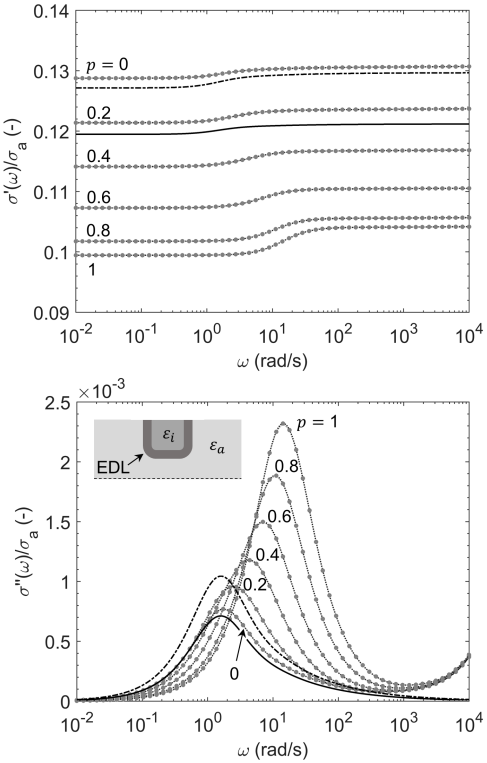

Figure 6.6: Complex-conductivity spectra of the cylindrical membrane-polarization model for different ratios $p = -\Sigma_S^{(0)}/\Sigma$. Complex-valued conductivties in terms of real (top) and imaginary parts (bottom) normalized to the bulk conductivity σ_a. Numeric results (grey circles) for all values of p are displayed along with the analytical models for $p = 0$ after Bücker and Hördt (2013a) (dash-dotted line) and using the new average ion concentrations defined in equation (6.42) (solid line). The sketch in the bottom panel shows that the EDL is discontinuous in the wide pore. Pore lengths and radii are $L_1 = 90$ μm, $L_2 = 10$ μm, $R_1 = 2$ μm, and $R_2 = 0.2$ μm; all other parameter values as in Table 6.1.

larger if the counter-charges are mainly located in the diffuse layer. At low frequencies, the Stern layer polarizes completely and does not contribute to σ' at all and at high frequencies, its contribution is limited by the significantly smaller ion mobility in the Stern layer (remember that $\mu_S = \mu/10$). Also, the variation of the imaginary part σ'' with p displayed in the bottom panel of Figure 6.6 resembles the one observed in the case of a spherical particle. Again, the σ'' peak increases with the amount of counter-charges located in the Stern layer, i.e. with increasing p, and shifts towards higher angular frequencies.

Figure 6.6 also shows that our modified membrane polarization model, i.e. the use of equation (6.42) for the computation of the mean ion concentrations, matches the numerically obtained σ'' better than the original model by Bücker and Hördt (2013a). For $p = 0$, the relative deviations between the analytical and the numerical σ'' curves are $< 20\%$ for the modified and $< 50\%$ for the original model for frequencies < 100 rad/s. Because the analytical model does not include the contribution of the Maxwell-Wagner polarization, which becomes dominant at high frequencies, the misfit increases rapidly at angular frequencies > 100 rad/s. The original membrane polarization model, however, matches the real part σ' much better. The relative deviation between the analytical models and the numerical solution are $\approx 7\%$ for the modified and $< 1\%$ for the original model.

In summary, the good qualitative match of the analytical curves with the independently validated numerical model for the case $p = 0$ confirms the validity of the model developed by Bücker and Hördt (2013a) and further improved in the present study. Bücker and Hördt (2013a) also propose a simple modification of the mean counter-ion concentration intended to take the contribution of the Stern layer into account. However, for the selected set of model parameters, the analytical model rather predicts a continuous decrease of the polarization magnitude (σ'') with increasing p and a practically constant characteristic frequency (not shown here for brevity), which indicates that the polarization mechanism in the Stern layer is more complex than assumed by this possibly over-simplified approach.

Figure 6.6 shows that the variation of the polarization response with p changes significantly, if the EDL is assumed to be continuous in the wide pore. Height and characteristic frequency of the main σ'' peak located around 2 rad/s decrease only slightly from $p = 0$ through $p = 0.4$ and increase not much steeper for larger values of p. In comparison to the significant increase of both height and characteristic frequency observed in Figure 6.6 for the discontinuous EDL,

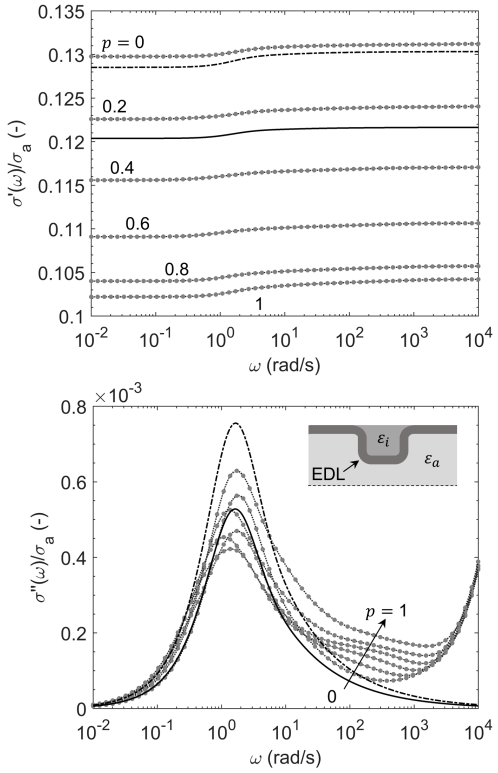

Figure 6.7: As Figure 6.6 but with a continuous EDL in the wide pore as illustrated in the sketch in the bottom panel.

here, the σ'' peak remains almost unchanged. Furthermore, at intermediate frequencies between 100 and 1000 rad/s a smaller secondary polarization peak appears for $p > 0$ and increases monotonically with the amount of counter-charge in the Stern layer. The real part σ' reflects the usual decrease of the surface conductivity with increasing p. The relative deviations between the numerical results for $p = 0$ and the two analytical models are similar to those reported for the model with the discontinuous Stern layer.

6.5 Discussion

In this study we have developed a new analytical model combining the effects of Maxwell-Wagner, Stern-layer, and diffuse-layer polarization around spherical grains, which we validated with the corresponding numerical finite-element solution of the underlying equations. Numeric and analytical results for typical model parameters consistently confirm earlier studies, which predicted a significantly smaller contribution of the diffuse-layer polarization to the macroscopic response than the one of the Stern-layer polarization (e.g. de Lima and Sharma, 1992; Lesmes and Morgan, 2001).

Although the actual polarization of the diffuse layer can therefore safely be neglected in most cases, our study confirmed the strong coupling of the varying surface charge distribution in the Stern layer with the corresponding field-induced diffuse layer in the electrolyte as predicted by Lyklema et al. (1983). Fortunately, the model proposed by Lyklema and co-workers can easily be obtained from the model by Schwarz (1962) by dividing the relaxation time τ_S by the coefficient M. For a typical charge density in the Stern layer of $\Sigma_S^{(0)} \approx 0.01$ C/m^2 and a bulk ion concentration of 1 mol/m^3, equation (6.33) predicts $M \approx 6.4$. The effect of M can also be interpreted in terms of an efficient diffusion coefficient $D_S^{\text{eff}} = D_S M$, which in our case (i.e. $D_S = D/10$) is only a factor ≈ 2 smaller than the diffusion coefficient of the ions in the bulk electrolyte.

This result is particularly interesting as it is a possible explanation of the large diffusion coefficients D_S needed to adjust the model by Leroy et al. (2008) to measured complex-conductivity spectra. The model by Leroy and co-workers does not include the correction of the relaxation time proposed in Lyklema et al. (1983), but often requires the assumption of equal or similar diffusion coefficients in Stern layer and bulk electrolyte (e.g. Leroy et al., 2008; Leroy and Revil, 2009; Revil and Florsch, 2010; Schmutz et al., 2010). Independent determinations of the diffusion coefficient in the Stern layer from experimental surface conductivity

and particle mobility data, however, normally rather predict a reduction of the counter-ion mobility by a factor 10 or more (e.g. Zukoski and Saville, 1986; Revil and Glover, 1998). Based on our findings, the difference between the predictions of the two experiments could be reduced significantly, if the Stern-layer relaxation time used in the model by Leroy and co-workers was replaced by the one defined in equations (6.32) and (6.33).

Although this correction might be able to justify the strong and to date unexplained assumption inherent to the model by Leroy et al. (2008), it also questions the often-used simple relation between relaxation time and grain size by introducing an additional dependence on chemical characteristics of pore fluid and solid surface: The coefficient M strongly depends on the electrolyte concentration and the surface charge density in the Stern layer. Consequently, besides the grain diameter and the diffusion coefficient in the Stern layer, variations of experimentally determined relaxation times might partly be due to variations of these chemical parameters.

We have also applied our finite-element model to study the membrane-polarization mechanism, which to date has not been investigated in the same detail as was done with the polarization mechanisms around spherical grains. In the limiting case of a sole diffuse-layer polarization, we found that a slightly improved analytical model based on the work by Marshall and Madden (1959) and Bücker and Hördt (2013a) described the numerical results to a great extend. However, the analytical model was not able to match our numerical results for the coupled polarization of diffuse and Stern layer. Because the general numerical implementation was previously validated for the grain geometry, this result demonstrates the limitations of the analytical membrane-polarization model and indicates that the incorporation of the Stern-layer polarization in the model by Bücker and Hördt (2013a) is insufficient in its current form. However, the numerical results obtained for the coupled model can therefore substantially contribute to our understanding of the role of the Stern layer in the context of membrane polarization.

According to our modelling results, also in the membrane-polarization geometry the Stern-layer polarization can dominate the coupled response, especially if the EDL is discontinuous. Certain similarities of the coupled membrane-polarization response with the coupled polarization response around spherical grains stand out – namely the generally larger response of the Stern-layer polarization and the simultaneous increases of characteristic frequency and magnitude of the Stern-layer polarization response with the surface charge density in the Stern layer.

However, we saw that the particular geometrical configuration of the EDL in the membrane-polarization model can largely reduce the difference between the respective magnitudes of diffuse-layer and Stern-layer polarization. For instance, if the EDL is assumed to be continuous in both pores, our results indicate that the relative contributions of both polarization mechanisms can become practically equal.

Although we have taken an important step towards this long-term goal, it is beyond the scope of this study to provide an analytical model that integrates membrane polarization and the polarization around spherical grains; neither do we apply the developed numerical modelling framework to three-dimensional models as can be obtained from computerized tomography scans of real porous media. Nevertheless, we can put our results into a broader context and draw some preliminary conclusions regarding the relative contributions of the various polarization mechanisms.

Because they only account for grain-electrolyte interactions and largely ignore grain-grain interactions, grain-based polarization models are best suited for the modelling of dilute suspensions of dielectric particles. For practical purposes and using suitable mixing laws, these models can even be applied to higher particle concentrations. In this manner, the induced-polarization responses of unconsolidated sediments or other loosely packed granular media (e.g. Leroy et al., 2008) have been matched successfully with this type of models. For typical parameter combinations, the polarization response of isolated grains is controlled by Stern-layer polarization only and contributions of a simultaneously occurring diffuse-layer polarization can be neglected.

With increasing degree of compaction and cementation of the granular medium grain-grain interactions are expected to become more important (e.g. Lesmes and Morgan, 2001). Grain-grain interactions include, but are not limited to, the interaction of the polarization dipoles of adjacent grains as well as percolating diffuse and Stern layers. As a limiting case, also the membrane-polarization mechanism can be interpreted in terms of a grain-grain interaction. Based on the above mentioned good agreement between experimental data and the responses of grain-based polarization models, the interaction of polarization dipoles can safely be neglected – even in the case of densely packed granular media.

To date, the issue of the eventual effects of percolating diffuse and Stern layers on the polarization response has only been touched in passing. Leroy et al. (2008), for instance, argue that a diffuse layer above the percolation threshold cannot polarize and therefore only consider its contribution to the DC conductivity

in their model. In the same sense, they postulate that the Stern layers of adjacent particles must be discontinuous as the model based on the polarization of this inner layer accurately describes the experimental observations. While the results of this reasoning – the vanishing contribution of the diffuse-layer polarization and the dominating role of the Stern layer – agree with the findings of the present study, the explanation given by Leroy and co-workers must be reconsidered. As we saw from the modelled polarization response of the grain-based geometry, even around isolated particles the contribution of the diffuse-layer polarization is negligible, such that it is not necessary to assume that the diffuse layers are percolating or "shorted". On the other hand, the results of the membrane-polarization model indicate that even in the case of continuous (or percolating) diffuse and Stern layer geometries both layers can polarize. Thus, the discontinuity of neither of the two layers is needed to generate a polarization response. Clearly, more systematic research into the Stern-layer polarization in such percolating systems is needed. However, our results strongly suggest that the currently prevailing view on this important mechanism needs to be reconsidered.

The direct comparison of a purely grain-based polarization with the membrane-polarization furthermore indicates that the transition between the two models with increasing degrees of compaction and cementation can be expected to be gradual. Interestingly, the fundamental responses of both processes are rather similar as long as the EDLs and particularly the Stern layers are assumed to be discontinuous at the pore scale. Because in both models the Stern layer dominates the polarization response, the distinction between effects related to the individual grains and effects related to pore constrictions becomes somewhat obsolete or at least a mere question of the point of view. Ultimately, this means that responses caused by pore constrictions, i.e. typical membrane-polarization responses, can – at least to a certain degree – be adjusted using grain-based models and vice versa. This is particularly plausible, if we consider that in granular media made of near-spherical particles the pore diameters and lengths are of the same order of magnitude as the typical grain sizes and thus all relaxation times are controlled by similar characteristic lengths.

6.6 Conclusions

We have investigated the low-frequency electrical conductivity of porous media by means of improved analytical and numerical models for single-grain and

pore-constriction geometries. Our results allowed us to assess the relative contributions of polarization mechanisms originating from the diffuse part and the Stern layer of the EDL covering charged mineral surfaces.

To match our numerical results obtained for the single-grain geometry, we assembled a new analytical model by combining the Dukhin-Shilov model (Dukhin and Shilov, 1974), which accounts for the diffuse-layer polarization, with the Schurr model of the Stern-layer polarization (Schurr, 1964) including the correction of the relaxation time of the Stern layer proposed by Lyklema et al. (1983). The use of the corrected relaxation time, which accounts for the interaction of the charges in the Stern layer with the electrolyte solution, improved the agreement of the analytical model with the numerical results significantly. If the correction is not considered, untypically high effective diffusion coefficients of the counter-ions in the Stern layer have to be assumed to compensate for neglecting the effect. For typical model parameters, the relative contribution of the diffuse-layer polarization was seen to be insignificant in comparison to the large response of the Stern layer. At high frequencies, our new analytical model also considers the effect of Maxwell-Wagner polarization.

Our numerical results for the pore-constriction geometry show a good agreement with the analytical membrane-polarization model by Bücker and Hördt (2013a), if we relate the mean ion concentrations of the cylindrical pores to Bikerman's expression for the surface conductivity of highly charged surfaces (Bikerman, 1933) and as long as no Stern layer is considered. For the first time we examine the role the Stern layer plays in the pore-constriction geometry in detail. Here, the diffuse layer makes a much smaller contribution to the total response than the Stern layer – at least as long as the charged surfaces are below the percolation threshold, i.e. the individual EDLs are not interconnected at the system scale. In the opposite case, diffuse and Stern-layer polarization are of the same magnitude for typical model parameter.

In conclusion, the modelled responses of single-grain and pore-constriction geometries are more similar than usually assumed, particularly if the polarization responses of both parts of the EDL are taken into account in both geometries. Below the percolation threshold, the Stern-layer dominates the macroscopic response, but as soon as the EDL becomes percolating, this dominance breaks down and both mechanisms contribute similar magnitudes. More detailed studies on specific pore geometries are clearly required to conclusively assess the relative importance of the different polarization mechanisms, but our study is a significant step towards this long-term goal and sets the basis for extensive

numerical studies.

Appendices

6.A Implementation into the COMSOL coefficient form PDE

The COMSOL partial differential equation (PDE) interface in coefficient form allows the definition of PDEs and systems of PDEs of the general type

$$e_a \frac{\partial^2 u}{\partial t^2} + d_a \frac{\partial u}{\partial t} + \nabla \cdot (-c\nabla u - \alpha u + \gamma) + \beta \cdot \nabla u + au = f \tag{6.49}$$

with the general boundary conditions

$$-\mathbf{n} \cdot (-c\nabla u - \alpha u + \gamma) = g - qu \quad \text{and} \tag{6.50}$$

$$u = s, \tag{6.51}$$

where u denotes the dependent variable and $\mathbf{n}$ is the inward-pointing unit normal vector (i.e. into the respective domain or subdomain).
Due to the cylindrical symmetry of the modelled problems, the system of PDEs only needs to be solved on two-dimensional modelling domains (see Figures 6.2 and 6.5) with coordinates $\mathbf{r} = (x, y)^T$ and gradient operator $\nabla = (\partial/\partial x, \partial/\partial y)^T$. As explained in more detail in the appendix of Bücker et al. (2018b), multiplying all coefficients in equations (6.49) and (6.50) by y yields a problem description in cylindrical coordinates.

6.A.1 Static solution

Te static problem set up by equations (6.6) and (6.7) is readily implemented by defining the dependent variable $u_1 = U^{(0)}(\mathbf{r})$ and setting the PDE coefficients $c_1 = y\varepsilon_0\varepsilon_a$ and $f_1 = -y2C_{\pm}^{\infty} e \sinh(u_1 e/(kT))$ in the electrolyte and $c_1 = y\varepsilon_0\varepsilon_a$ and $f_1 = 0$ in the solid phase. Note that throughout this appendix we will make use of the convention that all coefficients are assumed to be zero if not specified differently.
The fixed surface charge described by boundary condition (6.16) is realized by setting $g = -y\Sigma_d^{(0)}$ on all charged outer and inner boundaries. The definition of the reference potential at a distance far from the charged surfaces, equation 6.14), depends on the specific model: In the grain geometry, it is set by $s = 0$ on the left, right, and top boundary. In the membrane geometry, we establish the reference potential by defining the point-wise constraint $u_1 = 0$ at the two positions $(x = \pm(L_1 + L_2)/2, y = 0)$ located on the left and right boundary, respectively. In this case, on the remaining parts of left and right boundary, as

well as on the uncharged parts of the top boundary, standard no-flow boundary conditions are active. Because the axis $y = 0$ is defined as symmetry axis (selecting rotational symmetry in the model setup), no specific boundary conditions are needed on this boundary.

6.A.2 Frequency-dependent solution

For the frequency-dependent problem set up by the system of three coupled PDEs (6.8) and (6.9), which describe the physics in the electrolyte, the Laplace equation (6.13), which controls the electric field in the solid phase, and equation (6.11), which controls the variable surface charge in the Stern layer, need to be solved simultaneously. We combine the solution in the electrolyte and the solid phase in one dependent variable u_2 and define suitable PDE coefficients on each of the two subdomains (i.e. for electrolyte and solid phase separately). The variable u_2 is a column vector of length 3 and writes

$$\mathbf{u}_2 = \begin{bmatrix} u_{21} \\ u_{22} \\ u_{23} \end{bmatrix} = \begin{bmatrix} \delta C_-(\mathbf{r},\omega) \\ \delta C_+(\mathbf{r},\omega) \\ \delta U(\mathbf{r},\omega) \end{bmatrix}. \tag{6.52}$$

Assuming isotropy of all its elements, the coefficient c_2 is a 3-by-3 coefficient matrix. In the electrolyte it writes

$$\underline{c}_2 = \begin{bmatrix} yD & 0 & -y\mu C_-^\infty \exp(\frac{e}{kT}u_1) \\ 0 & yD & y\mu C_+^\infty \exp(-\frac{e}{kT}u_1) \\ 0 & 0 & y\varepsilon_0\varepsilon_a \end{bmatrix} \tag{6.53}$$

and in the solid phase

$$\underline{c}_2 = \begin{bmatrix} 0 & 0 & 0 \\ 0 & 0 & 0 \\ 0 & 0 & y\varepsilon_0\varepsilon_i \end{bmatrix}. \tag{6.54}$$

The dependent variable u_1 was defined above and denotes the static solution for the electrical potential. The coefficient matrix $\underline{\alpha}$ writes

$$\underline{\alpha}_2 = \begin{bmatrix} -y\mu\nabla u_1 & 0 & 0 \\ 0 & y\mu\nabla u_1 & 0 \\ 0 & 0 & 0 \end{bmatrix}, \tag{6.55}$$

in the electrolyte and is equal to the null matrix in the solid phase. Note that on our two-dimensional modelling domain each element of the matrix $\underline{\alpha}_2$ is a

two-element vector. The matrix $\underline{a}_2$ is

$$\underline{a}_2 = \begin{bmatrix} yi\omega & 0 & 0 \\ 0 & yi\omega & 0 \\ yF & -yF & 0 \end{bmatrix} \tag{6.56}$$

in the electrolyte. In the solid phase, $\underline{a}_2$ is the same except for the last line, which has to be filled with zeros instead.

Equation (6.11), which describes the perturbation surface charge density $\delta\Sigma_S$, has to be solved on the solid-liquid interface only. By means of a lower-dimensional physics interface, the curvature of this interface can be taken into account correctly. Because the electric potential in the Stern layer has to be equal to the potentials δU_i and δU_a on the corresponding boundaries, the only dependent variable on the one-dimensional subdomain is $u_3 = \delta\Sigma_S(\mathbf{r}_S, \omega)$. The coefficients take the form $c_3 = yD_S$, $a_3 = yi\omega$, and $\gamma_3 = -y\mu_S\Sigma_S^{(0)}\nabla u_{23}$, where u_{23} denotes the perturbation potentials on the adjacent two-dimensional subdomains.

The problem description is completed by the following set of boundary conditions. The boundary condition (6.17) describing the external excitation and the condition on the perturbation concentrations (6.18) are realized by setting $\mathbf{s}_2 = (0, 0, \pm E_0 L)^T$, respectively. In the membrane polarization model with the continuous EDL, this boundary is not located at a distance far from the charged surface. However, because of the symmetry of the problem with respect to $x = 0$, we expect the perturbation ion concentrations to vanish in this geometry, too (see e.g. concentration profiles in Blaschek and Hördt, 2009). For the same reason, also the perturbation surface charge density $\delta\Sigma_S$ is expected to vanish on the left and right boundary and we set $s_3 = 0$ (only applies in the model with the continuous EDL).

On the boundaries representing the solid-liquid interface, we implement zero-flux boundary conditions (6.20) on the two ion flux densities, and the condition on the displacement current (6.21) by defining $\mathbf{g} = (0, 0, yu_3)^T$.

On the top boundary, we implement a zero-flux boundary condition for all three components of the dependent variable u_2 resulting in vanishing normal fluxes for both ion species and a vanishing normal electrical field. In the case of the membrane-polarization model with the continuous EDL, parts of the top boundary represent charged surfaces and are thus furnished with the corresponding boundary conditions described above. In the membrane-polarization model with the discontinuous EDL, the one-dimensional domain representing the Stern layer also ends at the top boundary. In this case, we define no-flux boundary conditions for u_3, too.

Again, due to the rotational symmetry, no boundary conditions must be defined on the symmetry axis (i.e. along $y = 0$) for any of the dependent variables.

CHAPTER 7

Conclusion and perspectives

This thesis offers improvements of the theoretical description and basic understanding of all five principal induced-polarization mechanisms in geologic media, i.e. electrode polarization, Stern- and diffuse-layer polarization, membrane polarization, and (in passing) Maxwell-Wagner polarization. This final chapter summarizes the advances achieved regarding the mathematical description and modelling of these mechanisms and the progress made towards the development of a generalized theoretical treatment. At this point, significance and limitations of the individual developments can be discussed in a broader context than in the previous chapters, which also allows to identify challenges and specific tasks for future investigations into this matter.

Electrode polarization. The derivation of the full solution to the boundary-value problem for the Poisson-Nernst-Planck (PNP) model set up by Wong (1979) to describe electrode polarization, the derivation of explicit expressions for the relaxation times inherent to this model, and the (numerical) extension of the model to charged metallic particles are the main achievements regarding this polarization mechanism. Besides the obvious improvement of its mathematical description, these developments also offer a clearer view on the underlying polarization process.

In passing, the findings of chapters 4 and 5 disproved recent re-interpretations of the electrode-polarization process in terms of the polarization of the Stern-layer around dielectric particles (e.g. Gurin et al., 2015; Placencia-Gómez and Slater, 2015). The main arguments against such approach where the different variations of the relaxation times of electrode polarization and Stern-layer polarization with the particle radius a, $\tau_{\mathrm{dl}} \propto a\lambda_D$ and $\tau_S \propto a^2$, respectively, and the exactly opposite dependencies of the polarization magnitudes on surface charge.

Especially the critical particle radius a_c derived from the two relaxations times and the predicted sensitivity of the diffuse-layer charging mechanism to surface charge have important practical implications. The knowledge of the chemical

control on the dominating relaxation process (i.e. diffuse-layer charging vs. volume diffusion) contained in the critical particle radius can guide the selection of fluid compositions that favour the experimental observation of transitions between the two processes at sufficiently low frequencies. The general practical significance of the predicted control of surface charge on the polarization process lies in the improved theoretical basis for the exciting possibility to use IP data to infer the electrochemical surface state (i.e. surface potential, reactivity, etc.) of metallic nano- and micro-scale particles. Although more research into the relation between IP spectra and surface properties of metallic particles is required, the presented findings principally favour this kind of application.

Future tasks and challenges regarding the theoretical description of electrode polarization comprise – among others – (1) the incorporation of a frequency-dependent Stern-layer impedance into the boundary condition on the reaction current (e.g. Merriam, 2007), (2) the numerical investigation of more complex geometries than dilute suspensions of spherical particles (e.g. densely packed granular media, porous membranes, surface roughness, etc.), and (3) the extension of the theory to semi-conducting solid phases as initiated by Misra et al. (2016a) and Revil et al. (2015b).

Stern- and diffuse-layer polarization. The new analytical model of the coupled Stern- and diffuse-layer polarization around spherical particles improves the mathematical description of this process significantly. In particular, it recalls the simple but necessary correction of the Stern-layer relaxation time proposed by Lyklema et al. (1983) and replaces the incorporation of the diffuse-layer polarization via the model of Fixman (1980) by the better-suited model of Dukhin and Shilov (1974). Both modifications were shown to be necessary to obtain a good match with the numerical modelling results.

Special significance of the rediscovery of the corrected Stern-layer relaxation time derives from the explanation it offers for the to date unexplained disagreement between the high Stern-layer diffusion coefficients needed to adjust the model by Leroy et al. (2008) to measured IP data and the much lower values determined by independent experiments. Furthermore, the strong dependence of the corrected relaxation time on the electro-chemical properties of pore fluid and solid surface (i.e. salinity, surface charge and ζ-potential) has important practical implications as it puts a limitation on the often-used simple relation between relaxation time and grain size.

Possible shortcomings of the analytical and numerical descriptions of this polarization process around spherical particles regard (1) the simple implementation

of the Stern layer as a two-dimensional surface of vanishing thickness and (2) the neglect of ion-exchange reactions between Stern-layer and diffuse layer and/or bulk electrolyte. Useful future extensions of the theoretical treatment should examine the importance of the error introduced by these simplifications. Systematic studies using double-layer and bulk-electrolyte parameters based on a detailed double-layer model (e.g. Revil and Glover, 1997, 1998) could provide further insight into the polarization response for representative subsets of the large multi-dimensional parameter space of this polarization model.

Finally, the comparison of Stern- and diffuse-layer polarization processes around spherical grains and in pore-constriction geometries revealed unexpected similarities between the responses. This finding and the dominant role of the Stern-layer polarization in both geometries suggest that even (measured) IP responses produced by microscopic settings, which would classically be related to a membrane-like behaviour, might be interpreted in terms of a grain-based polarization model. Further (numerical) studies should therefore focus on the intermediate geometries to examine the gradual transition between the two processes.

Membrane polarization. Progress was also made regarding the theoretical description of membrane polarization. A previously developed analytical model (Bücker and Hördt, 2013a) was shown to provide a suitable description of the polarization process due to the diffuse layer covering the pore walls of the pore-constriction geometry. Equipped with an alternative incorporation of the mean ion concentrations for the case of highly charged pore walls (and sufficiently thin diffuse layers compared to the pore radius), this analytical model showed a good agreement with the corresponding numerical results. The numerical treatment furthermore provided a suitable means to study the relative contributions of diffuse- and Stern-layer polarization to the membrane-polarization response.

The extension of the analytical membrane-polarization model to the case of an additional immiscible liquid phase in the pore space permitted the investigation of the control wetting and non-wetting hydrocarbon contaminants might exert over the polarization response. The predictions of the extended model are particularly interesting, as they offered a theoretical explanation of the to date unexplained IP data from a hydrocarbon-contaminated site reported by Flores Orozco et al. (2012). Furthermore, due to the similar electrical properties (i.e. vanishing electrical conductivity and moderately charged surfaces) of liquid hydrocarbons, air-bubbles, CO_2-bubbles, and ice, the new analytic model can also be consulted to understand the membrane-polarization response of partially

saturated materials, materials containing free CO_2 gas, as well as freezing and thawing processes in permafrost sediments and rocks.

The main limitation of the analytical membrane-polarization model regards (1) the over-simplified incorporation of the Stern-layer contribution and (2) the cylindrical geometry, which has been argued to be unsuitable to represent the more complex geometrical configurations of real granular media. It might be possible to obtain a more adequate incorporation of the Stern layer by modelling its contribution in terms of a second impedance arranged in parallel to the impedance of the diffuse layer. The availability of a validated numerical modelling framework brings the analysis of more complex geometrical configurations within an achievable range.

Generalized numerical modelling framework. The validated numerical modelling framework described in this thesis is valuable in its own right. This becomes particularly apparent considering earlier unsuccessful searches for appropriate boundary conditions (and adaptations of the PNP system) to incorporate fixed surface charges into numerical modelling schemes (e.g. Volkmann and Klitzsch, 2010). The detailed description of the numerical implementation in a widely-used commercial finite-element modelling software provided in this thesis is therefore also connected to the hope to facilitate and promote future numerical investigations.

Moreover, the numerical implementations of the polarization problems around charged metallic and dielectric solids presented in chapters 5 and 6, respectively, can readily be combined to a generalized modelling framework including all five polarization mechanisms. With the detailed descriptions of PNP systems, boundary conditions, and post-processing tasks (e.g. the determination of the effective electrical conductivity) at hand, the generalization to asymmetric electrolytes, multi-component electrolytes, unequal mobilities of the involved ion species, and more complex geometric configurations of systems consisting of two or even more solid, liquid, and gaseous phases has come within reach. Besides the exploration of such geometrically and chemically complex systems, it would be desirable to make use of the generalized numerical modelling framework to aid the search for and validation of a generalized analytical treatment.

Generalization of analytical treatment. As the new coupled Stern- and diffuse-layer polarization model shows, a good approximation of the response of various simultaneously acting polarization processes can be obtained by a simple superposition of the individual responses. However, the quality of such combined models is limited by the quality of the individual models. Therefore, the new

coupled model, which also includes the effect of Maxwell-Wagner polarization at high frequencies, represents an important step towards the development of a generalized analytical treatment.

The PPIP-SCAIP model developed by Misra et al. (2016a) represents a suitable approach to combine the polarization responses of semiconducting (or metallic) and dielectric particles based on rather simple mixing formulae derived from effective-medium theory. Consequently, the integration of the electrode-polarization model with the coupled Stern- and diffuse-layer polarization model (including the Maxwell-Wagner response) is only a small step away. Similar volume-averaging approaches also allow for the generalization to mixtures containing grains of different sizes characterized by a grain-size distribution (e.g. Lesmes and Morgan, 2001; Leroy et al., 2008).

Such effective-medium approaches work well for the modelling of the responses of composite media, which can be described in terms of a homogeneous background phase (here the electrolyte) and homogeneously distributed inclusions (solid phase or phases). Therefore, the incorporation of the membrane-polarization phenomenon, the theoretical description of which is based on cylindrical pores, requires the use other up-scaling strategies. Recent studies report mathematical treatments of the IP responses of pore networks (e.g. Maineult et al., 2017; Stebner and Hördt, 2017). In particular, Stebner and Hördt (2017) describe the combination of membrane-polarization responses derived from the model by Bücker and Hördt (2013a) within two- and three-dimensional pore networks. In terms of the homogeneous background conductivity, the effective complex-conductivity response determined by such an up-scaling scheme could enter into the effective-medium description of grain-based polarization models. This would be the last step required to obtain a first analytical model describing the combined response of all five polarization mechanisms.

Hopefully, the developments presented in this thesis will be useful for the interpretation of a wealth of experimental IP data, for which mechanistic models were unavailable before, and promote the continued search for improved theoretical descriptions of the IP response of geological media.

Bibliography

Abdel Aal, G. Z. and Atekwana, E. A. (2013). Spectral induced polarization (SIP) response of biodegraded oil in porous media. *Geophysical Journal International*, 196(2):804–817.

Abdel Aal, G. Z., Atekwana, E. A., and Werkema, D. D. (2017). Complex conductivity response to silver nanoparticles in partially saturated sand columns. *Journal of Applied Geophysics*, 137:73–81.

Abdel Aal, G. Z., Slater, L. D., and Atekwana, E. A. (2006). Induced-polarization measurements on unconsolidated sediments from a site of active hydrocarbon biodegradation. *Geophysics*, 71(2):H13–H24.

Abdul, A. S., Kia, S. F., and Gibson, T. L. (1989). Limitations of monitoring wells for the detection and quantification of petroleum products in soils and aquifers. *Groundwater Monitoring & Remediation*, 9(2):90–99.

Abdulsamad, F., Florsch, N., and Camerlynck, C. (2017). Spectral induced polarization in a sandy medium containing semiconductor materials: experimental results and numerical modelling of the polarization mechanism. *Near Surface Geophysics*, 15(6):669–683.

Abramowitz, M. and Stegun, I. (1965). *Handbook of mathematical functions*. Dover Publications, NY.

Angoran, Y. and Madden, T. R. (1977). Induced polarization: A preliminary study of its chemical basis. *Geophysics*, 42(4):788–803.

Ashby, N. (1975). Relaxation of charge imbalances in conductors. *American Journal of Physics*, 43(6):553–555.

Atekwana, E. A. and Atekwana, E. A. (2010). Geophysical signatures of microbial activity at hydrocarbon contaminated sites: A review. *Surveys in Geophysics*, 31(2):247–283.

Atekwana, E. A., Sauck, W. A., and Werkema, D. D. (2000). Investigations of geoelectrical signatures at a hydrocarbon contaminated site. *Journal of applied Geophysics*, 44(2):167–180.

Atekwana, E. A. and Slater, L. D. (2009). Biogeophysics: A new frontier in earth science research. *Reviews of Geophysics*, 47(4).

Atkins, P. and De Paula, J. (2013). *Elements of physical chemistry*. Oxford University Press, USA.

Bairlein, K., Bücker, M., Hördt, A., and Hinze, B. (2016). Temperature dependence of spectral induced polarization data: experimental results and membrane polarization theory. *Geophysical Journal International*, 205(1):440–453.

Bazant, M. Z., Thornton, K., and Ajdari, A. (2004). Diffuse-charge dynamics in electrochemical systems. *Physical review E*, 70(2):021506.

Bikerman, J. (1933). Ionentheorie der Elektrosmose, der Strömungsströme und der Oberflächenleitfähigkeit. *Z. Physikalische Chemie A*, 163:378–394.

Blaschek, R. and Hördt, A. (2009). Numerical modelling of the IP effect at the pore scale. *Near Surface Geophysics*, 7(5-6):579–588.

Börner, F., Gruhne, M., and Schön, J. (1993). Contamination indications derived from electrical properties in the low frequency range. *Geophysical Prospecting*, 41(1):83–98.

Boulangé-Petermann, L., Doren, A., Baroux, B., and Bellon-Fontaine, M.-N. (1995). Zeta potential measurements on passive metals. *Journal of colloid and interface science*, 171(1):179–186.

Bruggeman, D. A. G. (1935). Berechnung verschiedener physikalischer Konstanten von heterogenen Substanzen. I. Dielektrizitätskonstanten und Leitfähigkeiten der Mischkörper aus isotropen Substanzen. *Annalen der Physik*, 416(7):636–664.

Buchheim, W. and Irmer, G. (1979). Zur Theorie der induzierten galvanischen Polarisation in Festkörpern mit elektrolytischer Porenfüllung. *Gerlands Beitr. Geophysik*, 88:53–72.

Bücker, M., Flores Orozco, A., Hördt, A., and Kemna, A. (2017). An analytical membrane-polarization model to predict the complex conductivity signature of immiscible liquid hydrocarbon contaminants. *Near Surface Geophysics*, 15(6):547–562.

Bücker, M., Flores Orozco, A., and Kemna, A. (2018a). Electro-chemical polarization around metallic particles – Part 1: The role of diffuse-layer and volume-diffusion relaxation. *Geophysics*, 83(4):1–53.

Bücker, M. and Hördt, A. (2013a). Analytical modelling of membrane polarization with explicit parametrization of pore radii and the electrical double layer. *Geophysical Journal International*, 194(2):804–813.

Bücker, M. and Hördt, A. (2013b). Long and short narrow pore models for membrane polarization. *Geophysics*, 78(6):E299–E314.

Bücker, M., Undorf, S., Flores Orozco, A., and Kemna, A. (2018b). Electrochemical polarization around metallic particles – Part 2: The role of diffuse surface charge. *accepted for publication in Geophysics*.

Buckley, J., Takamura, K., Morrow, N., et al. (1989). Influence of electrical surface charges on the wetting properties of crude oils. *SPE Reservoir Engineering*, 4(03):332–340.

Busscher, H., Van de Belt-Gritter, B., and Van der Mei, H. (1995). Implications of microbial adhesion to hydrocarbons for evaluating cell surface hydrophobicity 1. Zeta potentials of hydrocarbon droplets. *Colloids and surfaces B: Biointerfaces*, 5(3-4):111–116.

Butt, H. J., Graf, K., and Kappl, M. (2003). *Physics and chemistry of interfaces, 2003*. Wiley-VCH.

Cassiani, G., Binley, A., Kemna, A., Wehrer, M., Flores Orozco, A., Deiana, R., Boaga, J., Rossi, M., Dietrich, P., Werban, U., et al. (2014). Noninvasive characterization of the trecate (italy) crude-oil contaminated site: links between contamination and geophysical signals. *Environmental Science and Pollution Research*, 21(15):8914–8931.

Cassiani, G., Kemna, A., Villa, A., and Zimmermann, E. (2009). Spectral induced polarization for the characterization of free-phase hydrocarbon contamination of sediments with low clay content. *Near Surface Geophysics*, 7(5-6):547–562.

Cassidy, D. P., Werkema Jr, D. D., Sauck, W., Atekwana, E., Rossbach, S., and Duris, J. (2001). The effects of lnapl biodegradation products on electrical conductivity measurements. *Journal of Environmental & Engineering Geophysics*, 6(1):47–52.

Caterina, D., Orozco, A. F., and Nguyen, F. (2017). Long-term ert monitoring of biogeochemical changes of an aged hydrocarbon contamination. *Journal of contaminant hydrology*, 201:19–29.

Chambers, J., Loke, M., Ogilvy, R., and Meldrum, P. (2004). Noninvasive monitoring of dnapl migration through a saturated porous medium using electrical impedance tomography. *Journal of contaminant hydrology*, 68(1):1–22.

Chatzis, I., Morrow, N. R., and Lim, H. T. (1983). Magnitude and detailed structure of residual oil saturation. *Society of Petroleum Engineers Journal*, 23(02):311–326.

Chew, W. and Sen, P. (1982a). Dielectric enhancement due to electrochemical double layer: thin double layer approximation. *The Journal of Chemical Physics*, 77(9):4683–4693.

Chew, W. and Sen, P. (1982b). Potential of a sphere in an ionic solution in thin double layer approximations. *The Journal of Chemical Physics*, 77(4):2042–2044.

Cole, K. S. and Cole, R. H. (1941). Dispersion and absorption in dielectrics I. Alternating current characteristics. *The Journal of chemical physics*, 9(4):341–351.

Comba, S. and Sethi, R. (2009). Stabilization of highly concentrated suspensions of iron nanoparticles using shear-thinning gels of xanthan gum. *Water research*, 43(15):3717–3726.

Cozzarelli, I. M., Herman, J. S., Baedecker, M. J., and Fischer, J. M. (1999). Geochemical heterogeneity of a gasoline-contaminated aquifer. *Journal of Contaminant Hydrology*, 40(3):261–284.

Daily, W., Ramirez, A., LaBrecque, D., and Barber, W. (1995). Electrical resistance tomography experiments at the oregon graduate institute. *Journal of Applied Geophysics*, 33(4):227–237.

de Lima, O. A. and Sharma, M. M. (1992). A generalized Maxwell-Wagner theory for membrane polarization in shaly sands. *Geophysics*, 57(3):431–440.

Deceuster, J. and Kaufmann, O. (2012). Improving the delineation of hydrocarbon-impacted soils and water through induced polarization (IP) tomographies: A field study at an industrial waste land. *Journal of Contaminant Hydrology*, 136:25–42.

DeLacey, E. H. and White, L. R. (1981). Dielectric response and conductivity of dilute suspensions of colloidal particles. *Journal of the Chemical Society, Faraday Transactions 2: Molecular and Chemical Physics*, 77(11):2007–2039.

Dukhin, S. and Shilov, V. (1974). *Dielectric Phenomena and the Double Layer in Disperse Systems and Polyelectrolytes*. Wiley, New York.

Farooq, U., Simon, S., Tweheyo, M. T., Sjöblom, J., and Øye, G. (2013). Electrophoretic measurements of crude oil fractions dispersed in aqueous solutions of different ionic compositions—evaluation of the interfacial charging mechanisms. *Journal of Dispersion Science and Technology*, 34(10):1376–1381.

Fixman, M. (1980). Charged macromolecules in external fields. I. The sphere. *The Journal of Chemical Physics*, 72(9):5177–5186.

Flekkøy, E. G. (2013). A physical basis for the Cole-Cole description of electrical conductivity of mineralized porous media. *Geophysics*, 78(5):D355–D368.

Flores Orozco, A., Kemna, A., Oberdörster, C., Zschornack, L., Leven, C., Dietrich, P., and Weiss, H. (2012). Delineation of subsurface hydrocarbon contamination at a former hydrogenation plant using spectral induced polarization imaging. *Journal of contaminant hydrology*, 136:131–144.

Flores Orozco, A., Velimirovic, M., Tosco, T., Kemna, A., Sapion, H., Klaas, N., Sethi, R., and Bastiaens, L. (2015). Monitoring the injection of microscale zerovalent iron particles for groundwater remediation by means of complex electrical conductivity imaging. *Environmental science & technology*, 49(9):5593–5600.

Flores Orozco, A., Williams, K. H., and Kemna, A. (2013). Time-lapse spectral induced polarization imaging of stimulated uranium bioremediation. *Near Surface Geophysics*, 11(5):531–544.

Flores Orozco, A., Williams, K. H., Long, P. E., Hubbard, S. S., and Kemna, A. (2011). Using complex resistivity imaging to infer biogeochemical processes associated with bioremediation of an uranium-contaminated aquifer. *Journal of Geophysical Research: Biogeosciences*, 116(G3).

Forté, S. and Bentley, L. R. (2013). Effect of hydrocarbon contamination on streaming potential. *Near Surface Geophysics*, 11(1):75–83.

Fridrikhsberg, D. and Sidorova, M. (1961). A study of relationship between the induced polarization phenomenon and the electro-kinetic properties of capillary systems (in Russian). *Vestnik Leningradskogo Universiteta, Seria Chimia*, 4:222–226.

Gaiser, C., Fellmuth, B., Haft, N., Kuhn, A., Thiele-Krivoi, B., Zandt, T., Fischer, J., Jusko, O., and Sabuga, W. (2017). Final determination of the boltzmann constant by dielectric-constant gas thermometry. *Metrologia*, 54(3):280.

Garcia, A., Grosse, C., and Brito, P. (1985). On the effect of volume charge distribution on the Maxwell-Wagner relaxation. *Journal of Physics D: Applied Physics*, 18(4):739.

Grahame, D. C. (1947). The electrical double layer and the theory of electrocapillarity. *Chemical reviews*, 41(3):441–501.

Grosse, C. and Shilov, V. N. (1996). Theory of the low-frequency electrorotation of polystyrene particles in electrolyte solution. *The Journal of Physical Chemistry*, 100(5):1771–1778.

Günther, T. and Martin, T. (2016). Spectral two-dimensional inversion of frequency-domain induced polarization data from a mining slag heap. *Journal of Applied Geophysics*, 135:436–448.

Gurin, G., Titov, K., Ilyin, Y., and Tarasov, A. (2015). Induced polarization of disseminated electronically conductive minerals: A semi-empirical model. *Geophysical Journal International*, 200(3):1555–1565.

Gvirtzman, H. and Roberts, P. V. (1991). Pore scale spatial analysis of two immiscible fluids in porous media. *Water Resources Research*, 27(6):1165–1176.

Hanai, T. (1960). Theory of the dielectric dispersion due to the interfacial polarization and its application to emulsions. *Kolloid-Zeitschrift*, 171(1):23–31.

Hanai, T. (1962). Dielectric theory on the interfacial polarization for two-phase mixtures. *Bulletin of the Institute for Chemical Research, Kyoto University*.

Hinch, E. J., Sherwood, J. D., Chew, W. C., and Sen, P. N. (1984). Dielectric response of a dilute suspension of spheres with thin double layers in an asymmetric electrolyte. *Journal of the Chemical Society, Faraday Transactions 2: Molecular and Chemical Physics*, 80(5):535–551.

Hördt, A., Bairlein, K., Bielefeld, A., Bücker, M., Kuhn, E., Nordsiek, S., and Stebner, H. (2016). The dependence of induced polarization on fluid salinity and pH, studied with an extended model of membrane polarization. *Journal of Applied Geophysics*.

Hördt, A., Bairlein, K., Bücker, M., and Stebner, H. (2017). Geometrical constraints for membrane polarization. *submitted to Near Surface Geophysics*.

Hördt, A., Druiventak, A., Blaschek, R., Binot, F., Kemna, A., Kreye, P., and Zisser, N. (2009). Case histories of hydraulic conductivity estimation with induced polarization at the field scale. *Near Surface Geophysics*, 7(5-6):529–545.

Hunter, R. (1981). *Zeta Potential in Colloid Science: Principles and Applications*. Academic Press, London.

Jia, W., Ren, S., and Hu, B. (2013). Effect of water chemistry on zeta potential of air bubbles. *Int. J. Electrochem. Sci*, 8:5828–5837.

Johansson, S., Fiandaca, G., and Dahlin, T. (2015). Influence of non-aqueous phase liquid configuration on induced polarization parameters: conceptual models applied to a time-domain field case study. *Journal of Applied Geophysics*, 123:295–309.

Joyce, R. A., Glaser, D. R., Werkema, D. D., and Atekwana, E. A. (2012). Spectral induced polarization response to nanoparticles in a saturated sand matrix. *Journal of applied geophysics*, 77:63–71.

Kanicky, J. R., Lopez Montilla, J. C., Pandey, S., and Shah, D. O. (2001). Surface chemistry in the petroleum industry. *Handbook of applied surface and colloid chemistry*, 1:251–267.

Kemna, A., Binley, A., Cassiani, G., Niederleithinger, E., Revil, A., Slater, L., Williams, K. H., Flores Orozco, A., Haegel, F.-H., Hoerdt, A., et al. (2012). An overview of the spectral induced polarization method for near-surface applications. *Near Surface Geophysics*, 10(6):453–468.

Kemna, A., Binley, A., and Slater, L. (2004). Crosshole IP imaging for engineering and environmental applications. *Geophysics*, 69(1):97–107.

Kemna, A., Räkers, E., and Dresen, L. (1999). Field applications of complex resistivity tomography. In *SEG Technical Program Expanded Abstracts 1999*, pages 331–334. Society of Exploration Geophysicists.

Kijlstra, J., van Leeuwen, H. P., and Lyklema, J. (1992). Effects of surface conduction on the electrokinetic properties of colloids. *Journal of the Chemical Society, Faraday Transactions*, 88(23):3441–3449.

Klein, J. and Shuey, R. (1978). Nonlinear impedance of mineral-electrolyte interfaces: Part I. Pyrite. *Geophysics*, 43(6):1222–1234.

Kosmulski, M. (2006). Electric charge density of silica, alumina, and related surfaces. In Somasundaran, P., editor, *Encyclopedia of surface and colloid science*, volume 3, pages 1857–1867. CRC press, New York, London.

Lee, J. H., Oh, M. H., Park, J., Lee, S. H., and Ahn, K. H. (2003). Dielectric dispersion characteristics of sand contaminated by heavy metal, landfill leachate and BTEX (02-104b). *Journal of hazardous materials*, 105(1):83–102.

Leroy, P. and Revil, A. (2004). A triple-layer model of the surface electrochemical properties of clay minerals. *Journal of Colloid and Interface Science*, 270(2):371–380.

Leroy, P. and Revil, A. (2009). A mechanistic model for the spectral induced polarization of clay materials. *Journal of Geophysical Research: Solid Earth*, 114(B10).

Leroy, P., Revil, A., Kemna, A., Cosenza, P., and Ghorbani, A. (2008). Complex conductivity of water-saturated packs of glass beads. *Journal of Colloid and Interface Science*, 321(1):103–117.

Lesmes, D. P. and Frye, K. M. (2001). Influence of pore fluid chemistry on the complex conductivity and induced polarization responses of berea sandstone. *Journal of Geophysical Research: Solid Earth*, 106(B3):4079–4090.

Lesmes, D. P. and Morgan, F. D. (2001). Dielectric spectroscopy of sedimentary rocks. *Journal of Geophysical Research: Solid Earth*, 106(B7):13329–13346.

Li, C., Tercier, P., and Knight, R. (2001). Effect of sorbed oil on the dielectric properties of sand and clay. *Water Resources Research*, 37(6):1783–1793.

Lyklema, J., Dukhin, S., and Shilov, V. (1983). The relaxation of the double layer around colloidal particles and the low-frequency dielectric dispersion: Part I. Theoretical considerations. *Journal of Electroanalytical Chemistry and Interfacial Electrochemistry*, 143(1-2):1–21.

Maineult, A., Revil, A., Camerlynck, C., Florsch, N., and Titov, K. (2017). Upscaling of spectral induced polarization response using random tube networks. *Geophysical Journal International*, 209(2):948–960.

Marinova, K., Alargova, R., Denkov, N., Velev, O., Petsev, D., Ivanov, I., and Borwankar, R. (1996). Charging of oil- water interfaces due to spontaneous adsorption of hydroxyl ions. *Langmuir*, 12(8):2045–2051.

Marshall, D. J. and Madden, T. R. (1959). Induced polarization, a study of its causes. *Geophysics*, 24(4):790–816.

Martinho, E., Almeida, F., and Matias, M. S. (2006). An experimental study of organic pollutant effects on time domain induced polarization measurements. *Journal of Applied Geophysics*, 60(1):27–40.

Maxwell, J. C. (1891). *A Treatise on Electricity and Magnetism*. Clarendon Press, Oxford.

Maxwell, J. C. (1892). *A treatise on electricity and magnetism*. Clarendon, Oxford, England, 3rd edition.

Merriam, J. (2007). Induced polarization and surface electrochemistry. *Geophysics*, 72(4):F157–F166.

Misra, S., Torres-Verdín, C., Homan, D., and Rasmus, J. (2017). Dispersive and directional electrical conductivity and dielectric permittivity of conductive-mineral-bearing samples derived from multifrequency tensor electromagnetic induction measurements. *Geophysics*, 82(4):D211–D223.

Misra, S., Torres-Verdín, C., Revil, A., Rasmus, J., and Homan, D. (2016a). Interfacial polarization of disseminated conductive minerals in absence of redox-active species—Part 1: Mechanistic model and validation. *Geophysics*, 81(2):E139–E157.

Misra, S., Torres-Verdín, C., Revil, A., Rasmus, J., and Homan, D. (2016b). Interfacial polarization of disseminated conductive minerals in absence of redox-active species—Part 2: Effective electrical conductivity and dielectric permittivity. *Geophysics*, 81(2):E159–E176.

Morris, D. A. and Johnson, A. I. (1967). Summary of hydrologic and physical properties of rock and soil materials, as analyzed by the hydrologic laboratory of the US Geological Survey, 1948-60. Technical report, US Govt. Print. Off.

Nernst, W. (1888). Zur Kinetik der in Lösung befindlichen Körper. *Zeitschrift für physikalische Chemie*, 2(1):613–637.

Nernst, W. (1889). Die elektromotorische Wirksamkeit der Jonen. *Zeitschrift für physikalische Chemie*, 4(1):129–181.

Newell, C. J., Acree, S. D., Ross, R. R., and Huling, S. G. (1995). Ground water issue: light nonaqueous phase liquids. Technical report, United States Environmental Protection Agency, Office of Research and Development, Office of Solid Waste and Emergency Response: Superfund Technology Support Center for Ground Water, Robert S. Kerr Environmental Research Laboratory.

Nordsiek, S. and Weller, A. (2008). A new approach to fitting induced-polarization spectra. *Geophysics*, 73(6):F235–F245.

O'Konski, C. T. (1960). Electric properties of macromolecules. V. Theory of ionic polarization in polyelectrolytes. *The Journal of Physical Chemistry*, 64(5):605–619.

Olhoeft, G. (1985). Low-frequency electrical properties. *Geophysics*, 50(12):2492–2503.

Olhoeft, G. R. (1992). Geophysical detection of hydrocarbon and organic chemical contamination. In *Symposium on the Application of Geophysics to Engineering and Environmental Problems 1992*, pages 587–595. Society of Exploration Geophysicists.

Pearce, C. I., Pattrick, R. A., and Vaughan, D. J. (2006). Electrical and magnetic properties of sulfides. *Reviews in Mineralogy and Geochemistry*, 61(1):127–180.

Pelton, W., Ward, S., Hallof, P., Sill, W., and Nelson, P. H. (1978). Mineral discrimination and removal of inductive coupling with multifrequency IP. *Geophysics*, 43(3):588–609.

Placencia-Gómez, E., Parviainen, A., Slater, L., and Leveinen, J. (2015). Spectral induced polarization (SIP) response of mine tailings. *Journal of contaminant hydrology*, 173:8–24.

Placencia-Gómez, E. and Slater, L. D. (2014). Electrochemical spectral induced polarization modeling of artificial sulfide-sand mixtures. *Geophysics*, 79(6):EN91–EN106.

Placencia-Gómez, E. and Slater, L. D. (2015). On the pore water chemistry effect on spectral induced polarization measurements in the presence of pyrite. *Journal of Applied Geophysics*.

Planck, M. (1890). Ueber die Erregung von Electricität und Wärme in Electrolyten. *Annalen der Physik*, 275(2):161–186.

Revil, A., Abdel Aal, G. Z., Atekwana, E. A., Mao, D., and Florsch, N. (2015a). Induced polarization response of porous media with metallic particles—part 2: Comparison with a broad database of experimental data. *Geophysics*, 80(5):D539–D552.

Revil, A. and Florsch, N. (2010). Determination of permeability from spectral induced polarization in granular media. *Geophysical Journal International*, 181(3):1480–1498.

Revil, A., Florsch, N., and Mao, D. (2015b). Induced polarization response of porous media with metallic particles—Part 1: A theory for disseminated semiconductors. *Geophysics*, 80(5):D525–D538.

Revil, A. and Glover, P. (1997). Theory of ionic-surface electrical conduction in porous media. *Physical Review B*, 55(3):1757.

Revil, A. and Glover, P. (1998). Nature of surface electrical conductivity in natural sands, sandstones, and clays. *Geophysical Research Letters*, 25(5):691–694.

Revil, A., Schmutz, M., and Batzle, M. L. (2011). Influence of oil wettability upon spectral induced polarization of oil-bearing sands. *Geophysics*, 76(5):A31–A36.

Reyes-Bozo, L., Escudey, M., Vyhmeister, E., Higueras, P., Godoy-Faúndez, A., Salazar, J. L., Valdés-González, H., Wolf-Sepúlveda, G., and Herrera-Urbina, R. (2015). Adsorption of biosolids and their main components on chalcopyrite, molybdenite and pyrite: Zeta potential and ftir spectroscopy studies. *Minerals Engineering*, 78:128–135.

Robinson, D. and Friedman, S. (2003). A method for measuring the solid particle permittivity or electrical conductivity of rocks, sediments, and granular materials. *Journal of Geophysical Research: Solid Earth*, 108(B2).

Sahloul, N., Ioannidis, M., and Chatzis, I. (2002). Dissolution of residual non-aqueous phase liquids in porous media: Pore-scale mechanisms and mass transfer rates. *Advances in water resources*, 25(1):33–49.

Sauck, W. A. (2000). A model for the resistivity structure of LNAPL plumes and their environs in sandy sediments. *Journal of Applied Geophysics*, 44(2):151–165.

Schmitt, M., Halisch, M., Müller, C., and Fernandes, C. (2016). Classification and quantification of pore shapes in sandstone reservoir rocks with 3-d x-ray micro-computed tomography. *Solid Earth Discussions*, 7(4):285–300.

Schmutz, M., Revil, A., Vaudelet, P., Batzle, M., Viñao, P. F., and Werkema, D. (2010). Influence of oil saturation upon spectral induced polarization of oil-bearing sands. *Geophysical Journal International*, 183(1):211–224.

Schumacher, D. (1996). Hydrocarbon-induced alteration of soils and sediments. In Schumacher, D. and Abrams, M. A., editors, *Hydrocarbon migration and its nearsurface expression: AAPG Memoir 66*, pages 71–89. AAPG Special Volumes.

Schurr, J. (1964). On the theory of the dielectric dispersion of spherical colloidal particles in electrolyte solution. *The Journal of Physical Chemistry*, 68(9):2407–2413.

Schwarz, G. (1962). A theory of the low-frequency dielectric dispersion of colloidal particles in electrolyte solution. *The Journal of Physical Chemistry*, 66(12):2636–2642.

Seigel, H., Nabighian, M., Parasnis, D. S., and Vozoff, K. (2007). The early history of the induced polarization method. *The Leading Edge*, 26(3):312–321.

Shi, Z., Fan, D., Johnson, R. L., Tratnyek, P. G., Nurmi, J. T., Wu, Y., and Williams, K. H. (2015). Methods for characterizing the fate and effects of nano zerovalent iron during groundwater remediation. *Journal of contaminant hydrology*, 181:17–35.

Shilov, V., Delgado, A., Gonzalez-Caballero, F., and Grosse, C. (2001). Thin double layer theory of the wide-frequency range dielectric dispersion of suspensions of non-conducting spherical particles including surface conductivity of the stagnant layer. *Colloids and Surfaces A: Physicochemical and Engineering Aspects*, 192(1):253–265.

Slater, L. and Binley, A. (2006). Synthetic and field-based electrical imaging of a zerovalent iron barrier: Implications for monitoring long-term barrier performance. *Geophysics*, 71(5):B129–B137.

Slater, L. and Glaser, D. (2003). Controls on induced polarization in sandy unconsolidated sediments and application to aquifer characterization. *Geophysics*, 68(5):1547–1558.

Soga, K., Page, J., and Illangasekare, T. (2004). A review of napl source zone remediation efficiency and the mass flux approach. *Journal of Hazardous Materials*, 110(1):13–27.

Sogade, J. A., Scira-Scappuzzo, F., Vichabian, Y., Shi, W., Rodi, W., Lesmes, D. P., and Morgan, F. D. (2006). Induced-polarization detection and mapping of contaminant plumes. *Geophysics*, 71(3):B75–B84.

Somasundaran, P. (2006). *Encyclopedia of surface and colloid science*, volume 2. CRC press, New York, London.

Sonavane, G., Tomoda, K., and Makino, K. (2008). Biodistribution of colloidal gold nanoparticles after intravenous administration: Effect of particle size. *Colloids and Surfaces B: Biointerfaces*, 66(2):274–280.

Stachurski, J. and MichaŁek, M. (1996). The effect of the ζ potential on the stability of a non-polar oil-in-water emulsion. *Journal of colloid and interface science*, 184(2):433–436.

Stebner, H. and Hördt, A. (2017). Simulation of membrane polarization of porous media with impedance networks. *submitted to Near Surface Geophysics*.

Sund, J., Alenius, H., Vippola, M., Savolainen, K., and Puustinen, A. (2011). Proteomic characterization of engineered nanomaterial–protein interactions in relation to surface reactivity. *Acs Nano*, 5(6):4300–4309.

Titov, K., Kemna, A., Tarasov, A., and Vereecken, H. (2004). Induced polarization of unsaturated sands determined through time domain measurements. *Vadose Zone Journal*, 3(4):1160–1168.

Titov, K., Komarov, V., Tarasov, V., and Levitski, A. (2002). Theoretical and experimental study of time domain-induced polarization in water-saturated sands. *Journal of Applied Geophysics*, 50(4):417 – 433.

Ustra, A., Slater, L., Ntarlagiannis, D., and Elis, V. (2012). Spectral induced polarization (SIP) signatures of clayey soils containing toluene. *Near Surface Geophysics*, 10(6):503–515.

Vanhala, H. (1997). Mapping oil-contaminated sand and till with the spectral induced polarization (SIP) method. *Geophysical prospecting*, 45(2):303–326.

Vanhala, H., Soininen, H., and Kukkonen, I. (1992). Detecting organic chemical contaminants by spectral-induced polarization method in glacial till environment. *Geophysics*, 57(8):1014–1017.

Vinegar, H. and Waxman, M. (1984). Induced polarization of shaly sands. *Geophysics*, 49(8):1267–1287.

Volkmann, J. and Klitzsch, N. (2010). Frequency-dependent electric properties of microscale rock models for frequencies from one millihertz to ten kilohertz. *Vadose Zone Journal*, 9(4):858–870.

Wagner, K. W. (1914). Erklärung der Dielektrischen Nachwirkungsvorgänge auf Grund Maxwellscher Vorstellungen. *Electrical Engineering (Archiv fur Elektrotechnik)*, 2(9):371–387.

Wainwright, H. M., Flores Orozco, A., Bücker, M., Dafflon, B., Chen, J., Hubbard, S. S., and Williams, K. H. (2015). Hierarchical bayesian method for mapping biogeochemical hot spots using induced polarization imaging. *Water Resources Research*.

Wait, J. R. (1958). A phenomenological theory of induced electrical polarization. *Canadian Journal of Physics*, 36(12):1634–1644.

Weller, A. and Börner, F. (1996). Measurements of spectral induced polarization for environmental purposes. *Environmental Geology*, 27(4):329–334.

Weller, A., Gruhne, M., Börner, F. D., and Seichter, M. (1997). Monitoring hydraulic experiments by complex conductivity tomography. In *Symposium on the Application of Geophysics to Engineering and Environmental Problems 1997*, pages 745–754. Society of Exploration Geophysicists.

Weller, A. and Slater, L. (2012). Salinity dependence of complex conductivity of unconsolidated and consolidated materials: Comparisons with electrical double layer models. *Geophysics*.

Weller, A., Slater, L., and Nordsiek, S. (2013). On the relationship between induced polarization and surface conductivity: Implications for petrophysical interpretation of electrical measurements. *Geophysics*, 78(5):D315–D325.

Weller, A., Zhang, Z., and Slater, L. (2015). High-salinity polarization of sandstones. *Geophysics*, 80(3):D309–D318.

Wong, J. (1979). An electrochemical model of the induced-polarization phenomenon in disseminated sulfide ores. *Geophysics*, 44(7):1245–1265.

Wong, J. and Strangway, D. (1981). Induced polarization in disseminated sulfide ores containing elongated mineralization. *Geophysics*, 46(9):1258–1268.

Yang, C., Dabros, T., Li, D., Czarnecki, J., and Masliyah, J. H. (2001). Measurement of the zeta potential of gas bubbles in aqueous solutions by microelectrophoresis method. *Journal of Colloid and Interface Science*, 243(1):128–135.

Zhao, W. and Ioannidis, M. (2003). Pore network simulation of the dissolution of a single-component wetting nonaqueous phase liquid. *Water resources research*, 39(10).

Zhao, W. and Ioannidis, M. A. (2007). Effect of NAPL film stability on the dissolution of residual wetting NAPL in porous media: A pore-scale modeling study. *Advances in water resources*, 30(2):171–181.

Zukoski, C. and Saville, D. (1986). The interpretation of electrokinetic measurements using a dynamic model of the stern layer: II. Comparisons between theory and experiment. *Journal of colloid and interface science*, 114(1):45–53.

List of symbols and abbreviations

a	Particle radius (m)
a_c	Critical particle radius (m)
A_1, A_2	Cross-sectional areas of wide and narrow pore (m^2)
$b_{p,n}$, $b_\pm$	Norm. mean concentrations of cations ($p/+$) and anions ($n/-$) (-)
c_0	Bulk ion concentration (mol/m^3)
c_j	Concentration of j-th ion species (mol/m^3)
c_j^∞	Bulk concentration of j-th ion species (mol/m^3)
$c_j^{(0)}$	Static background concentration of j-th ion species (mol/m^3)
$c_{p,n}$	Static background ion concentrations (mol/m^3)
$C_\pm$	Bulk ion concentration ($1/m^3$)
$C_\pm^{(0)}$	Static background ion concentrations ($1/m^3$)
Cl^-	Chloride ion
CO_2	Carbon dioxide
d	Distance from surface (m)
D	Diffusion coefficient (m^2/s)
$\mathbf{D}$	Displacement field ($C/(m^2)$)
D_j	Diffusion coefficient of j-th ion species (m^2/s)
$D_{p,n}$, $D_\pm$	Diffusion coefficient of cations ($p/+$) and anions ($n/-$) (m^2/s)
DC	*Direct current*
DL	*Diffuse layer*
D_S	Diffusion coefficient of ions in Stern layer (m^2/s)
$Du(\zeta)$	Dukhin number for spherical particles (-)
$Du(\zeta, R_i)$	Dukhin number for cylindrical pores (-)
e	Elementary charge (C)
e	Euler's number (-)
e^-	Free electron
$\mathbf{e_x}$	Unit vector in x-direction (-)
$\mathbf{E}$	Electric field vector (V/m)

E_0	Amplitude of external electric field (V/m)
$\mathbf{E}_{\text{ext}}$	External electric field vector (V/m)
EDL	*Electric double layer*
$f(\omega)$	Frequency-dependent reflection coefficient (-)
$f_d(\omega)$	Reflection coefficient of diffuse-layer polarization (-)
f_{DC}	Direct-current limit of reflection coefficient (-)
$f_k(\omega)$	Reflection coefficient model by O'Konski (1960) (-)
f_Q	Partition coefficient as defined by Leroy and Revil (2004) (-)
$f_S(\omega)$	Reflection coefficient of Stern-layer polarization (-)
F	Faraday constant (C/mol)
Fe(II)	Iron(II)-oxid ion
$\mathbf{H}$	Magnetic field (A/m)
HC	*Hydrocarbon*
i, j	Imaginary unit (-)
i	Exchange current density (C/(m^{2}s))
i_0	Equilibrium exchange current density (C/(m^{2}s))
IP	*Induced polarization*
$\mathbf{J}$	Total current density (C/(m^{2}s))
J_0	Bessel function of the second kind and order zero
$\mathbf{J}_\pm$	Current density (1/(m^{2}s))
$\mathbf{J}_c$	Conduction current density (C/(m^{2}s))
$\mathbf{J}_{\text{diff}}$	Diffusion flux density (mol/(m^{2}s))
$\mathbf{J}_j$	Flux density of j-th ion species (mol/(m^{2}s))
$\mathbf{J}_{\text{mig}}$	Migration flux density (mol/(m^{2}s))
$\mathbf{J}_{\text{reac}}$	Reaction flux density (mol/(m^{2}s))
k	Boltzmann constant (J/K)
k_+, k_-	Rate constants (m/s)
k_1	Spherical Bessel function of the second kind
k_1'	Derivative of k_1 with respect to r
K	Surface conductivity (S)
l	Distance of closest approach of metal ions (m)
L	Characteristic length scale of system (m)
L	Radius and half-length of cylindrical modelling domain (m)
L_1, L_2	Lengths of wide and narrow pore (m)
M	Correction coefficient of model by Lyklema et al. (1983) (-)
M^+	Metal ion in solution
$\text{M}_{(\text{ads})}$	Metal atom adsorbed to surface

$\mathbf{n}$	Unit normal vector to the surface/boundary (-)
N_A	Avogadro constant (1/mol)
Na^+	Sodium ion
NaCl	Sodium chloride
NAPL	*Non-aqueous phase liquid*
OH^-	Hydroxide ion
p	Ratio of surface charges in the Stern layer (-)
$\mathbf{P}$	Polarization density ($C/(m^2)$)
$\mathbf{P}_\varepsilon$, $\mathbf{P}_{\mathrm{IP}}$	Polarization density due to dielectric polarization, IP ($C/(m^2)$)
PNP	*Poisson-Nernst-Planck*
$\mathbf{r}$	Position vector (m)
r	Radial coordinate (m)
r_i	Radius of hydrocarbon droplet in i-th pore (m)
$\mathbf{r}_S$	Position vector in the Stern layer (m)
R	Pore radius (m)
R_0	Radius of outer cylinder (m)
R_1, R_2	Pore radius of wide and narrow pore (m)
RC	*Resistor-capacitor*
S_h	Hydrocarbon saturation (-)
S_w	Water saturation (-)
t	Time (s)
$t_{p,n}$, $t_\pm$	Average transference numbers of cations ($p/+$) and anions ($n/-$) (-)
T	Absolute temperature (K)
U	Electric potential (V)
$U^{(0)}$	Static background potential (V)
U_a	Total electric potential in liquid phase (V)
$U_a^{(0)}$	Static background potential in liquid phase (V)
U_i	Total electric potential in solid phase (V)
$U_i^{(0)}$	Static background potential in solid phase (V)
U_S	Total electric potential in Stern layer (V)
$U_S^{(0)}$	Static background potential in Stern layer (V)
V_h	Total hydrocarbon volume (m^3)
V_p	Total pore volume (m^3)
x	x-coordinate (Cartesian coordinates) (m)
y	y-coordinate (Cartesian coordinate system) (m)
Y_0	Bessel function of the second kind

z	z-coordinate (Cartesian coordinates) (m)
$z_\pm$	Ion valences of cations and anions (-)
z_j	Valence of j-th ion species (-)
Z	Impedance $\times$ area ($\Omega\mathrm{m}^2$)
Z_{DC}	Low-frequency limit of impedance $\times$ area ($\Omega\mathrm{m}^2$)
α	Reaction current parameter ($\mathrm{m}^2/(\mathrm{Vs})$)
β	Reaction current parameter (m/s)
δc_j	Perturbation concentration of j-th ion species ($\mathrm{mol}/\mathrm{m}^3$)
$\delta C_\pm$	Perturbation ion concentrations ($1/\mathrm{m}^3$)
δU	Perturbation potential (V)
δU_a	Perturbation potential in the electrolyte (V)
δU_{ext}	Perturbation potential due to external field (V)
δU_i	Perturbation potential in the solid phase (V)
δU_S	Perturbation potential in the Stern layer (V)
$\delta\Sigma_d^{(0)}$	Equiv. perturbation surface charge density of diffuse layer (C/m^2)
$\delta\Sigma_S^{(0)}$	Perturbation surface charge density in Stern layer (C/m^2)
ε	Permittivity ($\mathrm{C}/(\mathrm{Vm})$)
ε_0	Vacuum permittivity ($\mathrm{C}/(\mathrm{Vm})$)
ε_i	Relative permittivity of the solid phase (-)
$\varepsilon_{\mathrm{IP}}$	Eff. complex permittivity due to IP (S/m)
$\varepsilon_r, \varepsilon_a$	Relative permittivity of the pore fluid (-)
ζ	Zeta-potential (V)
ζ_h	Zeta-potential at hydrocarbon surface (V)
ζ_m	Zeta-potential at solid surface (V)
η	Current-producing overpotential (V)
η_0	Polarizability (-)
κ	Inverse Debye length (1/m)
λ_1, λ_2	Reciprocal length scales (1/m)
λ_D	Debye length (m)
μ	Uniform ion mobility ($\mathrm{m}^2/(\mathrm{Vs})$)
μ_j	Mobility of j-th ion species ($\mathrm{m}^2/(\mathrm{Vs})$)
$\mu_{p,n}$, $\mu_\pm$	Ion mobility of cations ($p/+$) and anions ($n/-$) ($\mathrm{m}^2/(\mathrm{Vs})$)
μ_S	Counter-ion mobility in the Stern layer ($\mathrm{m}^2/(\mathrm{Vs})$)
ν	Volume fraction of inclusions (-)
ν_{mod}	Volume fraction of inclusions of numerical model (-)

ρ	Charge density ($\mathrm{C/m^3}$)
ρ_0	Electrical resistivity of the bulk electrolyte (Ωm)
σ	Electrical conductivity (S/m)
σ^*, σ_{eff}	Effective complex conductivity (S/m)
σ'	Real part of electrical conductivity (S/m)
σ''	Imaginary part of electrical conductivity (S/m)
σ''_{max}	Maximum of imaginary part of electrical conductivity (S/m)
σ_a, σ_0	Low-frequency conductivity of bulk electrolyte (S/m)
σ_a^*	Complex conductivity of bulk electrolyte (S/m)
$\sigma_c^*(\omega)$	Effective conductivity of new coupled model (S/m)
σ_d	Effective conductivity of diffuse layer (S/m)
σ_{d+}	Effective conductivity of cations in diffuse layer (S/m)
σ_{d-}	Effective conductivity of anions in diffuse layer (S/m)
σ_d^*	Effective conductivity of Dukhin-Shilov model (S/m)
σ_{DC}	Direct-current limit of effective conductivity (S/m)
σ_i	Low-frequency conductivity of solid phase (S/m)
σ_i^*	Complex conductivity of solid phase (S/m)
σ_{IP}	Eff. complex conductivity due to IP (S/m)
$\sigma_{\mathrm{mod}}, \sigma^*_{\mathrm{mod}}$	Modelled effective conductivity (S/m)
σ_p	Effective particle conductivity (S/m)
σ_S	Effective conductivity of Stern layer (S/m)
σ_S^*	Effective conductivity of Schwarz-Lyklema model (S/m)
Σ	Surface charge density ($\mathrm{C/m^2}$)
Σ_0	Low-frequency limit of surface charge density ($\mathrm{C/m^2}$)
Σ_∞	High-frequency limit of surface charge density ($\mathrm{C/m^2}$)
Σ_d	Equiv. surface charge density of diffuse layer ($\mathrm{C/m^2}$)
Σ_{d+}	Equiv. surface charge density of cations in diffuse layer ($\mathrm{C/m^2}$)
Σ_{d-}	Equiv. surface charge density of anions in diffuse layer ($\mathrm{C/m^2}$)
$\Sigma_d^{(0)}$	Equiv. static background surface charge density of diffuse layer ($\mathrm{C/m^2}$)
Σ_S	Surface charge density in Stern layer ($\mathrm{C/m^2}$)
$\Sigma_S^{(0)}$	Static background surface charge density in Stern layer ($\mathrm{C/m^2}$)
τ_α	Relaxation time of static diffuse layer (s)
τ_{dl}	Relaxation time of field-induced diffuse layer (s)
τ_{el}	Relaxation time of electrolyte solution (s)
τ_{vd}	Relaxation time of volume-diffusion mechanism (s)
τ_c	Inverse critical angular frequency (s)

τ_i	Relaxation time of i-th pore (s)
τ_S	Relaxation time of Stern layer (s)
θ	Inclination (spherical coordinates) (rad)
φ	Phase shift (rad)
ϕ	Azimuth (spherical coordinates) (rad)
Φ	Porosity (-)
ω	Angular frequency (rad/s)
ω_c	Critical angular frequency (rad/s)
ω_{dl}	Inverse relaxation time of the diffuse layer (rad/s)
ω_{el}	Inverse relaxation time of the electrolyte solution (rad/s)
ω_{vd}	Inverse relaxation time of the volume diffusion (rad/s)